VIBRATIONAL RELAXATION AND ENERGY TRANSFER OF MATRIX ISOLATED HCl AND DCl

Jay Martin Wiesenfeld

Abstract

Vibrational kinetic and spectroscopic studies have bee performed on matrix-isolated HCl and DCl between 9 and 20 K. Vibrational relaxation rates for v=2 and v=1 have been measured by a tunable infrared laser-induced, time-resolved fluorescence technique. In an Ar matrix, vibrational decay times are faster than radiative and it is found that HCl relaxes about 35 times more rapidly than DCl, in spite of the fact that HCl must transfer more energy to the lattice than DCl. This result is explained by postulating that the rate-determining step for vibrational relaxation produces a highly rotationally excited guest in a V→R step; rotational relaxation into lattice phonons follows rapidly. HCl v=1, but not v=2, excitation rapidly diffuses through the sample by a resonant dipole-dipole vibrational energy transfer process. Molecular complexes, and in particular the HCl dimer, relax too rapidly for direct observation, $\lesssim$1 μs, and act as energy sinks in the energy diffusion process. The temperature dependence for all these processes is weak--less than a factor of two between 9 and 20 K. Vibrational relaxation of HCl in N_2 and O_2 matrices is unobservable, presumably due to rapid V→V transfer to the host. A V→R binary collision model for relaxation in solids is successful in explaining the HCl(DCl)/Ar results as

well as results of other experimenters. The model considers relaxation to be the result of "collisions" due to molecular motion in quantized lattice normal modes--gas phase potential parameters can fit the matrix kinetic data.

And also because all Creation is simpler
Than some of our crafty philosophers think.

B. Pasternak[*]

[*] Dr. Zhivago, Signet, New York (1958): "False Summer," in the "Poems of Yurii Zhivago.

ACKNOWLEDGEMENTS

Well, here I am, being a bit introspective and trying to minimize nostalgia. In retrospect, my experiences look very easy, although that was not always clear as I was working my way through them. They have also been very satisfying. One must fully enjoy the high points when he is there. It is difficult to acknowledge everyone who has been important to me during the past few years, and I acknowledge them en masse here. My experiences have certainly been enriched by the people who have been there with me.

I am particularly fortunate to have performed the research described in this Thesis under the direction of Professor C. Bradley Moore. He suggested the topic for the research and provided valuable guidance at all stages. At the same time, he allowed me the freedom to develop the project in my own way. I am grateful to Brad's influence on my scientific development.

Fellow members of the research group have been, simultaneously, teachers, colleagues, and friends. We have shared scientific problems, philosophical discussions, excessive drink, etc. I have benefited from the experiences, and I thank them all for help in the lab and friendship outside it.

Steve Leone and Jack Finzi taught me many of the techniques of the laser-induced fluorescence experiments. Glen Macdonald on various occasions extricated me from experimental difficulties and on many occasions listened to and critically evaluated my ideas--both scientific and otherwise.

I have benefited from many (midnight) discussions with Cam Dasch, concerning both science and the remainder of the domain of human endeavor. We rarely agreed, but as a result I learned a great deal. I appreciate his help and friendship, and have been lucky to have Cam as a contemporary.

I have enjoyed many desk-desk conversations and extra-curricular activities with Floyd Hovis. We also stretched the art of surgery on lasers to some new limits.

I wish to acknowledge help and stimulating discussions concerning a wide variety of topics with Andy Kung, Nick Nogar, Mike Berman, and Mark Johnson. I have also discovered, with them, some novel demonstrations of energy transfer on a basketball court. I thank Linda Young for assistance in some of the later experiments, and for patiently suffering through my expositions on matrix experiments.

My life and fortunes were made much easier by the efforts of Jackie Denney. I thank her for the range of her activities which extended well beyond duty, for many stimulating *non*-scientific discussions, and for other amenities.

I thank Cordelle Yoder for patiently and expertly typing the entire manuscript.

I have benefited from the staff and shops of the Chemistry Department. The services are outstanding, and I know that I have become irreparably spoiled. I wish to gratefully acknowledge fellowship support from the IBM Corporation (U. C. University Fellowship) and from the National Science Foundation.

I have confined my acknowledgements to people directly concerned with my work. In truth, that work is part of a broader experience

covering the past several years. It is, perhaps, impossible in this short space to acknowledge and thank everyone who has contributed. I will endeavor to do so, however, in other ways.

Finally, I thank my parents for their constant support. I know that I can count on that always.

In the spirit of brevity, I stop here.

Work performed under the auspices of the U. S. Department of Energy.

TABLE OF CONTENTS

TABLE OF CONTENTS (continued)

varies between transparent and totally opaque. The signal from v=2 is assumed to have a δ=1, since v=2 → 1 emission cannot be absorbed by ground state HCl guests. Integrating Eqs. (17) and (18) over all time gives:

$$S_2 = \int_0^\infty S_2(t)\, dt = gA_2N_0\tau_2 \tag{19}$$

$$S_1 = \int_0^\infty S_1(t)\, dt = g\delta\xi A_1N_0\tau_1 \tag{20}$$

where $\tau_2 = 1/k_{21}$ and $\tau_1 = 1/k_{10}$. S is the experimentally measured parameter. With a suitable choice for δ, the value of ξ can be deduced, thus indicating the extent of V → V processes in the relaxation of v=2.

A simple one dimensional model for optical density is illustrated in Fig. 8. It is assumed that the decay lifetimes are short relative to the radiative lifetimes, so that lifetime distortions due to radiation trapping may be neglected. The number of photons emitted between x and dx is $\tilde{n}(x)dx$. The number of photons surviving the thickness l after emission at x is

$$n(x) = \tilde{n}(x)\, e^{-\gamma x}\, dx.$$

Assuming that the initial excitation is uniform so that $\tilde{n}(x)$ is independent of x, $\tilde{n}(x) = n_o/l$ where n_o is the total number of emitted photons. The number of photons emerging after the thickness l is

$$n = \int_0^l \frac{n_o}{l}\, e^{-\gamma x}\, dx = \frac{n_o}{\gamma l}\,(1-e^{-\gamma l}).$$

The optical density factor is then

$$\delta = \frac{n}{n_o} = \frac{1}{\gamma l}\,(1-e^{-\gamma l}). \tag{21}$$

TABLE OF CONTENTS (continued)

LIST OF TABLES

LIST OF TABLES (continued)

LIST OF FIGURES

LIST OF FIGURES (continued)

LIST OF FIGURES (continued)

CHAPTER I

INTRODUCTION

Vibrational relaxation and energy transfer processes in the gas phase have been comparatively well studied and many of the basic features of these collisional processes have been ascertained. Studies of vibrational relaxation and energy transfer in simple condensed phase systems, however, are just beginning to yield interesting results.[1] A variety of processes may follow vibrational excitation of a diatomic or the lowest energy mode of a polyatomic guest species in a simple solid host: 1) the molecular vibration may relax by radiative decay; 2) the vibration may relax by coupling with delocalized lattice phonons (V→P); 3) the vibration may relax into modes localized at the lattice site of the guest, such as guest rotation (V→R); 4) vibrational energy may be resonantly transferred from one guest molecule to another leading to energy diffusion; 5) the excitation may be non-resonantly transferred to a chemically different guest species; and 6) a chemical reaction of the excited molecule may occur. Processes 2 and 3 are the mechanisms for vibrational relaxation of an isolated guest species and are collectively labeled V→R,P processes. Processes 4 and 5 are V→V processes.

When, after pulsed vibrational excitation, the ensemble returns to equilibrium, the energy of excitation will have been transformed to the lowest energy, highest density modes of the system--the delocalized lattice phonons. For simple monatomic solids, only acoustic phonons of energies below 100 cm^{-1} exist. Vibrational energies of the simple molecules considered here exceed 2000 cm^{-1}, so ultimately, at least 20 lattice phonons will be created in the relaxation process. Study of

the relaxation behavior of various guest/host systems allows deduction of the principal energy decay route and hence, gives information concerning the most important guest-host interactions in solids. Conceptually, the simplest system to study is that of a diatomic molecule, which has only one vibrational coordinate, in a monatomic lattice, in which only low frequency acoustic phonons are present. The vast majority of experiments performed to this date have concerned vibrational relaxation of diatomic molecules or the lowest frequency normal mode of polyatomic molecules.

In 1965, Sun and Rice[2] performed a calculation which suggested that vibrational relaxation of small guest molecules in cryogenic solids might be slow, in contrast to the notion prevalent at the time that relaxation in solids ought to be rapid since the large number of phonon modes in the solid produces a huge density of final states for the relaxation process. The first experimental observation of slow vibrational relaxation was by Tinti and Robinson[3] who observed vibrationally unrelaxed phosphorence from x-ray excited $N_2(A^3\Sigma)$ in Ar, Kr, and Xe matrices. The first direct measurement of a vibrational lifetime of a matrix isolated species was due to Dubost et al.,[4] who measured the relaxation rate of CO in an Ar lattice. (Subsequent work showed that relaxation of CO in Ar is radiative,[5] and that the earlier measured rates were due to V→V transfer to impurities.)

Experimentally observed vibrational relaxation times of matrix isolated species span several orders of magnitude. Molecules with large vibrational frequencies and large moments of inertia (hence small B constants) relax very slowly. The vibrational lifetime of CO in Ar or Ne matrices is 14 ms and energy decay is radiative.[5] Homonuclear

diatomics relax even more slowly: The vibrational relaxation time of C_2^- in Kr is 288 ms,[6] that of N_2 ($X^1\Sigma$) in solid N_2 is tens of milliseconds,[7] and vibrational relaxation within N_2 ($A^3\Sigma$) in rare gas matrices requires about one second.[3] The vibrational lifetime of N_2 in pure liquid N_2 exceeds 56 seconds.[8] Molecules with smaller moments of inertia relax more rapidly. Vibrational relaxation of OH/OD ($A^2\Sigma^+$)[9] and NH/ND ($A^3\pi$)[10] in rare gas solids as well as the ν_2 mode of NH_3 in N_2[1,11] and the ν_3 mode of CH_3F/CD_3F in Kr[12] occur on a 1-10 μs timescale. In these hydride/deuteride systems as well as in NH/ND ($X^3\Sigma$) in Ar,[13] the hydrides are observed to relax more rapidly than the deuterides, Bondybey and Brus[9,10] have accounted for this by proposing that guest rotation is the accepting mode for vibrational relaxation in the solid. Legay[1] has correlated existing experimental data to this hypothesis with a good degree of success. Radiative decay competes with and can be faster then relaxation into rotation for molecules with large moments of inertia. Processes 1 and 3 appear to be more important than process 2 for vibrational relaxation in solids.

Resonant and non-resonant energy transfer processes (processes 4 and 5) which lead to concentration of vibrational energy on a small number of highly excited guest molecules have been reported for CO in Ar and Ne.[5] Long-range energy transfer unaided by energy diffusion has been reported for NH/ND ($A^3\pi$) as the energy donor species with various acceptor species.[14] Very recently, Ambartzumian and co-workers have reported the photodissociation of SF_6 in an Ar matrix upon absorption of many photons of CO_2 laser radiation.[15] This is the only reported example of process 6.

Experiments described in this thesis have been concerned with the vibrational relaxation of matrix isolated HCl and DCl. The HCl system is a particularly useful prototype. It is a stable molecular species and solid solutions of known concentration can be prepared. The vibrational spectroscopy of matrix-isolated HCl and DCl has been extensively studied, both experimentally[16] and theoretically,[17] and the forces responsible for the spectral perturbations are known.[17] Most of the experiments were performed on HCl in an Ar matrix. The HCl-Ar interaction has been well studied in the gas phase by molecular beam scattering techniques[18] and by spectroscopic observation of the ArHCl van der Waals molecule.[19-21] A single potential function for HCl-Ar which describes many phenomena of the HCl-Ar system has been proposed.[22] Finally, vibrational relaxation of HCl by Ar in the gas phase has been studied.[23] The results of this study are not explained by the proposed potential function of Reference 22, however. From an experimental point of view, HCl has widely separated absorption lines so that it can easily be excited to a single rotation-vibration level. A single vibrational band is readily observed in fluorescence, so the detailed kinetics of a single vibrational level can be followed.[24]

The logical structure of the experiments reported in this thesis is as follows: Prepare an ensemble of guest molecules initially excited to a single rotation-vibration level. Observe the decay kinetics of the ensemble subsequent to excitation and relate this to the level excited and the perturbations experienced by the guest. The questions asked are: What is the vibrational decay mechanism? What is the role of ensemble processes such as V→V transfers in the overall decay process? How are guest properties determined from measurement of static

spectroscopic properties related to the kinetic behavior? The experiments performed are both spectroscopic studies and kinetic studies by a laser-induced, time-resolved infrared fluorescence technique.

The thesis is organized as follows: Chapter II is a presentation of the experimental techniques. In Chapter III, the spectroscopy of the systems studied is described in detail. In particular, the energy level structure for HCl and DCl is determined and the forces responsible for the shift of the gas phase free rotor structure to the observed level structure in the matrix are described. A very complete description of the energy levels thermally accessible at cryogenic temperature results. In Chapter IV various kinetic schemes and models for the behavior of an ensemble of excited guest species are described. Chapter V contains the kinetic results and a description of the observed decay mechanism. Rotation is found to be the energy accepting mode in the rate-limiting step of vibrational relaxation. V→V phenomena such as energy transfer from HCl monomer to HCl dimer are also observed. Finally, in Chapter VI, theoretical models for the vibrational relaxation of an isolated guest molecule are discussed. Direct V→P mechanisms are found to be unsatisfactory. A binary collision model for V→R,P relaxation is proposed and compared to available relaxation data for matrix isolated species. Other recent V→R,P theories are also discussed. A general overview of each chapter is provided in the introduction to the chapter.

The major conclusions of this work as as follows: 1) Non-radiative relaxation of HCl/Ar is due to V→R,P relaxation, and is not extremely rapid; 2) Species which are complexes of HCl (such as dimer) relax rapidly and can serve as energy traps when HCl monomer vibrational

excitation diffuses about the sample; and 3) Relaxation can be described in terms of a binary collision model in the solid in which relaxation is due to short-ranged repulsive interactions; the part of the potential primarily responsible for vibrational relaxation is not the part of the potential primarily responsible for spectroscopic perturbations.

Many questions about vibrational relaxation in matrices remain unanswered. Interpretable data concerning the effect of host lattice on V→R,P processes is lacking. The role of diffusion in aiding V→V transfer from a donor guest species to an acceptor guest species is not well understood and experimental demonstration of the full range of ensemble-averaging discussed in Chapter IV does not exist. The study of intra-molecular V→V processes of a polyatomic matrix-isolated guest is just beginning.[25] Also, studies of chemical reaction of vibrationally excited species in matrices are just beginning.[15]

CHAPTER I

REFERENCES

1. F. Legay, in Chemical and Biological Applications of Lasers, Vol. II, C. B. Moore, ed., Academic Press, New York (1977), Chapter 2.

2. H.-Y. Sun and S. A. Rice, J. Chem. Phys., 42, 3826 (1965).

3. D. S. Tinti and G. W. Robinson, J. Chem. Phys., 49, 3229 (1968).

4. H. Dubost, L. Abouaf-Marguin, and F. Legay, Phys. Rev. Lett., 29, 145 (1972).

5. H. Dubost and R. Charneau, Chem. Phys., 12, 407 (1976).

6. L. J. Allamandola, H. M. Rojhantalab, J. W. Nibler, and T. Chappell, J. Chem. Phys., 67, 99 (1977).

7. K. Dressler, O. Oehler, and D. A. Smith, Phys. Rev. Lett., 34, 1364 (1975).

8. S. R. J. Brueck and R. M. Osgood, Chem. Phys. Lett., 39, 568 (1976).

9. L. E. Brus and V. E. Bondybey, J. Chem. Phys., 63, 786 (1975).

10. V. E. Bondybey and L. E. Brus, J. Chem. Phys., 63, 794 (1975).

11. L. Abouaf-Marguin, H. Dubost, and F. Legay, Chem. Phys. Lett., 22, 603 (1973).

12. L. Abouaf-Marguin, B. Gauthier-Roy, and F. Legay, Chem. Phys., 23, 443 (1977).

13. V. E. Bondybey, J. Chem. Phys., 65, 5138 (1976).

14. J. Goodman and L. E. Brus, J. Chem. Phys., 65, 1156 (1976).

15. R. V. Ambartzumian, Yu. A. Gorokhov, G. N. Makarov, A. A. Puretzky, and N. P. Furzikov, JETP Lett., 24, 256 (1976); in Laser Spectroscopy III, J. L. Hall and J. L. Carlsten, eds., Springer-Verlag, Berlin (1977).

16. H. E. Hallam, in Vibrational Spectroscopy of Trapped Species, H. E. Hallam, ed., Wiley, New York (1973), Chapter 3.

17. A. J. Barnes, in Vibrational Spectroscopy of Trapped Species, H. E. Hallam, ed., Wiley, New York (1973), Chapter 4.

18. J. M. Farrar and Y. T. Lee, Chem. Phys. Lett., 26, 428 (1974).

19. S. E. Novick, P. Davies, S. J. Harris, and W. Klemperer, J. Chem. Phys., 59, 2273 (1973).

20. S. E. Novick, K. C. Janda, S. L. Holmgren, M. Waldman, and W. Klemperer, J. Chem. Phys., 65, 1114 (1976).

21. S. L. Holmgren, M. Waldman and W. Klemperer, J. Chem. Phys., to be published.

22. W. B. Neilsen, and R. G. Gordon, J. Chem. Phys., 58, 4149 (1973).

23. R. V. Steele and C. B. Moore, J. Chem. Phys., 60, 2794 (1974).

24. S. R. Leone, Thesis, University of California, Berkeley (1974).

25. L. Young and C. B. Moore, private communication.

CHAPTER II

EXPERIMENTAL

A. Introduction

The fundamental goal of these studies is to observe the energy relaxation processes which return a vibrationally excited ensemble of guest molecules isolated in a host lattice to thermal equilibrium. The simplest guest-host system is chosen for study--a diatomic guest in a monatomic or diatomic host lattice. Since the simple host lattices are van der Waals solids, it is necessary to prepare samples at cryogenic temperatures. Vibrational disequilibrium is produced by exciting a single vibration-rotation level of the guest molecule with a tunable infrared optical parametric oscillator (OPO). Spectrally and temporally resolved infrared fluorescence yields kinetic data on the processes returning the ensemble to equilibrium. Emission and fluorescence excitation spectra provide information as to which states are involved in the relaxation process. Absorption spectroscopy provides information concerning the energy states of the system populated in thermal equilibrium, as well as the identities and concentrations of species that are present in the sample.

The experiments performed involved two phases: sample preparation and characterization by infrared absorption spectroscopy; and fluorescence experiments. Samples are prepared by the matrix isolation technique using a closed cycle helium refrigerator capable of cooling to 9 K. Infrared absorption spectra are recorded on a medium resolution spectrometer using standard infrared techniques. The source for the

fluorescence experiments is the OPO, used successfully by this group for studies of energy transfer in the gas phase. The OPO is capable of producing pulses of up to 30 μJ energy in 80-200 nsec, with a spectral linewidth much narrower than the sample absorption linewidth. Thus, the laser source produces a monochromatic delta function excitation pulse. Fluorescence is observed using doped Ge infrared detectors capable of responding to times shorter than one microsecond. A variety of post-detector electronics is used depending upon the type experiment being performed.

This chapter is divided into three further sections, each elaborating on one of the aspects mentioned above. The details of the matrix isolation procedures used in this work are described in Part B; both hardware characteristics and experimental procedure are treated. The details of the absorption spectroscopic techniques are presented in Part C. Finally, the variety of fluorescence experiments are described in Part D.

B. Matrix Isolation

1. General Aspects

The techniques of matrix isolation involves trapping a molecule to be studied in a rigid, inert host lattice. The trapped molecule (guest) is usually present in a very dilute concentration so that guest-guest interactions are minimal; typically, M/A ratios (inverse mole fractions--matrix to absorber ratios) exceed 1000. The most frequently used host materials are the rare gases and nitrogen, so the production of a rigid host lattice requires cryogenic temperatures. Even though the guest species is present as a dilute species, it can be present at large concentration relative to the gas phase, since solids have a molecular

density equivalent to about 1000 atmospheres. Guest molecules are effectively isolated since the rigid lattice precludes translation, and all guest-guest interactions must therefore be relatively weak, long-ranged ones. The guest-host interactions are usually weak. The cryogenic temperatures used simplify the guest system since only a few quantum states of the guest have an appreciable population. Since the introduction of the matrix isolation technique in 1954 by Whittle, Dows, and Pimentel[1] and by Norman and Porter,[2] the primary applications have been spectroscopic. Two comprehensive reviews of the techniques and results of matrix isolation studies have recently appeared.[3,4]

A particular matrix sample may be characterized by several properties: a) temperature, b) concentration, c) degree of isolation, d) crystalline quality of the host lattice, and e) purity. A matrix is a non-equilibrated system constrained from reaching equilibrium by barriers that are large relative to the thermal energy available at cryogenic temperatures. The properties of the matrix will therefore depend somewhat on the preparation and the history of the sample, particularly on the temperature history. When the guest is a stable molecular species, matrices are usually prepared by vapor deposition of a pre-mixed gaseous sample onto a support maintained at cryogenic temperature. The lattices formed by this method are by no means perfect crystals.

The concentration of a guest in the host is usually taken to be the same as that of the premixed gaseous sample. The guest and host species may have different sticking coefficients onto the support, but the guest is present in small concentration, and a continual back-pressure of host gas during the deposition process should prevent the

guest from escaping if it should initially not stick to the support. It is likely that the effective sticking coefficient of the guest will be nearly the same as that of the host. The sticking coefficient for Ar, Kr, and Xe gases impinging on a target at 8 K has been reported to be 0.95 ± 0.05.[5]

The guest species is isolated because it is trapped in the host lattice. Diffusion within the solid lattice occurs when the temperature becomes high enough for the solid to become non-rigid. Generally, diffusion will cause the guest species to form molecular aggregates, thus leading to a loss of isolation of the guest molecules. As a rule of thumb, the temperature at which diffusion begins to occur is one-third the melting temperature of the host lattice.[3] During deposition from the vapor phase, some diffusion will occur, since the gas must be cooled from ambient temperatures to cryogenic temperatures. Upon initial condensation, the solid will be soft and diffusion will occur on the newly formed solid surface. In general, this diffusion that is inherent in the deposition process will cause guest aggregates to be present in greater than statistical quantity. In dilute samples, the probability of formation of any aggregate beyond dimer becomes remote, and aggregation can be minimized by working at high dilution. The greatest degree of isolation is obtained by depositing the matrix on a support held at the lowest temperature possible, since this will cause the solid to become rigid in the shortest possible time.

The host lattice formed by vapor deposition is composed of microcrystallites,[6,7] estimated to be about 100 Å in size.[7] The polycrystalline nature of the lattice is due to rapid crystal formation upon cooling from the vapor phase, and causes matrices to be quite scattering to

incident radiation. Many atoms and molecules in the matrix are condensed in non-equilibrium sites and are trapped there. Deposition at higher temperatures improves the crystalline quality of the matrix and produces a less scattering sample. Also, a warming of the matrix after deposition (annealing process) will improve the crystalline quality of the lattice. Crystalline quality improves when the length of time for crystal formation from the vapor phase is lengthened, but these are conditions under which diffusion occurs. Thus, the goal of producing a good crystalline matrix is somewhat opposed to the goal of producing a high degree of guest isolation, and a suitable compromise must be reached when deciding upon deposition conditions. The crystal structure of the matrix is generally that of the pure crystal of the host lattice[6,7] which is face centered cubic (fcc) for the rare gas crystals. It has been observed, however, that large amounts of impurity can stabilize the metastable hexagonal close packed (hcp) structure of solid Ar.[8] Some useful properties of the most frequently used matrix host lattices--the rare gases, nitrogen, oxygen, and carbon monoxide - are collected in Table 1.

The variables under the control of the experimenter during the matrix deposition process are concentration, temperature of deposition, and rate and method of deposition. Aggregation effects are reduced by working at high dilution, but high dilution requires a large amount of sample in order to observe useful experimental signals, and large amounts of sample makes spectroscopy difficult, since matrices are scattering. Deposition at a low temperature yields good isolation, but produces a scattering matrix. Deposition at a fast rate produces a large thermal load on the cryogenic cooler, and causes the effective deposition

Table II-1a. Some Physical Properties of Rare Gas Solids[a,b]

		Ne	Ar	Kr	Xe
Crystal structure		fcc	fcc	fcc	fcc
Lattice constant (Å)		4.46	5.31	5.64	6.13
Nearest neighbor dist. (Å)		3.16	3.76	3.99	4.34
Number density ($10^{22}/cm^3$)		9.52	2.67	2.87	2.00
Mass density (g/cm^3)		1.51	1.77	3.09	3.78
Melting temp. (K)		24.6	83.3	115.8	161.4
Debye temp. (K)		75	92	72	64
Debye frequency (cm^{-1})		52	64	50	44
ϵ/K (K)[c]		36.3	119	159	228
σ (Å)[c]		3.16	3.87	4.04	4.46
Heat Capacity (cal/mole-k)	10K	1.25	0.90	1.46	1.94
	20K	4.37	2.82	3.67	4.00
	30K		4.39	5.01	5.19
	70K		6.96	6.57	6.32
Thermal conductivity (mW/cm-K)	2K	30			
	3K	46			
	4.2K	42		4.8	
	8K		60		
	10K	8	37	17	
	20K	3	14	12	
	77K		3.1	3.6	
Refractive index, λ =	.500μ[d]		1.28	1.34	1.47
	.546μ[e]	1.23	1.26	1.28	
	.645μ[d]			1.34	1.43
	.694μ[d]		1.27		
	10.0μ[f]		1.41		

[a] Data with unspecified temperature is for 4.2 K. Only heat capacity and thermal conductivity vary by more than a few percent between 0 and 20 K.

Table II-1a. Footnotes (continued)

[b] Sources for unreferenced data:

H. E. Hallam, Vibrational Spectroscopy of Trapped Species, Wiley, New York (1973), Chapter 2.

C. Kittel, Introduction to Solid State Physics, 4th ed., Wiley, New York (1971).

G. L. Pollack, Rev. Mod. Phys., 36, 748 (1964).

D. E. Gray, ed., American Institute of Physics Handbook, 3rd ed., McGraw-Hill, New York (1972).

[c] Parameters for Lennard-Jones (6, 12) potential.

[d] J. Marcoux, Can. J. Phys., 48, 1949 (1970).

[e] J. Kruger and W. Ambs, J. Opt. Soc. Am., 49, 1195 (1959).

[f] G. J. Jiang, W. B. Person, and K. G. Brown, J. Chem. Phys., 62, 1201 (1975).

Table II-1b. Some Physical Properties of Molecular Solids[a,b]

	N_2	O_2	CO
Crystal structure	fcc	monoclinic	fcc
Lattice parameter (Å)	5.64		5.63
Mean site diamter (Å)	3.99	3.64	4.00
Site shape (Å)	4.52 x $(3.42)^2$	4.18 x $(3.20)^2$	4.61 x $(3.48)^2$
Number density ($10^{22}/cm^3$)	2.45	2.96	
Mass density (g/cm^3)	1.14	1.57	
Melting temperature (K)	63.2	54.4	68.1
Debye temperature (K)	68	91	
Debye frequency (cm^{-1})	47	63	
ϵ/K (K)[c]	90	110	100
σ (Å)[c]	3.7	3.5	3.7
Phase transition	fcc→hcp	monoclinic → rhombohedral	fcc→hcp
Transition temperature (K)	35.6	23.8	61.6
Heat capacity (cal/mole-K) 10K	1.06	0.60	2.0 (15K)
Heat capacity (cal/mole-K) 20K	4.50	3.27	3.7
Heat capacity (cal/mole-K) 30K	8.26	11.0	5.9
Refractive index, λ = .546μ[d]	1.22	1.25	
Refractive index, λ = 10.0μ[e]			1.40

[a] Data with unspecified temperature pertains to 4 K.

[b] Sources for unreferenced data:

H. E. Hallam, Vibrational Spectroscopy of Trapped Species, Wiley, New York (1973), Chapter 2.

J. O. Clayton and W. F. Giaque, J. Am. Chem. Soc., 54, 2610 (1932).

C. S. Barett, L. Meyer, and J. Wasserman, J. Chem. Phys., 47, 592 (1967).

Table II-1b. Footnotes (continued)

D. E. Gray, ed., American Institute of Physics Handbook, 3rd ed., McGraw-Hill, New York (1972).

J. O. Hirschfelder, C. F. Curtiss, and R. B. Bird, Molecular Theory of Gases and Liquids, Wiley, New York (1954).

[c] Parameters for Lennard-Jones (6, 12) potential.

[d] J. Kruger and W. Ambs, J. Opt. Soc. Am., 49, 1195 (1959).

[e] G. J. Jiang, W. B. Person, and K. G. Brown, J. Chem. Phys., 62, 1201 (1975).

temperature to be higher than the temperature of the support medium. The slower the deposition rate, however, the more time required to prepare a sample, and impurities which leak into the apparatus will be incorporated into the matrix in a proportionately large amount. All of these effects depend a great deal on the nature of the guest and host materials. As can be seen, there are many tradeoffs involved in producing a matrix, and all effects are inter-related. The combined effect is to make production of matrices a bit of "black magic."

A very simple way of viewing a matrix isolated species is as a "cold gas,"[3] suspended in an inert structureless medium of finite dielectric constant. The guest molecules are assumed to have identical properties to single gas phase guest molecules, and to be distributed uniformly and randomly throughout the sample. At higher levels of sophistication other effects must be included. The guest-host interactions will modify the properties of the guest molecule relative to the gas phase guest. In particular, vibrational frequencies are usually shifted by a few percent, and rotational motion is either quenched or hindered to varying degrees. At moderate and high guest concentrations ($M/A < 1000$) guest-guest interactions can become important; the strongest such interactions lead to multimer formation. The fact that the matrix is an imperfect crystal must also be considered, and in many cases multiple guest trapping sites are observed. The guests may also interact with impurities, and in some cases guest-impurity absorption features have been confused with guest aggregates or multiple trapping sites--sample purity is very important in matrix work.

This has been a brief and selective discussion of some general aspects of matrix isolation studies. Some of these points will be covered in more detail later on, as they are needed.

2. Cryostat

Cryogenic temperatures were produced by an Air Products Inc. Model CSA-202 closed cycle helium refrigerator utilizing a modified Solvay cycle[9] and two stages of expansion. The refrigerator was capable of producing a temperature of 9 K and of holding this temperature indefinitely (it has been run continuously for up to three weeks). The first cooling stage terminates in a 40 K cold station and the second stage terminates in a copper block. For the majority of the experiments, a one inch diameter by 3 mm thick sapphire window was used as the matrix support material. This was mounted in a window holder supplied by Air Products which could be screwed into the copper block at the second cold station. Sapphire was chosen as the support window because it is transparent in the regions of interest for the HCl and DCl experiments (transparent from the ultraviolet to 6.5 μ) and because it has a very large thermal conductivity in the region of cryogenic temperatures.[10] In some experiments CsI was used as a support material--although its thermal conductivity is not as high as that of sapphire, its transmission range extends to 80 μ.[11] All surfaces are joined with an intervening layer of indium foil which is lightly greased with Apiezon N high vacuum grease. Thermal contact between various surfaces (such as the matrix window and the window holder) is made by tightening the connection between the surfaces and tightly squeezing the indium foil.

A radiation shield supplied by Air Products screws around the 40 K cold station. At high vacuum the main source of thermal conductivity from the outer walls of the cryostat to the cold station is radiative.[3] According to the Stefan-Boltzmann law, the flux of radiative energy transfer is proportional to T^4; the effect of the radiation shield is to

let the cold station see a 40 K background instead of a 300 K background, thereby reducing the thermal load on the refrigerator by a factor of 3000. The effect of the radiation shield has been demonstrated on our refrigerator; with the radiation shield in place the refrigerator cools to 9 K, without it the minimum achievable temperature is 12 K.

A vacuum shroud supplied by Air Products seals around the central displacer assembly by means of two O-rings. The bottom of the shroud is rectangular and has four square flange assemblies which are vacuum sealed to the shroud by means of O-rings. These flanges are used for mounting windows, nozzles, or any other devices useful for a particular experiment. The shroud is rotatable with respect to the displacer assembly, and hence the orientation of the windows mounted on the flanges with respect to the matrix window may be varied. The shroud also has two inlets for 1/16" tubing which can be used as nozzles for matrix deposition; the two inlets are located at a 45° angle with respect to the flanges. A cross section of the lower part of the cryostat is shown in Figure 1.

The cryostat has three windows mounted on the flanges. Two NaCl windows are mounted on opposite flanges. Since the aperture of the matrix window holder is 3/4", the NaCl windows need be no larger than this. The NaCl windows used are 1¼" in diameter by 3 mm thick, and are attached to the flange with either high vacuum epoxy or black wax. The windows are polished with isopropanol, until they are transparent in the visible. Under normal usage the windows remain transparent for many months, and a quick polishing while the windows are mounted often suffices to return the windows to full transparency after they begin to fog. The third window is CaF_2 and is 1-3/4" in diameter by 3 mm thick. The

Figure II-1. Cross-section of the bottom region of the cryostat. The sapphire window is surrounded by a circular radiation shield with openings to permit optical access. Four flanges are attached to the shroud by compressed O-rings. The 1/4" nozzle is welded to one flange. Two auxillary 1/16" nozzle inlets are not used. The NaCl windows mounted on parallel flanges are attached by epoxy or black wax. The CaF_2 window is attached to the shroud by two sets of O-rings compressed by an outer flange. The window and radiation shield can rotate with respect to the shroud.

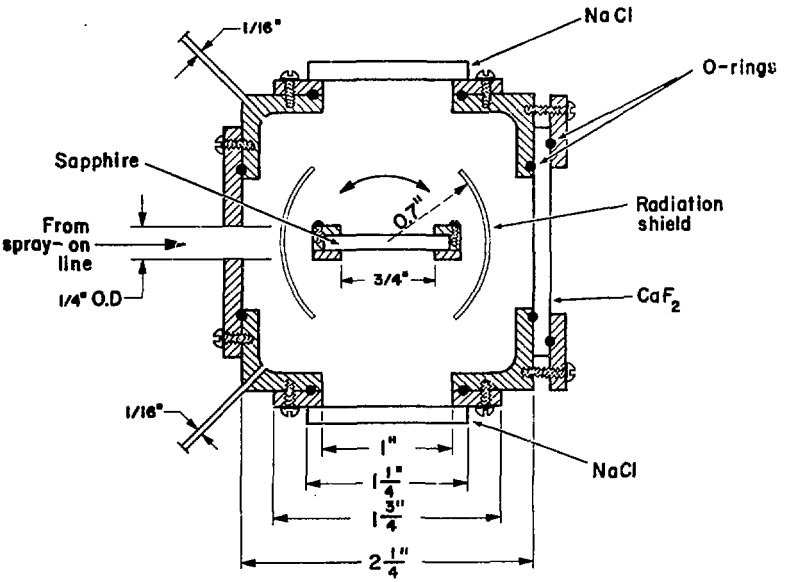

XBL7711-2184

aperture upon which the flanges seal is 1-3/8", and the CaF_2 window is sealed directly to the O-ring on the shroud by means of a retaining plate, as illustrated in Figure 1. This method of sealing the window permits the use of the maximum aperture in the flange.

The positioning and diameter of the nozzle will influence the physical size of the matrix and will also influence both isolation and crystalline quality of the matrix. When the nozzle is far from the matrix window, the vapor stream spreads out during deposition and the matrix forms over a large area. In practice, the nozzle is ended just before the radius defined by the radiation shield, at a distance of 3/4" from the support window. Even this close to the matrix window, a bit of the sample is sprayed onto the frame of the window holder. The diameter of the nozzle affects the uniformity of thickness of the matrix. The thickness profile of the matrix is peaked directly in front of the nozzle; small diameter nozzles produce samples that are more peaked than do larger diameter samples. Most matrices were prepared with a 1/4" diameter nozzle which was normal to the matrix window during deposition; in thick samples some peaking was observable upon visual inspection of the matrix, but the entire window was filled with fairly uniformly thick sample. In the final design, the 1/4" nozzle was made of stainless steel and welded into the center of one of the flanges on the shroud, as illustrated in Figure 1. It is very important to eliminate all leaks around the nozzle, since gas leaking around the nozzle will be deposited in the matrix. The welded nozzle assembly was very leak-tight. In some experiments, a 1/16" nozzle was introduced through the ports in the shroud; matrices prepared with this nozzle were very thick in the center--roughly three times as thick in the center of the matrix as at the edge of the matrix window.

Other cryostats were used briefly during some stages of the present study. The first matrices were prepared in a conventional double-dewar cryostat using liquid hydrogen as a refrigerant. A few spectroscopic studies of the overtone absorption spectra of HCl and DCl in various matrices were performed using a Cryogenic Technology Inc. Model 21 Cryocooler.[12] Since the great majority of the work reported herein was performed with the Air Products refrigerator, these systems will not be described more fully here.

3. Temperature Control

Temperature of the matrix is a useful and accessible experimental variable. The refrigerator operating temperature is determined by the heat load on the refrigerator; the greater the heat load, the higher the temperature at the cold station. The minimum attainable temperature corresponds to that temperature at which the heat load due to all sources--radiation, residual thermal contact through the vacuum shroud, etc.--is equal to the cooling power of the refrigerator. Temperatures higher than the minimum are produced by using a resistive heater which is wrapped around the copper block at the cold station to impose an additional heat load. A heat load of 2.0 watts through the 47 ohm resistive heater has been measured to produce a temperature of 20.0 K, for example.

There are two methods used to measure the temperature on the cryostat cold station--a hydrogen vapor pressure thermometer and a thermocouple. The hydrogen vapor pressure thermometer consists of a metal bulb soldered to the copper block and connected by a metal capillary to a 0-60 psi gauge. The gas in the bulb equilibrates with

the copper block and the pressure reading of the gauge corresponds to that of H_2 gas at the temperature of the cold station. The pressure is converted to a temperature using a graph given by Scott.[13] During the course of these experiments the zero on the gauge suffered two discontinuous changes--first to 1.4 psi and then to 1.9 psi. The cause of these changes is unknown. The refrigerator cools to 9 K at which temperature the vapor pressure of H_2 is less than 0.1 psi, so the reading of the gauge when the refrigerator has no heat load can be taken to be the zero of the gauge. When necessary, the gauge zero can be checked by pumping out the H_2. The true pressure reading can be found from the formula

$$P_{true} = P_{observed} - P_{zero}.$$

The gauge can be read accurately to about 0.1 psi, so the useful range of the hydrogen vapor thermometer is from 13 to 24 K. Below this the uncertainty in reading the pressure amounts to 20% of the reading, and above 24 K the vapor pressure varies slowly with temperature, and the effect of the finite quantity of H_2 in the thermometer makes readings unreliable. The gauge reading depends upon the orientation; only in the upright position are the gauge readings accurate. In the range 13-24 K, however, with the refrigerator in an upright orientation, the H_2 vapor pressure thermometer is taken as indicating the true temperature.

Temperatures are also measured with a KP vs iron-doped gold (0.7 atomic per cent doping) thermocouple, supplied with the refrigerator. Junctions between these materials are very difficult to make and any trick that successfully produces a junction is acceptable. The difficulty in junction making is that the melting point of the KP wire is

much greater than that of the gold wire, and temperatures which soften the KP wire vaporize the gold wire. Two techniques have been successful. Both require the wire surfaces to be clean. The first technique is to solder the wires together using indium solder with a very low heat on the soldering iron--typically the soldering iron is plugged into a Variac set at about 70 volts. The success rate of this method is low. A second technique is to use a low blue flame from an oxy-butane torch. In this technique the gold is wrapped around the KP wire leaving about an eighth inch of the KP wire extending beyond the gold. Moving the torch slowly from the end of the KP wire to the gold wire allows the KP to heat up before the gold wire vaporizes. The latter method produces mechanically stronger junctions.

The signal junction was originally soldered into the copper block at the cold station. During the course of these experiments this junction became undone, and a new junction was placed between the copper block and the matrix window holder, wedged very tightly between two pieces of indium foil. A reference junction exterior to the cryostat could be placed in an ice-water bath. The thermocouple produces an emf which is proportional to the difference in temperatures between the two junctions. Standard tables of thermocouple emfs for the KP vs iron-doped gold system exist,[14] and it is possible to calibrate a particular thermocouple against the tables. It is easier to calibrate the thermocouple against the hydrogen vapor pressure thermometer and to extrapolate the calibration to lower temperatures. The temperature derivative of the emf of the thermocouple varies between 15.7 and 17.0 μV/deg between 9 and 55 K,[14] so the extrapolation can be taken as linear with a maximum error of 0.08 K/degree. Since the maximum extrapolation is from 13 to

9 K, this amounts to 0.3 K. For accurate temperature measurement, the emf difference between the two junctions is read on a digital microvoltmeter, to a precision of 1 μV. The jitter in the reading of the microvoltmeter is about ± 3-5 μV, or about 0.2-0.3 K.

There are a number of possible systematic errors involved in the temperature measurement. Neither temperature sensor is located at the matrix window, and it is assumed that the copper block of the cold station is thermally equilibrated with the matrix. Since the thermal conductivity of the van der Waals solids used as matrix hosts are considerably lower than the thermal conductivities of the other parts of the cold station (17 vs 1210 vs 20 mwatt/cm-deg for Ar, sapphire, and brass at 4.2 K[3]) the matrix itself may not quickly reach a uniform temperature. The result of such systematic errors is that the true matrix temperature would be higher than the indicated temperature. The reading of the H_2 thermometer has a variation of about 0.1 psi at a pressure of 13.4 psi--this corresponds to a temperature uncertainty of less than 0.1 K at 20.0 K. This is perhaps due to temperature cycling of the refrigerator during its operating cycle. The error in temperature reading from the thermocouple is likely due to fluctuations within the microvoltmeter. The readings of the thermocouple and H_2 thermometer always agree in real time.

The simplest method of maintaining a temperature above 9 K is to pass a dc current through the resistive heater; as the current is increased the heat load on the refrigerator will increase and the temperature will rise. Upon increasing the dc current the temperature should monotonically rise until the cooling power of the refrigerator just balances the imposed heat load. A 15 V dc power supply with a variable

shunt resistance is used as the current source for the manual control heater. In practice, the voltage across the 47 ohm resistive heater is always constant to within about 10 mV, and the temperature attained is constant to within 0.2-0.3 K, as discussed above. Occasionally, however, the temperature will make an excursion of several degrees while the dc current remains unchanged. The cause of the excursion is still a puzzle--it may be due to variable thermal contact between the heater and the cold station, or it is possible that some contaminant in the He gas inside the refrigerator is becoming trapped in the displacer, and then being cleared out by a pressure buildup, resulting in a short term temperature fluctuation.

A second method of temperature control utilized an Air Products Model APD IC-1 proportional controller. The desired temperature is set on the front panel of the controller and heating pulses are delivered to the heater until the set and actual temperatures are equivalent. The controller is made for a KP vs iron-doped gold thermocouple and has an internal reference junction. In order to make use of the proportional controller compatible with direct manual temperature control, the emf of the thermocouple after the reference junction is fed into the proportional controller. This causes the indicated temperature on the proportional controller to give a value about 20 K too high. However, it does not affect the stability of the proportional controller. Usually the proportional controller will be set for an actual temperature in the range of 15-21 K, and the hydrogen thermometer is used to accurately read the temperature maintained by the controller. The readout on the proportional controller is accurate to about 1 K, and the long term stability of the set temperature is about 1 K. The constant feedback

from the thermocouple allows the proportional controller to maintain a desired temperature when the thermal load of the refrigerator is changing, as during the deposition process.

The proportional controller is used during cooldown, deposition, and warm-up phases of the matrix experiment, where a stability of 1 K is sufficient. The proportional controller is particularly useful for deposition at a temperature above 9 K, since it does maintain the set temperature with a changing thermal load; the temperature of the refrigerator would continually increase if a constant dc current were maintained during the deposition process. The manual control circuit is more accurate and stable, however, and is used during the fluorescence experiments.

A matrix diffusion experiment is a process wherein the matrix is warmed to allow partial aggregation of the guest species. In Ar, the diffusion temperature is about 35 K. A reproducible method of performing a diffusion experiment uses the manual temperature control circuit.[15] With the manual controller set to produce a temperature of about 20 K, the bypass valve on the compressor module of the refrigerator is opened one quarter turn. This reduces the cooling power of the refrigerator and the temperature rise of the sample can be followed on the thermocouple readout. When the temperature reaches about 35 K (a reading of 4780 μV when the reference junction is in an ice-water bath), the bypass valve is closed, and the manual heater is turned off. The refrigerator will then cool to 9 K in about one minute. The entire process, from 20 to 35 to 9 K takes about two minutes.

4. Deposition Conditions

The important variables during the deposition of the matrix are the temperature of the matrix window, the rate of deposition and the method of deposition. In the majority of the present work, matrices were prepared by a pulsed deposition method,[16] in which discrete gas pulses of small volume and relatively high pressure are allowed to impinge on the matrix support. In some experiments, the more conventional continuous deposition technique was used, in which the matrix gas flows at low but steady rate through a needle valve and onto the support window. For the HCl/Ar system, pulsed deposition produces a higher degree of isolation than continuous deposition. The general effects of rate and deposition have been discussed above. More details of the spectroscopic effects of deposition conditions as they pertain to matrix-isolated HCl will be presented in Chapter III.

Pulses of the matrix gas mixture originated in a 12 ml volume between two high vacuum solenoid valves formed by ½" diameter monel tubing. The solenoid valves opened sequentially, filling and then discharging the pulse volume, with an open time of 2 seconds and a delay between valves of about 5 seconds. The pulse rate was either two or four pulses per minute. The pulse volume was filled to a pressure of 40 to 200 torr, so each pulse contained 25 to 130 μmoles, and the average deposition rates were between 3 and 30 m-moles per hour; matrix properties were not overly sensitive to average deposition rate within these limits. Typically, 10-30 μ-mole of guest are deposited.

Temperature of deposition plays a more important role in the final characteristics of the matrix. Matrices were deposited at a fixed temperature between 9 and 20 K. Samples deposited at 20 K were transparent

with large cracks; samples deposited at 9 K were snowy and opaque. The optical quality of samples deposited at 20 K degrades upon cooling to 9 K. Samples deposited at 20 K have a smaller degree of isolation than do samples deposited at 9 K. This point will be discussed in more detail in Chapter III. A summary of the various deposition conditions used is given in Table II. As is evident, deposition conditions varied continuously between the cases given; nevertheless, the classification is useful. The majority of matrices were deposited either under high temperature, low rate or low temperature, high rate conditions.

5. Gas Handling System and Procedures

Gas mixtures are prepared and matrices deposited from a mercury diffusion pumped, greased vacuum line, capable of producing a vacuum of better than 1×10^{-6} torr. Pressures are measured with a mercury triple-McLeod gauge and a mercury manometer with accuracies of better than two percent in the ranges used. The McLeod gauge is calibrated by gas expansion against the manometer, which is the primary pressure standard, and can measure pressures as low as 0.05 torr with the aforementioned accuracy.

The cryostat is attached to the vacuum system by a "spray-on line," and a return line; the matrix is deposited through the spray-on line and the cryostat is evacuated through the return line. Both lines must be disconnected when the cryostat is moved into position for the fluorescence experiments. Leaks and outgassing in the spray-on line are critical to the purity of the matrices prepared, and numerous spray-on lines have been used. The ideal spray-on line must be quickly sealed with a high vacuum fitting and must outgas completely overnight. In the

Table II-2. Typical Deposition Conditions

Type	Rate (m-mole/hr)	T (K)
slow, high	3-7	17-20
slow, low	4-7	9
fast, high	28	20-21
fast, low	16-30	9

final version, the removable portion of the spray-on line connects to the vacuum system after the solenoid valves and to the cryostat before a valve to the nozzle. The line is constructed of stainless steel and the removable connections are Cajon VCR fittings sealed with teflon gaskets. The valves are stainless bellows valves and all valves and fittings are welded to the appropriate tubing. The valve to the vacuum line is located close to the cryostat, so that only about an eight inch length of tubing is exposed to atmosphere when the cryostat is disconnected from the vacuum line. The exposed portion of the spray-on line is heated with a heat gun and/or with heating tape when it is reconnected to facilitate outgassing. The overall length of the line is about five feet from the solenoid valves to the end of the deposition nozzle.

Earlier versions of the spray-on line pointed out some problems, the result of which was water and/or nitrogen impurity in the matrix sample. Flexible tubing, either brass or stainless, is unacceptable for the spray-on line because it has a large surface area which outgasses very slowly; heating flexible tubing often results in a puncture in the tubing. The original fittings between the removable and fixed portions of the spray-on line were Cajon Ultra-torr unions; these fittings leak at a very small rate when there is a transverse force on the fittings--this small leak was unobservable in static leak rate measurements, but it introduced impurities into the matrix sample. The stainless tubing used is corroded by the HCl and DCl to which it is exposed; after repeated use and exposure to air the outgassing period of the tubing became very long, and most matrices contained traces of water. This situation is remedied by using fresh tubing. The importance of a

leak-tight outgassed spray-on line in producing impurity-free matrices cannot be overemphasized. Since the termination of the spray-on line is the nozzle, and this is aimed directly at the matrix, any impurities introduced by the spray-on line will end up in the matrix sample.

Leaks in other parts of the vacuum system are also important, and periodically the static leak rates of several sections of the vacuum system were measured; the steady state and acceptable leak rates are: less than 0.05 μ-ℓ/hr for the manifold and McLeod gauge (volume of about 2 ℓ), 0.1 μ-ℓ/hr and 0.2 μ-ℓ/hr for the return and spray-on lines (volumes of about 0.2 and 0.3 ℓ), and 0.7 μ-ℓ/hr for the cryostat (volume of 1 ℓ). The source of the comparatively large leak rate of the cryostat was undetectable with a He leak detector. The large leak in the cryostat is not overly important, however, since during refrigerator operation, the radiation shield is cold enough to condense air, and since the proportion of the cold surface inside the cryostat that is the matrix is small not much impurity will be introduced into the matrix sample

Gas samples for the matrix are mixed in a five liter bulb by first measuring in a small pressure of the guest gas using the McLeod gauge, then rapidly adding a high pressure of the host gas to the five liter bulb, measuring the total pressure on the manometer. The rapid influx of a large excess of host gas prevents the guest gas from escaping the mixing bulb and also produces some mixing of guest and host gases. Typical pressures are about 0.1-0.5 torr for the guest and 200-700 torr for the host gas. Before preparing the matrix gas mixture, the mixing bulb is carefully heated with a heat gun. Gas mixtures are allowed to stand at least eight hours before use to ensure complete mixing. Three component samples are prepared by first mixing one guest with the host

gas in a 12 ℓ bulb, allowing eight hours for mixing, and then adding this mixture to the second guest in the 5 ℓ bulb. Since HCl adsorbs on glass walls, it is always the second guest added.

Matrix concentrations were taken to be the same as those of the pre-mixed gas. HCl adsorbs to glass walls, so the gas samples were always used within two days of mixing. No explicit account was taken of adsorption on the walls; the error in introducing no correction is that matrix concentrations are perhaps overestimated. Heating the walls of the bulb prior to mixing prevents HCl already present on the walls from increasing the sample concentration. CO does not seem to adsorb very effectively on glass walls, in contrast to HCl. A single mixture of CO/Ar was used to make two matrices about a week apart; the peak intensities were proportional to the total amount of matrix deposited, indicating that the concentration of the matrix gas had not changed.

The pressure required to fill the pulsing volume is maintained by a 12 ℓ ballast bulb attached to the vacuum line. The rate of deposition of the matrix decreases during the course of deposition, since as gas is deposited, the pressure in the ballast bulb falls. The ballast bulb can be repressurized from the mixing bulb in order to maintain a more nearly uniform deposition rate. Under the fast deposition conditions, the ballast bulb is pressurized to about 140 torr. After two hours of pulsing at 4 pulses per minute, the ballast pressure has dropped to about 80 torr. At this point the ballast bulb pressure can be brought back to 140 torr by adding more gas from the mixing bulb. Deposition rates thus vary by almost 50% during the course of deposition. Refilling the ballast bulb more frequently would produce a more uniform deposition rate, but since matrices were not overly sensitive to

deposition rate, this is unnecessary. The amount of gas deposited is followed by watching the pressure change in the ballast bulb during the course of deposition.

When working with DCl samples all procedures are the same as other samples, except that the portions of the system used must be passivated with DCl before use. Before preparing a matrix gas mixture, the vacuum manifold and mixing bulb are passivated at least once with 5-10 torr DCl for about a half hour. The ballast bulb and spray-on line are passivated with 5-10 torr DCl for about an hour immediately prior to deposition of a sample. Since the volume of the system is large (about 20 ℓ) it is impossible to prepare samples without observable HCl. Typically, DCl matrices have a DCl/HCl ratio of ten, as measured spectroscopically.

6. Gases

DCl was prepared by photochemical reaction of D_2 and Cl_2. The reaction was initiated by a mercury lamp and was run with an excess of D_2. The reaction proceeds by a free radical mechanism and completion is monitored by disappearance of the yellow color of the Cl_2. It is assumed that all Cl_2 is removed by reaction. D_2 is removed by freezing the DCl product in a liquid nitrogen bath and pumping the reaction bulb. Before introducing the reactants, the reaction bulb is vigorously flamed. Other gases used were: HCl (Matheson Electronic Grade, >99.99%), D_2 (Matheson CP, >99.5% d, $<3 \times 10^{-2}$% non-hydrogen impurities), Cl_2 (Matheson Research Purity, >99.96%), CO (Matheson, Research Purity, >99.99%), Ar (Matheson Ultra-high Purity, >99.9995%), N_2 (Matheson Research Purity, >99.9995%), and O_2 (Matheson Research Purity, >99.99%).

HCl and DCl were distilled at least once between an isopentane-n pentane slush (-134 C) and liquid nitrogen. Before preparing a matrix sample, the HCl and DCl were subjected to at least one freeze-pump-thaw cycle. Ar, N_2 and O_2 were withdrawn from a bulb with a cold finger immersed in liquid nitrogen, after sitting in the bulb for several hours. This was a difficult procedure for Ar, since the vapor pressure of Ar at liquid nitrogen pressure is about 200 torr, and the technique of mixing matrix samples often requires a higher host gas pressure. Occasionally, the Ar was used directly from the cylinder.

C. Spectroscopy

1. IR Fundamental Region

Infrared absorption spectra of the vibrational fundamental region were taken on a Beckman IR-12 infrared spectrophotometer, which has a specified maximum resolution of 0.25 cm^{-1} at 923 cm^{-1} and a specified wave number accuracy of from 0.1% at 200 cm^{-1} to 0.02% at 4000 cm^{-1}. The absorption frequencies of the systems studied are available in the literature. Since wave number readings of the spectrometer agreed with published values to within its normal operating resolution of 1 cm^{-1}, routine wave number calibration of the spectrometer was not performed.

Due to the polycrystalline nature of the matrix samples, matrices were very scattering and some tradeoffs in spectrometer operating conditions were made. The fraction of incident light transmitted in a region of no absorption depends primarily on the thickness of the matrix and to a certain extent on the deposition history of the matrix, as can be seen in Table III. Matrices deposited at 20 K are less scattering than those deposited at 9 K. The cross section for Rayleigh scattering of

Table II-3. Rayleigh Scattering by Matrices

Total Sample (m-mole)	T^a (K)	Dep. Rate (m-mole/hr)	T^b (2000 cm^{-1})	T^b (4000 cm^{-1})
15	9	6.2	.42	.25
11	9	7.6	.57	.40
11	9	24	.55	.36
14	21	28	.63	.61
59	9	28	.055	.020
120	9	23	.003	$<3 \times 10^{-4}$

[a] Temperature of deposition and observation.

[b] $T = \frac{\text{Transmitted intensity after deposition}}{\text{Transmitted intensity before deposition}}$

electromagnetic waves by particles much smaller than the radiation wavelength is proportional to ω^4, where ω is the radiation frequency.[17] This effect is manifested as a sloping baseline in the matrix experiments with transmission decreasing between 2000 and 4000 cm^{-1}. The slope of the baseline increases as the overall opacity of the matrix increases. It is apparent from Table III that deposition at 20 K leads to a better optical quality matrix than deposition at 9 K, but, as discussed previously, deposition at 20 K decreases the degree of guest isolation.

To record an accurate infrared spectrum it is necessary that a sufficient amount of radiant energy fall on the thermocouple detector element of the spectrometer. The energy in the spectrometer system is proportional to the product of the square of the spectral slit width and the signal amplifier gain,[18] so it is necessary to run with some combination of high gain and relatively wide slits to record the spectrum of a scattering sample. For double beam operation, a screen is used to attenuate the reference beam. Since noise increases linearly with the spectrometer gain setting, and the time constants required for filtering can increase the time required to obtain a spectrum to beyond a reasonable length, system energy is often maintained by sacrificing resolution and widening the slits. Typically, for samples of ~15 m-moles, the best resolution obtainable with 1% photometric error is 1.0 cm^{-1}. Increased resolution to about 0.8 cm^{-1} is possible with large noise levels--the $H^{35}Cl$ and $H^{37}Cl$ isotopic peaks can be resolved in an Ar matrix at M/A = 1000, for example, but the relative intensities are not accurately recorded. Samples at very high dilution require a large amount of matrix to produce an observable absorption peak, so the matrix

is opaque and resolution must be sacrificed. Typically, when about 50 m-moles of matrix has been deposited, it is necessary to use a spectral width of 4-5 cm^{-1}. Only the grossest spectral features can be observed under such conditions.

The true absorption linewidths for HCl/Ar at 9 K are about 1 to 1.5 cm^{-1}--comparable to the best resolution of the spectrometer under operating conditions imposed by the low transmission of the sample. Linewidth measurements from recorded spectra are thus subject to errors of ≥100%.[19] For highly scattering samples, the effect of a 4-5 cm^{-1} slit width is to greatly reduce peak intensity of the absorption line, making observation of the line difficult. Detailed discussions of tradeoffs of various experimental parameters and the errors involved are discussed in more detail elsewhere.[18-20] What has been discussed here are those particular factors that apply to the spectroscopy of highly scattering, low transmission samples.

2. Quantitative Spectroscopy

It is possible to determine the relative concentrations of two species in the same matrix by measuring their absorbances, using Beer's Law, Eq. (1):

$$\ln \frac{I_o(\nu)}{I(\nu)} = \alpha(\nu)\, lc \qquad (1)$$

where $I_o(\nu)$ and $I(\nu)$ are the baseline and observed intensities at frequency ν, $\alpha(\nu)$ is the absorption coefficient of the species studied, l is the optical path length, and c is the concentration. When the spectrometer spectral slit width, J, exceeds half the absorption linewidth (FWHM), $\Delta\nu$, peak absorbances are underestimated (by about 20%

for a 30% absorbing peak) and linewidths are overestimated (by about 25% for a 30% peak).[19] These errors increase rapidly as the spectrometer slit width increases. Under such conditions, which are applicable for the matrix spectra, it is necessary to integrate eq. (1) over the full line contour, since the integrated absorbance, which is equal to the product of peak absorbance and linewidth (with a constant determined by the particular lineshape function), is much less sensitive to the value of $J/\Delta\nu$. For a value of $J/\Delta\nu$ of 2.2, the error in the measurement of the integrated absorbance, S, ($\log_e$) is less than 3% for a 30% absorbing peak and less than 12% for a 70% (true transmission) absorbing peak.[19]

In practice, integrated absorbances were obtained from recorded spectra as the product of peak absorbance and observed linewidth (FWHM); that is, assuming a triangular lineshape. Comparison of the results of this technique with more accurate methods, such as planimeter integration of peaks on an absorbance scale, indicates that errors are due to spectral resolution rather than to analysis procedure. Appropriate error limits for quantitative spectroscopy as normally performed are ± 25% for peaks with absorbances less than 0.1, and ± 15% for peaks with absorbances between 1 and 1.5.

Measured integrated absorbances are converted to relative populations using the gas phase expression for the absorption strength for the transition connecting level (v,J) and level (v',J'):[21]

$$S_{vJ}^{v'J'} = \frac{8\pi^3 N_{v,J}}{3hc(2J+1)}\,\omega_{vJ}^{v'J'}\,|m|\,\left|M_v^{v'}(m)\right|^2 \qquad (2)$$

where

$$m = \begin{cases} J+1 & \text{R branch} \\ -J & \text{P branch} \end{cases}$$

and the squared dipole matrix element is the product of a squared pure vibrational factor $R_v^{v'}$ and a vibration-rotation factor $F_v^{v'}(m)$:

$$|M_v^{v'}(m)|^2 = |R_v^{v'}|^2 F_v^{v'}(m).$$

$F_v^{v'}(m)$ is taken to be equal to one. $\omega_{vJ}^{v'J'}$ is the frequency of the vibration-rotation transition in wavenumbers, and N_{vJ} is the population of the lower level in number per cm^3. For non-rotating species, such as the HCl dimer, the factor $|m|/(2J+1)$ in Eq. (2) is set equal to one. Since values of the squared transition moment are unknown for species such as the HCl dimer, Eq. (2) allows a calculation of only a relative population ratio between different species. Equation (2) reproduces the relative intensity of resolvable rotation-translation lines R(0) and P(1) of HCl/Ar quite well. Further aspects of quantitative spectroscopic results are discussed in Chapter III.

3. Spectroscopy of Vibrational Overtones

Overtone absorption spectra of very thick matrices were recorded on a Cary 14 spectrophotometer.[22] These samples are very opaque due to their thickness, and it was necessary to attenuate the reference beam with screens totaling about three optical density units. The overtone region of the Cary 14 was calibrated to within 0.7 cm^{-1} in the region about 5600 cm^{-1} by v=0 → v=2 absorption of gaseous HCl, using observed frequencies for $H^{35}Cl$ of Rank, et al.[23] The spectra were taken at 3 cm^{-1} resolution. Spectra of the overtone region of DCl around 4100 cm^{-1} were recorded at 1.5 cm^{-1} resolution. The spectrometer was not directly calibrated in this region; the wave number accuracy is 0.6 cm^{-1} according to the instrument manual.

D. Fluorescence Experiments

The majority of the experimental work performed involved fluorescence experiments, which in all cases are initiated by narrow bandwidth pulses from a Nd:YAG laser pumped optical parametric oscillator (OPO) tuned to one of the absorption lines of the species being studied. Vibrational fluorescence from the excited sample is detected with one of several doped germanium photoconductive infrared detectors. The detector responds with a signal proportional in real time to the fluorescence intensity. The post-detector electronics varies depending upon the particular experiment being performed. Three types of fluorescence experiments are performed: time resolved emission studies, emission spectroscopy, and fluorescence excitation spectroscopy. This section begins with descriptions of the common elements of all fluorescence experiments--the laser and OPO sources and the infrared detectors, and then describes the equipment and techniques used for the different experiments.

1. Nd:YAG Laser

The first element in the fluorescence experiments is a Chromatix Model 1000-E Nd:YAG laser. The principles and operating procedures for this laser have been described in detail in previous theses in this research group.[24,25] For completeness a brief summary of the laser principles and operating procedures will be presented here. Also, some new aspects of laser operation will be discussed.

Nd:YAG is a four level laser system which operates on four sets of transitions in the near infrared.[26] In the Chromatix laser wavelength selection is obtained by using a fixed prism between the YAG rod and the

rear cavity mirror, and rotating the rear mirror to resonate a particular wavelength. The output is internally frequency doubled with an angle-tuned $LiIO_3$ crystal. The output coupling front mirror is highly reflective in the near infrared and highly transmitting in the visible, so that the doubling crystal is effectively the output coupler for the laser. The laser is Q-switched acousto-optically with a quartz transducer.

The entire optical path of the laser is hermetically enclosed since the coatings on the optics are damaged by both moisture and dust during high power operation. The dessicant bottles on the optical enclosure must be regularly inspected and replaced. Should it become necessary to open the optical cavity, the entire laser head should be covered with a "clean box." It is possible to damage the laser optics by improper manipulation of the front panel controls of the laser power supply. Finzi[25] has outlined the safe and optimum procedure for laser use. Some additional comments useful for laser operation are presented below.

The Chromatix cavity can be precisely aligned to produce a TEM_{00} optical mode, which is characterized by a uniform elliptical beam cross section in the far field region. Observation of the far field pattern of the laser output is a very important diagnostic for laser operation. Burn spots in the optical cavity are manifested as holes or diffraction patterns in the far field. If an irregularity is present in the far field output the optical alignment may be walked around so as to avoid the damaged portion of the optical cavity. This is done by alternately adjusting the front and rear mirrors. When the damage to an optical component is located such that the beam cannot successfully be walked around the damaged spot, the damaged optical component must be replaced.

Under normal circumstances, the laser should be aligned using the rear mirror and doubler only, since rotation of the front mirror affects the direction of the output beam and may require total realignment of the OPO. Alignments can sometimes be improved by rotating the doubling crystal up or down one entire revolution. Acceptable laser alignment is indicated by three things: clean, TEM_{00} far field beam cross section; smooth, steady temporal output as observed with a fast photodiode; and low threshold.

The spectral linewidth of the laser is determined by the gain width of Nd^{3+} ions in the YAG host and is 1 cm^{-1}. This corresponds to about 100 longitudinal modes of the laser cavity. The laser can be operated at variable frequency between 2 and 80 hertz. The thermal load on the YAG rod affects the lensing characteristics of the rod, so the alignment is a function of the repetition rate. The thermal load will also vary between Q-switched and non Q-switched operation. Upon first starting the laser it is best to align the laser at the operating repetition rate, and then let the laser run under Q-switched conditions for a period of ten to twenty minutes. At that time the laser is thermally equilibrated to actual operating conditions. It should be un-Q-switched and realigned. Upon subsequent Q-switched operation, the alignment should be stable for several hours.

The two laser lines used for these experiments are the 0.532 μ green line and the 0.562 μ yellow line. These are the strongest gain lines in their groups, and the 0.532 μ line is the strongest line output by the laser. The 0.532 μ line produces a pulse of between 80 and 140 ns depending upon the precise alignment. Tightening the iris in the laser cavity produces the shortest pulses. Pulses of 120-160 ns are obtained when the laser is run with the refrigerator circuit breaker turned off.

Under normal situations the laser is operated so that the average energy per pulse as measured on a calibrated Eppley thermopile is less than 0.6 mJ. It is possible to safely operate the laser at higher energies, up to about one millijoule per pulse, if the operator is cognizant of the fact that for the short pulsewidth of this line, large peak powers (≥10 kW) are produced. Thus, focusing the output into the OPO could damage one of the optical surfaces of the OPO, for example, if the OPO were not well aligned. Safe operating procedure dictates that 0.6 mJ be exceeded only with caution.

The output pulse of the 0.562 μ line is considerably longer. Originally the Q-switched pulse width (FWHM) was 450-600 ns. During the course of these experiments it was necessary to perform a total optical realignment of the YAG laser. After the realignment the pulse width of the 0.562 μ line increased to 700-800 ns. The maximum power obtainable is 0.7-0.8 mJ per pulse--this corresponds to running the YAG power supply at maximum power at forty hertz. It is difficult to successfully pump the OPO with pulsewidths of 700-800 ns because of the low peak power, so it is necessary to shorten the Q-switched pulse. This may be done by slightly detuning the $LiIO_3$ doubling crystal.[27]

In the configuration of the Chromatix laser, the doubling crystal is both the output coupler and a non-linear loss for the infrared fundamental frequency.[28] The frequency doubled output will increase as the square of the intracavity power of the fundamental until the point where the output power is equal to the single pass gain of the oscillator at the fundamental frequency. The pulse will now last until the population inversion is depleted. When the doubler is detuned from optimum phase-matching, the power at the fundamental frequency required

to produce a particular output power will be increased compared to the optimally phase-matched case. Thus, maximum output power will not occur until a fundamental power level is reached which rapidly depletes the population inversion and the pulse will be shortened. When the detuning is not too great, the total output energy of the frequency doubled pulse should be unaffected by the shortened pulsewidth.[28]

The following procedure should be used when shortening the pulse at 0.562 μ. This is the only operation performed while the laser is running in the Q-switched mode, and the operator should be cognizant of the opportunities for damage to the laser optics. The laser is aligned and Q-switched and then set so that the average output energy per pulse is less than 0.3 mJ. The output energy should be measured. Looking at the laser pulse on an oscilloscope, the doubler is slightly detuned until the pulse just begins to shorten. At the low pumping levels which produce less than 0.3 mJ/pulse output energy, the pulse is quite long and the shortened pulse may still be about 700 ns. The pulsewidth sharpens under higher pumping conditions. Next, the far field pattern of the beam should be observed. It should remain TEM_{00}. If the doubler has been tilted too far, the beam will begin to show evidence of a double lobe pattern characteristic of TEM_{01}. If this occurs, the doubler should be repositioned for optical phase matching under non-Q-switched conditions, and the above procedure repeated. Next the output energy should be measured; it should be within 15% of the original energy. The laser power can now be increased and the pulsewidth at higher output energies measured. The pulse can usually be narrowed to 550 ns without much sacrifice of energy, and this is short enough to successfully pump the OPO. If the pulse has not been shortened enough, the above procedure should be repeated.

Since the pulsewidth is much longer at 0.562 μ than at 0.532 μ, peak power for a given output energy is reduced. Hence, energies of 0.7-0.8 mJ/pulse at 0.562 μ can be routinely used to pump the OPO.

2. Optical Parametric Oscillator

A parametric interaction can convert power incident at a high frequency, termed the pump, ω_p, into two lower frequencies termed the signal, ω_s, and the idler, ω_i. By convention, the signal frequency is the higher of the two parametrically generated frequencies. Parametric interactions have been observed in the microwave region for many years.[29] In order to couple energy between fields of different frequency, it is necessary that the fields propagate within some medium which has a non-linear, but not dissipative, response to the fields. In an OPO the frequencies are in the visible and infrared and the non-linear medium is placed within an optical resonator so that the signal and idler fields can be built up by multiple passes through the medium. The non-linear response to the fields is the non-linear electric susceptibility of a crystal. The parametric process requires both conservation of energy:

$$\omega_p = \omega_s + \omega_i \tag{3}$$

and phase-matching, which is conservation of photon momentum:

$$\underset{\sim}{k}_p = \underset{\sim}{k}_s + \underset{\sim}{k}_i \tag{4}$$

where $\underset{\sim}{k}$ is the wave-vector of the propagating electromagnetic field. For collinearly propagating waves, the phase matching condition becomes:

$$n_p\omega_p = n_s\omega_s + n_i\omega_i \tag{5}$$

where n_j is the index of refraction of the medium at the frequency ω_j. The most frequently used method for satisfying Eq. (5) employs a birefringent medium in which different fields have differing polarizations.[30] The particular signal and idler frequencies generated for a given pump frequency depend upon the set of indices of refraction--anything that varies the indices of refraction can tune the signal and idler frequencies. The two most common ways of doing this are by angle tuning or temperature tuning. In the angle tuned method the index of refraction seen by the extraordinary wave is a combination of ordinary and extraordinary indices of refraction, the particular combination depending upon the angle of propagation relative to the optic axis. Thus, varying the angle between the direction of propagation and the optic axis will change the extraordinary index of refraction, changing the signal and idler frequencies. Temperature tuning relies on the fact that indices of refraction vary independently with temperature, so that the particular frequencies satisfying the phase matching conditions become a function of crystal temperature. More detailed considerations on theoretical and practical aspects of optical parametric oscillators can be found elsewhere.[31-33]

The OPO used in the present experiments consists of a 5 cm long $LiNbO_3$ crystal, which is 90° phase matched (signal and idler polarizations are perpendicular to the pump polarization) and temperature tuned, placed within a confocal resonant cavity. The detailed construction and mode-matching conditions have been discussed by Leone[24] and Finzi,[25] but for completeness, some aspects will be discussed here.

The optical resonator is resonant for the idler only, since doubly resonant cavities are not continuously tunable. The linewidth of the

resonated frequency is determined by the gain width of the crystal and the parameters of the optical resonator, while the linewidth of the non-resonant frequency will reflect the linewidth of the pump.[33] For the present experiments, the linewidth of the resonated idler is 0.2-0.3 cm^{-1},[34,35] so that the signal linewidth will reflect the 1 cm^{-1} linewidth of the doubled Nd:YAG pump. It is possible to narrow the linewidth of the idler using an etalon inside the cavity of the OPO,[24,25,34] but that is not necessary for the present experiments.

The $LiNbO_3$ crystal is housed in an oven which is stable to 0.05 C in the range 50-450 C. The useful operating temperature range for the OPO is above 230 C. A resistor has been placed in parallel with the crystal oven such that the voltage across the resistor is proportional to the temperature of the oven. The voltage is read to five figures with a digital voltmeter to a precision of 0.1 mV. Wave number calibration of the output of the OPO is made against this voltage--1 cm^{-1} corresponds to between 0.3 and 0.5 mV, depending upon the particular temperature. The fluctuation of the voltage reading is ± 0.1 mV.

Four pairs of mirrors of 9.2 cm radius of curvature allow operation of the OPO to produce idler frequencies between 1.7 and 3.5 μ. Leone[24] has described the alignment procedure of the OPO in detail, using a method of successive back reflections. Observation that the OPO is in fact oscillating is most readily made by observing the signal output after using a red glass filter to separate the red signal from the green or yellow pump. The initial alignment may be improved by adjusting mirrors so as to increase the intensity of the signal beam. Observation of the infrared idler pulse after filtering pump and signal frequencies can be made with an InSb PEM detector. This provides a measurement of

the time evolution of the idler pulse and a quick visual diagnostic of the OPO alignment. Due to the small area of the PEM detector, however, walk-off effects in varying the OPO alignment can drastically affect the PEM response, so the PEM is not a useful diagnostic for final alignment. When the OPO is pumped with 0.562 μ to produce an idler at 1.7 μ, the signal frequency is 0.84 μ which is not observable to the eye. Alignment with the 1.7-2.1 μ set of mirrors (P-4) is best done at about 300 C, where the signal and idler frequencies are 0.78 and 2.0 μ. 0.78 μ is visible if the room lights are extinguished. Operation with the 3.0-3.5 μ set of mirrors (P-1) has a very high threshold, and since the output is often weak upon initial alignment, the signal beam is best observed with the room lights extinguished. Operation between 2.0 and 3.0 μ with the P-2 and P-3 sets of mirrors is much easier, and the signal beam is easily observed with room lights on.

It is important in aligning the OPO to make certain that the pump beam passes through the centers of the input and output mirrors. This will ensure that the signal, pump, and idler beams will exit normal to the surface of the curved rear mirror, and hence will propagate collinearly if the OPO is properly aligned. The collinearity of the pump and signal beams can be checked on a screen located across the room from the OPO. When the pump and signal have parallel propagation vectors, the phase-matching condition, eq. (4), requires that the $\underset{\sim}{k}$ vector of the idler must be parallel to those of the pump and signal. Hence, the infrared idler may be aligned using the visible, collinear signal or pump beams. This is particularly useful for the present experiments, since the sample is located about two meters from the OPO.

Representative threshold and operating conditions in the three frequency regions used are given in Table IV. Operation in the 3.0-3.5 μ region is more difficult than in the other regions.[24] The gradient control is crucial to operation here. The OPO is best aligned at 3.3 μ (390 C), where a threshold of 0.4 mJ/pulse in a 140 ns 0.532 μ pump pulse has been obtained. Operation at 3.46 μ is never far above threshold; many pump pulses do not produce parametric response, so it is difficult to measure idler power. In performing signal averaging experiments at 3.46 μ it is best to use the 0.629 μ signal pulse impinging on a photodiode to trigger the experiment--only pump pulses producing parametric response will then be averaged. The YAG pump energy has been increased to 0.85 mJ/pulse for some experiments at 3.46 μ. No damage to the OPO was observed, but short duration pulses of this much energy should be used cautiously. The longest wavelength produced was 3.5 μ (2860 cm^{-1}, 427 C).

3. Wave Number Calibration of the OPO

The OPO idler frequency can be calibrated in the infrared by two techniques: single beam spectroscopy[24] or spectrophone absorption[25] of gaseous samples. In practice the calibration is performed as a function of the voltage reading in parallel to the crystal oven, as described above. The calibration gases are HCl, v=0 → v=2 absorption for 1.77 μ; DCl, v=0 → v=2 absorption for 2.43 μ; and HCl, v=0 → v=1 absorption for 3.46 μ.

Use of the OPO as a single beam spectrometer has been described and illustrated by Leone[24] and Finzi.[25] Briefly, the idler pulse is observed on the InSb PEM detector after passing through a 20 cm gas cell

Table II-4. OPO Operating Characteristics

	Idler wavelength (μ)		
	1.77	2.43	3.46
Idler (cm^{-1})	5650	4120	2890
Signal (μ)	.823	.681	.629
Pump (μ)	.562	.532	.532
Threshold conditions			
Pump width (ns)	500	160	130
Pump energy (mJ)	.49	.15	~.7
Pump power (kW)	.98	.94	~5.6
Rep. rate (Hz)	40	40	40
Operating conditions			
Pump width (ns)	500	130	130
Pump energy (mJ)	.70	.60	.73
Rep. rate (Hz)	40	40	40
IR width (ns)	200	80	40[b]
IR energy (μJ)	13	25[a]	2±2
Photons/pulse (10^{14})	1.2	3.1	.3±.3
Crystal temp (C)	244	312	425
Calibration (cm^{-1}/0.1 mV)	.290	.204	.22

[a] Measured using an uncoated Ge filter. Reported value is twice the experimental measurement.

[b] From Reference 23.

containing several hundred torr of the calibration gas. The output pulse of the PEM is sent into a Tektronix 1S1 sampling unit, which samples the magnitude of the PEM pulse at a set time delay relative to a trigger, which is the YAG pump pulse. The time delay is chosen so that the time of peak idler intensity is sampled, and the 1S1 outputs a dc voltage proportional to the peak amplitude of the idler pulse. The dc voltage is sent to a strip chart recorder and the OPO temperature is scanned at a rate of about 0.1 C or 1 cm^{-1} per minute. When the laser is scanned through an absorption, the peak intensity of the idler is reduced and the dc output of the 1S1 changes--this appears as an absorption peak on the strip chart recorder. The main source of noise on the single beam absorption spectrum is due to pulse to pulse fluctuations in idler output and typically can be 10% of the full signal. The spectrum is improved by RC filtering the output of the 1S1, but strong absorptions, and hence high gas pressures, are required to produce peaks substantially greater than the noise level. Nevertheless, the absorption spectrum technique was used most frequently to calibrate the OPO in the 1.77 μ and 2.43 μ regions. Since OPO operation is barely above threshold at 3.46 μ, calibration even with very strong absorptions is difficult using the PEM and 1S1, since the pulse to pulse fluctuation can be as high as 100%.

The best method for calibrating the OPO in the 3.46 μ region is to use a spectrophone filled with 5-10 torr of HCl. Finzi[25] has detailed the construction and operation of simple spectrophones using foil-electret microphone elements, and these are suitable. The noise produced by the spectrophone is not due to pulse to pulse fluctuation of the OPO, and signal-to-noise ratio depends mainly on the amount of energy

actually absorbed by the gas. For strong idler pulses interspersed with weaker ones, as under near threshold operation, observation of absorption using a spectrophone is best performed using an oscilloscope to display the spectrophone signal. Signal-to-noise ratios as high as five on certain shots are interspersed with much weaker responses; nevertheless identification of absorption is unambiguous. If the spectrophone output were sampled by the ISI in this region, the resulting dc output would be as noisy as that resulting from sampling the PEM signal. Calibration in the 3.46 μ range, then, consists of visually monitoring the output of the spectrophone while scanning the idler wavelength.

The result of the calibration is a plot of oven voltage vs wave number. These plots are exceedingly linear over regions of about 100 cm^{-1}, slopes being constant to about 1%. The slopes of the calibration plots in cm^{-1} per 0.1 mV units of the digital voltmeter output are included in Table IV. The reading of the voltmeter has an uncertainty of ± 0.1 mV, which corresponds to 0.3 cm^{-1} uncertainty. When scanning the temperature the voltmeter reading leads the true oven temperature by as much as 0.2 mV, so that during a scan the voltage reading is systematically in error by about 0.6 cm^{-1}. Thus, the overall uncertainty in calibration plots is about 1 cm^{-1}. This can be reduced by manually setting the OPO to the absorption frequencies of the calibration gas and allowing the OPO oven enough time to equilibrate, so that an accuracy of 0.3 cm^{-1} is attainable. Such accuracy was not necessary for the present experiments.

The exact voltage reading of the oven temperature depends upon the particular digital voltmeter used. With the same voltmeter, the

Figure II-2. General experimental schematic. The output of the OPO is collimated, filtered, and directed into the matrix; sometimes the excitation is focused as shown. Fluorescence is collected with a lens and detected by a Ge:Hg photoconductive detector cooled with pumped liquid H_2 or with liquid He. After amplification, the signal can be averaged to produce a fluorescence decay trace, or integrated to produce an excitation spectrum. A photodiode pulse synchronized with the YAG pulse triggers the experiments. More details in the text.

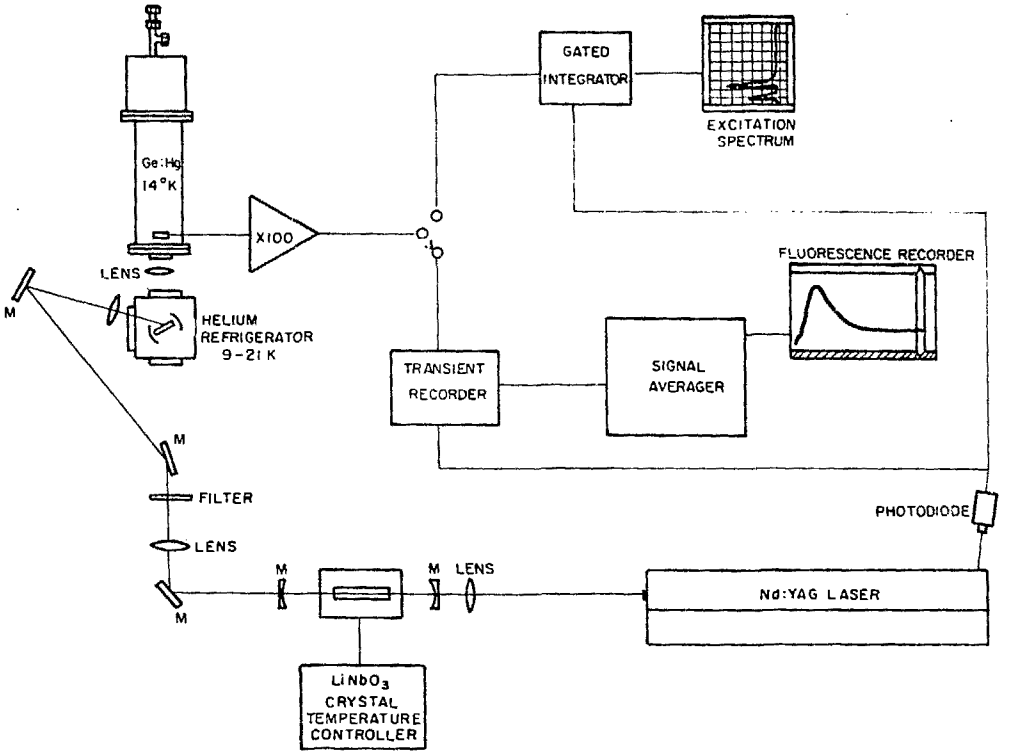

XBL 7710-10006

calibration drifted by no more than 0.5 mV during a period of a year, so it is unnecessary to calibrate the OPO frequently.

4. Experimental Arrangement

The overall schematic for the experimental arrangement is shown in Fig. 2. The beams emerging from the OPO are collimated by a 25 cm focal length quartz lens, and in some experiments, focused into the matrix by a 4 cm focal length CaF_2 lens, to a spot diameter of 60-80 μ. The collimated beam has a diameter of 260-370 μ at the position of the matrix. Two excitation geometries were used. In experiments in which the first overtone is excited, the beam is directed perpendicularly through the matrix toward the detector, which is shielded from the excitation pulse by a cooled dielectric filter which allows transmission of only $\Delta v=1$ transitions of the molecule being studied. In these experiments scattered light is present as a sharp spike at the beginning of the fluorescence decay curve, but its level is well below saturation of the detector. In other experiments the beam excited the front surface of the matrix, entering the cryostat through the CaF_2 side window, as illustrated in Fig. 2. No scattered light is observed with this geometry, even after signal averaging, with $\Delta v=2$ excitation. Experiments directly exciting the fundamental required front surface excitation.

The infrared detectors are mounted vertically above the matrix sample. Fluorescence from the matrix is focused in a 1:1 magnification ratio by a 5 cm f/1 CaF_2 lens. Details on the detector performance are given in subsection 6. Alignment of the detector is quite straightforward. Since the pump, signal, and idler beams emerging from the OPO

are collinear, either the visible pump or signal beam can be used for alignment purposes. The Q-switched pump beam should not be used for alignment, however, since alignment requires that the beam impinge directly on a dielectric interference filter, and some filters are damaged at Q-switched YAG power levels. The alignment beam is directed upward by a gold mirror so that it impinges on the dielectric filter covering the detector aperture. (The detector should be off during alignment.) The focusing lens is placed a distance equal to twice its focal length below the height of the detector element (which is about one inch above the bottom of the detector dewar, depending upon the detector dewar). The lens is positioned so that the alignment beam is brought back to the detector aperture--it should now be passing through the center of the fluorescence lens. Next, the refrigerator is positioned so that the matrix is placed a distance twice the focal length below the fluorescence lens and the beam passes through the center of the matrix. This is the "straight through" excitation geometry. The detector and fluorescence lens are now well aligned for optimum 1:1 focusing of the fluorescence. For front surface excitation the mirror below the matrix is rotated and the beam is bounced off a second mirror and brought back to the original illuminated spot on the matrix. Final alignment is optimized by minor adjustments of lenses and mirrors--this is especially easy when single shot signals can be directly observed on an oscilloscope. When the 4 cm focusing lens is used, it is put in last, 4 cm from the position of the matrix inside the refrigerator. It is positioned so that it illuminates at the same spot on the matrix.

The pump beam is removed by a red glass filter during the fluorescence experiments in the 1.8 μ and 2.4 μ regions. At 3.5 μ it is necessary to filter the 0.532 μ pump with Ge, since glass will not transmit

3.5 μ. In some experiments at 1.8 and 2.4 μ the power of the excitation pulse was varied using neutral density filters. The transmission of these filters was checked at 1.8 and 2.4 μ on a Cary 14 spectrometer, and found to agree with their calibrated transmission in the visible. The neutral density filters were positioned near the red glass filter.

5. Sample Heating Effects

The energy absorbed by the guest and not reradiated will ultimately be dissipated into lattice phonons producing heat. The bulk temperature rise in the sample, and thermal relaxation, are estimated below. Assume an instantaneous excitation pulse which has a cross-sectional area πr^2 and passes through a length l of the matrix. The energy absorbed will be

$$E = E_0(1-e^{-\alpha c l})$$

where E_0 is the total pulse energy, and α and c are the absorption cross-section and concentration of the guest species. For overtone excitations for which α is small or for short distances l, $E \approx E_0 \alpha c l$. The energy is absorbed in a volume $\pi r^2 l$, and the instantaneous temperature rise of the irradiated volume is $\Delta T = E/C_v$, assuming the absorbed energy is immediately released as heat. C_v is the heat capacity of the volume $\pi r^2 l$. Expressing the concentration of the guest as a mole fraction, $c=x\rho$, where ρ is the number density of the host lattice, the maximum temperature rise is given by

$$\Delta T = \frac{E_0 \alpha x}{\pi r^2 C m} \qquad (6)$$

where C is the specific heat and m is the atomic mass of the host atom (in grams). For HCl v=0 → v=2 absorption, $\alpha \sim 1 \times 10^{-19}$ cm^2/molecule. With C at 10 K and m for Ar taken from Table I, E_0 = 20 μJ/pulse, and assuming tight focusing to r=30 μ, the temperature rise is

$$\Delta T = (1.3 \times 10^4)x \text{ K}.$$

For $x = 10^{-3}$, ΔT = 13 K.

Also important is the thermal relaxation time. The problem is mathematically formulated with a diffusion equation[36]

$$\nabla^2 u(r,t) - \frac{1}{\beta^2} \frac{\partial u(r,t)}{\partial t} = 0$$

$$\beta^2 = K/mC\rho \qquad (7)$$

where u(r,t) is the temperature distribution function and corresponds to the difference between actual temperature and equilibrium temperature. K is the thermal conductivity and ρ, m, and C have been previously defined. For the present problem, the coordinate system is cylindrical and the boundary conditions are i) $u(r_o,t) = 0$ and ii) $\frac{\partial u}{\partial r}(0,t) = 0$, and the initial condition is iii) $u(r,0) = T_o$ for $0 \le r \le r_o$ and $u(r,0) = 0$ for $r > r_o$. This corresponds to an instantaneous temperature rise by $\Delta T = T_o$ upon irradiation of the volume of the matrix intercepted by the excitation beam. Equation (7) is solved by[37]

$$u(r,t) = \sum_{s=1}^{\infty} \frac{2T_o}{j_{0,s} J_1(j_{0,s})} J_0\left(\frac{j_{0,s}}{r_o} r\right) e^{-t/\tau_s}$$

$$\tau_s = r_o^2/(\beta j_{0,s})^2 \qquad (8)$$

where J_0 and J_1 are the zeroth and first order Bessel functions, and $j_{0,s}$ is the s^{th} root of J_0. The thermal decay is a sum of exponentials, the slowest of which has a relaxation time of τ_1. For r_o = 30 μ, using the values necessary to compute β from Table I, and using $j_{0,1}$ = 2.405, τ_1 has a value of 7.1 μs at 10 K for Ar, which is the upper limit for the thermal decay time of the irradiated volume.

Heating effects should be negligible because heat cannot be released faster than the non-radiative decay of the excited guest species. For all experiments performed, measured non-radiative decay rates exceed 10 μs, and are slower than thermal decay rates. Thus, heat is dissipated as rapidly as it is produced and the temperature will never build up to the extent predicted by Eq. (6).

6. Infrared Detectors and Signal Amplifiers

Finzi[25] has described in detail the theory and practical details of the infrared detectors used in the present studies. The majority of the HCl experiments were performed with a mercury-doped germanium (Ge:Hg) photoconductive detector, operated with the LH0033 buffer pre-amplifier circuit described by Finzi. In some experiments, a 0.3 mm by 10 mm copper-doped germanium (Ge:Cu) photoconductive detector, also described by Finzi was used.

The electronics system which produces a time resolved fluorescence signal is composed of the detector and its pre-amplifier followed by a signal amplifier with a gain of 10 to 1000. The overall system is characterized by a frequency bandwidth, which will distort the fluorescence signal if a characteristic time of the fluorescence signal approaches either the high frequency or low frequency cut-off of the electronics.

Dasch[38] has analyzed the response of an electronic network composed of a high pass and a low pass filter to a pulse which is a sum of exponentials. For a single exponential pulse,

$$S(t) = e^{-kt}$$

the pulse emerging from the network is given by[38]

$$S'(t) = \frac{\omega_H}{\omega_H - k}\left[\frac{k e^{-kt} - \omega_L e^{-\omega_L t}}{k-\omega_L} - e^{-\omega_H t}\right] \qquad (9)$$

where ω_H and ω_L are the high and low cut-off frequencies (angular frequencies). In practice, both the preamplifier and the signal amplifier have high and low frequency cut-offs, and the electrical network should consist of a series of RC filters. If the low frequency (high frequency) cut-offs of the pre-amplifier and signal amplifier are very different, only the highest (lowest) low (high) frequency cut-off will affect the signal and Eq. (9) is appropriate. For the present experiments, the effects of low frequency response are more of a problem than those at high frequency. For a network of two low pass filters in series, the response to an input exponential pulse is

$$S'(t) = \frac{k^2 e^{-kt}}{(k-\omega_1)(k-\omega_2)} + \frac{\omega_1^2 e^{-\omega_1 t}}{(\omega_1-\omega_2)(\omega_1-k)} + \frac{\omega_2^2 e^{-\omega_2 t}}{(\omega_2-\omega_1)(\omega_2-k)} \qquad (10)$$

where ω_1 and ω_2 are the low frequency cut-offs of the two high pass filters. Equation (10) agrees with Eq. (9) when $\omega_1 = \omega_L$, $\omega_H \to \infty$, and $\omega_2 = 0$.

High frequency and low frequency responses can be measured using Eq. (9), but some features made evident by Eq. (10) must be considered. If the input pulse is short so that $k >> \omega_H >> \omega_L$, Eq. (9) is reduced to the sum of a rising and falling exponential; the falling exponential has

the decay time ω_H. For moderately long pulses, $\omega_H > k > \omega_L$, Eq. (9) has a slowly rising negative component $e^{-\omega_L t}$. This is responsible for baseline "droop" seen in many fluorescence decay traces and is due to the fact that the electronic system attenuates those low frequency components of the signal necessary for a smooth approach to a level baseline. The relative magnitude of the droop is given by the ratio of t=0 amplitudes of the e^{-kt} and $e^{-\omega_L t}$ terms in Eq. (9), (assuming $\omega_H \to \infty$) and is

$$\frac{A_{\omega_L}}{A_k} = -\frac{\omega_L}{k} . \tag{11}$$

This becomes increasingly important as k approaches ω_L.

All of the preceding paragraph assumes that there is effectively only one high pass filter in the electronic system. Equation (10) yields a response signal which is the sum of three exponentials, two falling, k and ω_2, and one rising, ω_1, for $k > \omega_1 > \omega_2$. The $e^{-\omega_1 t}$ produces baseline droop. For ω_2 small, the effect of the second high pass filter is small. For the case of two identical high pass filters, $\omega_1=\omega_2$, the response will have only one falling and one rising exponential. The relative amplitudes at t=0 of the rising and falling exponentials is

$$\frac{A_{\omega_1}}{A_k} = -\frac{\omega_1}{k}\left(\frac{2k-\omega_1}{k}\right). \tag{12}$$

Comparison of (9) and (10) and of (11) and (12) with $\omega_1=\omega_L$ produces the following conclusions: For two equal high pass filters in series, the frequency characteristic of the baseline droop is the same as that produced by only one high pass filter. However, the magnitude of the

droop is enhanced with two filters, since $(2k-\omega_1)/k$ in Eq. (12) is greater than one if $k > \omega_1$. The experimental manifestation of this result will be discussed below.

In the detector pre-amplifier system, the high frequency cut-off, ω_H, is due to an RC formed by the load resistor and a small stray capacitance inherent in the pre-amplifier and detector mounting. The intrinsic time constants of doped Ge photoconductive detectors are much faster than 100 ns, and can be made as fast as 1 ns.[39] Finzi[25] has measured ω_H for the Ge:Hg detector with a 30 K load resistor by using scattered light from the OPO ($1/k \sim 70$ ns) as a very fast input pulse. The 375 ns decay of the signal gives the detector-pre-amplifier high frequency time constant. The high frequency time constant of the Ge:Cu detector is 110 ns.[25]

The low frequency time constant can be measured by using a relatively long fluorescence decay pulse as the input optical signal, and observing the rise time of the recovery of the weak baseline droop. Figure 3 shows such a measurement for the Ge:Hg detector when a fluorescence signal of 200 μs decay time is used as the input pulse. The rise of the baseline droop has a time constant of 11 ms, close to a calculated value of 17 ms.[25] The measurement presented in Fig. 3 used a Keithley 103 amplifier which has a low frequency cut-off of 0.1 Hz. Low frequency responses of other detector-amplifier arrangements have also been measured in the same way. Using a Keithley 104 amplifier in place of the 103 also yields a low frequency time constant of 11 ms. However, the magnitude of the droop is greater using the 104 than it is using the 103. The low frequency cut-off of the 104 is specified to be about 15 Hz, comparable to the low frequency cut-off of the pre-amp.

Figure II-3. Long-time response of detector system to an intermediate pulse. The detector system is the Ge:Hg detector with the Keithley 103 amplifier with the buffer follower. The fluorescence signal is from an HCl/Ar sample, M/A = 527 ± 5, at 9K; τ = 230 μs. The upper curve shows the fluorescence peak with a small droop; it is expanded 16 times to produce the lower curve, and clearly shows the exponential recovery of baseline droop. The inset shows the analysis for the low frequency cut-off: $\omega_L = 90\ \text{sec}^{-1}$, $\tau_L = 11$ ms.

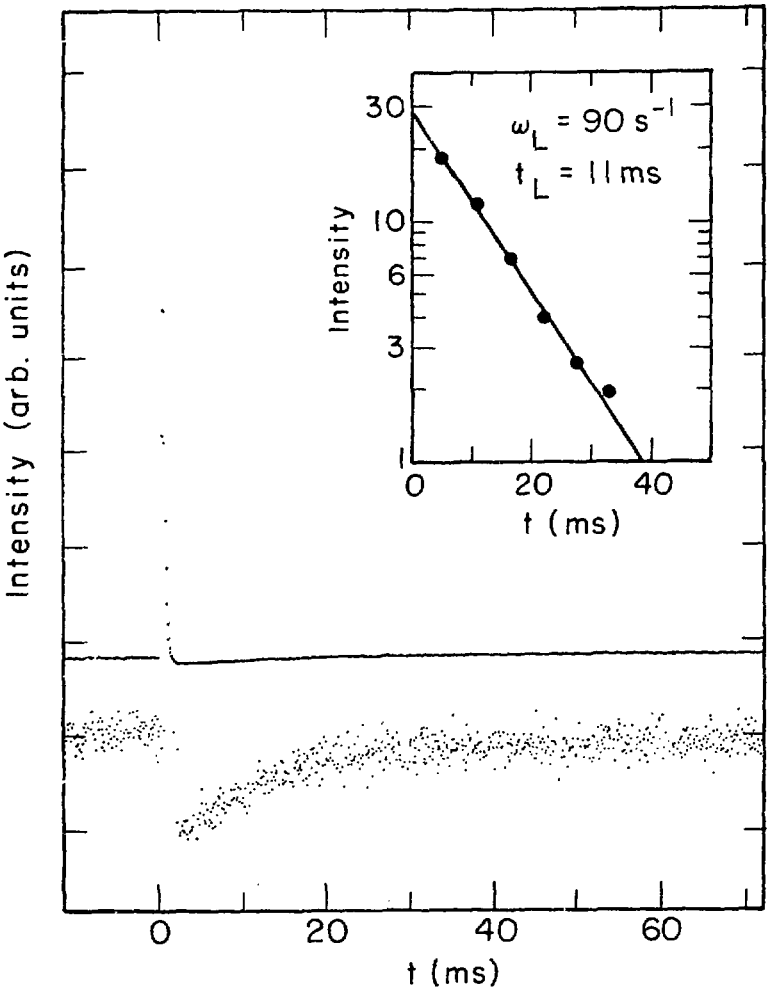

XBL 7711-10364

The droop is large with the 104 since the electronic system has two equal high pass filters in series, as described by Eq. (10). The Ge:Cu detector uses a Santa Barbara Research Corporation Model A 320 amplifier, which has been measured by the present technique to have a low frequency time constant of 3 ms (55 Hz).

In principle, amplifier distortions of a fluorescence signal which is the sum of exponentials can be accounted for using equations like (9) and (10) if the amplifier cut-off frequencies are known. In practice, it is preferable to use electronics with a bandwidth much larger than the range defined by the characteristic frequencies of the fluorescence signals, since this will yield a decay trace with a smooth baseline. The errors involved in analyzing decay traces with baseline droop will be discussed in Chapter IV.

For the DC1 experiments, the Ge:Hg detector was moved to a dewar which could accommodate a circular variable filter, identical to the dewar described by Finzi[25] for the Ge:Cu detector. Since the fluorescence decay times of DC1 are as long as 20 ms, a new, dc coupled pre-amplifier was built for the Ge:Hg detector--when used with the 103 amplifier the low frequency response of the electronics should extend to the 0.1 Hz cut-off of the 103 amplifier. Thus, problems of baseline droop are avoided. The pre-amplifier circuit is shown in Fig. 4. This pre-amplifier differs from that described previously[25] in two respects: The 0.56 μF coupling capacitor has been removed and a 300 kΩ voltage limiting resistor has been placed in series with the detector and 30 kΩ load resistor. The detector is biased at 45 V. The voltage limiting resistor prevents the dc level of the input to the LH0033 from exceeding 5 V, protecting the chip. During operation, under conditions of high

Figure II-4. Electrical schematic for the dc coupled Ge:Hg preamplifier. See text and reference 25 for details.

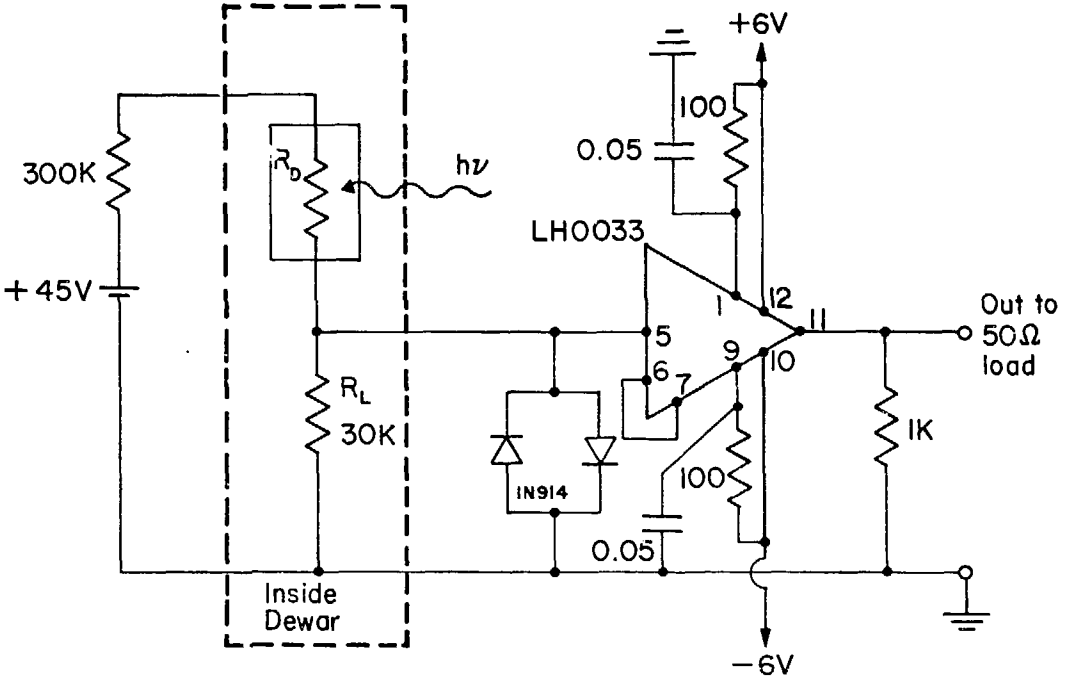

XBL7711-2181

background flux, the output of the pre-amp can have a dc level as high as 2-3 V, which exceeds the maximum specified dc input for the Keithley 104 amplifier. When using the 104 with the Ge:Hg detector with the dc pre-amp, the dc level of the pre-amp output should be measured, and a 50 ohm terminator placed in parallel with the input to the 104, if the dc level exceeds the specified amplifier tolerance of 2.5 V.

The 300 kΩ voltage limiting resistor is not cooled during detector operation, and will contribute Johnson noise to the detector system. In fact, the peak to peak noise level referred to the input of the 104 amplifier increased from 0.14 mV to 0.18 mV under otherwise identical conditions, upon modification of the Ge:Hg detector pre-amp. For the present experiments, this noise increase is viewed as the price for dc coupling, although the noise could be reduced by cooling the voltage limiting resistor. This was not necessary for the present experiments.

The high frequency time constant of the revised Ge:Hg detector was measured to be 450 ns. The high frequency response of the detector is affected by the 30 kΩ voltage limiting resistor. For short signals, such as scattered light (70 ns), the pre-amplifier shows a baseline undershoot with a recovery time of about 5 μs. For fluorescence signals from DCl, which are much longer than this, no short term distortions are observable. The dc response of the amplifier was measured by observing the peak amplitude of a chopped cw source as a function of chopping frequency, using the 103 amplifier, since an intermediate duration pulse necessary for using the baseline droop technique would have to be very long. At the minimum attainable chopping frequency of 7 Hz, the peak amplitude was attenuated by 20 ± 10% from the high frequency (100 Hz) value, which corresponds to a low frequency time constant of 0.3-1.0 second.

The 45 V bias level was chosen empirically by measuring signal-to-noise response of the detector to both a chopped cw source and a short pulsed (OPO) source. In general, the signal-to-noise response of a background limited photoconductive detector, as characterized by D^*, is constant with bias voltage until a critical voltage is reached, at which point increasing bias voltage decreases D^*.[40] For Ge:Hg, the critical voltage lies between 45 and 90 V, by empirical observation.

In order to estimate the magnitude of decay constants implied by null results of a fluorescence decay experiment, two questions arise concerning the limits of detector performance and experiments that can be performed: 1) How strongly must the sample be excited in order to produce an observable response from the detector and 2) What is the fastest decay to which the detector can respond? These are really two aspects of the same question. For a power P_s, incident on a background limited detector element, the signal-to-noise response of the detector will be

$$\frac{V_S}{V_N} = \frac{P_S D^*}{(A_d \Delta f)^{\frac{1}{2}}} \tag{13}$$

where V_S and V_N are the signal and noise voltages produced, D^* is the specific detectivity of the detector, A_d is the detector area in cm^2, and Δf is the bandwidth (Hz) of the signal processing electronic system. D^* can be interpreted as "the signal-to-noise ratio when one watt is incident on a detector having a sensitive area of 1 cm^2 and the noise is measured with an electrical bandwidth of 1 Hz."[41] For a fuller discussion of D^* and other detector parameters, the reader is directed elsewhere.[25,40,41]

For laser excited samples, the incident power is due to the fluorescence collected by the detector optics. For instantaneous excitation of N_0 molecules in the image of the detector at the sample at t=0,

$$P_S = P_0 e^{-kt}$$

$$P_0 = gAh\nu N_0 \tag{14}$$

where g is the geometrical factor equal to the fraction of a sphere subtended by the detector optics, A is the Einstein coefficient for emission at frequency ν, and k is the decay constant for the excited sample. The signal, V_S, is distorted by the high frequency and low frequency cut-offs of the post-detector electronics, as given by Eq. (9), whereas the noise voltage is proportional to the square root of the electrical bandpass, since the noise spectrum is independent of frequency. Considering only the high frequency cut-off, ω_H, the observed signal-to-noise ratio is

$$\frac{V_S}{V_N} = \frac{P_0 D^*}{(A_d \Delta f)^{\frac{1}{2}}} \frac{\omega_H}{\omega_H - k} \left[e^{-kt} - e^{-\omega_H t} \right] \tag{15}$$

The maximum signal-to-noise ratio will occur at time t_{max}, given by

$$t_{max} = \frac{1}{\omega_H - k} \ln\left(\frac{\omega_H}{k}\right). \tag{16}$$

All of the above refers to the case of a background limited photoconductive detector in which the source of noise is the fluctuation in intensity of the background thermal radiation striking the detector. In actual practice, the Ge:Hg detector noise arises from other sources as well, such as Johnson noise from the voltage limiting and load resistors

and amplifier noise. For the rough estimates of the present section, (to within a factor of about 2) however, the detector may be considered as background limited; background fluctuation is about 50% of the noise of the Ge:Hg detector system.

The value of D^* depends on the conditions of measurement and operation, and, in particular, on the detector field of view and the presence of a cooled interference filter which reduces the thermal background flux.[25] For the Ge:Hg detector used in these experiments, D^* has been measured by the Santa Barbara Research Corporation. For a 300 K background reduced by a cooled interference filter transmitting from short wavelengths only to 3.2 μ, with a 0.64 π steradian field of view, a 30 kΩ load resistor and a -60 V bias, the D^* value measured for 3.2 μ is 3.0×10^{11} cm $(Hz)^{\frac{1}{2}}$/watt. D^* decreases by about 20% as the bias is changed from -60 to -30 V. Typical values of D^* for Ge:Hg detectors without benefit of a cooled interference filter are about 1×10^{10} at 3.2 μ.[39] For the following considerations a conservative estimate of $D^* = 1 \times 10^{11}$ for the detector in experimental conformation is used.

Question (1) is answered assuming $\omega_H >> k$, and requiring $V_S/V_N > 1$ in Eq. (15). In this case $t_{max} = 0$. For the Ge:Hg detector with a Keithley 104 amplifier, $\Delta f = 3 \times 10^6$ sec^{-1} and $A_d = 0.3$ cm^2, so $P_0 = 9.5 \times 10^{-9}$ watt. For HCl, with $A = 33.9$ sec^{-1} and $\nu = 8.6 \times 10^{13}$ sec^{-1}, $gN_0 = 5 \times 10^9$. Assuming a collection efficiency, g, of 1%, 5×10^{11} molecules of HCl must be excited to produce an observable single shot S/N of 1. Equations (15) and (16) reveal the tradeoff between peak fluorescence intensity and detector time constant. As k becomes much faster than ω_H, the peak fluorescence intensity must rapidly increase to

maintain a constant S/N ratio at t_{max}. For a particular transition and collection geometry, this requires that N_0 must increase. Signals can be observed (although distorted in time) from samples decaying faster than the detector response time, provided that enough molecules are excited. Equation (15) can be evaluated at t_{max} and recast in a dimensionless form, using the variable $x = k/\omega_H$; the resulting equation is plotted in Figure 5. For a value of $P_0 D^* / (A_d \Delta f)^{\frac{1}{2}} = 5$, a S/N of 1 can be observed at $x = 2.8$. For the value of $\omega_H = 3 \times 10^6$ sec^{-1}, this corresponds to a decay time of 120 ns. Question (2) is answered by considerations such as these.

These considerations seem, perhaps, a bit esoteric. However, in Chapter V it will be observed that no fluorescence signal results upon excitation of the HCl dimer in Ar. Considerations such as the preceding will enable an estimate to be made of the dimer decay time implied by the null results.

To maximize S/N it is desirable to run with the minimum ω_H that will not distort the fluorescence signal, since this will reduce the bandwidth of the electronics and hence reduce the noise. From consideration of Eqs. (15) and (16) the peak amplitude of the fluorescence signal will be attenuated by less than 2% when $\omega_H/k > 100$, and by less than 0.7% when $\omega_H/k > 1000$. A variable low pass filter is used with the 104 amplifier to accomplish this;[42] the schematic for this filter is given in Fig. 6. The 103 amplifier has a variable high frequency cut-off. Since the 103 has a high output impedance of 2000 ohms, an impedance matching buffer follower, shown schematically in Fig. 7,[43] is used between the amplifier and the Biomation 8100.

Figure II-5. Tradeoff between S/N and time constant for observable decay. Equation (15) is evaluated at t_{max}, as given by Eq. (16). The ordinate is the reduced variable $(V_S/V_N)/X_o$. $X_o = P_o D^* / (A_d \Delta f)^{\frac{1}{2}}$. When $k=\omega_H$, the S/N has been reduced to 37% of the low frequency intensity limited signal.

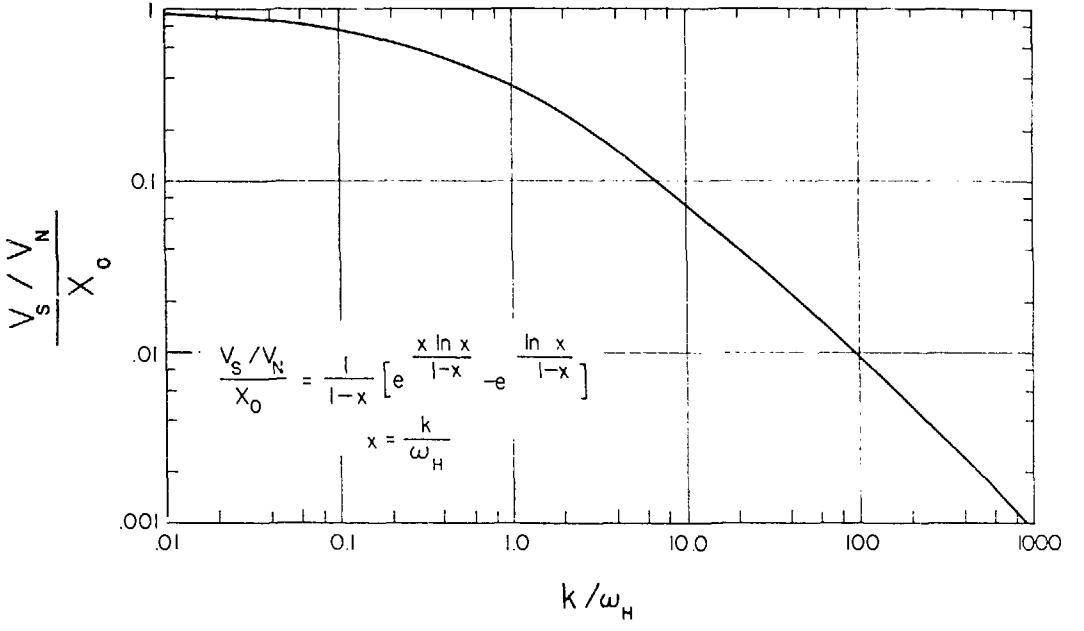

XBL7711-2183

Figure II-6. Variable low pass filter. High frequency cut-offs can be ∞, 5.0, 2.5, 1.0, 0.5, 0.1, 0.05, or 0.01 MHz.

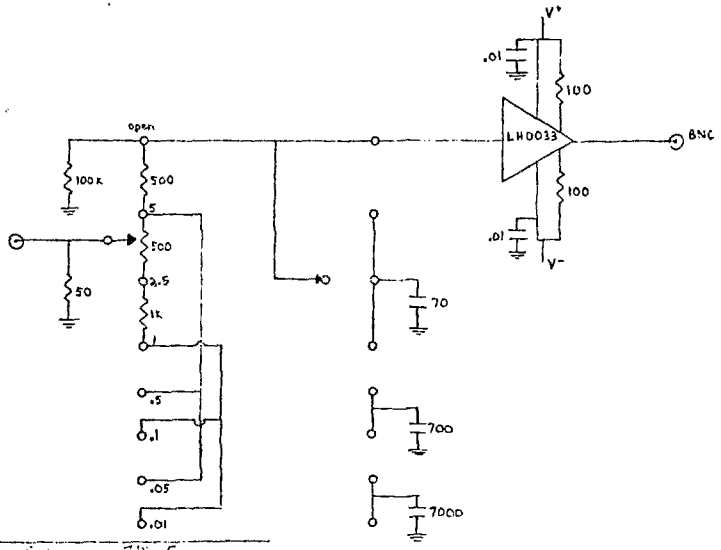

Setting	3Db Frequency (MHz)
Open	35
5	3.6
2.5	1.8
1	1.05
.5	.43
.1	.12
.05	.045
.01	.011

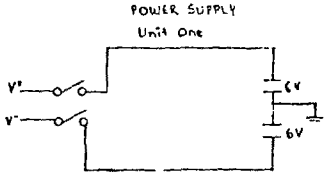

Refer to drawing 709A1-1

XBL 7711-10461

Figure II-7. Buffer follower. The LH0033 chip matches the 2000 ohm output impedance of the IC3 amplifier to the 50 ohm input impedance of the Biomation 8100.

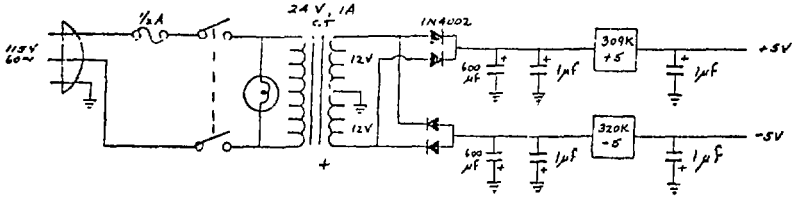

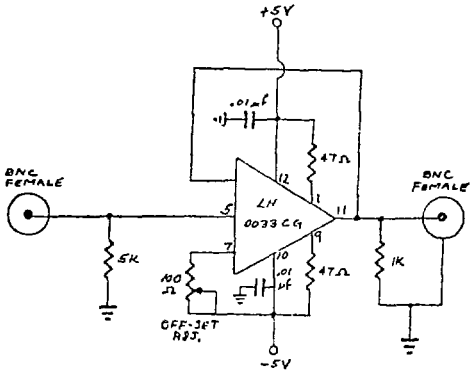

XBL 7711-10463

7. Filters

Beside reducing the background radiation received by the detector, the infrared dielectric filters can spectrally resolve fluorescence signals. In the majority of the experiments using the Ge:Hg detector, the detector dewar could accommodate only one filter. Experiments were performed with a 3-5 μ wide band filter inside the dewar and various filters external to the dewar. Narrow band filters were used to separate HCl v=2 → v=1 and v=1 → v=0 fluorescence and DCl v=2 → v=1 and v=1 → v=0 fluorescence.

Some experiments were performed using a detector dewar which could accommodate a 3-6 μ circular variable filter (CVF). The CVF is a multilayer dielectric filter with layers of wedged thickness. The central wavelength of transmission is a linear function of the exact position on the filter circumference through which radiation passes, and the resolution depends on the angle of the filter subtended by the fluorescence collection optics. Upon cooling from room temperature to cryogenic temperature, the transmission characteristics of multilayer dielectric filters are blue shifted by 1-2%, so it is necessary to calibrate the CVF in situ. Calibration is performed in the 3 μ region using scattered radiation from the OPO, which itself has been calibrated against HCl v=0 → v=1 absorption. The CVF was calibrated in the DCl region by scattered light from a frequency doubled TEA CO_2 laser, using a Te crystal for frequency doubling.[44]

The resolution of the CVF could be ascertained by observing the range of settings for which a fixed calibration frequency could be observed. The resolution can be increased by narrowing a slit in front of the detector element inside the CVF dewar. With a slit width of 2 mm,

the resolution of the CVF at 3.5 μ is 33 cm^{-1} (FWHM). Frequency accuracy and reproducibility is about 4 cm^{-1}.

8. Signal Averaging Electronics

Single shot signal-to-noise ratios as high as ten were observed in some cases, but for excitation on lines other than R(0) typical S/N ratios were unity or less. Fluorescence decay traces with enhanced S/N are produced with a digital signal averaging apparatus composed of a Biomation 8100 transient recorder interfaced with a Northern NS-575 signal averager. The Biomation digitizes the signal into 2048 channels of time increment of 0.01 μs or longer. The digital data is transferred in groups of 512, 1024, or 2048 channels into the Northern, where results of successive laser pulses are added. After N shots, the signal has increased N-fold, whereas the noise, which is random, increases by $\sqrt{N}$; thus, the signal-to-noise ratio increases by $\sqrt{N}$. Typically 1000-10,000 shots are averaged to produce final S/N ratios of at least ten. Single shot S/N ratios of less than 0.1 cannot be averaged to produce usable results.

The data stored digitally in the Northern comprises fluorescence intensity vs channel number. For most of the fluorescence decay experiments, the data was plotted on an x-y point plotter to produce fluorescence intensity vs time plots. Decay times are extracted by manually replotting the data in semi-logarithmic form. During the later stages of this research, Dasch[38] constructed an interface between the Northern and the Lawrence Berkeley Laboratory CDC 6600 computer. This allowed for direct computer analysis of decay traces. Some additional comments on the systematics of data analysis will be presented in Chapter IV.

9. Fluorescence Spectroscopy

Fluorescence spectra were taken using the CVF as the dispersing element. The purpose of the fluorescence spectra is two-fold. First, the vibrational levels populated during the relaxation process can be observed. Second, from the relative intensities, the proportion of relaxation by V → V processes as compared to V → R,P processes can be estimated. Spectra were taken for a fixed excitation frequency to v=2 of an HCl/Ar sample by incrementing the central transmission wavelength of the CVF in 20 cm^{-1} steps, and integrating the fluorescence decay curve produced at each setting with a planimeter. The integral was scaled to the input parameters of the Biomation 8100 and to the power of the YAG pump to the OPO. The resolution of the CVF was 33 cm^{-1} (FWHM).

Assume a model in which v=2 is initially excited to a population of N_0 at t=0 and decays with rate k_{21}, creating ξ molecules of v=1. ξ varies between 1 and 2. A value of ξ=1 means that depopulation of v=2 has occurred by loss of a quantum of vibration from the ensemble; ξ=2 means that v=2 has decayed in a V → V process to make 2 molecules in v=1. An intermediate value of ξ indicates a combination of the two processes. Molecules of v=1 subsequently decay with rate k_{10}. The fluorescence signals observed from v=2, S_2, and v=1, S_1, are

$$S_2 = gA_2N_0 e^{-k_{21}t} \tag{17}$$

$$S_1 = \frac{g\delta A_1 N_0 k_{21}\xi}{(k_{21} - k_{10})}\left(e^{-k_{10}t} - e^{-k_{21}t}\right) \tag{18}$$

A_2 and A_1 are the Einstein emission coefficients for v=2 → 1 and v=1 → 0 fluorescence, g is a geometrical factor described in subsection II.D.6, and δ is an optical density factor, varying between 1 and 0 as the sample

varies between transparent and totally opaque. The signal from v=2 is assumed to have a δ=1, since v=2 → 1 emission cannot be absorbed by ground state HCl guests. Integrating Eqs. (17) and (18) over all time gives:

$$S_2 = \int_0^\infty S_2(t)\, dt = gA_2N_0\tau_2 \tag{19}$$

$$S_1 = \int_0^\infty S_1(t)\, dt = g\delta\xi A_1N_0\tau_1 \tag{20}$$

where $\tau_2 = 1/k_{21}$ and $\tau_1 = 1/k_{10}$. S is the experimentally measured parameter. With a suitable choice for δ, the value of ξ can be deduced, thus indicating the extent of V → V processes in the relaxation of v=2.

A simple one dimensional model for optical density is illustrated in Fig. 8. It is assumed that the decay lifetimes are short relative to the radiative lifetimes, so that lifetime distortions due to radiation trapping may be neglected. The number of photons emitted between x and dx is $\tilde{n}(x)dx$. The number of photons surviving the thickness l after emission at x is

$$n(x) = \tilde{n}(x)\, e^{-\gamma x}\, dx.$$

Assuming that the initial excitation is uniform so that $\tilde{n}(x)$ is independent of x, $\tilde{n}(x) = n_o/l$ where n_o is the total number of emitted photons. The number of photons emerging after the thickness l is

$$n = \int_0^l \frac{n_o}{l}\, e^{-\gamma x}\, dx = \frac{n_o}{\gamma l}\,(1-e^{-\gamma l}).$$

The optical density factor is then

$$\delta = \frac{n}{n_o} = \frac{1}{\gamma l}\,(1-e^{-\gamma l}). \tag{21}$$

Figure II-8. One dimensional model of optical density. The matrix is a uniform medium extending from x=0 to x=1. The number of photons emitted at the point x is $\tilde{n}(x)dx$, as indicated by the black dot. n(x) photons emerge from the sample headed to the detector. See text for details.

Detector optics

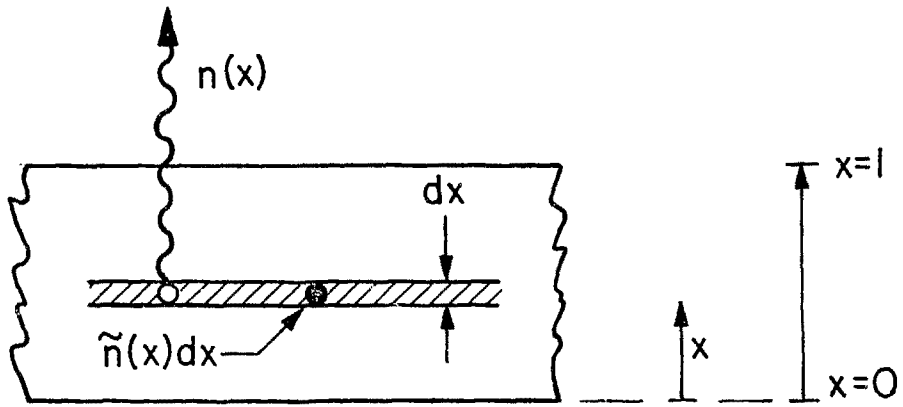

XBL7711-2180

A more detailed three dimensional analysis, assuming the matrix is thin compared to the distance between the matrix and the fluorescence collecting lens, gives

$$\delta = \frac{\cos\theta_1}{1-\cos\theta_1}\left(\frac{1}{\gamma l}\right)\ E_1\left(\frac{\gamma l}{\cos\theta_1}\right) - E_1(\gamma l) - \ln(\cos\theta_1) \qquad (22)$$

where θ_1 is the polar angle subtended by the fluorescence collecting lens and E_1 is an exponential integral.[45] For $\theta_1 = 0$, the three dimensional result reduces to Eq. (21). For a 5 cm f/1 fluorescence collecting lens, θ_1 is 14° and the difference between Eqs. (21) and (22) is very small. The factor γl in Eq. (21) can be obtained from the sample's absorption spectrum, since

$$\gamma l = \ln\left(\frac{I_o}{I}\right).$$

Due to the resolution problems in infrared spectroscopy of matrix samples, values of $\ln(I_o/I)$ tend to be underestimated. Integrated absorbances, however, are much less subject to error, and the true value for γl can be calculated from

$$(\gamma l)_{true} = \frac{(\Delta\nu)_{observed}(\gamma l)_{observed}}{(\Delta\nu)_{true}} \qquad (23)$$

where $\Delta\nu$ are linewidths. The "true" value for $\Delta\nu$ which is used is taken from fluorescence excitation spectra, since the resolution of these are better than the resolution of absorption spectra.

The optical density factor δ is a function of frequency ν. Since the bandpass of the CVF is broad, the effective δ will be a weighted average over the fluorescent transitions passed by a particular CVF setting. The problem is simplified by assigning one value for δ for all

CVF central transmission frequencies in the range of the v=1 → 0 transitions: 2945-2800 cm^{-1}, and δ=1 elsewhere. For v=1 → 0 transitions:

$$\delta = \sum_t P(J) \frac{|m|}{(2J+1)} \frac{1}{(\gamma 1)_t} (1-e^{-(\gamma 1)_t}) \qquad (24)$$

where J is the rotational level of the upper emitting state; P(J) is the Boltzmann factor for J; |m| is a line strength which equals J for an R branch transition and J+1 for a P branch transition; and $(\gamma 1)_t$ is the true value calculated from the observed absorption of the transition t using Eq. (23). In practice, for HCl/Ar, only R(0), P(1), and P(2) transitions are important.

The integrated intensities, S, are corrected for YAG laser power fluctuations, which are as high as 10%. This corresponds to about a 20% variation in OPO intensity, and constitutes a major source of error in the quantitative analysis of the emission spectrum. The use of a single value for δ is somewhat justified by the large bandpass of the CVF, but it tends to enhance the calculated response for the most strongly absorbing R(0) line, while detracting from the response of less strongly absorbing transitions such as P(1). Signals are undercorrected for P(1) by less than 10%, however.

The results of the emission spectra will be discussed in conjunction with the fluorescence decay measurements in Chapter V.

10. Fluorescence Excitation Spectroscopy

Fluorescence excitation spectra were taken by monitoring the fluorescence from the matrix sample while scanning the OPO idler frequency. This was accomplished, as shown in Fig. 2, using a gated integrator to sample the fluorescence and produce a dc voltage proportional to the

fluorescence intensity, which is displayed on a strip chart recorder. The OPO oven temperature is scanned at a rate of 0.1 C per minute which is roughly a scanning rate of 1 cm^{-1}/min. This subsection will begin with a discussion of the basic operating procedures of a gated electrometer, which is used as the gated integrator, followed by a discussion of the kinetic information obtainable from excitation spectra. The detailed results of excitation spectra will be considered in Chapter III.

A simplified electrical schematic of the gated integrator is given in Fig. 9. R_i is an input resistance which is actually due to the FET gate which opens and closes the electrometer input. For the present purposes it can be considered to have a resistance which becomes infinite when the gate is closed. An operational amplifier acts so that no current flows from the dotted junction in Fig. 9, so

$$\frac{V_{in}}{R_i} = \frac{V_{out}}{R_f} + C\frac{dV_{out}}{dt} \tag{25}$$

where R_f and C are the feedback resistor and capacitor. For an exponential input pulse, $V_{in} = V_o^S \exp(-t/\tau)$ with the initial condition that $V_{in} = 0$ at t=0, Eq. (25) is solved by

$$V_S = \frac{V_o^S}{\frac{R_i}{R_f} - \frac{RC}{\tau}}\left[e^{-t/\tau} - e^{-t/R_fC}\right] \tag{26}$$

where V_{out} has been shortened to V_S. R_fC is chosen to be much longer than τ, so that V rises rapidly within a time τ and decays very slowly. In practice, the response of the operational amplifier to an input pulse will have a rise time given by its slewing rate (mV/ms), S. For an input pulse of magnitude V_o, the rise time introduced by the operational

Figure II-9. Simplified schematic of an integrator. No current flows at the junction indicated by the dot. See text.

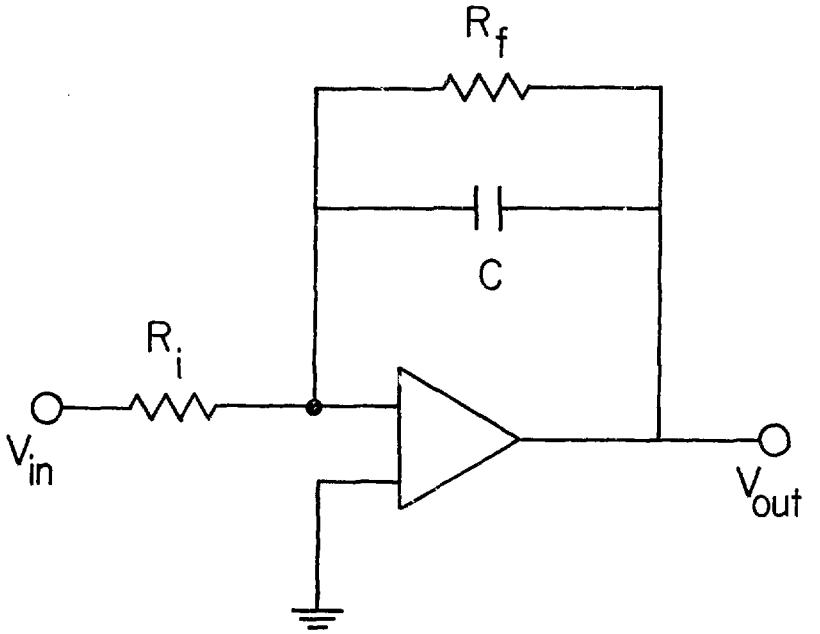

XBL7711-2182

amplifier will be $t_r = V_o/S$. Using Eq. (9) for an exponential pulse attenuated by a low pass filter of cut-off frequency $1/t_r$, and assuming that $R_fC \gg t_r$, τ, the pulse emerging from the electrometer is given by

$$V_S = \frac{V_o^S}{R_iC}\left(\frac{\tau}{\tau - t_r}\right)\left[\tau\left(e^{-t/R_fC} - e^{-t/\tau}\right) - t_r\left(e^{-t/R_fC} - e^{-t/t_r}\right)\right] \quad (27)$$

There are many sources of noise present when the gated electrometer is used with a voltage source, such as an infrared detector, and analytic treatment of the noise sources is not straightforward. The noise emanating from fluctuations in the thermal background flux on the detector is spectrally white, and in principle should integrate to zero for sufficiently long integration periods. It is not apparent how gating the electronics affects this source of noise. If a dc noise signal is present, it can be treated as a pulse with infinite τ, and neglecting slewing rate considerations, the output noise level of the electrometer is

$$V_N = V_o^N \frac{R_f}{R_i}\left[1 - e^{-t/R_fC}\right]. \quad (28)$$

After a time T, the signal-to-noise ratio can be calculated from Eqs. (27) and (28), and, assuming $T \ll R_fC$, the result is

$$S/N = \frac{V_o^S}{V_o^N}\,\frac{T}{\tau - t_r}\left[\frac{\tau}{T}\left(1 - e^{-T/\tau}\right) - \frac{t_r}{T}\left(1 - e^{-T/t_r}\right)\right]. \quad (29)$$

The expression in brackets reaches a maximum for some finite T and hence, when the noise can be represented by a dc input level, the value of T that maximizes the S/N corresponds to the optimum setting of the gate width. Equation (29) is suggestive of a possible mechanism explaining

the utility of gating the electrometer with voltage sources, but should not be taken more seriously. An explanation for a dc type noise voltage could be a voltage leak across the FET gate which corresponds to R_i.

The real enhancement in S/N in using the integrator is due to the fact that the signal is repetitively pulsed and is effectively signal averaged for the number of shots occurring within the R_fC decay time of the electrometer. According to the usual statistics for signal averaging, signal voltage is increased N-fold for N shots, while noise increases as a random variable, and hence by a factor of $\sqrt{N}$. For a laser repetition rate of f pulses/second, the S/N of the gated electrometer is

$$S/N = (fR_fC)^{\frac{1}{2}} \frac{V_o^S}{V_o^N} F(\tau, V_o, T) \qquad (30)$$

where $F(t,V_o,T)$ is a function depending on the input pulse characteristics and the gate setting.

The actual gated electrometer[46] can be divided into three parts: the pulser, the gate, and the electrometer, shown in Figs. 10a, 10b, and 10c. The gating circuit has been described by Rosen, et al.[47] The 2N4117A FET is the gate to the electrometer. The gate can be opened from an external pulse, or can be triggered internally by a pulse generator. The pulse generator and pulse shaping electronics for an external trigger are shown in Fig. 10a. The general timing of the device is as follows. A pulse, either externally or internally generated, opens the 2N4117A FET allowing the electrometer to sample the input signal. The gate is closed at a time set by the gate control on the front panel. The R_fC value of the electrometer is set at two seconds. The gated electrometer

Figure II-10a. Schematic of pulser for gated electrometer device. The pulser can generate triggering pulses or will shape external trigger pulses.

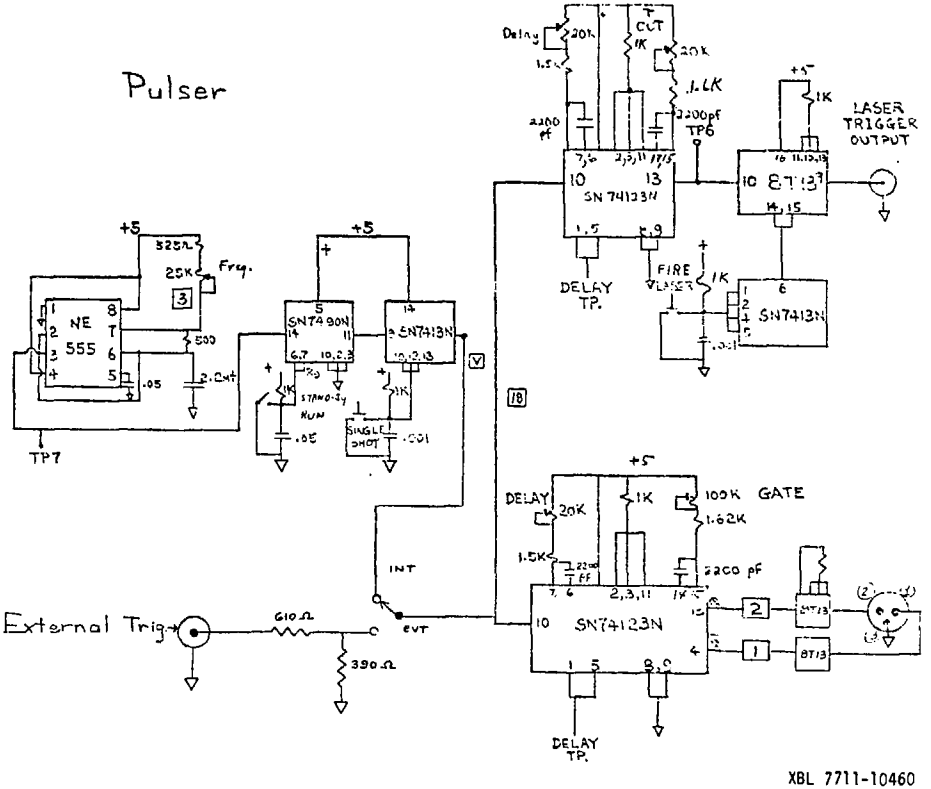
Pulser
+5
325Ω
25K
Freq.
NE 555
500
.05
2.2mf
TP7
SN7490N
SN7413N
STAND-BY
RUN
SINGLE SHOT
.001
.05
INT
EXT
External Trig
610Ω
390Ω
Delay
20K
1.5K
CUT
1K
20K
.1 LK
2200 pf
2200pf
TP6
SN74123N
DELAY TP.
FIRE LASER
1K
.001
SN7413N
LASER TRIGGER OUTPUT
DELAY
20K
1.5K
1K
100K GATE
1.82K
2200 pf
SN74123N
DELAY TP.
XBL 7711-10460

Figure II-10b. Schematic of gate for gated electrometer device. Signal is input to the source of the 2N4117A FET. Gating pulse opens the FET and the drain from the 2N4117A goes to the electrometer.

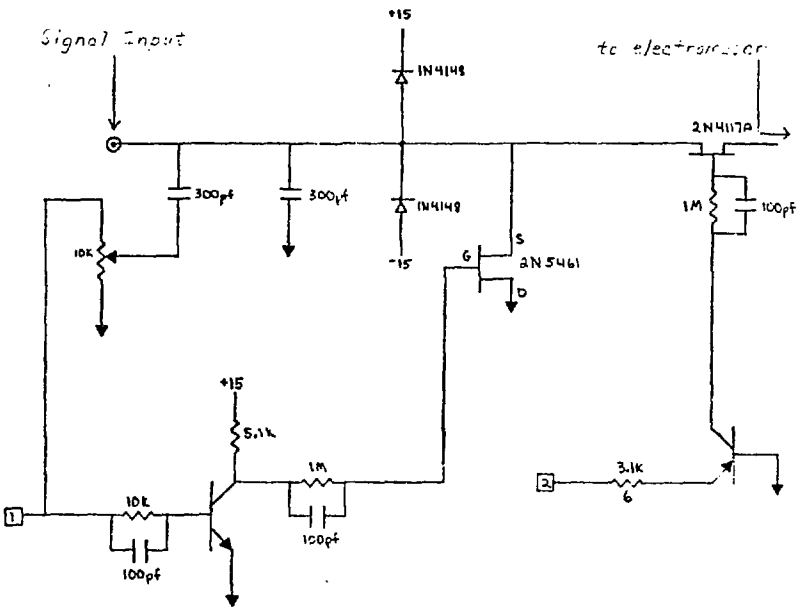

Analog Gate

XBL 7711-10462

Figure 11-10c. Schematic of electrometer for gated electrometer device. Input comes from the drain of the 2N4117A in the gate circuit. The product of feedback resistor and capacitor gives a 2 second integration time. The AD 118 op amp impedance matches the output of the integrator to a strip chart recorder.

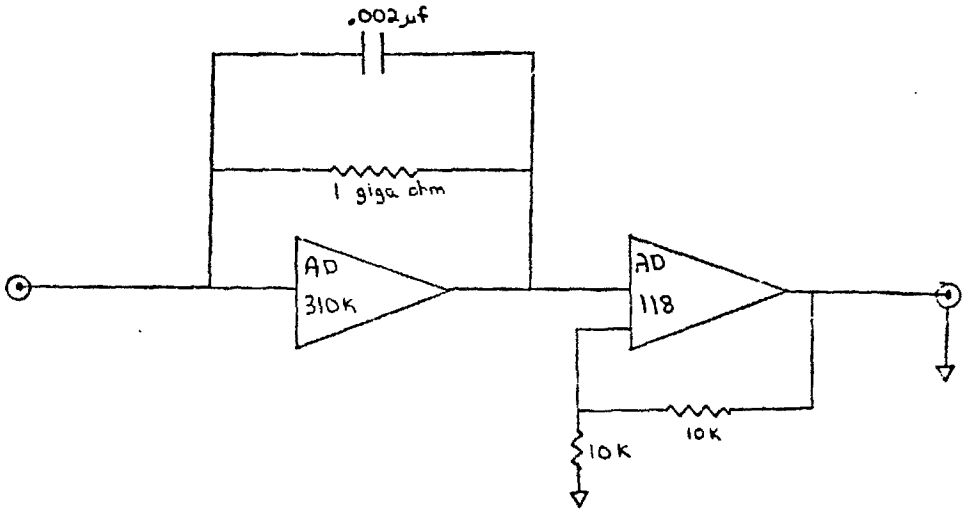

Electrometer

XBL 7711-10464

was designed to operate with current sources such as photomultipliers, rather than with voltage sources such as infrared detectors. Analysis of noise and gating advantages are more straightforward for photomultiplier applications.[47]

Experimental application of the gated electrometer in recording infrared fluorescence excitation spectra proceeds as follows. The electrometer gate is triggered externally by a positive photodiode pulse synchronized with the YAG pulse. The repetition rate of the laser system is as rapid as is convenient. The output of the IR detector is amplified by the Keithley 104 by a factor of 10 or 100, depending upon whether the gain of 100 saturates the electrometer output for a strong fluorescence signal. The gate width is set to maximize the dc level of the electrometer output when the OPO is set to the strongest fluorescing absorption line of the sample. The gate width can be varied between 2 μs and 1 ms. Empirically a gate width comparable to the fluorescent decay time appears optimal. The spectrum baseline is set with the detector on but shielded from fluorescence. The OPO is then positioned at a wavelength appropriate to begin the scan. The position of the delay setting is important only for internally triggered pulses, and so is not significant for these experiments.

In some experiments the position of the strongest fluorescing line (if any exists) is unknown. In this situation, the gate width is set to its maximum, since experience with observable pulses shows that the peak signal amplitude decreases more rapidly when the gate is too short than when it is too long. Otherwise, the set-up is as described above.

If the source of noise is uncorrelated to the signal, Eqs. (29) and (30) suggest (for $t_r \to 0$)

$$S/N \propto V_o \tau \sqrt{f}.$$

Furthermore, V_o should be proportional to the laser power and the absorption coefficient of the sample at the OPO frequency. Then, the empirical relation

$$S/N = \chi(\text{laser power})(\text{absorption coefficient})\ \tau\sqrt{f} \qquad (31)$$

should be valid, where χ is a function of at least laser bandwidth and gate setting of the electrometer. χ is certainly fixed in value once the conditions for an excitation spectrum have been set. Supposing that χ is not very sensitive to the gate width T, so long as $T>\tau$, χ should be nearly a constant. In fact, empirical correlations between excitation spectra of different samples and between different peaks on the same spectrum suggest that Eq. (31) is not unreasonable. Knowing the absorption intensity of a peak which does not fluoresce, and using χ values from spectra where there is a fluorescing peak, Eq. (31) can be used to estimate maximum lifetimes of the "non-fluorescing" species.

The resolution in fluorescence excitation spectra is determined by a combination of the linewidth of the OPO and the product of scan rate and integration time. The idler linewidth of a temperature stable OPO running multi-mode in the 1.7 - 3.0 μ range is 0.2 - 0.3 cm^{-1}.[34,35] For a scan rate of 1 cm^{-1}/minute and a 2 second integration time, the finite scanning speed contributes a width of 1/30 cm^{-1} to the limiting resolution of the spectrum--this is insignificant compared to the OPO linewidth. A more subtle question is whether temperature instabilities induced by temperature scanning the crystal oven affect the OPO linewidth. This question can be answered experimentally by observing the fluorescence excitation spectrum of a low pressure gas, whose Doppler linewidth is substantially less than 0.1 cm^{-1}. The observed linewidth

will represent the resolution obtainable in excitation spectroscopy using the OPO. Dasch[38] and Warmhoudt, et al.[35] have taken the fluorescence excitation spectra of HF in a Doppler broadened regime, at 2.6 μ, and obtain linewidths (FWHM) of 0.2 cm^{-1}--the temperature stable OPO linewidth. Thus, the resolution of the excitation spectrum is, conservatively, 0.2 - 0.3 cm^{-1}.

CHAPTER II

REFERENCES

1. E. Whittle, D. A. Dows, and G. C. Pimentel, J. Chem. Phys., 22, 1943 (1954).

2. I. Norman and G. Porter, Nature (London), 174, 508 (1954).

3. B. Meyer, Low Temperature Spectroscopy, American Elsevier, New York (1971).

4. H. E. Hallam, editor, Vibrational Spectroscopy of Trapped Species, Wiley, London (1973).

5. L. L. Levenson, Nuovo Cimento, Suppl. 5, 321 (1967).

6. A. E. Curson and A. T. Pawlowicz, Proc. Phys. Soc. (London), 85, 375 (1963).

7. E. M. Hoil and J. A. Suddeth, J. Appl. Phys., 32, 2521 (1961).

8. C. S. Barret and L. Meyer, J. Chem. Phys., 42, 107 (1965).

9. R. C. Longsworth, "A New Generation of Small Cryogenic Refrigerators for Laboratory and Commercial Applications," Air Products and Chemicals, Inc. Allentown, (1970).

10. Reference 3, p. 134.

11. W. L. Wolfe in Handbook of Military Infrared Technology, Office of Naval Research, Washington (1965), Chapter 8.

12. This was the experimental system used by Prof. L. Andrews during a sabbatical leave at Berkeley during 1975. Prof. Andrews was kind enough to allow use of his system for a few experiments.

13. R. B. Scott, Cryogenic Engineering, Van Nostrand, Princeton, (1963), page 298.

14. L. L. Sparks and R. L. Powell, J. Res. N.B.S., 76A, 263 (1972).

15. I am indebted to Dr. L. J. Allamandola for suggesting to me this method of performing diffusion experiments.

16. Originally introduced as the "pseudo matrix isolation method,"-- M. M. Rochkind, Anal. Chem., 39, 567 (1967); Ibid. 40, 762 (1968).

17. J. D. Jackson, Classical Electrodynamics, Wiley, New York (1962), p. 573.

18. W. J. Potts and A. L. Smith, Appl. Optics, 6, 257 (1967).

19. H. J. Kostkowski and A. M. Bass, J. Opt. Soc. Am., 46, 1060 (1956).

20. W. J. Potts, Chemical Infrared Spectroscopy, Vol. I, Techniques, Wiley, New York (1963).

21. R. E. Herman and R. F. Wallis, J. Chem. Phys., 23, 637 (1955).

22. The DCl and most of the HCl overtone spectra were recorded on the system of footnote 12. Some HCl overtone spectra were recorded using a conventional liquid helium cryostat.

23. D. H. Rank, D. P. Eastman, B. S. Rao, and T. A. Wiggins, J. Opt. Soc. Am., 52, 1 (1962).

24. S. R. Leone, Thesis, University of California, Berkeley (1974).

25. J. Finzi, Thesis, University of California, Berkeley (1975).

26. B. A. Lengyel, Lasers, Second Ed., Wiley-Interscience, New York (1971).

27. J. F. Young, J. E. Murray, R. B. Miles, and S. E. Harris, Appl. Phys. Lett., 18, 129 (1971).

28. J. E. Murray and S. E. Harris, J. Appl. Phys., 41, 609 (1970).

29. A. Yariv, Quantum Electronics, Wiley, New York (1967), Chapter 20.

30. F. Zernike and J. E. Midwinter, Applied Nonlinear Optics, Wiley New York (1973), Chapter 3.

31. Reference 29, Chapter 22.

32. Reference 30, Chapter 7.

33. S. E. Harris, Proc. IEEE, 57, 2096 (1969).

34. A. Hordvik and P. B. Sackett, Appl. Optics, 13, 1060 (1974).

35. J. Wormhoudt, J. I. Steinfeld, and I. Oppenheim J. Chem. Phys., 66, 3121 (1977).

36. H. S. Carslaw and J. C. Jaeger, Conduction of Heat in Solids, Second Edition, Clarendon Press, Oxford (1959), p. 9.

37. Ibid. p. 199.

38. C. J. Dasch, Thesis, University of California, Berkeley (1978).

39. Santa Barbara Research Center, Brochure, Goleta, CA (1975).

40. H. Levinstein, Appl. Optics, 4, 639 (1965).

41. R. D. Hudson, Infrared System Engineering, Wiley-Interscience, New York (1969), p. 270.

42. The variable low pass follower was introduced for the IR experiments in this group by Dr. R. G. Macdonald and was designed by D. Wilkinson of this department's electronics shop.

43. Designed by H. Warfield of this department's electronics shop.

44. J. D. Taynai, R. Targ, and W. B. Tiffany, IEEE J. Quant. Elect., QE-7, 412 (1971). The crystal was kindly loaned to us by Dr. J. C. Stephenson, National Bureau of Standards, Washington, D. C.

45. M. Abramowitz and I. A. Stegun, Handbook of Mathematical Functions, Dover, New York (1972), p. 228.

46. The gated electrometer used here was designed by D. Gee of this department's electronics shop, and R. Brickman, of this research group.

47. H. Rosen, P. Robrish, and G. Jan de Vries, Rev. Sci. Instrum., 46, 1115 (1975).

CHAPTER III

SPECTROSCOPY

A. Introduction

In order to understand the detailed dynamics of a molecular system, it is necessary to understand the energy levels accessible to that system; spectroscopy provides information concerning energy levels. The infrared spectroscopy of matrix isolated HCl and DCl has been well studied, both experimentally[1] and theoretically,[2] particularly in rare gas matrices. Absorptions due to monomeric and multimeric species have been assigned. In rare gas solids, monomeric hydrogen halides undergo nearly free rotation; the major perturbation on the free molecule states is due to rotation-translation coupling (RTC). In molecular solids, such as N_2, HCl and DCl monomers do not rotate in their lowest energy levels.

Spectroscopy can be used to identify the species present in a particular matrix sample. For example, the degree of isolation can be measured by observing the relative absorption strengths of monomer and dimer peaks. Unwanted impurities due to reagent contamination or leaks into the apparatus can be identified spectroscopically. Detailed interpretation of the spectrum of the matrix isolated monomer elucidates the forces experienced by the guest molecule in its lattice site. Linewidths also yield information concerning the environment of the matrix-isolated guest.

This chapter will be a mixture of review of previous work and new results. Section B will consider absorption spectroscopy of HCl and DCl in several host matrices. The theoretical interpretation of the monomeric

spectral features in the rare gas matrices are treated in Section C. The RTC model will be extended to include the J=3 level. Other perturbations on the guest molecule's wave functions will be detailed. Section D will discuss infrared fluorescence excitation spectroscopy. The resolution obtainable from excitation spectroscopy exceeds that obtained in our lab in absorption spectroscopy, as discussed in Chapter II, so information derivable from linewidths will be discussed. Section E will detail a series of experiments in which the absorption coefficient of HCl in an Ar matrix was measured, and will consider some quantitative effects of matrix deposition conditions.

In this chapter and in the remainder of this thesis several terms pertaining to lattice structure will be used. They are defined here. A lattice point is any point within the crystal unit cell which is connected to equivalent points in other cells by basic translation vectors. A lattice site will be taken to mean the equilibrium position of a molecule in a bravais lattice. A cell is the volume around the lattice site occupied by the molecule. For rare gas crystals, the atomic equilibrium position is the lattice site and the volume in which the atom moves is the cell.

B. Absorption Spectroscopy

Infrared absorption spectra yield information on the vibration and rotation-translation parts of the guest wave functions. The infrared spectra of the fundamental region of HCl and DCl in Ar and N_2 and HCl in O_2 will be presented here; as will spectroscopy of the first overtone region. In all matrices, monomer lines are distinguished from multimer lines. The vibrational wave function of the monomer is not perturbed

greatly by the matrix since vibrational frequencies and anharmonicities are not shifted much from the gas phase.

1. HCl/Ar, DCl/Ar--Fundamental Region

Infrared spectra of HCl/Ar taken in these laboratories are presented in Figures 1-3, and spectral assignments are listed in Table 1 Two kinds of transitions are assigned for the HCl/Ar system--those due to isolated monomeric species and those due to molecular complexes. Monomeric absorptions are the only peaks present in dilute samples (M/A > 2000), and their reversible temperature dependence, as seen in Figure 1, can be explained on the basis of discrete rotational levels. R(0) is the strongest HCl monomer line, even at 20 K. The resolution of Figures 1-3 is insufficient to resolve the $H^{35}Cl$ and $H^{37}Cl$ isotopic components of R(0) and P(1). The R(1) line is present as a broad structureless shoulder to the R(0) line--it is obviously strongly perturbed by the matrix environment, as discussed below. The weak $Q_R(00)$ transition at 2945 cm^{-1} is due to an RTC transition,[3] which is a transition with $\Delta v=1$, $\Delta J=0$, $\Delta n=1$, where v, J, and n are the quantum numbers for guest vibration, rotation, and translation. The pure R(0) rotational transition of HCl/Ar is observed at 18 cm^{-1} in the far IR[4,5] and the $Q_R(00)$ transition is observed at 72 cm^{-1} in the far ir,[6] confirming the mid-infrared assignments.

Multimer peaks of HCl are identified by their increasing intensity as the guest concentration is increased, and by an irreversible increase in intensity after a diffusion experiment; all peaks in Figures 1-3 below 2820 cm^{-1} are due to multimers. The first multimer peak to appear as concentration is increased from a very dilute sample is identified as

Figure III-1. Absorption spectrum of HCl/Ar at 9 K and 19 K, M/A = 960 ± 30. Assignments are in Table I. The high frequency edge of R(1) at 2913 cm^{-1}, visible at 19 K, is assigned to R(2). Deposition conditions: 17-19 K, 2 pulses/min., 9 m-moles/hour, total deposited = 47 m-mole.

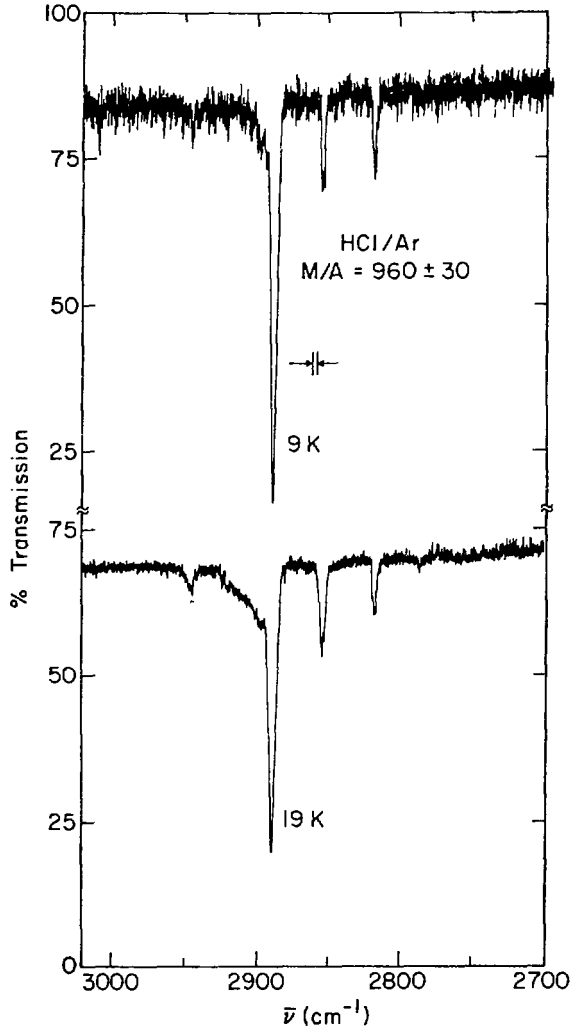

XBL 7711-10369

Figure III-2. Absorption spectrum of HCl/Ar, M/A = 530 ± 5, 9 K. Deposition conditions: 9 K, 4 pulses/min., 6 m-mole/hour, total deposited = 15 m-mole.

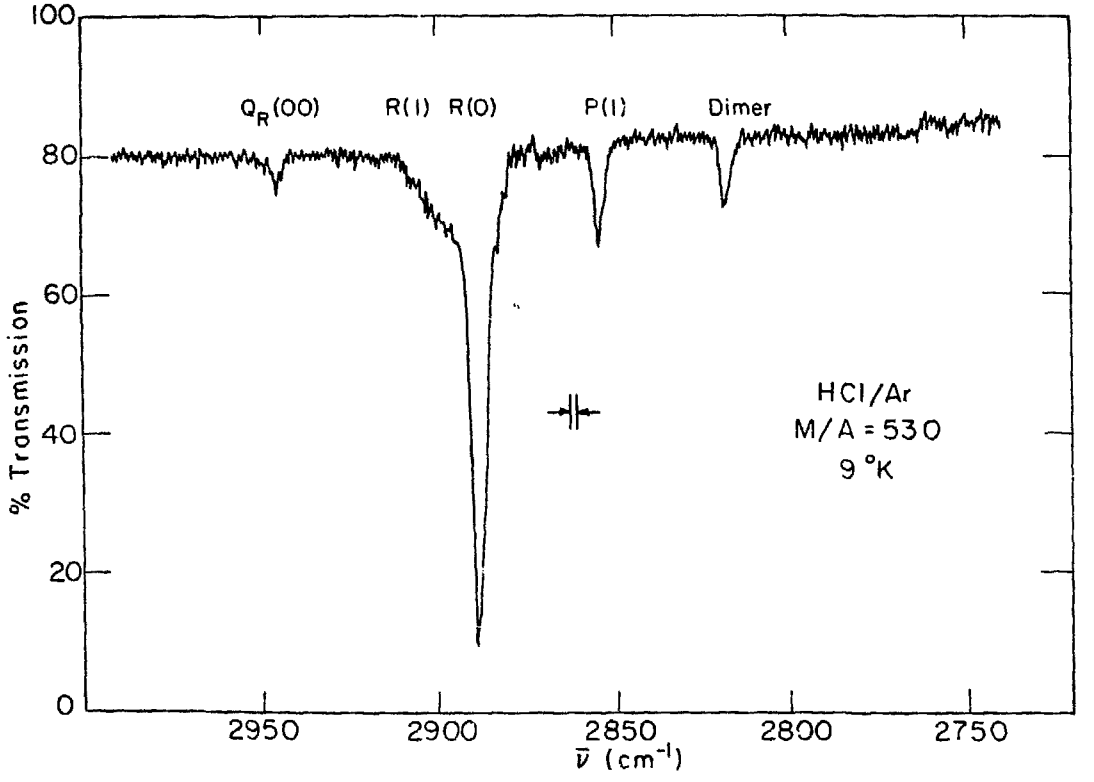

XBL 7710-10000

Figure III-3. Absorption spectrum of HCl/Ar, M/A = 228 ± 5, 9 K. Spectrum a is the virgin sample; spectrum b is the result of annealing. Assignments are in Table I. Notice that the HCl-N_2 peak at 2864 cm^{-1}, present as an impurity in the virgin sample, becomes more intense after annealing. Deposition conditions: 9 K 4 pulses/min., 19 m-mole/hour, total deposited = 8.6 m-mole.

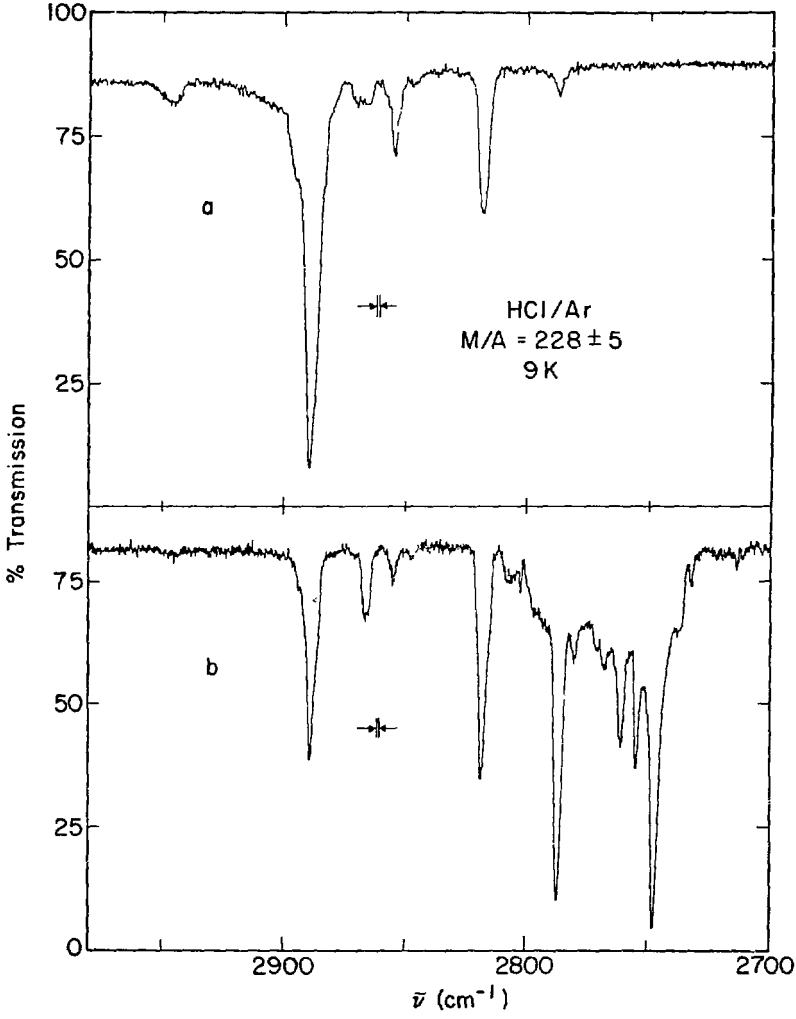

XBL 7711-10371

Table III-I. Absorption Frequencies of HCl and DCl in Ar Matrices

	Assignment[a]	HCl frequency[a]	DCl frequency[a]
Monomer:			
	$Q_R(00)$	2944	2149
	R(2)	2913	2108
	R(1) $T_{1u} \rightarrow E_g$	2897	2099[c]
	R(1) $T_{1u} \rightarrow T_{2g}$		2095[c]
	R(0) $H^{35}Cl$	2888	2090
	R(0) $H^{37}Cl$	2886	2088
	P(1) $H^{35}Cl$	2854	2070
	P(1) $H^{37}Cl$	2852	2067
	P(2)	2844	2061
Complexes:			
	$HCl-N_2$[b]	2864	2073
	$HCl-H_2O$[c]	2665	1935
	HCl dimer	2818	2040
	HCl timer	2786	2019
	HCl polymer	2748	1993[d]
Overtone:			
	R(1)[c]	5663	
	R(0)[c]	5656	4117
	P(1)[c]	5622	
	dimer[c]	5484 ± 2	

[a] Unless otherwise specified, frequencies and assignments are from Hallam, Ref. 1. All frequencies are accurate to ±1 cm^{-1} unless other error limits are quoted.

[b] From D. E. Mann, N. Acquista, and D. White, J. Chem. Phys., 44, 3453 (1966).

[c] This work.

[d] From J. B. Davies and H. E. Hallan, Trans. Faraday Soc., 67, 3176 (1971).

the dimer, the next is the trimer, and so on. The three strongest multimer peaks are the dimer, 2818 cm^{-1}, trimer, 2787 cm^{-1}, and high polymer, 2748 cm^{-1}. A plethora of multimer peaks appears subsequent to diffusion of a concentrated sample, as seen in Figure 3b. Barnes, et al.[7] have assigned all the peaks of Figure 3b--their detailed interpretation is perhaps speculative. Only the three strongest HCl multimer peaks are listed in Table I. Only one mid-IR absorption has been assigned to the dimer, so it is likely that the dimer possesses a degree of symmetry[1] such that the second dimer mode is IR inactive. Far infrared spectra of the dimer support this and suggests a cyclic geometry.[8]

Absorptions due to complexes of HCl-N_2 and HCl-H_2O in Ar matrices are listed in Table I. The HCl-H_2O complex has not been previously reported in Ar matrices. This very intense absorption is plainly visible even when the H_2O responsible for this absorption cannot itself be observed at 3757 or 3776 cm^{-1}.[9] The 200 cm^{-1} red shift of the HCl fundamental upon complexation with H_2O is consistent with a 200-300 cm^{-1} red shift observed for HCl upon complexation with H_2O in N_2 matrices.[10] The peak at 2864 cm^{-1} in Ar has been identified [11-13] as due to an HCl-N_2 complex. The HCl-H_2O and HCl-N_2 peaks are very sensitive indications of sample purity; clean samples with neither absorption can be produced.

The spectrum of DCl/Ar, Figure 4, is qualitatively the same as HCl/Ar; assignments are presented in Table I. Since DCl has a smaller rotational constant than HCl, R(1) and P(1) are relatively more intense for DCl than for HCl at 9 K. Transitions due to different isotopic species are just resolvable in Figure 4. The R(1) transition of DCl shows a resolvable doublet structure. Davies and Hallam[14] have reported a 3 cm^{-1}

Figure III-4. Absorption spectrum of DCl/Ar, M/A = 540 ± 30, 9 K. Spectrum a is the virgin sample; spectrum b is the result of annealing. Assignments are in Table I. The pair of arrows to the left of the R(0) doublet indicates the two R(1) transitions. The pair of arrows to the right of R(0) indicates the P(1) peaks for $H^{35}Cl$ and $H^{37}Cl$. Deposition conditions: 9 K, 4 pulses/min., 39 m-mole/hour, total deposited = 16 m-mole.

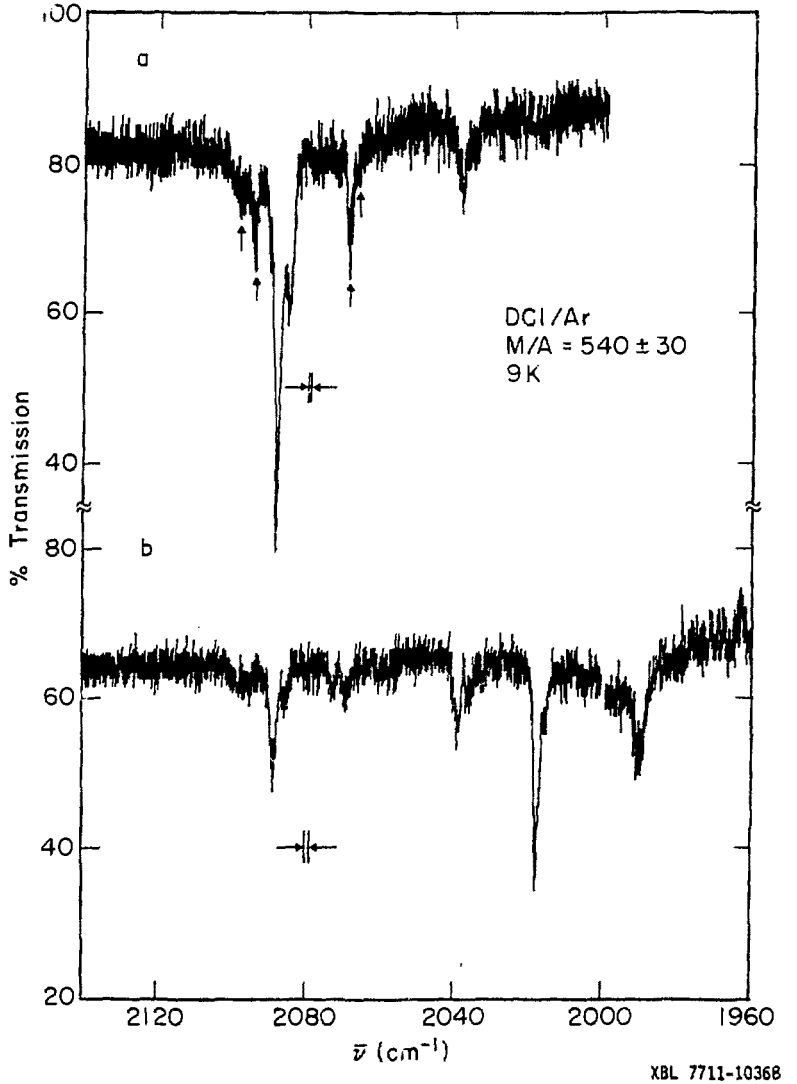

XBL 7711-10368

separation between peaks and interpreted the splitting on the basis of anisotropy of the crystal field. As seen from Figure 4, precise measurement of this splitting from IR absorption spectra is difficult due to resolution and signal-to-noise problems. Anticipating the results of the higher resolution fluorescence excitation spectra, to be discussed in Section D, a value of 4.5 ± 0.5 cm^{-1} for the splitting of R(1) in DCl is preferable.

DCl, like HCl, has three major multimer peaks, as observed in Figure 4b. We report the DCl-H_2O complex at 1935 cm^{-1}; the DCl-N_2 complex has been observed at 2071 and 2073 cm^{-1} for $D^{37}Cl$ and $D^{35}Cl$ in Ar.[12,14]

2. HCl/N_2, DCl/N_2--Fundamental Region

The absorption spectra of HCl and DCl in solid N_2, Figures 5 and 6, are dominated by a single isotopically resolvable peak, which is independent of temperature cycling in the range 9-20 K. This is assigned as isolated, non-rotating monomer. Upon diffusion of HCl/N_2, peaks appear at 2842 and 2815 cm^{-1}. The peak at 2815 cm^{-1} is identified as dimer by analogy to HCl/Ar. Barnes, et al.[15] observed the peak at 2842 cm^{-1} in a sample of M/A = 200, and assign it to isolated monomer in a trapping site distinct from the main absorption; they observe it to grow upon diffusion. Bowers and Flygare[11] observe only a single peak at 2855 cm^{-1} for M/A = 2000. Based upon concentration and diffusion behavior, it seems likely, contrary to Barnes, et al.,[15] that the peak at 2842 cm^{-1} may be a multimer species--perhaps a non-cyclic dimer.

The multimer structure of DCl/N_2 is the same as that of HCl/N_2. At M/A = 580 a weak absorption at 2059 cm^{-1} is assigned, by analogy to the 2842 cm^{-1} HCl peak, to non-cyclic dimer. Davies and Hallam[14] observe

Figure III-5. Absorption spectrum of HCl/N_2, M/A = 1030 ± 40, 9 K. Spectrum a is the virgin sample; spectrum b is the result of annealing. Deposition conditions: 9 K, 4 pulses/min., 19 m-mole/hour, total deposited = 16 m-mole.

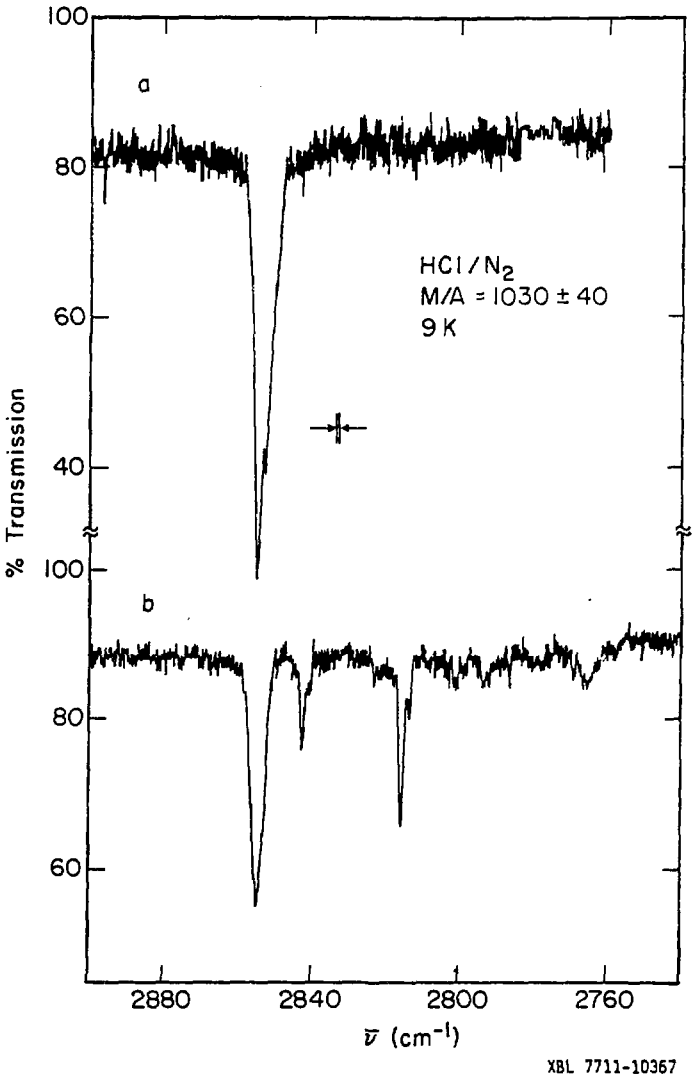
100
80
60
40
100
80
60
a
b
HCl / N2
M/A = 1030 ± 40
9 K
% Transmission
2880
2840
2800
2760
ν̄ (cm⁻¹)
XBL 7711-10367

Figure III-6. Absorption spectrum of DCl/N_2, M/A = 580 ± 10, 9 K. Deposition conditions: 9 K, 4 pulses/min., 12 m-mole/hour, total deposited = 12 m-mole.

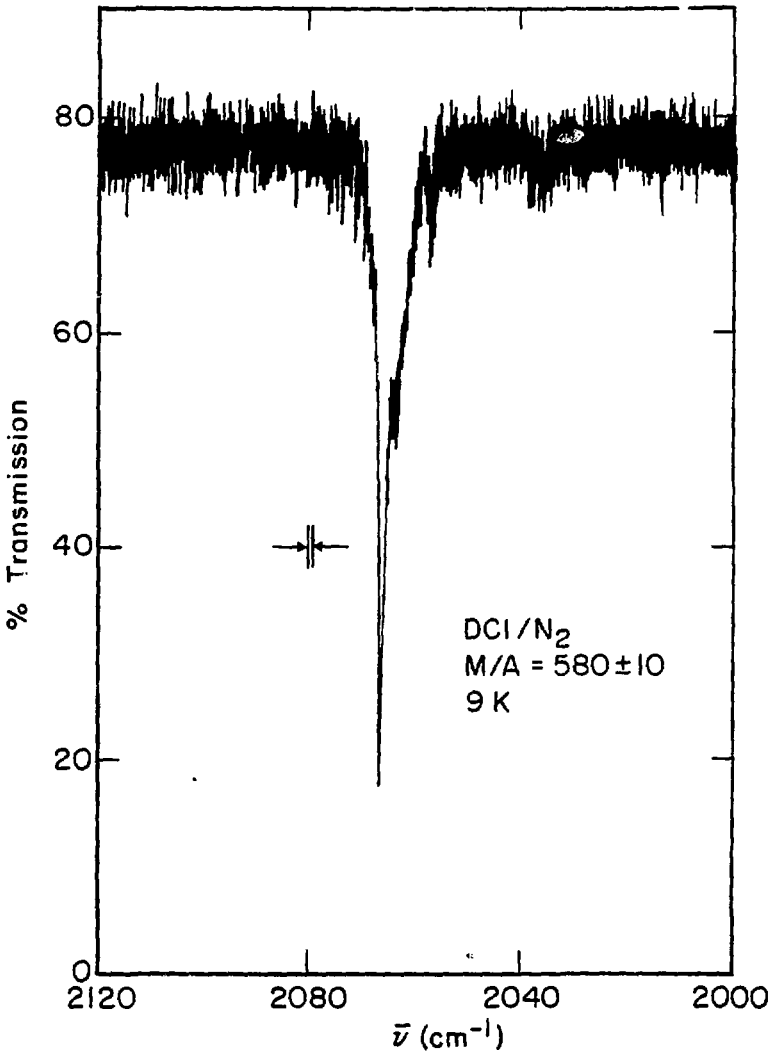

XBL 7711-10363

this peak to be relatively more intense at M/A = 200. Bowers and Flygare[11] observe only the monomer peak at 2067 cm^{-1}. Upon diffusion, the 2059 cm^{-1} peak increases, and a cyclic dimer at 2040 cm^{-1} appears.

The assignments for HCl and CDl in N_2 matrices are collected in Table II.

3. HCl/O_2

The spectrum of HCl isolated in an O_2 matrix, shown in Figure 7, has not been previously reported. The spectrum is dominated by an isotopic doublet at 2863 and 2861 cm^{-1}, which is assigned as non-rotating $H^{35}Cl$ and $H^{37}Cl$ monomers. Weak shoulders are present in the freshly deposited sample at 9 K as a doublet at 2869 and 2867 cm^{-1} and at 2858 cm^{-1}. The main peak is insensitive to temperature cycling between 9 and 20 K, although the shoulder at 2858 cm^{-1} disappears at 20 K and is not reformed upon subsequent cooling, and the high frequency shoulder weakens at 20 K and is only partly reformed upon cooling to 9 K. Upon diffusion to 35 K peaks appear at 2851, 2842, 2824, 2789, 2764, and 2736 cm^{-1}; the doublet at 2863 and 2861 cm^{-1} is reduced in intensity.

The deposition conditions for the sample of Figure 7 are similar to those for HCl/N_2 of Figure 5, in which no polymer is formed. It is possible that the shoulders observed in Figure 7 are due to HCl in minor trapping sites since: 1) they are near in frequency to the main trapping site; and 2) O_2 undergoes a phase transition[16] at 24 K from monoclinic to rhombohedral, so it is possible that the nascent sample produced by vapor deposition contains metastable rhombohedral domains which are removed upon gentle temperature cycling to 20 K. The high frequency

Table III-II. Absorption Frequencies of HCl and DCl in N_2 and O_2 Matrices

	Assignment	HCl frequency ($cm^{-1}\pm1$)	DCl frequency ($cm^{-1}\pm1$)
N_2 matrix:	^{35}Cl monomer	2855	2067
	^{37}Cl monomer	2853	2065
	non-cyclic dimer	2842	2058
	^{35}Cl cyclic dimer	2815	2037
	^{37}Cl cyclic dimer	2813	
	Polymer	2801	2029
		2792	2012
	High polymer	2765	2004
	Monomer Overtone		4080
O_2 matrix:	Monomers:		
	Major site: $H^{35}Cl$	2863	
	$H^{37}Cl$	2861	
	Site II: $H^{35}Cl$	2869	
	$H^{37}Cl$	2867	
	Site III	2858	
	Polymers:	2851 (w)	
		2842 (w)	
		2824 (w)	
		2789 (m)	
		2749 (m)	
		2744 (m)	
		2736 (m)	

Figure III-7. Absorption spectrum of HCl/O_2, M/A = 980 ± 40. Deposition conditions: 9 K, 4 pulses/min., 17 m-mole/hour, total deposited = 15 m-mole.

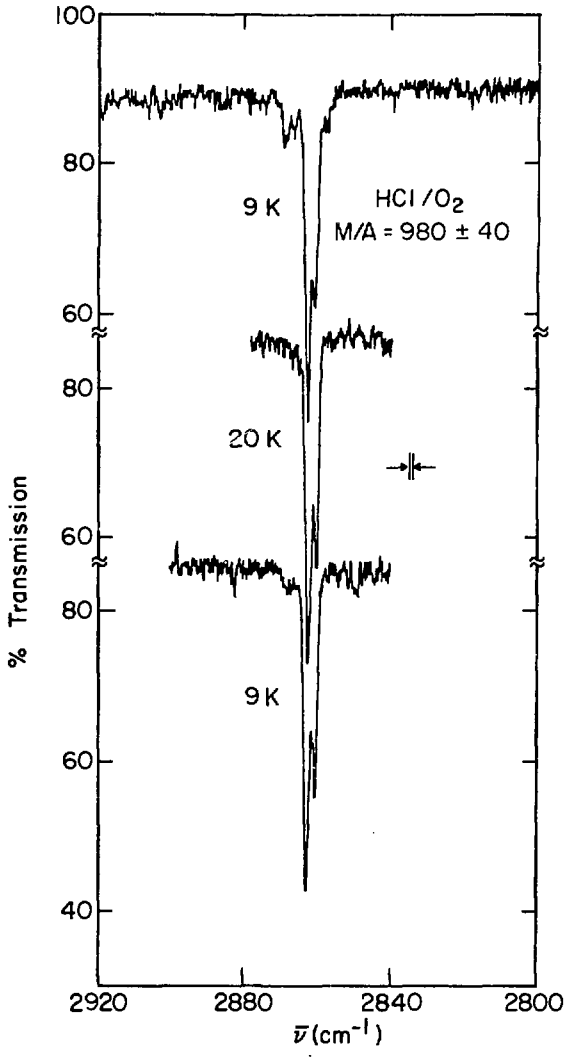

XBL 7711-10365

Figure III-8. Overtone absorption spectrum of HCl/Ar, M/A = 720 ± 10, 10-13 K. The top spectrum is the virgin sample; the bottom spectrum is the result of diffusion. Assignments are in Table I. Deposition conditions: 13-14 K, continuous deposition, 17 m-mole/hour, total deposited = 430 m-mole.

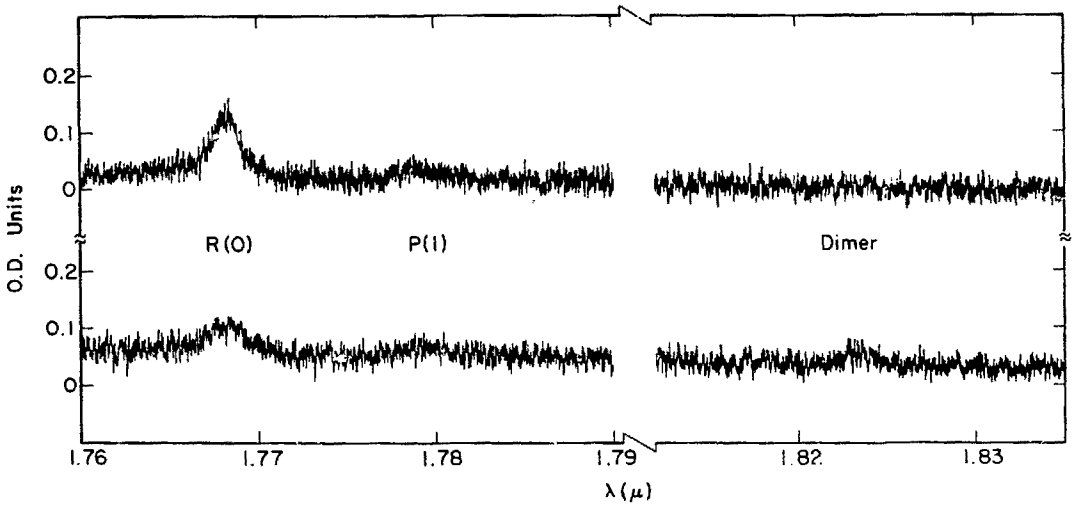

XBL 7711-10370

Table III-III. Frequency and Anharmonicity for HCl and DCl in Various Matrices

System[a]	$\omega_{0\to1}$[b]	$\omega_{0\to2}$[b]	ω_e	$\omega_e x_e$
HCl(gas)[c]	2886	5668	2991	52
HCl/Ar	2871 ± 1	5639 ± 1	2974 ± 4	52 ± 2
HCl/N_2	2855 ± 1			
HCl/O_2	2863 ± 1			
$(HCl)_2/Ar$	2818 ± 1	5484 ± 2	2970 ± 5	76 ± 2
DCl(gas)[c]	2091	4128	2145	27
DCl/Ar	2080 ± 1	4107 ± 1	2133 ± 4	27 ± 2
DCl/N_2	2067 ± 1	4080 ± 1	2121 ± 4	27 ± 2

[a] Values used are for the ^{35}Cl isotope.

[b] Pure vibrational frequency is $\frac{1}{2}[\omega_{R(0)} + \omega_{P(1)}]$.

[c] From D. H. Rank, D. P. Eastman, B. S. Rao, and T. A. Wiggins, J. Opt. Soc. Am., 52, 1 (1962). Uncertainties are less than 10^{-3} cm^{-1}.

shoulder is labeled site II and the low frequency shoulder is labeled site III. The plethora of multimer peaks subsequent to diffusion may be due to a variety of sites and domains caused by rapid heating and cooling through the O_2 phase transition.

The absorption frequencies and assignments for HCl/O_2 are listed in Table II.

4. Overtone Spectroscopy

Direct measurements of the first overtone absorptions were performed for HCl/Ar, DCl/Ar and DCl/N_2. Observed transitions are listed in Table I for Ar matrices and Table II for N_2. The overtone spectrum of HCl/Ar, M/A = 750 is shown in Figure 8. The rotational structure of the first overtone parallels that of the fundamental region: R(0) and P(1) are separated by 34 cm^{-1} and a broad, high frequency shoulder to R(0) is assigned as R(1). After diffusion, the monomer peaks are reduced in intensity and a weak peak appears at 5484 cm^{-1}. The strongest multimer peak upon diffusion at M/A = 750 should be due to the dimer, and the peak at 5484 cm^{-1} is so identified. The signal-to-noise ratio for the dimer peak is not impressive; nevertheless, several scans of the same region produced a peak at the same frequency.

Only one peak was observed for DCl/Ar, M/A = 740, and this is assigned as R(0). Only one peak is observed for DCl/N_2 at M/A = 250, and this is assigned as monomer.

The frequencies and anharmonicities derivable from fundamental and overtone spectra are presented in Table III. Anharmonicities are within experimental uncertainty equal to gas phase values. This is not really surprising since frequencies change by only 1%. The constancy of anharmonicity from gas phase to condensed phase has been observed in

other systems. Dubost and Charneau[17] have fit fluorescence spectra of CO in Ar and Ne matrices from levels as high as v=8 using a matrix adjusted ω_e and gas phase values for $\omega_e x_e$ and $\omega_e y_e$. Brueck, et al.,[18] observe that the anharmonicity of the ν_3 mode of CH_3F in liquid O_2 is equal to the gas phase value.

The implication of these results is that overtone frequencies can be reliably calculated in condensed phases from a knowledge of the fundamental frequency, which is a function of the environment, and the gas phase anharmonicity; it is not necessary to perform overtone spectroscopy for every system.

C. Theoretical Interpretation of Monomer Spectra

The wave function of a diatomic in the ground electronic state in the gas phase may be considered, to low order, to be the product of wave functions of an anharmonic oscillator, a rigid rotor, and a freely translating particle. These wave functions are modified by perturbations caused by neighboring atoms in the lattice. As discussed in Section B.4, the vibrational frequencies are not changed much by the matrix environment, and the perturbed vibrator can be thought of as having a new frequency and the same anharmonicity as the gaseous molecule. Translation is quenched by the rigidity of the solid lattice, and is replaced by oscillatory motion due to lattice vibrations--phonons. It is obvious from the preceding spectra that rotation is perturbed by the matrix. In N_2 and O_2 matrices, no rotational or librational transitions are observed.

In Ar matrices, the separation between R(0) and P(1) is reduced from the gas phase separation. The rotational spectrum in the matrix

cannot be simply interpreted on the basis of a reduced rotational constant, B, however, since R(1) is too near in frequency to R(0) to fit a rigid rotor spectrum. The deviation from free rotor states is due to an asymmetry of the system. The crystal field of a perfect fcc lattice has octahedral symmetry about a lattice site, and this asymmetry can shift and split rotational levels of a free rotor.[19,20] This effect predicts, however, that the R(0) - P(1) separation of DCl will be reduced relative to the gas phase separation more than that of HCl,[2] and the contrary is in fact observed. An asymmetry is also introduced by a heteronuclear diatomic molecule since in its equilibrium position the molecular center of mass will not necessarily reside at the lattice site. This will couple guest rotation and translation and produce relatively larger shifts for HCl than for DCl.

The major perturbation for HCl and DCl in Ar matrices is RTC, which has been developed by Friedmann and Kimel.[3,21-23] (References 22 and 23 will be referred to as FKI and FKII.) Friedmann and Kimel calculated RTC perturbations for $J \leq 2$. These calculations will be extended here to include J=3. The crystal field of the lattice can reduce the degeneracy of rotational levels for $J \geq 2$, and is in fact the cause of the observed splitting of R(1) for DCl/Ar. The broadness of the spectral transitions is due, at least in part, to the coupling of rotation with delocalized lattice phonons. This will be discussed briefly here and more fully after the fluorescence excitation spectra have been presented.

1. Rotation-Translation Coupling

In the RTC model[3,21-23] the isolated guest molecule occupies an undistorted lattice site and the potential governing the guest translational motion has spherical symmetry. Anisotropy is introduced into the

system by defining a molecular center of interaction, which is defined as the point about which the average angular dependence of the intermolecular potential is minimal. In this sense, the center of interaction (c.i.) is the "point" on the guest molecule at which the intermolecular forces are applied. The c.i. must lie on all symmetry elements of the guest molecule, but need not coincide with the center of mass (c.m.). For heteronuclear diatomic molecules, the c.i. lies in the internuclear axis a distance a from the c.m. In terms of the coordinates of the c.i. (r,Ω), the potential experienced by the guest is

$$V = V(r) + \Delta V(r,\Omega). \tag{1}$$

The c.i. is defined so that $\Delta V(r=0,\Omega)$ is minimal, and for the RTC model ΔV is neglected. At equilibrium, the c.i. resides at the center of the lattice cell.

We follow the derivation of FKII. Assume a harmonic cell potential,

$$\tilde{V}(r) = \frac{1}{2} kr^2 = 2\pi^2 c^2 \tilde{\nu}^2 m r^2 \tag{2}$$

where $\tilde{\nu}$ is the frequency of oscillational motion of the guest in its cell in cm^{-1} and m is the guest mass. The coordinate of the c.m., $\underline{r}_G$, may be expressed as

$$\underline{r}_G = \underline{r} - a\underline{\ell}_z \tag{3}$$

where $\underline{\ell}_z$ is a unit vector pointing along the molecular axis, which is taken as the z axis of the molecule fixed coordinate system. Substitution of Eq. (3) into Eq. (2) yields

$$\tilde{V}(r) = 2\pi^2 c^2 \tilde{\nu}^2 m(\underline{r}_G^2 + a^2 + 2a\underline{r}_G \cdot \underline{\ell}_z) \tag{4}$$

RTC arises from the $\underset{\sim}{r}_G \cdot \underset{\sim}{\ell}_z$ term in Eq. (4), which may be expressed as

$$V = 4\pi^2 c^2 \bar{\nu}^2 ma \sum_F F\Phi_{F_z} \tag{5}$$

where Φ_{F_z} is the direction cosine of the molecule fixed z axis with respect to the space fixed coordinate F(= X,Y,Z). The molecular Hamiltonian is

$$H = H^o + V$$

$$H^o = \frac{P^2}{2m} + \frac{J^2}{2I} + 2\pi^2 c^2 \bar{\nu}^2 m(r_G^2 + a^2) \tag{6}$$

where V is given by Eq. (5). Notice that Eq. (6) is expressed in terms of the c.m. coordinate, and is the Hamiltonian of an oscillating rotor to which a constant of energy of $2\pi^2 c^2 \bar{\nu}^2 ma^2$ has been added. V depends on a, which is small, and hence perturbation theory is appropriate.

The preceding derivation assumed a harmonic oscillator cell model (Eq. (2)), but the form of RTC as a term in $\underset{\sim}{r}_G \cdot \underset{\sim}{\ell}_z$ is more general. FKI derives an expression for RTC based on transforming the kinetic energy portion of the Hamiltonian to c.i. coordinates--the cell model is added later. The results of FKI with a harmonic oscillator cell model are identical to the results of FKII.

Noting the invariance of H^o of Eq. (6) to rotation and inversion about the center of the cell, FKII chooses the eigenfunctions of H^o to be eigenfunctions of the total angular momentum

$$\underset{\sim}{L} = \underset{\sim}{J} + \underset{\sim}{l}$$

and the projection of $\underset{\sim}{L}$ on the Z axis: M_L. In this representation, H^o is diagonal and E_o depends on J and n only, where J and n are the rotational and translational quantum numbers. Specifically:

$$H^{o}|JnlLM_L> = hcB\{J(J+1) + (n + \frac{3}{2})\xi + \frac{1}{4} b\xi^2\} \ |JnlLM_L> \qquad (7)$$

where $\xi = \nu/B$ and $b = ma^2/I$. l is the orbital angular momentum quantum number of the c.m., since rotation occurs about the c.i., and l = n, n-2, n-4, . . . 1 or 0.[24] The matrix elements of $r_C \cdot \ell_z$ are diagonal in L and independent of M_L in this representation and are listed in Table I of FKII. M_L is henceforth dropped from the list of quantum numbers in the basis functions. In the absence of other anisotropies, L states are 2L+1 - fold degenerate. The degeneracy of the Jn state is (1/2) x (n+1)(n+2) for n≤J, and (1/2)(J+1)(J+2) + (1/2)(2J+1)(n-J) - (1/4) x $[1-(-1)^{n-J}]$ for n>J.[23]

V has no diagonal terms in n, so there are no first order energy shifts. Using second order perturbation theory, FKII derives the second order energy shifts, such as

$$\frac{\Delta E^{(2)}(J00J)}{hcB} = -\frac{b\xi^3}{4(2J+1)}\left[\frac{J+1}{\xi+2(J+1)} + \frac{J}{\xi-2J}\right] \qquad (8)$$

Under conditions of resonance, $\xi = 2J$, where the translational frequency coincides with a rotational transition, Eq. (8) no longer is applicable and a more general perturbation theory is necessary. For HCl, $\xi = 6.5$ which is near resonance for J=3.

The zero order states may be classified according to L and parity; since H is invariant under operations of the rotation-inversion group, zero order states of different L and parity will not be mixed. For states near a resonance, the perturbation matrix element may be larger than the zero order energy separation, and normal perturbation theory is inapplicable. Following FKII, the perturbation V is written as

$$V = \sum_{ij} |i><i|V|j><j| = \sum_{ij} V_{ij}|i><j| \qquad (9)$$

The states $|i\rangle$ and $|j\rangle$ may be divided into two types of groups, α and β, and V decomposed as

$$V = V_I + V_{II}$$

$$V_I = \sum_{\alpha} \sum_{ij}^{(\alpha)} V_{ij} |i\rangle\langle j| \tag{10}$$

$$V_{II} = \sum_{\alpha,\beta} \sum_{i}^{(\alpha)} \sum_{j}^{(\beta)} V_{ij}(1-\delta_{\alpha\beta}) |i\rangle\langle j| \tag{11}$$

where α or β over the summation restricts summation to basis functions of that group. The sum $\sum_{\alpha}$ refers to summation over all groups.

The Hamiltonian is now written as

$$H = H_o' + V_{II} \tag{12}$$

$$H_o' = H^o + V_I \tag{13}$$

The groups α and β are defined so that the levels within α are closely spaced (quantitative criteria for this are discussed later) while levels in β are distant from levels in α. The eigenfunctions in α are determined by diagonalizing H_o'. The perturbation between these levels and β is due to V_{II}, and since the levels are well separated, perturbation theory is again applicable. Moreover, second order perturbation theory can be applied to the eigenstates of H_o' with the zero order states of β. Thus, the problem of resonance has been avoided by transforming the original basis set. FKII gives explicit expressions for V_I and V_{II} for the $|JnlL\rangle$ basis:

$$V_I = \sum_{\substack{Jnl \\ J'n'l'}}^{(\alpha LM)} V_{JnlL,J'n'l'L} \, |JnlL\rangle\langle J'n'l'L| \tag{14}$$

$$V_{II} = \sum_{\alpha,\beta} \sum_{Jnl}^{(\alpha L)} \sum_{J'n'l'}^{(BL)} V_{Jnl L, J'n'l'L} \, |Jnl L\rangle\langle J'n'l'L| \qquad (15)$$

FKII defines sets α by requiring the separation of levels within the set to be $hcB(2J-\xi)$ or less, and list all sets α for $J \leq 3$ in their Table IV.

Application of V_I to the basis states in (α) produces a new basis:

$$\psi_i^{\alpha}(\xi) = \sum^{(\alpha)} a^{(i,\alpha)}_{|Jnl L\rangle}(\xi) |Jnl L\rangle \qquad (16)$$

where the sum is over all $|Jnl L\rangle$ in (α). Second order perturbation theory is then applied between the $\psi_i^{\alpha}(\xi)$ and all other zero order states $|J'n'l'L\rangle$ from other sets. Only a few matrix elements are actually non-zero, due to the symmetry of V_{II}. The second order shift is

$$\Delta E_i^{(2)}(\xi) = \sum^{(\alpha)} a^{(i,\alpha)}_{|Jnl L\rangle}(\xi) \left[\sum^{(\beta)} \frac{|\langle J'n'l'L|V_{II}|Jnl L\rangle|^2}{E_o(Jn) - E_o(J'n')} \right] \qquad (17)$$

$E_o(Jn)$ is the zero-order energy of the state $|Jnl L\rangle$, given by Eq. (7).

The identity of the $\psi_i^{\alpha}(\xi)$ in terms of the particular $|Jnl L\rangle$ of (α) which dominates $\psi_i^{\alpha}(\xi)$ at ξ is determined by finding the resonances between the various levels in (α) as a function of ξ, and following the zero order states through the resonance. For example, suppose (α) contains the two zero order states $|J_1 n_1 l_1 L\rangle$ and $|J_2 n_2 l_2 L\rangle$ where $J_1 < J_2$. For $\xi=0$, $E(J_1 n_1) < E(J_2 n_2)$, and the lower energy eigenfunction of H_o', ψ_1^{α} is identified as $|J_1 n_1 l_1 L\rangle$. There will be a resonance when

$$J_1(J_1+1) + n_1 \xi_R = J_2(J_2+1) + n_2 \xi_R$$

or

$$\xi_R = \frac{J_2(J_2+1) - J_1(J_1+1)}{n_1 - n_2} .$$

For $\xi > \xi_R$, $E(J_1 n_1) > E(J_2 n_2)$, and the higher energy ψ_2^{α} is predominantly $|J_1 n_1 l_1 L\rangle$. This approach is easily generalized when (α) has more than two levels.

By use of the L and parity representation, no set (α) contains more than three elements for $J \leq 2$, and FKII works out in analytical form energy perturbations for $J \leq 2$. In particular, they derive formulae for levels: $|JnlL\rangle = |0000\rangle$, $|1001\rangle$, $|0111\rangle$, $|2002\rangle$, $|1110\rangle$, $|0200\rangle$, and $|1111\rangle$. To extend the model of FKII to higher levels, we have calculated the shifts for the levels $|1112\rangle$, $|0222\rangle$, $|2111\rangle$, $|2112\rangle$, $|2113\rangle$, and $|3003\rangle$. The calculation is a straightforward generalization of the method of FKII, but is somewhat involved, requiring in some cases numerical matrix diagonalization.

The parameters b and ξ which determine the zero order states are determined by fitting the HCl/Ar R(0)-P(1) and R(0)-R(1) spacings,[23] and are b = 0.20 and ξ = 6.5. The values for DCl are not independent of those for HCl; in particular:

$$a_{DCl} = a_{HCl} - r_e \left[\frac{m_D}{m_{DCl}} - \frac{m_H}{m_{HCl}} \right]$$

Using $a_{HCl} = 0.093$ Å[23] and $r_e = 1.27$ Å,[25] gives $a_{DCl} = 0.060$ Å and $b_{DCl} = 0.044$. Also

$$\xi_{DCl} = \xi_{HCl} \left(\frac{B_{HCl}}{B_{DCl}} \right) \left(\frac{m_{HCl}}{m_{DCl}} \right)^{1/2} = 1.92\ \xi_{HCl}$$

Thus, $\xi_{DCl} = 13$. In the following, energy levels are calculated as a function of ξ for b = 0.20 and 0.044.

According to FKII, the following levels form sets (α):

$|1112\rangle$, $|0222\rangle$, $|2002\rangle$

$|2111\rangle$, $|1201\rangle$, $|1221\rangle$, $|0311\rangle$

$|2112\rangle$, $|1222\rangle$

$|3003\rangle$, $|2113\rangle$, $|1223\rangle$, $|0333\rangle$.

The set $|2112\rangle$, $|1222\rangle$ can be solved analytically, and will be illustrated in detail.

The point of resonance of these two levels occurs when $6+\xi = 2+2\xi$ or at $\xi=4$. For $\xi<4$, $|1222\rangle$ is the lower level; for $\xi>4$, $|2112\rangle$ is the lower level. The matrix element between $|1222\rangle$ and $|2112\rangle$ is $\langle 2112|V_I|1222\rangle = (b\xi^3/20)^{\frac{1}{2}}$. The secular determinant to diagonalize H_o' is

$$\begin{vmatrix} 6+\xi-\lambda & \sqrt{b\xi^3/20} \\ \sqrt{b\xi^3/20} & 2+2\xi-\lambda \end{vmatrix} = 0 \qquad (18)$$

where $\lambda = E - (3/2)\xi - (1/4)\xi^2$ is the energy with the zero point translational motion removed.

The $a^{(i,\alpha)}(\xi)$ that define the eigenfunctions of H_o' are given by:

$$\psi(1222) = a_-|2112\rangle + a_+|1222\rangle \qquad (19)$$

$$\psi(2112) = a_+|2112\rangle + a_-|1222\rangle \qquad (20)$$

where

$$a_\pm = \left[\frac{1}{2} \pm \frac{1}{2}\,|4-\xi|\,H^{-1}\right]^{\frac{1}{2}} \qquad (21)$$

$$H = \left[(4-\xi)^2 + b\xi^3/5\right]^{\frac{1}{2}} \qquad (22)$$

In second order, the only non-zero matrix elements are:

$$\langle 3222|V_{II}|2112\rangle = (b\xi^3/5)^{\frac{1}{2}}$$

$$\langle 2312|V_{II}|1222\rangle = -(b\xi^3/50)^{\frac{1}{2}}$$

$$\langle 2332|V_{II}|1222\rangle = (7b\xi^3/25)^{\frac{1}{2}}.$$

Using the above matrix elements to compute second order energy shifts, and adding these to the first order energies calculated from the eigenvalues of Eq. (18) gives the final result:

$$\frac{E(21_12)}{hcB} - \frac{3}{2}\xi - \frac{1}{4}b\xi^2 = 4 + \frac{3}{2}\xi \pm \frac{1}{2}H - \frac{b\xi^3}{20}(6+\xi)^{-1} \times (4+\xi)^{-1}[26+5\xi-(10+\xi)|4-\xi|H^{-1}] \quad (23)$$

$$\frac{E(1222)}{hcB} - \frac{3}{2}\xi - \frac{1}{4}b\xi^2 = 4 + \frac{3}{2}\xi \mp \frac{1}{2}H - \frac{b\xi^3}{20}(6+\xi)^{-1}(4+\xi)^{-1} \times [26+5\xi + (10+\xi)|4-\xi|H^{-1}] \quad (24)$$

where the top sign in Eqs. (23) and (24) refers to $\xi<4$, and the bottom sign refers to $\xi>4$. Numerical evaluation of the RTC perturbed energies of $|2112\rangle$ and $|1222\rangle$ are calculable from Eqs. (23) and (24).

The RTC perturbations on the three other sets of (α) listed above required diagonalization of 3x3 or 4x4 matrices. Diagonalization was performed by computer (Lawrence Berkeley Laboratory, BKY Computer System, Source Library Program: JACVAT). Second order perturbation theory was applied and numerical values for E (in units of hcB) as a function of ξ were computed. The calculations are sketched in Tables IV-VI. The numerical value of the RTC perturbations minus the translational zero point energies for the levels calculated here, and the levels calculated by FKII, are in Table VII for HCl (b=0.20) and in Table VIII for DCl (b=0.044).

Table III-IV. RTC for $|2002\rangle$, $|1112\rangle$, $|0222\rangle$

Order of levels:

	$\|2002\rangle$	$\|1112\rangle$	$\|0222\rangle$	
$\xi < 2$	A	B	C	$E_A > E_B > E_C$
$2 < \xi < 3$	A	C	B	
$3 < \xi < 4$	B	C	A	
$4 < \xi$	C	B	A	

Secular determinant:

$$\begin{array}{c} \quad |2002\rangle \qquad\qquad |1112\rangle \qquad\qquad |0222\rangle \\ \begin{vmatrix} 6-\lambda & \sqrt{\frac{b\xi^3}{10}} & 0 \\ \sqrt{\frac{b\xi^3}{10}} & 2+\xi-\lambda & \sqrt{\frac{b\xi^3}{6}} \\ 0 & \sqrt{\frac{b\xi^3}{6}} & 2\xi-\lambda \end{vmatrix} = 0 \end{array}$$

$$E_{i,\alpha} = \lambda_i + \frac{3}{2}\,\xi + \frac{1}{4}\,b\xi^2$$

$$\psi_{i,\alpha} = a_1{}^i(\xi)\,|2002\rangle + a_2{}^i(\xi)\,|1112\rangle + a_3{}^i(\xi)\,|0222\rangle$$

Second order matrix elements:

$$\langle 3112|V_{II}|2002\rangle = \sqrt{3b^3/20} \qquad \langle 1312|V_{II}|0222\rangle = -\sqrt{b^3/15}$$

$$\langle 2002|V_{II}|1112\rangle = -\sqrt{b^3/15} \qquad \langle 1332|V_{II}|0222\rangle = \sqrt{7b^3/20}$$

$$\langle 2222|V_{II}|1112\rangle = \sqrt{7b^3/60}$$

Second order energy shifts:

$$\Delta E^{(2)}_{i,\alpha} = -\frac{b\xi^3}{60}\left\{[a_1{}^i(\xi)]^2\left(\frac{9}{6+\xi}\right) + [a_2{}^i(\xi)]^2\left(\frac{11}{4+\xi}\right) + [a_3{}^i(\xi)]^2\left(\frac{25}{2+\xi}\right)\right\}$$

Table III-V. RTC for $|2111\rangle$, $|1201\rangle$, $|1221\rangle$, $|0311\rangle$

Order of levels:

	$\|2111\rangle$	($\|1201\rangle$ and $\|1221\rangle$)[a]	$\|0311\rangle$
$\xi < 2$	A	B	C
$2 < \xi < 3$	A	C	B
$3 < \xi < 4$	B	C	A
$4 < \xi$	C	B	A

$E_A > E_B > E_C$.

[a] $|1201\rangle$ and $|1221\rangle$ are strongly mixed. The degeneracy is removed by RTC effects. The order of these levels is determined by examination of the eigenfunctions of H_o'.

Secular Determinant:

$$\begin{array}{c} \begin{matrix} |2111\rangle & |1201\rangle & |1221\rangle & |0311\rangle \end{matrix} \\ \begin{vmatrix} 6+\xi-\lambda & -\sqrt{\frac{b\xi^3}{9}} & \sqrt{\frac{b\xi^3}{180}} & 0 \\ -\sqrt{\frac{b\xi^3}{9}} & 2+2\xi-\lambda & 0 & \sqrt{\frac{5}{36}\,b\xi^3} \\ \sqrt{\frac{b\xi^3}{180}} & 0 & 2+2\xi-\lambda & -\sqrt{\frac{b\xi^3}{9}} \\ 0 & \sqrt{\frac{5}{36}\,b\xi^3} & -\sqrt{\frac{b\xi^3}{9}} & 3\xi-\lambda \end{vmatrix} \end{array} = 0$$

$$E_{i,a} = \lambda_i + \frac{3}{2}\,\xi + \frac{1}{4}\,b\xi^2$$

$$\psi_{i,a} = a_1^{\,i}(\xi)|2111\rangle + a_2^{\,i}(\xi)|1201\rangle + a_3^{\,i}(\xi)|1221\rangle + a_4^{\,i}(\xi)|0311\rangle$$

Table III-V (continued)

Second order matrix elements:

$$\langle 2111|V_{II}|1001\rangle = \sqrt{b\xi^3/6} \qquad \langle 2311|V_{II}|1221\rangle = -\sqrt{b\xi^3/450}$$

$$\langle 3221|V_{II}|2111\rangle = \sqrt{3b\xi^3/10} \qquad \langle 2331|V_{II}|1221\rangle = \sqrt{21b\xi^3/50}$$

$$\langle 1201|V_{II}|0111\rangle = -\sqrt{b\xi^3/18} \qquad \langle 1401|V_{II}|0311\rangle = -\sqrt{b\xi^3/9}$$

$$\langle 2311|V_{II}|1201\rangle = \sqrt{5b\xi^3/18} \qquad \langle 1421|V_{II}|0311\rangle = \sqrt{7b\xi^3/18}$$

$$\langle 1221|V_{II}|0111\rangle = \sqrt{5b\xi^3/18}$$

Second order energy shifts:

$$\Delta E^{(2)}{}_{\psi_{(i,\alpha)}} = \frac{b\xi^3}{90}\{[a_1{}^i(\xi)]^2\left(\frac{15}{4+\xi} - \frac{27}{6+\xi}\right) + [a_2{}^i(\xi)]^2\left(\frac{5}{2+\xi}\right.$$

$$\left. - \frac{25}{4+\xi}\right) + [a_3{}^i(\xi)]^2\left(\frac{25}{2+\xi} - \frac{38}{4+\xi}\right)$$

$$+ [a_4{}^i(\xi)]^2\left(\frac{45}{2+\xi}\right)\} .$$

Table III-VI. RTC for $|3003\rangle$, $|2112\rangle$, $|1223\rangle$, $|0333\rangle$

Order of levels:

	$\|2002\rangle$	$\|2113\rangle$	$\|1222\rangle$	$\|0333\rangle$	
$\xi < 2$	A	B	C	D	$E_A > E_B > E_C > E_D$
$2 < \xi < 3$	A	B	D	C	
$3 < \xi < 4$	A	C	D	B	
$4 < \xi < 5$	B	D	C	A	
$5 < \xi < 6$	C	D	B	A	
$6 < \xi$	D	C	B	A	

Secular determinant:

$$\begin{array}{c} \begin{matrix} |3003\rangle & |2113\rangle & |1223\rangle & |0333\rangle \end{matrix} \\ \begin{vmatrix} 12-\lambda & \sqrt{\frac{3b\xi^3}{28}} & 0 & 0 \\ \sqrt{\frac{3b\xi^3}{28}} & 6+\xi-\lambda & \sqrt{\frac{b\xi^3}{5}} & 0 \\ 0 & \sqrt{\frac{b\xi^3}{5}} & 2+2\xi-\lambda & \sqrt{\frac{b\xi^3}{4}} \\ 0 & 0 & \sqrt{\frac{b\xi^3}{4}} & 3\xi-\lambda \end{vmatrix} \end{array} = 0$$

$$E_i = \lambda_i + \frac{3}{2}\xi + \frac{1}{4}b\xi^2$$

$$\psi_{i,\alpha} = a_1{}^i(\xi)|3003\rangle + a_2{}^i(\xi)|2113\rangle + a_3{}^i(\xi)|1223\rangle + a_4{}^i(\xi)|0333\rangle$$

Table III-VI (continued)

Second order matrix elements:

$$\langle 2333|V_{II}|1223\rangle = \sqrt{3b\xi^3/25} \qquad \langle 1443|V_{II}|0333\rangle = \sqrt{3b\xi^3/7}$$

$$\langle 2313|V_{II}|1223\rangle = -\sqrt{2b\xi^3/25} \qquad \langle 1423|V_{II}|0333\rangle = -\sqrt{b\xi^3/14}$$

$$\langle 3223|V_{II}|2113\rangle = \sqrt{3b\xi^3/35} \qquad \langle 4113|V_{II}|3003\rangle = \sqrt{b\xi^3/7}$$

$$\langle 3203|V_{II}|2113\rangle = -\sqrt{b\xi^3/14}$$

Second order energy shifts:

$$\Delta E_i^{(2)} = -\frac{b\xi^3}{70}\{[a_1{}^i(\xi)]^2\left(\frac{10}{8+\xi}\right) + [a_2{}^i(\xi)]^2\left(\frac{11}{6+\xi}\right)$$

$$+ [a_3{}^i(\xi)]^2\left(\frac{14}{4+\xi}\right) + [a_4{}^i(\xi)]^2\left(\frac{35}{2+\xi}\right)\}$$

Table III-VII. HCl: RTC Level Shifts (E/B)[a]
b = 0.20

|JnlL>	ξ = 0	0.5	1.5	2.5	3.5	4.5	5.5	6.5	7.5
$\frac{3}{2}\xi + \frac{1}{4}b\xi^2$[b]	0	0.76	2.36	4.06	5.86	7.76	9.76	11.86	14.06
0000	0	0	-0.05	-0.17	-0.39	-0.70	-1.11	-1.62	-2.22
1001	2	2.00	2.07	1.56	1.37	1.05	0.63	0.10	-0.54
0111	0	0.50	1.35	2.63	3.42	4.15	4.81	5.38	5.85
1110	2	2.50	3.68	3.99	4.85	5.61	6.29	6.89	7.42
0200	0	1.00	2.81	5.47	7.53	9.64	11.78	13.94	16.11
1111	2	2.50	3.47	4.38	5.21	5.96	6.62	7.19	7.67
2112	6	6.50	7.50	8.52	9.72	9.31	10.06	10.66	11.13
1222	2	3.00	4.95	6.76	8.26	11.20	12.81	14.39	15.91
2002	6	6.00	6.01	6.17	6.05	4.16	3.89	3.43	2.84
1112	2	2.50	3.61	3.74	4.16	6.48	6.94	7.37	7.73
0222	0	0.99	2.76	5.16	7.30	9.04	10.75	12.39	13.95
2111	6	6.50	7.53	8.72	9.72	8.46	9.18	9.71	10.09
1201	2	3.00	5.18	6.09	7.47	11.33	13.05	14.79	16.50
1221	2	3.00	4.98	6.91	8.71	10.33	11.80	13.15	14.40
0311	0	1.49	4.19	7.80	10.96	13.75	16.50	19.16	21.74
3003	12	12.00	12.01	12.05	12.29	12.55	11.06	7.83	7.45
2113	6	6.50	7.52	8.78	9.33	7.75	7.95	11.44	11.71
1223	2	3.00	5.14	5.99	7.13	10.41	13.54	14.80	16.11
0333	0	1.49	4.18	7.64	11.00	13.99	16.72	19.42	22.06

Table III-VII (continued)

$\|JnlL\rangle$	ξ = 8.5	9.5	10.5	11.5	12.5	13.5	14.5
$\frac{3}{2}\xi + \frac{1}{4}b\xi^2$ [b]	16.36	18.76	21.26	23.86	26.56	29.36	32.26
0000	-2.92	-3.73	-4.63	-5.63	-6.74	-7.94	-9.24
1001	-1.27	-2.11	-3.06	-4.11	-5.26	-6.52	-7.89
0111	6.24	6.53	6.72	6.83	6.84	6.75	6.58
1110	7.88	8.27	8.59	8.84	9.02	9.13	9.18
0200	18.29	20.48	22.68	24.88	27.08	29.29	31.50
1111	8.04	8.33	8.51	8.59	8.58	8.47	8.26
2112	11.50	11.77	11.93	11.99	11.95	11.81	11.57
1222	17.36	18.71	19.97	21.14	22.22	23.21	24.09
2002	2.13	1.31	0.38	-0.66	-1.81	-3.06	-4.41
1112	8.00	8.19	8.27	8.25	8.13	7.90	7.58
0222	15.42	16.81	18.11	19.32	20.45	21.49	22.44
2111	10.35	10.49	10.50	10.40	10.18	9.84	9.39
1201	18.16	19.76	21.30	22.78	24.19	25.54	26.83
1221	15.53	16.55	17.46	18.25	18.93	19.50	19.96
0311	24.23	26.63	28.93	31.13	33.24	35.25	37.17
3003	6.88	6.16	5.30	4.31	3.21	1.99	0.67
2113	11.91	12.04	12.07	12.01	11.86	11.60	11.25
1223	17.38	18.57	19.68	20.70	21.62	22.45	23.17
0333	24.62	27.10	29.50	31.83	34.07	36.22	38.30

[a] Energies given do not include zero point energy. Units of energy are the rotational constant, B.

[b] Zero point energy.

Table III-VIII. DCl: RTC Level Shifts (E/B)[a]
b = 0.044

|JnlL>	ξ = 0	0.5	1.5	2.5	3.5	4.5	5.5	6.5	7.5
$\frac{3}{2}\xi + \frac{1}{4}b\xi^2$[b]	0	0.75	2.28	3.82	5.39	6.97	8.58	10.22	11.87
0000	0	0	-0.01	-0.04	-0.09	-0.15	-0.24	-0.36	-0.49
1001	2	2.00	2.02	1.88	1.86	1.79	1.70	1.58	1.45
0111	0	0.50	1.46	2.55	3.49	4.43	5.35	6.25	7.13
1110	2	2.50	3.55	4.33	5.33	6.27	7.19	8.09	8.98
0200	0	1.00	2.95	5.16	7.15	9.18	11.21	13.26	15.31
1111	2	2.50	3.49	4.47	5.44	6.38	7.31	8.21	9.10
2112	6	6.50	7.50	8.51	9.56	10.14	11.15	12.07	12.96
1222	2	3.00	4.99	6.95	8.79	11.14	12.99	14.89	16.78
2002	6	6.00	6.00	6.04	6.14	5.43	5.46	5.39	5.28
1112	2	2.50	3.53	4.27	5.07	6.66	7.45	8.30	9.15
0222	0	1.00	2.94	5.10	7.01	9.01	10.95	12.86	14.76
2111	6	6.50	7.51	8.55	9.67	9.87	10.92	11.86	12.74
1201	2	3.00	5.06	6.71	8.51	11.23	13.08	15.00	16.93
1221	2	3.00	5.00	6.98	8.94	10.84	12.70	14.54	16.36
0311	0	1.50	4.42	7.66	10.64	13.59	16.53	19.46	22.37
3003	12	12.00	12.00	12.01	12.06	12.25	12.07	10.65	10.76
2113	6	6.50	7.51	8.56	9.65	9.53	10.28	12.63	13.31
1223	2	3.00	5.05	6.67	8.36	11.11	13.29	15.03	16.86
0333	0	1.50	4.14	7.63	10.66	13.60	16.55	19.48	22.39

Table III-VIII (continued)

$\|Jn1L\rangle$	ξ = 8.5	9.5	10.5	11.5	12.5	13.5	14.5
$\frac{3}{2}\xi + \frac{1}{4}b\xi^2$ [b]	13.55	15.24	16.96	18.71	20.47	22.26	24.06
0000	-0.64	-0.82	-1.02	-1.24	-1.48	-1.75	-2.03
1001	1.29	1.11	0.90	0.68	0.43	0.16	-0.14
0111	8.00	8.84	9.65	10.45	11.23	11.98	12.72
1110	9.84	10.68	11.51	12.31	13.10	13.87	14.62
0200	17.37	19.43	21.50	23.58	25.65	27.74	29.82
1111	9.96	10.80	11.62	12.42	13.12	13.95	14.69
2112	13.83	14.67	15.49	16.29	17.06	17.81	18.54
1222	18.65	20.50	22.34	24.15	25.95	27.72	29.47
2002	5.13	4.95	4.76	4.54	4.29	4.02	3.73
1112	9.99	10.81	11.61	12.38	13.14	13.87	14.59
0222	16.64	18.50	20.33	22.15	23.95	25.73	27.48
2111	13.60	14.43	15.23	16.01	16.76	17.49	18.20
1201	18.86	20.77	22.68	24.57	26.44	28.31	30.16
1221	18.15	19.91	21.64	23.34	25.02	26.66	28.28
0311	25.26	28.13	30.98	33.81	36.62	39.41	42.17
3003	10.72	10.60	10.44	10.24	10.01	9.76	9.48
2113	14.06	14.84	15.61	16.38	17.13	17.85	18.56
1223	18.69	20.51	22.31	24.09	25.85	27.59	29.30
0333	25.29	28.16	31.02	33.86	36.68	39.48	42.26

[a] Energies given do not include zero point energy. Units of energy are the rotational constant (B).

[b] Zero point energy.

The mixing of translational and rotational levels makes transitions involving the translational quantum number, n, optically allowed. In particular, there will be an RTC series of lines with the selection rules: $\Delta n = \pm 1$, $\Delta J = 0, \pm 2$.[3] From the $|0000\rangle$ ground state, the following transitions are possible:

$$R_Q(00) = R(0) \qquad Jn = 00 \rightarrow 10$$

$$Q_R(00) \qquad Jn = 00 \rightarrow 01$$

$$S_R(00) \qquad Jn = 00 \rightarrow 21$$

The S transition is much weaker than the Q and R and will be neglected.[23] The intensity ratio of $Q_R(00)$ to $R(0)$ is[23]

$$\frac{Q_R(00)}{R(0)} = \frac{\bar{\nu}_{Q_R(00)}}{\bar{\nu}_{R(0)}} \frac{4b\xi^3}{3(\xi^2-4)^2} \tag{25}$$

except near $\xi=2$. A more general expression is given in FKII for cases of near resonance. Transitions from the thermally populated Jn=10 state are:

$$R_Q(10) = R(1) \qquad Jn = 10 \rightarrow 20$$

$$P_Q(10) = P(1) \qquad Jn = 10 \rightarrow 00$$

$$Q_R(10) \qquad Jn = 10 \rightarrow 11$$

$Q_R(10)$ has three fine structure components, since the final state can be $|1110\rangle$, $|1111\rangle$, or $|1112\rangle$. Generalization to transitions from higher levels is straightforward.

That the RTC effect is weaker for DCl than for HCl is seen, for example, from Eqs. (8) and (25). The energy shift, E(J00J), and the intensity ratio of $Q_R(00)$ to R(0) are proportional to b, and hence to a^2. This will be larger for the hydride than for the deuteride. The intensity ratio of $Q_R(00)$ to R(0) is .051 for HCl/Ar and .005 for DCl/Ar. Examination of Tables VII and VIII also shows that the shifts are larger for HCl than for DCl.

The RTC model requires two parameters, a (or b) and ξ. The parameter a is almost a molecular constant, since the c.i. to c.m. separation should not be influenced much by the particular molecules with which the guest interacts. In fact, for HCl, a is 0.098, 0.093, 0.095, and 0.090 Å for Ne, Ar, Kr, and Xe matrices.[23] The value of a for DCl is, of course, fixed once a has been determined for HCl. In a more detailed theory which includes the lattice dynamics of the host crystal,[26] the value of ξ can be calculated from a knowledge of force constants and the density of phonon states of the pure host crystal. ξ is a greater function of host material than a. For HCl, ξ is 8.3, 6.5, 5.5, and 4.1 for Ne, Ar, Kr, and Xe lattices. The variation of the thermally important energy levels: $|0000>$, $|1001>$, $|0111>$, $|2002>$, $|1110>$, $|1111>$, $|1112>$, and $|3003>$ as a function of ξ are given for HCl in Figure 9 and for DCl in Figure 10. After a choice of ξ, predicted IR and RTC spectra can be calculated from these figures.

FKII has illustrated the fit of the R(0), R(1), P(1), and $Q_R(00)$ lines of HCl and DCl in rare gas matrices to the RTC model. The inclusion of the level Jn=30 in the present extension of FKII allows calculation of R(2) and P(2) frequencies. Barnes[2] has assigned the R(2) transition for HCl/Ar to a weak peak at 2914 cm^{-1} (visible in Fig. 1).

Figure III-9. Variation of thermally important levels of HCl as a function of reduced translational frequency, $\xi = \nu/B$. The dotted lines follow particular levels through resonances. The solid line at $\xi = 6.5$ corresponds to HCl/Ar. The levels $|111L\rangle$ stay closely spaced in energy. Some levels abruptly end in this figure because they mix with thermally inaccessible levels, which are not shown.

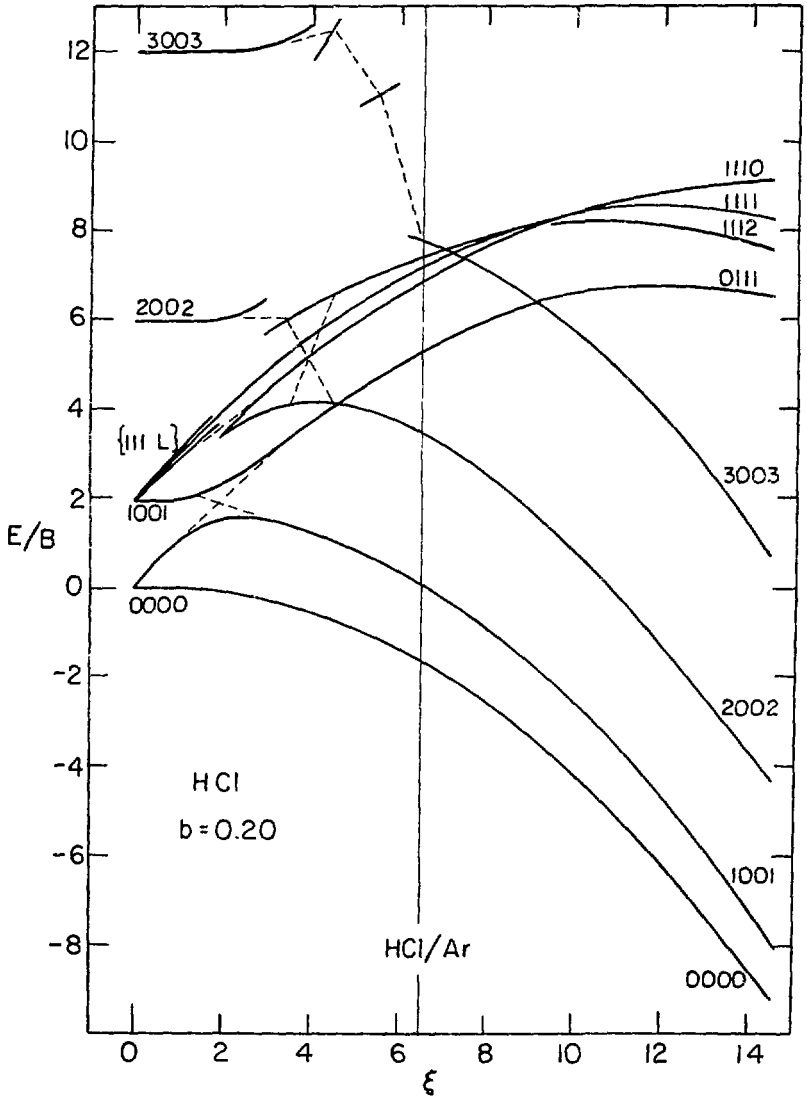

XBL 7711-10470

Figure III-10. Variation of thermally important levels of DCl as a function of ξ. The solid line at ξ = 13 corresponds to DCl/Ar. The levels $|111L\rangle$ form a very closely spaced set. See also the caption to Figure 9.

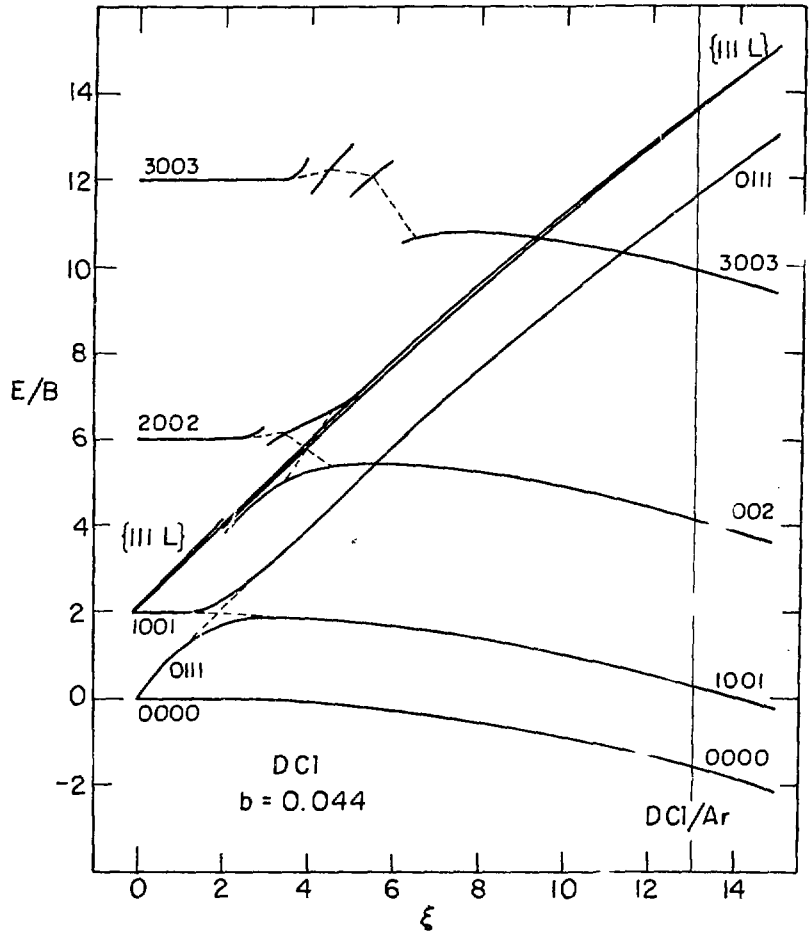

XBL 7711-10469

For $\xi = 6.5$ and a vibrational frequency of 2871 cm^{-1} for HCl $v=0 \rightarrow v=1$, R(2) is predicted from Figure 9 to have a frequency of 2917 cm^{-1}, thus confirming Barnes' assignment and the extension of RTC.

From the assignments of Table I, the lowest energy states for HCl/Ar and DCl/Ar can be determined--these are shown in Figures 11 and 12. (The levels $|111L>$, which are not observed spectroscopically since they couple to states of small thermal population, are not shown in Figures 11 and 12. They lie above J=3 for DCl and just below J=3 for HCl, as can be seen in Figures 9 and 10.) Also shown are the shifts caused by RTC on the zero order free rotor states--the agreement is very good, with the possible exception of ω_n=10 for HCl/Ar. Some fine points of the spectra remain to be explained, however. Most notably, R(1) for DCl/Ar is split into two peaks. R(1) for HCl/Ar is very broad and is shifted more than predicted by RTC. These finer effects are due to the lattice crystal field and coupling of rotation to phonons, and will be discussed below.

2. Crystal Field Model

The anisotropic part of the potential experienced by the guest molecule in its lattice position, $\Delta V(r,\Omega)$ in Eq. (1) was neglected in computing RTC effects. This may now be included as a perturbation on the RTC levels, since it will be a small additional effect. The crystal field anisotropy will shift and remove the degeneracy of free rotor states. Devonshire[19] has calculated the shifts of free rotor levels in a field of octahedral symmetry as a function of the barrier K to rotation. The results of his calculation are displayed graphically in Figure 13. For levels $J \geq 2$, the degeneracy of m_J levels is partially

Figure III-11. Energy levels and perturbations for HCl/Ar. Free rotor levels are rearranged by RTC and crystal field effects. The level $|0111\rangle$ corresponding to the first excited translational state has no pure free rotor analogue. Phonon broadening effects are indicated for J=2 and, less confidently, for J=3. The right hand levels are deduced from absorption spectra. The position of J=3 is not well-known due to the weakness and breadth of R(2).

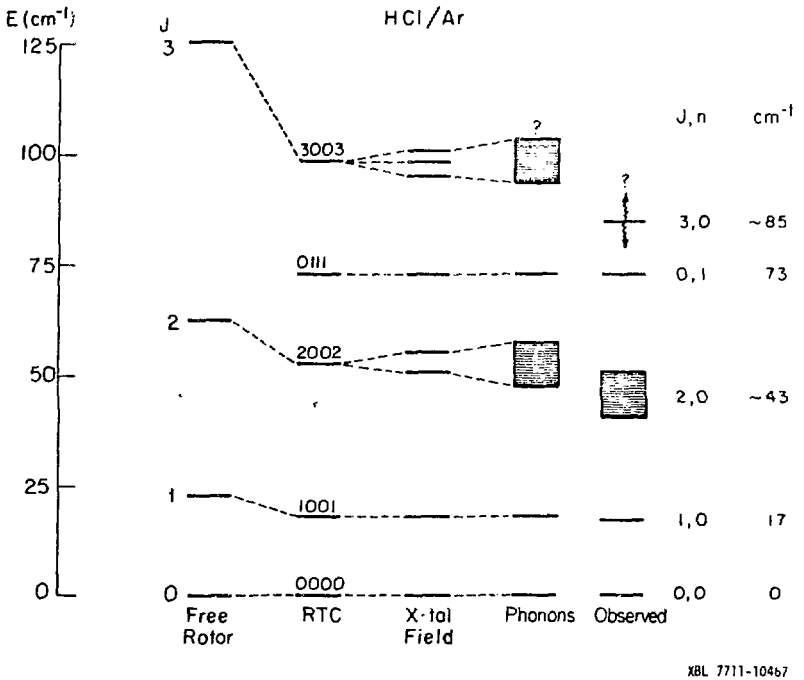
E(cm⁻¹)
125
100
75
50
25
0
J
3
2
1
0
HCl/Ar
3003
0111
2002
1001
0000
?
?
J,n
cm⁻¹
3,0
~85
0,1
73
2,0
~43
1,0
17
0,0
0
Free Rotor
RTC
X-tal Field
Phonons
Observed
XBL 7711-10467

Figure III-12. Energy levels and perturbations for DCl/Ar. Free rotor states are perturbed by RTC and crystal field effects. The level $|0111\rangle$ has no free rotor analogue. No phonon broadening effects are included. The right hand levels are deduced from absorption spectra.

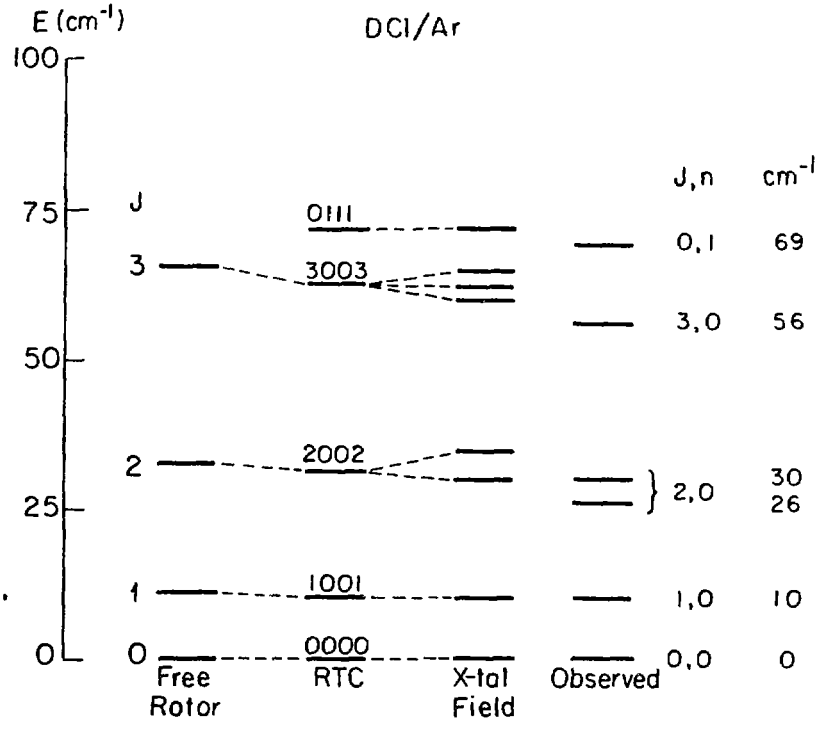

XBL 7711-10468

Figure III-13. Perturbations on a rigid rotor due to a crystalline field of octahedral symmetry (after Devonshire, Ref. 19). Negative barriers are indicated for HCl/Ar and DCl/Ar. See text.

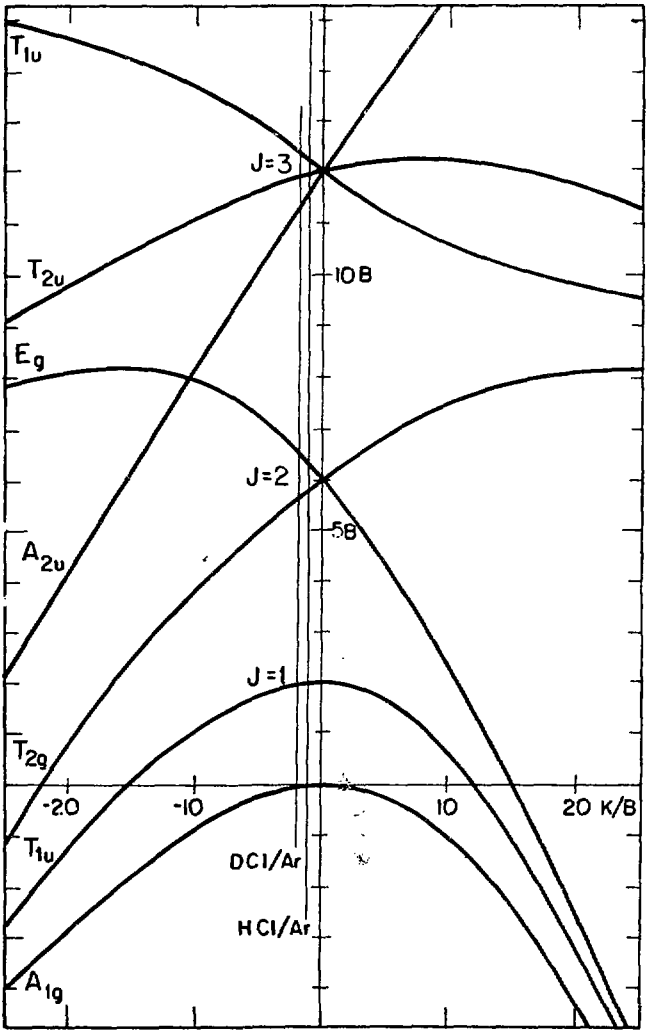

XBL 7711-10466

removed; J=2 is split into E_g and T_{2g} sublevels. The barrier to rotation is a function of intermolecular potentials and is independent of isotopic composition. Since the effect scales as K/B, it is larger for DCl than for HCl.

The lower frequency R(1) line of DCl/Ar is more intense than the higher frequency component, so the lower sublevel of J=2 should have a higher degeneracy than the higher sublevel, and is identified as T_{2g}. Thus, the barrier to rotation is negative, as suggested by Flygare.[20] This implies that the most favorable Ar-HCl geometry is a co-linear one with Ar along the HCl axis. It is interesting to compare this with the potential surfaces calculated to fit the spectroscopy of the gas phase Ar-HCl dimer, in which the Ar-HCl minimum also occurs in a linear geometry,[27,28] with H between Ar and Cl. The calculated Ar-HCl intermolecular separation is 3.80 or 3.88 Å.[28] Since this is close to the nearest neighbor distance of 3.76 Å in an Ar crystal, the HCl fit in the lattice is not tight.

It is difficult to precisely measure the R(1) splitting from absorption spectroscopy. Anticipating the results of excitation spectra (Fig. 17), the splitting is 4.5 ± 0.5 cm^{-1}, which predicts K = 9.3 cm^{-1} from Figure 13. This predicts for HCl a splitting of R(1) of 5.5 cm^{-1}. It also predicts $T_{1u} - T_{2u}$ and $T_{2u} - A_{2u}$ splittings of 2.8 cm^{-1} for J=3 of HCl/Ar. The broadness of R(1) for HCl/Ar is partially explained as unresolved splitting. It is also due to phonon broadening, which is discussed next. The effects of the crystal field are included in Figures 11 and 12 as small modifications of the RTC shift.

3. Phonon Effects

In the treatment of RTC presented above, the rare gas lattice creates a harmonic cell potential in which the guest molecule oscillates with frequency $\bar{\nu}$. The lattice motion is totally ignored. The cell model corresponds to the extreme limit of a localized phonon mode.[29] Mannheim and Friedmann[26] (hereafter called MF) have extended the RTC model to include the motion of the lattice. In reality, the oscillational motion of the guest is not totally decoupled from the vibrations of the remainder of the lattice, and the guest translational motion will have contributions from all lattice phonon modes. The physics of the situation is that guest rotation is coupled to guest translation, and guest translation is due to participation in lattice phonon modes as well as localized modes. From considerations of mass and force constant changes upon substitution of HCl for Ar in an otherwise perfect lattice with use of the pure Ar lattice density of phonon modes, MF shows that the motion of the HCl impurity in Ar is predominantly due to a localized mode and calculates the frequency to be 76 cm^{-1}, in good agreement with the experimentally observed value of 73 cm^{-1} (from $Q_R(00)$). The success of the RTC theory of FKII is in fact partly due to the fact that the local mode for HCl/Ar is not coupled strongly to the lattice, and the cell model description of guest translation is in fact a very good one.[30]

The coupling of rotation to lattice phonons by way of guest translation produces a broadening of the rotor level J due to transitions between J and J±1 with corresponding absorption or emission of a phonon.[26] The transition rate, and hence level width due to this effect, is proportional to the phonon density of states at the energy corresponding to the rotational transition (see Eq. (26) below). For HCl, the J=2 → 1

transition at 42 cm^{-1} is close to the first maximum of the Ar phonon density of states,[31] so the level J=2 is broadened by the phonon emission. MF calculates the width of R(1) of HCl/Ar to be 10 cm^{-1} at 0 K. For DCl/Ar, the J=2 → 1 transition occurs at 22 cm^{-1}, well below the phonon maximum; hence the phonon density of states is smaller than for the corresponding HCl transition, and R(1) is not broadened as much. The effect of phonon broadening for HCl/Ar is included in Figure 11. A more detailed discussion of linewidths will be presented in Section D.3.

Pandey[32] has considered the shift of the R(0)-P(1) separation for some hydrogen halides in rare gas matrices due to interaction with bulk lattice phonons. The shifts amount to 0.6-0.8 cm^{-1} and do not depend much on the particular system.

4. Summary

The experimentally observed energy levels of HCl/Ar and DCl/Ar can be fitted excellently with a combination of theoretical models, as is evident in Figures 11 and 12. The main perturbation is RTC, which couples guest rotation with the localized phonon mode which dominates guest translation. RTC fits the observed spectral features well, with perhaps the exception of R(1) for HCl. Finer details, such as the splitting of the R(1) line of DCl and the width of the R(1) line of HCl are explained by anisotropy of the lattice crystal field and coupling of guest rotation to bulk phonons. The validity of this picture as compared to other interpretations of the spectra of HCl/Ar is discussed in more detail elsewhere.[2] Crystal field effects cannot be the most important feature, since this would predict that the reduction in separation of R(0) and P(1) relative to the gas phase would be greater

for DCl than for HCl, contrary to experiments. Assignments other than R(2) for the weak absorption at 2917 cm^{-1} in HCl/Ar can be proposed. Interpretations in which this is one component of an R(1) transition split due to crystal field effects are incompatible with the spectrum of DCl/Ar, so the assignment as R(2) seems correct. The good agreement of the RTC calculations for J=3 suggest that the other energy levels calculated, but not observable spectroscopically, may in fact exist near the calculated positions.

The detailed interpretation of the spectroscopy in Ar matrices has led to a detailed energy level diagram for the lowest rotational-translational states. The major forces acting on the guest HCl and DCl species in Ar near the equilibrium position of the guest in its lattice site have been detailed. The forces discussed here have been illustrated for HCl and DCl in Ar. In fact, the same qualitative description of the monomer levels holds for all hydrogen halides in rare gas matrices,[2,23,26] and may be even more general.

D. Fluorescence Excitation Spectra

A fluorescence excitation spectrum of the first overtone region of HCl/Ar, M/A = 960 at 9 K is shown in Figure 14. The increased resolution of the excitation spectrum compared to IR absorption spectra is obvious. Information from the excitation spectrum concerns: 1) identity and intensity of observed peaks and 2) the fine spectral details of observed peaks, such as relative separations and linewidths.

i. Identity of Observed Peaks

All peaks observed in excitation spectra of HCl and DCl in Ar matrices arise from isolated monomeric species. Spectra have been

Figure III-14. Fluorescence excitation spectrum for overtone excitation, HCl/Ar, M/A = 980 ± 30, 9 K. Deposition conditions: 9 K, 4 pulses/min., 19 m-mole/hour, total deposited = 12 m-mole.

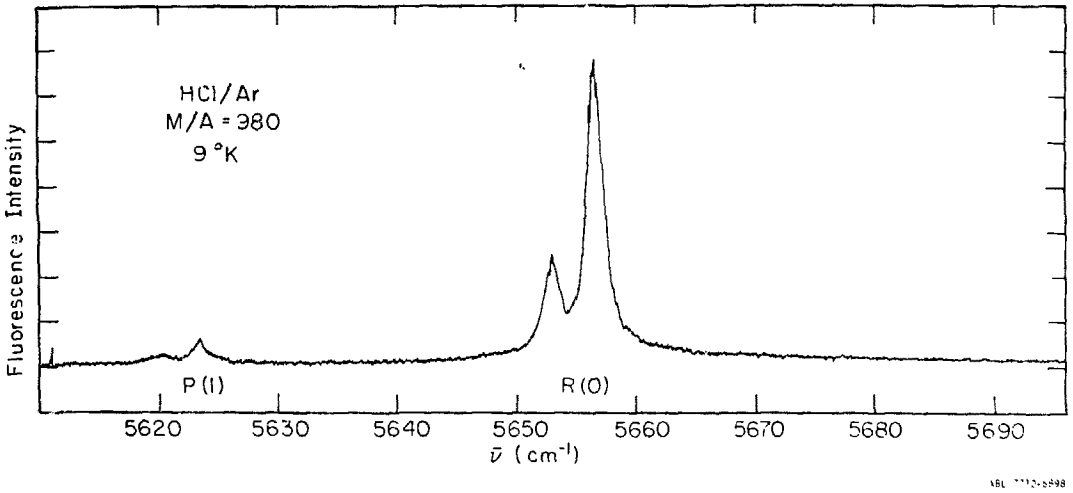
HCl/Ar
M/A = 380
9 °K
Fluorescence Intensity
P(1)
R(0)
5620
5630
5640
5650
5660
5670
5680
5690
$\bar{\nu}$ (cm^{-1})

scanned over the range 5720 to 5350 cm^{-1} for HCl/Ar and 4155 to 3960 cm^{-1} for DCl/Ar, and only monomer peaks appear, even when the sample contains significant dimer or impurities leading to complexes such as $HCl-N_2$. A discussion of the kinetic implications of the fact that no signals from dimer or complex absorptions are observed is deferred to Chapter V.

The spectrum in Figure 14 reproduces in detail the monomer absorptions of HCl/Ar: R(0) and P(1) for both $H^{35}Cl$ and $H^{37}Cl$. Excitation spectra of DCl/Ar at 9 K and 20 K are presented in Figures 15 and 16. Isotopic doublets of P(1) and R(0) as well as the split R(1) transitions are well resolved. The temperature dependence of the peaks matches that of the IR absorption spectra.

Excitation spectra have been recorded at 9 K for HCl/N_2 over the range 5645-5111 cm^{-1} and for HCl/O_2 over the range 5666-5543 cm^{-1}. No peaks were observed. The kinetic implications of this null result are discussed in Chapter V.

2. Fine Spectral Details

The 0.2-0.3 cm^{-1} resolution of fluorescence excitation spectra as compared to the 1-2 cm^{-1} resolution of IR absorption spectroscopy suggests that for those species that do fluoresce excitation spectroscopy is a very good method of studying fine details such as separations between near peaks and linewidths. Furthermore, S/N is very good, for excitation spectroscopy of even highly scattering matrix samples. To a very good approximation the rotational structure of the $v=0 \rightarrow 2$ transition should be identical to the $v=0 \rightarrow 1$ transition (since $B_1 = 10.14$ and $B_2 = 9.84$ cm^{-1},[33] the difference in rotational spacing is 0.3 cm^{-1}, which is equivalent to the resolution).

Figure III-15. Fluorescence excitation spectrum for overtone excitation, DCl/Ar, M/A = 4800 ± 100, 9 K. Peaks are, from low frequency to high: $P(1)^{37}$, $P(1)^{35}$, $R(0)^{37}$, $R(0)^{35}$, R(1): $T_{1u} \rightarrow T_{2g}$, R(1): $T_{1u} \rightarrow E_g$. Deposition conditions: 9 K, 4 pulses/min., 20 m-mole/hour, total deposited = 120 m-mole.

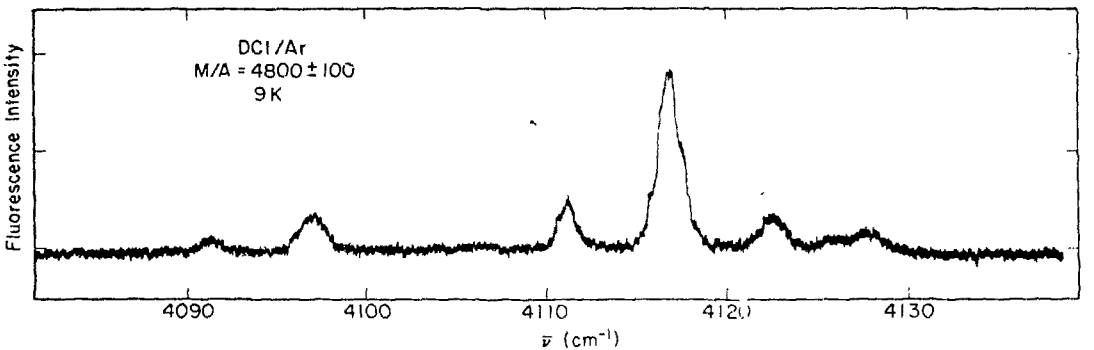

XBL 7710-10358

Figure III-16. Fluorescence excitation spectrum of DCl/Ar, M/A = 4800 ± 100, 20 K. Assignments and deposition conditions are given in the caption to Figure 15. The small peak at about 4087 cm^{-1} may be P(2).

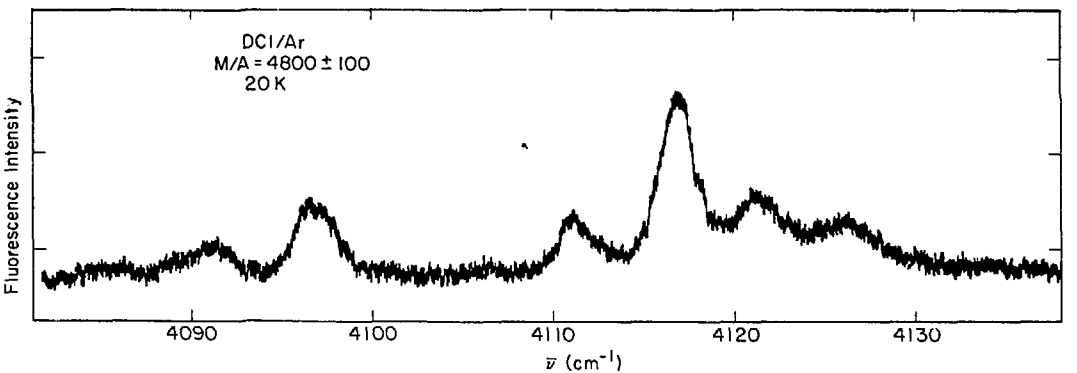

XBL 7710-10357

That the positions and widths of the peaks in the excitation spectrum should be identical to absorption peaks is not a priori necessary. It is possible that part of an absorption line profile is inhomogeneous such that fluorescence quantum yields may vary across the profile. However, measurements of vibrational lifetimes (Chapter V) indicate that different positions of the line profile have the same kinetic behavior, so it is unlikely that the fluorescence quantum yield varies substantially across the line profile.

The resolution of excitation spectra can be exploited to measure $H^{35}Cl$ and $H^{37}Cl$ splittings of R(0) and P(1). The measured splittings for HCl v=0 → 1 and v=0 → 2 excitations are 2.0 ± 0.2 and 4.1 ± 0.3 cm^{-1}, in agreement with values of 2.1 and 4.1 cm^{-1} calculable from gas phase data.[34] The DCl isotopic splitting of the R(0) lines for v=0 → 2 excitation, as measured from spectra such as Figures 15 and 16, is 6.0 ± 0.2 cm^{-1}, in agreement with a value of 5.9 cm^{-1} calculable from chemical laser emission data.[35]

The rotational structure of the overtone excitation spectrum mimics that of the fundamental absorption spectrum, but at higher resolution. The splitting of R(1) for DCl/Ar can be measured easily; the R(1) peaks are shown on an expanded scale in Figure 17. The separation between $T_{1u} \rightarrow T_{2g}$ and $T_{1u} \rightarrow E_g$ peaks is 4.5 ± 0.5 cm^{-1}, and the separation between the $R(0)^{35}$ and the $T_{1u} \rightarrow T_{2g}$ peaks is 4.6 ± 0.5 cm^{-1}. The splittings measured by excitation spectroscopy are the basis for the frequency values quoted in Table I for DCl/Ar. There should be an isotopic splitting for the R(1) peaks--this may be reflected in the high baseline level of these peaks in Figure 17.

Figure III-17. Detail of R(1) peaks in overtone fluorescence excitation spectrum of DCl/Ar; M/A = 1000 ± 20, 9 K. The $R(0)^{37}$ and $R(0)^{35}$ peaks saturated the gated electrometer. The R(1) peaks are well resolved. The small peak at 4107 cm^{-1} is spurious--it is not reproducible. Compare this spectrum to Figure 15. Deposition conditions: 17-18 K, 2 pulses/min., 3.1 m-mole/hour, total deposited = 67 m-mole.

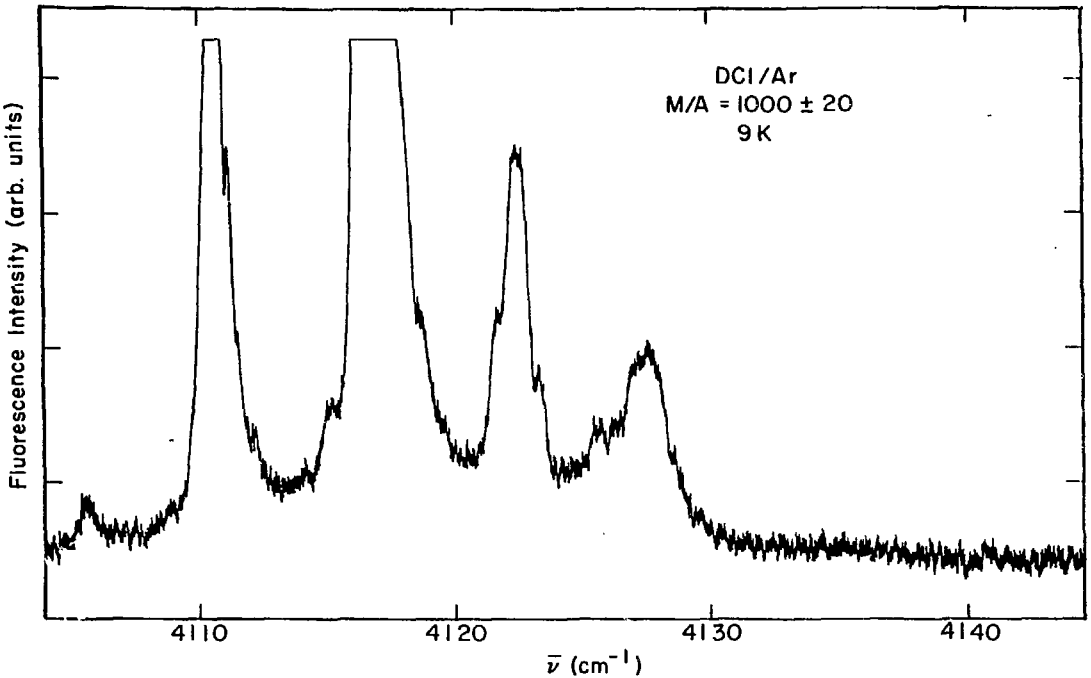

XBL 7711-10471

The R(1) transition of HCl/Ar is very broad and structureless, even with the high resolution of the excitation spectrum. R(1) is present as a high frequency shoulder to $R(0)^{35}$, as seen for a sample of M/A = 670 at 20 K in the top spectrum of Figure 18.

3. Linewidths

We assert that linewidths measured from excitation spectra are equivalent to linewidths obtainable from absorption spectra taken under comparable resolution. The linewidths measured are all greater than 1.0 cm^{-1}, so that convolution of the linewidth with the finite resolution of the excitation spectrum is unnecessary. The linewidths of R(0) and P(1) for HCl/Ar are equal within experimental uncertainty as are those for $H^{35}Cl$ and $H^{37}Cl$ peaks. The R(0) linewidth depends on temperature, whether the sample has been annealed and to some extent on concentration. Linewidths broaden reversibly with temperature, as can be seen comparing Figures 15 and 16, and from the top two spectra of Figure 18, from a value of 2.0 at 9 K to 4.6 cm^{-1} at 20 K for the sample shown in Figure 18. Linewidths decrease upon diffusion to a value of 1.2 cm^{-1} at 9 K for the bottom spectrum of Figure 18. After multiple diffusions the linewidth of R(0) decreases to a limiting value of 1.1 ± 0.2 cm^{-1}. Even after diffusion, however, the linewidth is reversibly broadened by warming to 20 K to 4.0 cm^{-1} for the sample of Figure 18.

The linewidth of R(0) increases with increasing HCl concentration; the extreme case is illustrated in Figure 19, for a sample of M/A = 127. At 9 K the isotopic components of R(0) are barely resolvable; at 20 K the two lines broaden into each other. The R(0) region of the spectrum of an unannealed sample at M/A = 5100 at 9 K is shown for comparison in Figure 19--the linewidth of this sample is 1.2 cm^{-1}.

Figure III-18. Effect of temperature and annealing on linewidth. Fluorescence excitation spectrum of HCl/Ar, M/A = 670 ± 20. Spectrum a is the virgin sample at 20 K; spectrum b is the virgin sample at 9 K; spectrum c is at 9 K after one diffusion. R(1) for HCl/Ar is a broad, structureless shoulder to the high frequency side of R(0) in spectrum a. The weak peak at 5713 cm^{-1} is $Q_R(00)$ in spectrum a. Note that in this figure frequency increases from right to left. Deposition conditions: 14-15 K, 4 pulses/min., 17 m-mole/hour, total deposited = 21 m-mole.

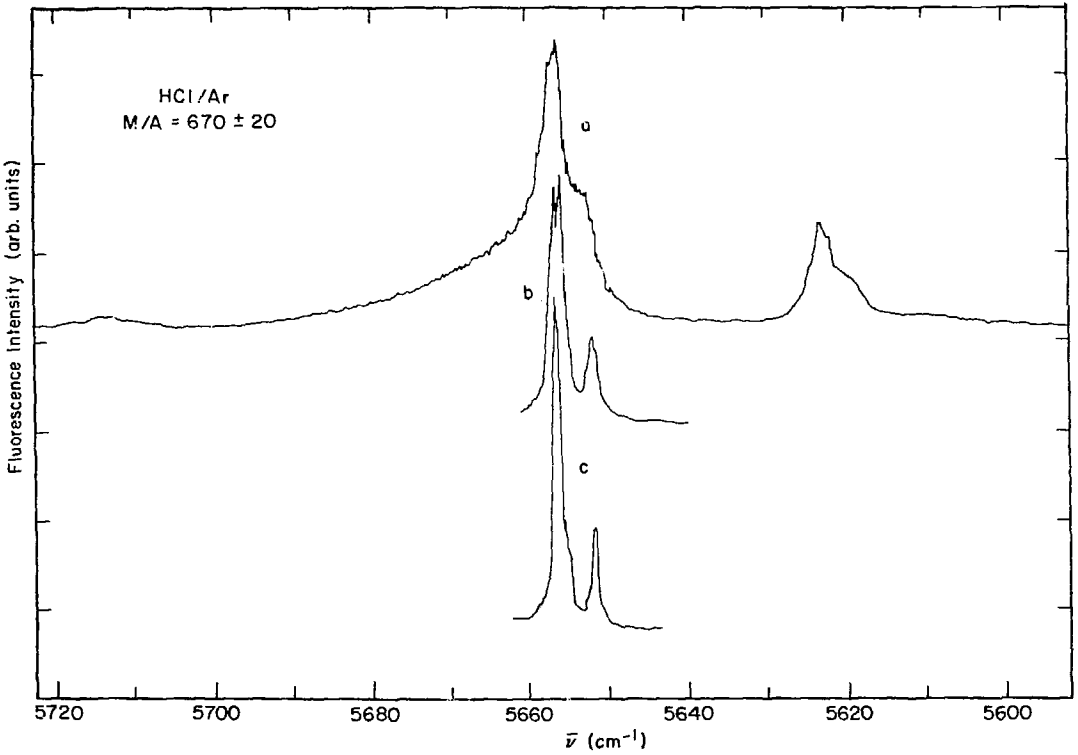

XBL 7711-10360

Figure III-19. Effect of concentration on linewidth. Spectrum a is HCl/Ar, M/A = 123 ± 2 at 20 K; spectrum b is the same sample at 9 K. Spectrum c is M/A = 5100 ± 100 at 9 K. All samples are unannealed. Deposition conditions: M/A = 123, 9 K, 4 pulses/min., 21 m-mole/hour, total deposited = 5.7 m-mole; M/A = 5100, 9 K, 4 pulses/min., 23 m-mole/hour, total deposited = 52 m-mole.

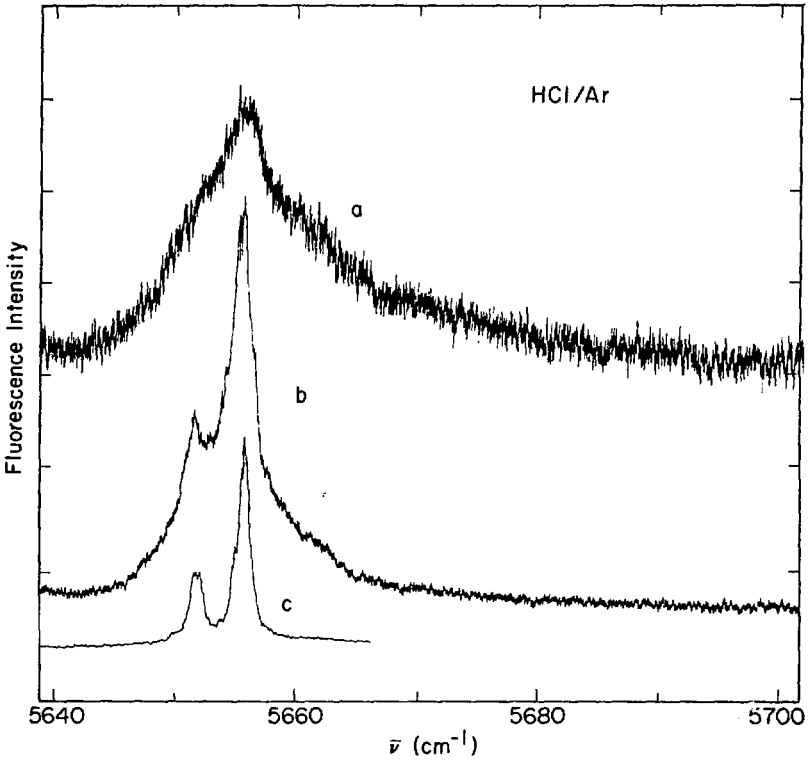

XBL 771-10359

The linewidth data for R(0) and P(1) lines for HCl/Ar and DCl/Ar is collected in Table IX. The following points are worth noting: 1) The linewidth of a virgin, unannealed sample at 9 K increases as the HCl concentration increases; 2) Upon diffusion the linewidth of all samples observed decreases to about 1.1 cm^{-1}--multiple diffusions do not subsequently reduce this width; 3) Linewidths increase as a function of temperature; the degree of increase may be an increasing function of concentration. The data for DCl is less extensive, but similar observations are valid. The nominal uncertainty of measurements reported in Table IX is 0.2 cm^{-1}. Occasionally the scan drive of the OPO temperature controller slipped, so in some cases linewidths may be subject to a random error which overestimates the linewidth. The difference between R(0) and P(1) widths for some samples may reflect this and the fact that S/N for the P(1) peak is lower than that for R(0), so amplitude errors become more important.

The linewidth is composed of inhomogeneous and homogeneous parts. The inhomogeneous part may be due to a distribution of trapping sites which differ in proximity to lattice defects and other guest species. During the matrix annealing process, lattice defects are removed. Also, those HCl molecules near to other HCl molecules tend to polymerize, so that the average separation between remaining monomeric HCl molecules after diffusion is greater than before diffusion. Both of these effects tend to reduce the variety of environments in which an HCl guest may be trapped and hence would reduce the inhomogeneous part of the linewidth.

The fact that the monomer linewidth for R(0) reaches a limit of 1.1 cm^{-1} at 9 K which does not decrease upon further annealing suggests that this may be the homogeneous width. For HCl the homogeneous width

Table III-IX. Linewidths from Fluorescence Excitation Spectra, $\Delta\nu$[a]

Sample	M/A	T(K)	R(0)	P(1)	R(0)-1D[b]	R(0)-2D[b]
HCl/Ar	127	9	3.1			
	127[c]	21	11.6[d]	8.4 ± 1.5[e]		
	670	9	2.0	1.9	1.2	1.1
	670[c]	20	4.6		4.0	
	920[f]	9	1.3 ± .3			
	930[g]	9	1.5		1.3	
	980	9	1.6	1.4	1.2	
	1000	9	1.6	1.7		
	1000[c]	21	3.8	3.0		
	2900	9	1.4			
	2900[c]	21	2.4	2.3		
	4000-5000	9	1.3			
	5100	9	1.2	1.2	1.0	
	10,000	9	1.2			
DCl/Ar	1000	9	1.9	1.5 ± .3		
	1000[c]	19	2.3	3.0 ± .3		
	1020	9	1.4	1.5		
	3270	9	1.7			
	4800	9	1.5		1.4	1.1[h]
	4800[c]	20	2.9		2.8	

[a] cm^{-1}, ± 0.2.

[b] 1D means one time diffused; 2D means two times diffused.

[c] The sample is identical to the one immediately above it.

[d] Unresolved R(1) and $R(0)^{35}$ and $R(0)^{37}$-FWHM of entire band. See Figure 19.

[e] Unresolved $P(0)^{35}$ and $P(1)^{37}$-FWHM of entire band.

[f] v=0 → 1 excitation.

[g] Air doped sample: HCl/Air/Ar = 1/0.2/930

[h] After 3 and 4 diffusions, $\Delta\nu$ = 1.1 ± .1 cm^{-1}.

increases to 2.4 ± 0.2 cm^{-1} at 21 K at M/A = 2900. The R(0) widths at 20 K at M/A = 670 or 1000 may be larger than this due to concentration dependent effects. Two broadening mechanisms are illustrated in Figure 20: coupling of rotation to phonons, and resonant rotational energy transfer from monomer to monomer. We neglect broadening mechanisms such as vibrational dephasing. The width of a transition is equal to the sum of the widths of the levels connected by the transition. The width of a level (in sec^{-1}) is given by the total of all decay rates removing the molecule from its given initial state.

Phonon-rotation interaction is considered first. A guest molecule may be removed from its initial state by the exothermic process: emission of a phonon and simultaneous downward rotational transition (for J>0), or by the endothermic process: absorption of a phonon and simultaneous upward rotational transition. Exothermic processes are proportional to $(\bar{n}+1)$ where $\bar{n} = [\exp(h\omega/kT)-1]^{-1}$ is the thermal population of the phonon mode of frequency ω involved, and endothermic processes are proportional to $\bar{n}$. At 0 K only exothermic processes contribute to level widths, since $\bar{n}=0$. Mannheim and Friedmann[26] give the expression for the 0 K width of level J, due to coupling of the rotational transition J → J-1 with a phonon of energy $h\omega_J = 2hcBJ$ by the RTC mechanism:

$$\Gamma(J) = \pi a \frac{M^2(0)}{3} \omega_J^3 |\chi(0,\omega_J)|^2 g(\omega_J) \frac{J}{2J+1} \qquad (26)$$

where a is the distance between molecular c.i. and c.m., M(0) is the mass of the guest species, $\chi(0,\omega_J)$ is the expansion coefficient of the displacement of the guest molecule due to the lattice phonon mode ω_J, and $g(\omega_J)$ is the phonon density of states at ω_J. RTC couples the rotational motion of the guest into its translational motion, which is composed of

Figure III-20. Mechanism for broadening of the level J=1 of HCl/Ar. The level considered is shown as broadened. Interaction with phonons: J=1 → J=0 transition with production of a 17 cm^{-1} phonon; absorption of a 26 cm^{-1} phonon to cause the transition J=1 → J=2. Resonant rotational energy transfer: another guest in J=2 transfers a rotational quantum to J=1, or, a rotational quantum is transferred from J=1 to another guest in J=0. These processes are proportional to guest mole fraction, x, and a Boltzmann factor for the appropriate level, as indicated.

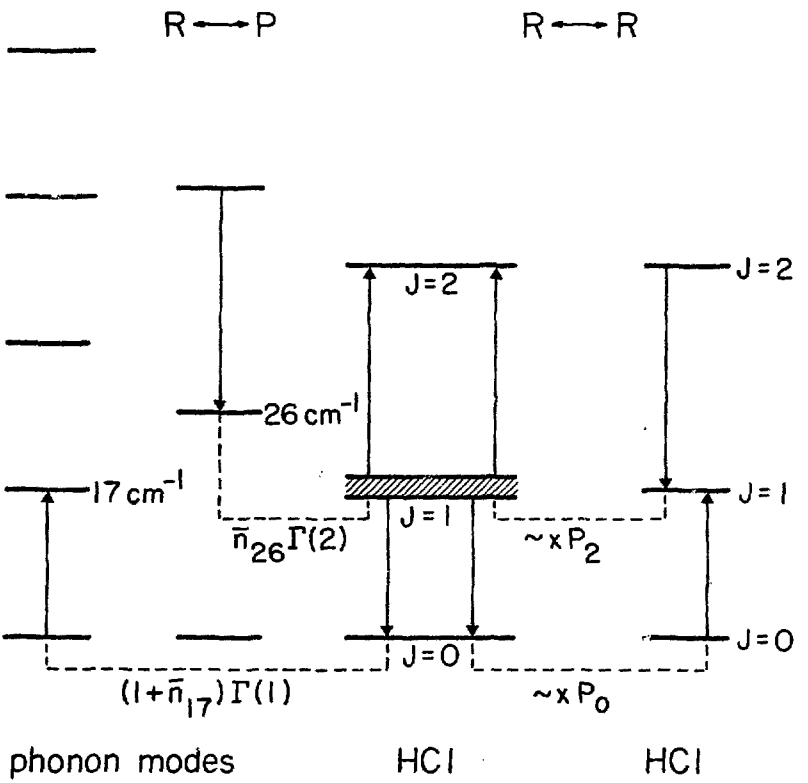

XBL 7711-10465

contributions from the phonon modes. The 0 K widths of J=1 and J=2 of HCl/Ar are calculated to be 0.4 and 10 cm^{-1}.[26]

Consider the linewidths of R(0) and P(1)--these should be equal since the same two levels, J=0 and J=1 are connected. The width of J=0 is determined by the endothermic phonon absorption process to J=1 while the width of J=1 is the sum of an endothermic process to J=2 and an exothermic process to J=0. Specifically,

$$\Gamma(T) = (1+2\bar{n}_1)\Gamma(1) + \bar{n}_2\Gamma(2) \qquad (27)$$

where $\bar{n}_1$ and $\bar{n}_2$ are the thermal populations of the 17 and 27 cm^{-1} phonons[36] connecting J=0 and 1 and J=1 and 2, respectively. For Mannheim and Friedmann's values of $\Gamma(1)$ and $\Gamma(2)$, the total predicted widths are:

$$\Gamma(0) = 0.4 \text{ cm}^{-1}$$
$$\Gamma(9) = 1.2$$
$$\Gamma(20) = 3.0$$

The value of 3.0 cm^{-1} is a bit high to fit the experimental width of R(0) at 20 K. Assuming an empirical value of 7 cm^{-1} for $\Gamma(2)$ gives

$$\Gamma(0) = 0.4 \text{ cm}^{-1}$$
$$\Gamma(9) = 1.2$$
$$\Gamma(20) = 2.5$$

These values fit the data of Table IX satisfactorily, and the rotation-phonon coupling is capable of explaining the observed homogeneous widths of HCl/Ar. The exact calculated values and temperature dependence of linewidths by this mechanism is very sensitive to the position of J=2

relative to J=1.[36] To better sort out what value should be used for the phonon frequency coupling J=1 and J=2, as well as empirical values for $\Gamma(1)$ and $\Gamma(2)$, a more complete study of the effect of temperature on linewidth is necessary.

For DCl/Ar the data suggests that the homogeneous R(0) width may be 1.1 cm^{-1} at 9 K and 2.8 cm^{-1} at 20 K. Taking the phonon frequencies connecting J=0 and 1 and J=1 and 2 as ω_1 = 10 cm^{-1}, and a mean value of 18 cm^{-1} for ω_2, and using $\Gamma(1)$ = 0.7 cm^{-1} and $\Gamma(2)$ = 2.0 cm^{-1} gives

$$\Gamma(0) = 0.7 \text{ cm}^{-1}$$

$$\Gamma(9) = 1.2$$

$$\Gamma(20) = 3.0$$

in agreement with experiment. The values imposed for $\Gamma(2)$ is lower for DCl than the corresponding value for HCl. This can be rationalized by the $\omega_J^3 g(\omega_J)$ factor in Eq. (26), since DCl rotational transition is lower in energy than the corresponding HCl transitions, and hence samples a smaller phonon frequency and density of states.

A second mechanism of line broadening, one which is concentration dependent, involves resonant rotational energy transfer from guest to guest by a dipole-dipole coupling, as indicated schematically in Figure 20. The physics and mathematics of this effect are analogous to those of vibrational or electronic energy transfer by dipole-dipole coupling, except that the rotational process involves permanent dipole moments whereas the other processes involves dipole transition moments. A detailed discussion of energy transfer due to dipole-dipole coupling is presented in Chapter IV. In this chapter the concepts will be used as they apply. Details not referenced here can be found in Chapter IV.

Consider a donor molecule at lattice site 0 in state J and an acceptor molecule in state J' at a distance R. The rate of energy transfer from donor to acceptor is given by the golden rule expression.

$$W = \frac{2\pi}{\hbar} |V|^2 \rho(E_f) \tag{28}$$

where, for orientationally averaged dipole-dipole coupling

$$|V|^2 = \frac{2}{3n^4R^6} |\langle J|\mu_D|J'\rangle|^2 |\langle J'|\mu_A|J\rangle|^2 \tag{29}$$

n is the refractive index of the host medium, and μ is the dipole moment operator. For resonant transitions with a Lorentzian lineshape of FWHM $h\Delta\nu_{J,J'}$, the density of final states is

$$\rho(E_f) = (\pi h \Delta\nu_{J,J'})^{-1}. \tag{30}$$

The width $\Delta\nu_{J,J'}$ is the homogeneous width and is due to rotation-phonon coupling. For non-resonant transitions, such as J=2 + J=0 → 2J=1, $\rho(E_f)$ is much smaller than given by Eq. (30) and hence non-resonant rotational transfer as a source of line broadening is insignificant compared to the resonant process. For a random distribution of orientations, the matrix element of μ should be summed over all M states with the result[37] that

$$|\langle J|\mu|J'\rangle|^2 = \mu^2(J+1)\ \delta_{J+1,J'} + \mu^2 J\ \delta_{J-1,J'} \tag{31}$$

where μ here is the permanent dipole moment. Equation (28) can be rewritten as

$$W = C/R^6 \tag{32}$$

$$C = C_- + C_+ = \frac{2\mu^4}{3\pi\hbar^2 n^4}\left[\frac{J^2\delta_{J-1,J'}}{\Delta\nu_{J,J-1}} + \frac{(J+1)^2\delta_{J+1,J'}}{\Delta\nu_{J,J+1}}\right] \tag{33}$$

where $\mu_D = \mu_A = \mu$. Summing the interaction over all guest molecules in the sample leads to a total decay rate of

$$W = C_- \sum_i \frac{1}{R_i^6} + C_+ \sum_j \frac{1}{R_j^6} \tag{34}$$

$$W = x(C_-P_- + C_+P_+) \sum_k \frac{1}{L_k^6} \tag{35}$$

C_+ and P_+ are the interaction constant and Boltzmann factor for acceptors in $J' = J+1$, located at distance R_i; C_-, P_-, and R_j are similarly defined for $J' = J-1$; x is the total guest mole fraction; and L_k is the distance from site 0 to the k^{th} lattice site. A random distribution of guest molecules is assumed. The sum in Eq. (35) can be evaluated to give[38]

$$W = (C_-P_- + C_+P_+)\frac{14.45x}{d_o^6} \tag{36}$$

d_o is the nearest neighbor distance in the crystal. Equation (36) gives the width of the level J due to resonant rotational energy transfer in sec^{-1}. For HCl/Ar at 9 K, the relevant parameters for J=1 broadening are: $\mu = 1.08$ D,[39] $n = 1.27$, $\Delta\nu_{1,0} = 1.1\ cm^{-1}$, $\Delta\nu_{2,1} = 10\ cm^{-1}$, $d_o = 3.76$ Å, $P_0 = 0.84$, $P_1 = 0.16$, $P_2 = .004$. The width of J=1 is calculated to be $[4.3 \times 10^5] \times cm^{-1}$. For $x = 10^{-4}$ (M/A = 10,000) the predicted width of J=1 is 43 cm^{-1}, greatly in excess of experimental observation!

The sum in Eq. (35) should not really include nearest neighbors, since in this case the donor is not isolated. Assume that rotational

transfer is meaningful only for distances greater than R_o from the donor. The summation is replaced by an integral

$$\sum_k \frac{1}{L_k^6} \rightarrow \rho \int_{R_o}^{\infty} \frac{4\pi R^2 dR}{R^6} = \frac{4\pi}{3} \frac{\rho}{R_o^3}$$

where ρ is the density of lattice sites (number/cm^3). The width of the donor level is now given by

$$W = (C_- P_- + C_+ P_+) \frac{4\pi}{3} \frac{\rho x}{R_o^3} \tag{37}$$

The width of R(0) and P(1) transitions is the sum of widths of J=0 and J=1, so γ, the width of the transition, is

$$\gamma = W(J=0) + W(J=1)$$

$$= \frac{4\pi}{3} \frac{\rho x}{R_o^3} [C_{1,0} P_0 + 2C_{1,2} P_2 + C_{1,0} P_1] \tag{38}$$

For HCl/Ar at 9 K, the data of Table IX suggests that for R(0) and P(1) $\gamma = 2$ cm^{-1} for $x = 10^{-2}$. From Eq. (38) this gives a value of R_o of 38 Å. With this value for R_o the broadening due to resonant transfer is 0.2 cm^{-1} at $x = 10^{-3}$. γ decreases with increasing temperature, since $\Delta\nu$ increases with temperature. From Eq. (38), at 20 K and $x = 10^{-2}$, $\gamma = 0.8$ cm^{-1}.

What is the meaning of R_o? Clearly, without imposing a minimum separation between isolated monomer and its nearest guest neighbor resonant transfer would cause excessive broadening. The mean separation of guest molecules at $x = 10^{-2}$ is 17 Å in Ar, much less than the value of R_o. However, there is a great deal of aggregation at $x = 10^{-2}$, and since much of the HCl is present in closely spaced groups (polymers),

the monomers may well be separated by something like 38 Å. Perhaps during the matrix deposition process there is enough diffusion for HCl guests originally deposited within 38 Å of each other to aggregate before cooling, so only truely distant molecules remain isolated. During matrix annealing, those guests close to each other will aggregate, and R_o should increase subsequent to diffusion, producing a line-narrowing. Legay[38] finds a similar situation for rapid V→V transfer between different isotopic species of CO in an Ar matrix: calculated rates are too fast unless an R_o is postulated.

The above treatment of line broadening by rotational energy transfer is over-simplified and is meant to be suggestive rather than quantitative. It correctly shows that resonant rotational energy transfer produces concentration dependent broadening and that the broadening so produced decreases with temperature. For a more correct treatment, it is necessary to divide the guest system into classes of guests with identical distributions of other guests around them. The lineshape for each class is a Lorentzian with width determined by the rotational lifetime for energy transfer from a guest in this class. The true lineshape will be a sum of such Lorentzians weighted by the distribution of classes.

It is worthwhile to recapitulate this section. The major features of linewidths for HCl/Ar and DCl/Ar can be described by rotation-phonon coupling. This broadening is homogeneous and can be made to explain the dilute and diffused samples and their temperature dependence with empirical (but reasonable) choices of the 0 K level widths. Inhomogeneous broadening is perhaps due to two effects: site distributions and resonant rotational energy transfer. The site distribution is narrowed upon annealing. The resonant rotational transfer mechanism

produces a concentration dependent width which is also narrowed upon annealing. The width produced by rotational transfer decreases with temperature, but the decrease is masked by the increasing width due to rotation-phonon coupling. It is difficult to explain the extreme width of the sample of M/A = 127 at 20 K, however, only by rotation-phonon coupling. The data presented in Table IX is by no means a complete characterization of linewidths. Further experimental studies of HCl/Ar and HCl in other matrices, such as Kr or Xe, would be useful in further specifying the empirical level widths employed in fitting the homogeneous widths.

E. Quantitative Spectroscopic Results

Experiments were performed to measure the integrated absorption coefficient of HCl in Ar. A rough quantitative estimate of the enhanced dipole transition moment of HCl in polymeric form as compared to monomeric form is presented. The effects of matrix deposition conditions on matrix isolation (monomer/polymer ratio) will be discussed.

1. Integrated Absorption Coefficient of Monomer

From a knowledge of the integrated absorption coefficient of a molecule in a solid it is possible to calculate the molecular transition moment and hence, the radiative lifetime. An estimate of the radiative lifetime is important to decide whether vibrational relaxation procedes radiatively or non-radiatively. The ratio of radiative decay rates in solid and gas (Einstein coefficients) is given by

$$\frac{A_s}{A_g} = n\left(\frac{n^2+2}{3}\right)^2 \left|\frac{\mu_s}{\mu_g}\right|^2 \qquad (39)$$

where μ_s and μ_g are the transition dipole moments in the solid and gas phases. Equation (39) and other relationships between Einstein coefficients and absorption coefficients in condensed phases are derived in Appendix A. Since the vibrational frequencies of most molecules change by only one or two percent from gas phase to matrix, it is unlikely that μ changes greatly, and the change in radiative lifetime should result from the index of refraction factors in Eq. (39) only. That this is true for HCl is experimentally demonstrated below.

The ratio of transition moments can be calculated from measured integrated absorption coefficients, A, since, from Appendix A

$$\frac{A_s}{A_g} = \frac{1}{n}\left(\frac{n^2+2}{3}\right)^2 \left|\frac{\mu_s}{\mu_g}\right|^2 . \qquad (40)$$

The experimental difficulty in measuring A consists in measuring the thickness of an optical path through the matrix.

Jiang et al.[40] have deduced the absolute absorption coefficient for CO in Ar matrices and pure solid CO by measuring the thickness of their samples by counting interference fringes of a transmitted monochromatic infrared beam during matrix deposition. They find that the ratio of absorption coefficients is given by Eq. (40) with $\mu_s = \mu_g$. Dubost and Charneau[17] find that the radiative decay of vibrationally excited CO in Ar matrices is given by the index of refraction factors in Eq. (39) only, using the value n = 1.40, confirming the result of Jiang, et al. that the dipole transition moment of CO is essentially unperturbed by the matrix environment.

We have prepared matrices of HCl/CO/Ar dilute enough (HCl: M/A = 750-4360; CO: M/A = 2040, 3940) so that multimer absorptions are

negligible compared to monomer absorptions. Integrated absorption coefficient ratios of HCl to CO are measured, and no direct measurement of the matrix thickness is required. The samples were prepared and spectra recorded at 9 K or 20 K and spectra of each sample were recorded for three values of the spectral resolution. The results did not vary with temperature or spectral resolution. The result of five samples gives a value of 0.55 ± .05 for the ratio of HCl to CO integrated absorption coefficients. The ratio of gas phase integrated absorption coefficients for HCl to CO is 0.57 ± .02[41,42] so from Eq. (40) the ratio $|\mu_s/\mu_g|^2$ is unity within 10% for HCl. The gas phase radiative lifetimes for HCl v=1 and v=2 are 20.5 and 15 ms,[43] so from Eq. (39) with n = 1.27, the radiative lifetimes for HCl v=1 and v=2 in solid Ar should be 16 and 8.1 ms. DCl should behave similarly. Its gas phase lifetimes are 95 and 52 ms for v=1 and v=2,[44] so its radiative lifetimes in solid Ar should be 51 and 28 ms. Care was taken in the above experiments to exclude the presence of HCl dimers which, as discussed below, have an absorption coefficient greater than that of the monomer.

Verstegen et al.[45] measured the absolute absorption coefficient of HCl in solid Ar by counting interference fringes and found the value to be about four times greater in the matrix than in the gas phase. All of their spectra shown[45] contain significant polymer, which if weighted equally to monomer would increase the absorption coefficient reported. They also concluded that the ratio of monomer and polymer absorption coefficients was unity. The exact cause of the discrepancy between their results and the present results is unclear. Nevertheless, we find the HCl/CO/Ar results compelling evidence that the transition moment of HCl is essentially the same in gas and matrix.

2. Monomer vs Polymer Absorption

A casual glance at Figure 3 will convince the reader that the HCl absorption coefficient is enhanced in a polymeric environment, since the diffusion process does not change the total number of molecules of HCl. Relative dimer/monomer concentrations can of course be ascertained by measuring the relative dimer and monomer absorption intensities. For a quantitative estimate of dimer concentration, it is necessary to know the dimer transition moment. Quantitative estimation of the dimer transition moment can be obtained in principle by performing a gentle diffusion of a dilute sample, with the goal of producing only dimeric polymer, and relating the measured integrated absorption of monomer and dimer after diffusion to that of the monomer before diffusion (requiring that the total number of HCl molecules is conserved). In practice, at least three polymer peaks (dimer, trimer, and high polymer at 2748 cm^{-1}) are produced after the gentlest diffusion. There need be no relationship between the transition moments per HCl molecule in monomer, dimer, trimer, or high polymer, so two spectra of the matrix under different aggregation conditions is not enough to determine transition moments of dimer, trimer, and high polymer.

In order to estimate the polymer transition moment, it was assumed that the transition moment per HCl molecule is the same in all polymers (dimer, trimer, etc.) and different from the monomeric transition moment. Two samples in which only three well resolved polymeric peaks formed subsequent to diffusion were studied. The results were an increase of the squared transition moment per HCl molecule by a factor of 2.6 ± .5 for a sample of M/A = 5100, and 4.1 ± .7 for a sample of M/A = 980. An overall average ratio is 3±1. For personal historical reasons, a value

of 2.4 has been used in these experiments in calculating dimer concentrations from absorption spectra. The large uncertainty in the ratio of transition moments introduces a systematic error into values used for dimer concentrations, but does not affect any qualitative conclusions. The present results can be compared to Verstegen et al.[45] who report that monomer and polymer transition moments per molecule are equal. The present measurements and Figure 3 are in discord with their result.

3. Quantitative Effects of Deposition Conditions

The majority of the matrices have been prepared with pulsed deposition. Pulsed deposition has been reported to result in greater isolation of the guest species than the conventional steady spray-on technique[46,47] under otherwise similar deposition conditions. This result is entirely consistent with the present experiments. Matrices of HCl/Ar of M/A = 1000 prepared by pulsed deposition at 20 K at an average rate of 6 m-mole/hour contain about 2% dimer. Spectra shown by Barnes et al.[7] for HCl/Ar, M/A = 1000, deposited at 20 K at 6-10 m-mole/hour by a steady spray-on technique show a dimer peak larger than the P(1) peak at 20 K as well as a trimer peak; this can be estimated to mean about 20% dimer in their sample. Presumably the difference in dimer (and trimer) concentrations reflects the different deposition techniques.

A study was performed to see the effect of deposition conditions on degree of isolation for HCl/Ar, at an M/A near 500. The results are given in Table X. The following points can be observed: 1) Isolation decreases when the deposition temperature is increased from 9 K to about 20 K; 2) The larger the mass of gas in the pulsing volume, the more polymer is formed; 3) Otherwise, deposition rate does not matter much:

Table III-X. Effect of Deposition Conditions on Polymer Formation

M/A	μ-mole HCl	T_{dep} (K)	Rate[a] (m-mole/hr)	Pulses/min	P_{pulse} (torr)	$\frac{A_{dimer}}{A_{P(1)}}$[b]	$\frac{A_{trimer}}{A_{P(1)}}$[b]
515 ± 5	56	17-18	7.0	2	54-79	1.4	.48
515 ± 5	27	9	7.0	2	60-80	.78	0
514 ± 5	. 31	9	16.0	2	142-164	1.6	0
514 ± 5	27	9	14.0	4	60-80	.69	0
527 ± 5	28	9	6.2	4	25-36	.58	0
527 ± 5	21	9	24.0	4	106-130	1.3	0
527 ± 5	27	21	28.0	4	125-145	2.1	.64

[a] Rate is for total matrix.

[b] Ratio of integrated absorptions.

there is no difference between 2 and 4 pulses/minute for a given pulse pressure. The effect of deposition temperature on polymer formation is much greater than the effect of pulse pressure. The most typical deposition conditions were rapid deposition at low temperature: 4 pulses/min, 80-100 torr pulse pressure, and 9 K deposition temperature. These conditions were chosen to minimize polymer formation and allow complete deposition within a reasonable time.

CHAPTER III

REFERENCES

1. H. E. Hallam, in Vibrational Spectroscopy of Trapped Species, Wiley, New York (1973), Chapter 3 and references therein.

2. A. J. Barnes in Vibrational Spectroscopy of Trapped Species, Wiley, New York (1973), Chapter 4 and references therein.

3. H. Friedmann and S. Kimel, J. Chem. Phys., 44, 4359 (1966).

4. A. J. Barnes, J. B. Davies, H. E. Hallam, G. F. Scrimshaw, G. C. Hayward, and R. C. Milward, Chem. Comm. 1089 (1969).

5. W. G. VonHolle and D. W. Robinson, J. Chem. Phys., 53, 3768 (1970).

6. B. Katz, A. Ron, and O. Schnepp, J. Chem. Phys., 46, 1926 (1967).

7. A. J. Barnes, H. E. Hallam, and G. F. Scrimshaw, Trans. Faraday Soc., 65, 3150 (1969).

8. B. Katz, A. Ron, and O. Schnepp, J. Chem. Phys., 47, 5303 (1967).

9. R. L. Redington and D. E. Milligan, J. Chem. Phys., 37, 2162 (1962).

10. B. S. Ault and G. C. Pimentel, J. Phys. Chem., 77, 57 (1973).

11. M. T. Bowers and W. H. Flygare, J. Chem. Phys., 44, 1389 (1966).

12. D. E. Mann, M. Acquista, and D. White, J. Chem. Phys., 44, 3453 (1966).

13. A. J. Barnes, H. E. Hallam, and G. F. Scrimshaw, Trans. Faraday Soc., 65, 3172 (1969).

14. J. B. Davies and H. E. Hallam, Trans. Faraday Soc., 67, 3176 (1971).

15. A. J. Barnes, H. E. Hallam, and G. F. Scrimshaw, Trans. Faraday Soc., 65, 3159 (1969).

16. H. E. Hallam in Vibrational Spectroscopy of Trapped Species, Wiley, New York (1973), Chapter 2.

17. H. Dubost and R. Charneau, Chem. Phys., 12, 407 (1976).

18. S. R. J. Brueck, T. F. Deutsch, and R. M. Osgood, Chem. Phys. Lett., 51, 339 (1977).

19. A. F. Devonshire, Proc. Royal Soc. (London), A153, 601 (1936).

20. W. H. Flygare, J. Chem. Phys., 39, 2263 (1963).

21. H. Friedmann and S. Kimel, J. Chem. Phys., 41, 2552 (1964).

22. H. Friedmann and S. Kimel, J. Chem. Phys., 43, 3925 (1965); FKI.

23. H. Friedmann and S. Kimel, J. Chem. Phys., 47, 3589 (1967); FKII.

24. A. Messiah, Quantum Mechanics, Wiley, New York (1958), Chapter XII.

25. G. Herzberg, Spectra of Diatomic Molecules, Van Nostrand, Princeton (1950).

26. P. D. Mannheim and H. Friedmann, Phys. Stat. Sol. 39, 409 (1970); MF.

27. A. M. Dunker and R. G. Gordon, J. Chem. Phys., 64, 354 (1976).

28. S. L. Holmgren, M. Waldman, and W. Klemperer, J. Chem. Phys. (to be published).

29. A. S. Barker and A. J. Sievers, Rev. Modern Phys., 47, Suppl. 2 (1975).

30. P. D. Mannheim, J. Chem. Phys., 56, 1006 (1972).

31. D. N. Batchelder, M. F. Collins, B. C. G. Hayward, and G. R. Sidey, J. Phys. C., Solid State Phys., 3, 249 (1970).

32. G. K. Pandey, J. Chem. Phys. 49, 1555 (1968).

33. D. H. Rank, D. P. Eastman, B. S. Rao, and T. A. Wiggins, J. Opt. Soc. Am., 52, 1 (1962).

34. E. K. Plyler and E. D. Tidwell, Z. Electrochem., 64, 717 (1960).

35. T. F. Deutsch, IEEE J. Quant. Elect., QE-3, 419 (1967).

36. The position of J=2 is, spectroscopically, 26 cm^{-1} above J=1. Since it is severely broadened, $\bar{n}_2\Gamma(2)$ in Eq. (27) should contain an integral over this distribution. Since $\Gamma(J)$ is weighted by ω_J^3, a value of 27 cm^{-1} instead of 26 cm^{-1} is used in the present calculation. The calculated R(0) linewidths is very sensitive to ω_2. For ω_2 = 33 cm^{-1}, $\Gamma(0)$ = 0.5 and $\Gamma(20)$ = 2.5 cm^{-1}.

37. W. Gordy, W. V. Smith, and R. F. Trambarulo, Microwave Spectroscopy, Dover, New York (1966), p. 201.

38. F. Legay in Chemical and Biochemical Applications of Lasers, Vol. II, ed. by C. B. Moore, Academic Press, New York (1977), Chapter 2.

39. A. McClellan, Tables of Experimental Dipole Moments, Freeman, San Francisco (1963).

40. G. J. Jiang, W. B. Person, and K. G. Brown, J. Chem. Phys., 62, 1201 (1975).

41. R. A. Toth, R. H. Hunt, and E. K. Plyler, J. Mol. Spect., 32, 85 (1969).

42. R. A. Toth, R. H. Hunt, and E. K. Plyler, J. Mol Spect., 35, 110 (1970).

43. J. K. Cashion and J. C. Polanyi, Proc. Roy. Soc. (London), A258, 529 (1960).

44. F. G. Smith, J. Quant. Spect. Rad. Transfer, 13, 717 (1973).

45. J. M. P. J. Verstegen, H. Goldring, S. Kimel, and B. Katz, J. Chem. Phys., 44, 3216 (1966).

46. R. N. Perutz and J. J. Turner, J. Chem. Soc. Faraday Trans. II, 69, 452 (1973).

47. L. J. Allamandola, Thesis, University of California, Berkeley (1974).

CHAPTER IV

KINETICS

In this chapter various models for the kinetic behavior of a system of molecules, some of which have been vibrationally excited by a pulsed excitation source will be discussed. The kinetic models discussed here will be a basis for understanding the kinetic results of Chapter V. Some of the results presented here have been referred to in Chapter III.

The decay kinetics for a system of non-interacting guests is presented in Section A. In Section B, the effects of guest-guest communication are discussed. In particular, resonant energy transfer leads to energy diffusion; non-resonant energy transfer contributes a new deactivation channel. The decay kinetics of a system interacting via long-ranged multipolar forces depends on the relative contributions of resonant and non-resonant transfer processes--it can lead to non-exponential behavior following pulsed excitation. Some practical aspects of analyzing experimental kinetic results are discussed in Section C. Particular questions asked are: How non-exponential must decay before it can be observably non-exponential for a real, experimental decay curve? How much error does the "baseline droop" discussed in Chapter II contribute to measured decay times? How well can a signal which is the sum of two exponentials of nearly equal decay constant be analyzed?

In all kinetic models, it is assumed that rotational thermalization is very rapid on the time scale of vibrational relaxation, so rate expressions will deal only with vibrational levels. This is experimentally justifiable and will be discussed in Chapter V.

A. Kinetics of Isolated Molecules

When guest molecules are present in low concentration, they interact only with the crystal lattice and the radiation field. Hence, vibrational relaxation is due to the "unimolecular" processes of radiative decay or non-radiative V→R,P processes. Subsequent to excitation of N molecules to v=2 by a delta function pulse at t=0, the populations of v=2, $n_2(t)$, and v=1, $n_1(t)$, will evolve according to

$$n_2(t) = N \exp(-k_{21}t) \tag{1}$$

$$n_1(t) = \frac{Nk_{21}}{(k_{21}-k_{10})}\left[e^{-k_{10}t} - e^{-k_{21}t}\right] \tag{2}$$

where k_{21} and k_{10} are the rate of deactivation of v=2 to v=1 and v=1 to v=0, respectively, and direct deactivation of v=2 to v=0 is neglected. When v=1 is excited initially, the time dependence of v=1 is

$$n_1(t) = N \exp(-k_{10}t). \tag{3}$$

In the above model, relaxation is due to loss of vibrational quanta from the HCl system by one quantum processes only.

B. Kinetics of Interacting Guests

When the guest concentration increases sufficiently, guests may interact with each other by exchanging vibrational quanta. If such processes are resonant, no new loss mechanisms are introduced, and although the energy migrates about the sample, the kinetics of the ensemble is still described by Eqs. (1)-(3). When a second guest species is present so that energy may be transferred to it, a V→V decay channel arises and Eqs. (1)-(3) must be modified. The initially excited species will be

referred to as the donor (D) and the second guest species as the acceptor, (A). The acceptor may be chemically the same as D, but in a different state so that V→V transfer is non-resonant (for example: v=2 + v=0 → 2v=1 for anharmonic molecules is non-resonant; v=2 is D and v=0 is A). In some cases non-resonant V→V transfer may lead to non-exponential decay kinetics.

The microscopic rate law for energy transfer between D and A by a multipolar interaction will be considered in Section 1. The behavior of an ensemble of donors and acceptors will be considered in Section 2 and kinetic expressions for the time evolution of the donor population for several cases will be given. In Section 3 a general formulation of the donor decay kinetics will be used and the temporal behavior of the acceptor population will be described. The behavior for a special case will be considered.

1. Multipolar Interactions

The theory of energy transfer by multipolar interaction was developed by Förster[1] for the case of dipole-dipole coupling and extended by Dexter[2] to include higher multipolar interactions. From first order perturbation theory, the rate of resonant transfer from D to A is

$$W = \frac{2\pi}{\hbar} \left|\langle D_1 A_0 | V | D_0 A_1 \rangle\right|^2 \rho(E) \tag{4}$$

where D_1 and A_1 are excited states, D_0 and A_0 are unexcited states, and $E = E_{D_1} - E_{D_0} = E_{A_1} - E_{A_0}$ is the energy exchanged. For dipole-dipole coupling

$$V = \frac{1}{n^2 R^3} \left[\underline{\mu}_D \cdot \underline{\mu}_A - 3(\underline{\mu}_D \cdot \underline{R})(\underline{\mu}_A \cdot \underline{R})/R^2\right] \tag{5}$$

where n is the refractive index of the host medium, $\underset{\sim}{\mu}$ are dipole transition operators, and $\underset{\sim}{R}$ is the position vector of A relative to D. Substituting Eq. (5) into (4) and averaging over orientations yields

$$W = \frac{4\pi}{3\hbar}\frac{1}{n^4 R^6}\,|\langle D_1|\mu_D|D_0\rangle|^2\,|\langle A_1|\mu_A|A_0\rangle|^2\,\rho(E) \tag{6}$$

The density of states is given by the overlap in energy space of the normalized lineshape functions for the transitions of D and A:

$$\rho(E) = \int f_D(E) f_A(E)\,dE \tag{7}$$

The transition moments appearing in Eq. (6) can be related to the integrated absorption coefficient or either Einstein coefficient. In particular, in terms of the A coefficient:[2] $\mu^2 = (3\hbar^4 c^3/4E^3)A$, and $A = 1/\tau$ where τ is the radiative lifetime, so

$$W = \frac{3\pi\hbar^7 c^6}{4n^4 R^6}\,\frac{1}{\tau_D}\,\frac{1}{\tau_A}\int \frac{f_D(E) f_A(E)}{E^6}\,dE\ . \tag{8}$$

In this formula, τ is the radiative lifetime in the gas phase, and it is assumed that dipole transition moment and transition frequency are not changed by the host medium. E has been taken inside the integral in Eq. (8), which is the correct result for transitions with finite widths.[2] However, for vibrational transitions in which widths are much smaller than the transition energies, E is effectively constant over the transition linewidth, and can be placed in front of the integral. Measuring frequencies in cm^{-1}, ν, the transition rate is[3,4]

$$W = C/R^6 \tag{9}$$

$$C = \frac{3}{512\pi^6 c n^4 \nu^6}\,\frac{1}{\tau_D}\,\frac{1}{\tau_A}\int f_D(\nu) f_A(\nu)\,d\nu. \tag{10}$$

For Lorentzian lineshapes of FWHM $\Delta\nu$, the overlap integral can be calculated by contour integration to give

$$\int f_D(\nu) f_A(\nu) d\nu = \frac{1}{2\pi} \frac{(\Delta\nu_A + \Delta\nu_D)}{(\nu_o^A - \nu_o^D)^2 + \frac{1}{4}(\Delta\nu_A + \Delta\nu_D)^2} \tag{11}$$

where ν_o is the central frequency of the transition. For resonant transitions where $\Delta\nu_A = \Delta\nu_D = \Delta\nu$ and $\nu_o^A = \nu_o^D$, the overlap integral is

$$\int f_D(\nu) f_D(\nu) d\nu = \frac{1}{\pi\Delta\nu} \tag{12}$$

In general for multipolar interactions, $W = C_s/R^s$, where s = 6,8,10 . . . for dipole-dipole, dipole-quadrupole, quadrupole-quadrupole interactions, etc. The perturbation treatment for s=8 and 10 has been presented by Dexter.[2]

2. Ensemble Averaging for Donor Population

Resonant energy transfer between like molecules leads to energy diffusion. Legay calculates the diffusion constant, D, for a multipolar interaction of order s as

$$D = \frac{C_{DD}}{6} \sum_i \frac{1}{R_i^{s-2}}$$

where R_i is the position of a guest relative to a particular guest at a position arbitrarily labeled site 0, and C_{DD} is evaluated from Eq. (10) with D=A. For a random distribution of guests,

$$D = \frac{xC_{DD}}{6} \sum_i \frac{1}{L_i^{s-2}}$$

where the sum is over all lattice sites of the crystal, L_i is the distance

from site 0 to the i^{th} site, and x is the mole fraction of the guest. For fcc lattices and dipole-dipole coupling, this has the value[3]

$$D = 25.3 \frac{xC_{DD}}{6d_o^4} \tag{13}$$

where d_o is the nearest neighbor distance in the crystal.

Energy diffusion can be viewed as a resonant hopping of excitation from one guest molecule to another in a random walk fashion. A more intuitive quantity than D is the number of hops made by the excitation during a length of time, t. This is given by $N = t\langle W\rangle$, where $\langle W\rangle$ is the average rate of transfer from a given molecule. For dipole-dipole interactions

$$N = tC_{DD} \sum_i \frac{1}{R_i^6}$$

$$= \frac{14.45xC_{DD}t}{d_o^6} \tag{14}$$

where the result is valid for fcc or hcp lattices and the sum has been evaluated by Legay.[3]

When an accepting species different from the donor is present, V→V transfer from donor to acceptor becomes possible and a new energy loss mechanism for the donor system exists. Legay[3] and Weber[5] have reviewed the decay kinetics of an ensemble of donors excited at t=0 when long-range multipolar transfer and diffusion-aided transfer to acceptors can compete. The results are valid for acceptor species with a large intrinsic (V→R,P) decay rate and present in low concentration. These conditions prevent acceptor sites from becoming saturated and unable to accept energy. Weber distinguishes three cases: (A) long-range transfer

only--no diffusion, (B) fast diffusion, and (C) diffusion limited relaxation. They are reviewed below.

A) Long-range transfer: Since the interactions are very dependent on distance, the decay rate of a donor will depend very much on the distribution of acceptors relative to that donor. The donor system may be divided into classes[6] which have similar acceptor distributions.[6] Each class decays exponentially. The observable signal is the sum of the different exponential decays arising from each class, and is non-exponential. For the multipolar interaction $W = CR^{-s}$, the time evolution of the donor population is[5]

$$n_D(t) = n_D(0)\ \exp[-k_o^D t - \frac{4\pi}{3}\,\Gamma(1-\frac{3}{s})\,x_A\rho(C_{DA}t)^{3/s}] \qquad (15)$$

where k_o^D is the unimolecular V→R,P decay rate of the donor, x_A is the acceptor mole fraction, ρ is the density of lattice sites, and Γ is the gamma function. The donor decay rate, which is $(1/n_D)(dn_D/dt)$ decreases as a function of time. This is physically reasonable. At early times those excited donors with a distribution of acceptors in close positions will decay rapidly by V→V processes, while those with no near acceptors will decay by slower V→R,P processes. At later times, only donors distant form acceptors will remain excited, and these will decay with rate k_o^D.

B) Fast diffusion: When the excitation rapidly moves among donor sites throughout the sample, all donor sites become equivalent. The donor decay rate is

$$k = k_o^D + \sum_i \frac{C_{DA}}{R_i^s} = k_o^D + x_A C_{DA} \sum_i \frac{1}{L_i^s}$$

For s=6 and fcc or hcp lattices:[3]

$$n_D(t) = n_D(0)\ e^{-kt}$$

$$k = k_o^D + \frac{14.45 x_A C_{DA}}{d_o^6} \qquad (16)$$

C) In the intermediate case, diffusion in the donor system can allow energy absorbed at a donor site distant from any acceptor to migrate to a site near an acceptor, and hence will increase the total V→V rate over that of case (A). The donor population decays with an initial non-exponential portion followed by an exponential phase, with decay constant given, for dipole-dipole interactions, by[7]

$$k = k_o^D + (0.6759)(4\pi) x_A \rho\ C_{DA}^{1/4}\ D^{3/4} \qquad (17)$$

The exponential phase dominates for times

$$t > \left[\frac{\frac{4}{3}\pi x_A \rho \sqrt{\pi C_{DA}}}{(k_o^D + .6759(4\pi) x_A \rho C_{DA}^{1/4} D^{3/4})} \right]^2$$

This has been generalized to higher order multipolar interactions.[3] An approximate expression valid for the temporal behavior of the donor population and extending to shorter times has recently been formulated by Gösele, et al.,[8] by means of a Padé approximate:

$$n_D(t) = n_D(0)\ \exp[-k_o^D t - \frac{4}{3}\pi x_A \rho (\pi C_{DA} t)^{1/2}\ B] \qquad (18)$$

$$B = [(1+5.47y+4.00y^2)/(1+3.34y^{3/4} \qquad (19)$$

where $y = DC_{DA}^{-1/3} t^{2/3}$. For large t, Eqs. (18) and (19) reduce to (17).

The case of intermediate diffusion is somewhat problematical. As D→0, the above equations reduce to those of case (A), as they should.

However, when D becomes very large, the equations do not reduce to the fast diffusion rate, Eq. (16). There is no good criterion to distinguish between the fast diffusion and intermediate diffusion cases.

Gösele and co-workers,[8,9] have generalized the problem somewhat. They include an encounter distance, r_{AD}, which corresponds to a separation between donor and acceptor at which energy transfer is instantaneous. In solutions, this corresponds to a hard sphere diameter. In rigid media, r_{AD} may reflect a very high order multipolar or exchange type interaction, which is very short-ranged. A parameter, z_o, where

$$z_o = \frac{1}{2r_{AD}^2}\left(\frac{C}{D}\right)^{1/2} \tag{20}$$

is useful in separating two regions. For $z_o>1$, diffusion-aided transfer is dominated by long-ranged dipole-dipole interactions and Eqs. (17)-(19) are valid. For $z_o<1$, energy transfer is dominated by close encounter and standard liquid phase diffusion kinetics[10] are applicable. In both cases the donor population evolves as

$$n_D(t) = n_D(0)\ \exp\left[-(k_o^D + a + 2bt^{-1/2})t\right] \tag{21}$$

where, for $z_o>1$: $a = (.676)(4\pi)x_A\rho C_{DA}^{1/4} D^{3/4}$

$$b = \frac{2}{3}\pi x_A \rho\sqrt{\pi C_{DA}}$$

and for $z_o<1$: $a = 4\pi D r_{AD} x_A \rho$

$$b = 2\pi x_A \rho r_{AD}^2 \sqrt{D/\pi}$$

Gösele et al.[9] have discussed the region of overlap near $z_o=1$. In neither case will Eq. (21) reduce to Eq. (16). Equation (21) is a general form for intermediate and slow diffusion-aided energy transfer by dipole-dipole coupling.

The donor system will exhibit non-exponential decay only for times such that $2bt^{-\frac{1}{2}} > k_o^D + a$. If the long-range dipole coupling constant is small so that b is small, diffusion will be important and the donor system decays exponentially. For the case where $z_o < 1$, the non-exponential portion of Eq. (21) will occur for times less than $r_{AD}^2/4\pi D$. For large diffusion or small encountere distance, non-exponential decay will be unobservable.

3. General Formulation and Example

The kinetic behavior of the acceptor population can be calculated from the kinetic behavior of the donor population. The non-exponential decay of the donor population can be considered to result from a time dependent donor decay constant, k_{ET}. The kinetic equations for the donor and acceptor populations are

$$\frac{dn_D(t)}{dt} = - k_o^D n_D - k_{ET}(t)\, n_D \tag{22}$$

$$\frac{dn_A(t)}{dt} = k_{ET}(t)\, n_D - k_o^A n_A \tag{23}$$

where, from Eq. (21), $k_{ET}(t) = a + bt^{-\frac{1}{2}}$. Equation (23) is solved in Appendix B. The result is

$$n_A(t) = \frac{2n_D(0)}{p} \exp(-k_o^A t - b^2/p^2)$$

$$\times \{\frac{a}{2p} [e^{-(b/p)^2} - e^{-(p\sqrt{t}+b/p)^2}]$$

$$+ (b - \frac{ab}{p^2}) \sqrt{\frac{\pi}{2}} [\mathrm{erf}(p\sqrt{t} + \frac{b}{p}) - \mathrm{erf}\ (\frac{b}{p})]\} \tag{24}$$

$$p^2 = (k_o^D - k_o^A + a)$$

where erf is the error function.

In the limit where b is small, the decay of the donor population, Eq (21), becomes exponential, and the behavior of the acceptor system becomes the sum of rising and falling exponentials, analogous to Eq. (2). The rise if given by $(k_o^D + a)$ and fall by k_o^A.

We consider an example, the results of which will be useful to bear in mind when considering the relaxation behavior of HCl (v=1) in Ar.

Example: In this case, v=1 is populated by V→R,P decay of v=2, and depopulated by a combination of V→R,P decay to v=0 and diffusion-aided V→V transfer to an acceptor species, A. The kinetic scheme is

$$HCl(v=2) \xrightarrow{k_{21}} HCl(v=1) \tag{25a}$$

$$HCl(v=1) \xrightarrow{k_{10}} HCl(v=0) \tag{25b}$$

$$HCl(v=1) + A \xrightarrow{k_{ET}} HCl(v=0) + A^{\dagger} \tag{25c}$$

The differential equation for the population of v=1 is

$$\frac{dn_1}{dt} = k_{21}n_2 - k_{10}n_1 - (a + bt^{-1/2})\, n_1 \tag{26}$$

The solution to Eq. (26) is given in Appendix B. The result is

$$n_1(t) = \frac{k_{21}N_o}{q} e^{-(k_{10}+a)t}\, e^{-2b\sqrt{t}}\, e^{-2b^2/q} \{1 - \exp[-qt+2b\sqrt{t}] + b\sqrt{\frac{\pi}{q}} [\mathrm{erf}(\sqrt{qt} - \frac{b}{\sqrt{q}}) + \mathrm{erf}\ (\frac{b}{\sqrt{q}})]\} \tag{27}$$

where

$$q = k_{21} - k_{10} - a.$$

In the limit that b = 0, Eq. (27) reduces to the sum of rising and falling exponentials, with rise k_{21} and fall (k_{10} + a). The values for a and b are discussed after Eq. (21).

In this section we have discussed a general kinetic form which arises in a system in which diffusion and long-ranged energy transfer by dipole-dipole coupling occur. Diffusion is accounted for by a and non-exponential behavior of the populations is due to b. Exact solutions with several competing processes, such as Eq. (27), are very messy and are difficult to apply to analysis of experimental data.

C. Practical Considerations

1. Exponential vs Non-Exponential Decay

Non-exponential decay in the donor system, Eq. (21), manifests itself as a rapid initial decrease in fluorescence intensity. It is not obvious, from Eqs. (24) or (27), how b manifests itself when V→V transfer is convoluted with more than one exponential decay; nor is it obvious how large it must be to be observable in the decay trace. To investigate this, Eq. (27) was evaluated as a function of t for various values of a and b. The numbers used for k_{21} and k_{10} were 3.8×10^3 and 0.8×10^3 sec^{-1}, which are the V→R,P rates for HCl/Ar at 9 K (see Chapter V). a was varied between 0 and 2.9×10^4 sec^{-1}, and b was 3.5×10^{-4}, 0.1, or 10 $sec^{-\frac{1}{2}}$. Decay curves were analyzed as a double exponential, such as Eq. (2) by hand, and derived rate constants were compared to input rate constants; the two decay rates were k_{21} and k_{10} + a. In no case did the logarithmic plot of the decay curve look non-exponential. For b = 3.5×10^{-4} and 0.1, the derived rate constants

were close (within plotting error) to the input rates. For b = 10 and a = 0, the value of the rising exponential was increased from an input value of 3.8×10^3 to an analyzed value of 4.7×10^3--an increase of 25%. For a larger the effect of b = 10 was overcome and input and derived rate constants were equal. Thus, the conditions under which the acceptor decay may appear non-exponential are large b and small $(k_{10} + a)$.

For $z_o > 1$, b is related to the multipolar interaction constant, C_{DA}. A value of b = 10 $sec^{-\frac{1}{2}}$ corresponds to $x_A \sqrt{C_{DA}} = 1.0 \times 10^{-22}$ cm^3 $sec^{-\frac{1}{2}}$ where $\rho = 2.67 \times 10^{22}$ cm^{-3} has been used. For $x_A = 10^{-3}$, this corresponds to $C_{DA} = 1.0 \times 10^{-38}$ cm^6/sec. Now, using Eqs. (10) and (11) and the data from Appendix C, the HCl-HCl coupling coefficient for R(0) and P(1) transitions is calculated to be 4.6×10^{-35}. Coupling of HCl to any other species would be expected to be weaker since the overlap of Eq. (11) for a thermally accessible HCl transition with possible acceptor transitions is small (see Section V.B). $C_{DA} = 10^{-38}$ cm^6/sec may be a reasonable value for some acceptor, and derived rate constants may be affected by non-exponential decay if the acceptor is present at $x_A = 10^{-3}$. For samples containing only HCl/Ar, however, the most concentrated acceptors should be HCl polymers, and the most concentrated of these, the dimer, may be present at $x_A \sim 10^{-5}$ for M/A = 1000. For observably non-exponential decays, then, the HCl monomer-dimer coupling constant, would have to be $\sim 10^{-36}$ cm^6/sec, almost as large as the HCl-HCl coupling constant. Due to the non-resonance of HCl monomer and dimer transitions, such a large coupling constant is unlikely.

The overall conclusion, then, is that for HCl/Ar the v=1 decay will not be observably affected by the non-exponential factor $b\sqrt{t}$, unless the acceptor is present at large ($x_A > 10^{-3}$) concentrations.

2. Validity of Derived Rate Constants

Two problems arising in the analysis of decay curves are discussed here: (A) The actual decay trace may be modified by the low frequency response of the signal processing electronics (see Section II.D.6). How does this affect derived decay constants? (B) The signal from v=1 is a rising and falling exponential when v=2 is initially excited. How well can the two rate constants be deduced from the fluorescence decay curve?

(A) For an exponential pulse with decay constant k passing through a high pass filter with cut-off frequency ω_o, the observed signal is, from Eq. (II-9):

$$S = \frac{S_o}{k-\omega_o} (ke^{-kt} - \omega_o e^{-\omega_o t}). \tag{28}$$

As described in Section II.D.6, this produces baseline undershoot. The minimum value of the signal (the point of maximum undershoot) is

$$S_{min} = \frac{S_o}{k} \left(\frac{\omega_o}{k}\right)^{2\omega_o/k} \left[\left(\frac{\omega_o}{k}\right)^2 - \left(\frac{\omega_o}{k}\right)^{2\omega_o^2/k^2}\right]. \tag{29}$$

The best way to extract the true rate constant, k, from Eq. (28) is to use a baseline corresponding to $-(S_o\omega_o/(k-\omega_o))\, e^{-\omega_o t}$. This is a difficult procedure. Two other methods of analysis are: (1) Take the "true", $t\to\infty$ baseline, or (2) Draw a horizontal baseline from the minimum of the signal, as given by Eq. (29). The apparent rate constant can be defined as

$$k_{app} = -\frac{1}{t} \ln \frac{S(t)}{S(0)}. \tag{30}$$

Calculated values of k_{app} have been obtained for $k = 1 \times 10^3$ sec^{-1} with a variety of ω_o for both methods of analysis. The results are given in Table I. The following points should be noted: For $k/\omega_o > 100$, the error in either approximation is 1% or less. Method (2) produces smaller errors.

Errors are appreciable, when $k/\omega_o < 10$. In experiments described in this thesis, ω_o was adjusted so that for decay experiments $k/\omega_o > 50$, and method (2) was used for analysis.

(B) It is sometimes quite difficult to extract two correct rate constants from a decay curve corresponding to Eq. (2) when the two decay constants, k_{10} and k_{21}, are nearly equal. The effect is particularly pronounced when the rate constants are within a factor of two. Under such conditions it takes about three decades for the decaying signal to become truly exponential and free of influence from the fast rise. Most experiments have signal-to-noise allowing use of at most two decades of data. The apparent slow decay is, after two decades, decreasing more slowly than the true decay, and the derived rise is faster than the true rise.

To be more quantitative, a decay curve such as Eq. (2) was evaluated numerically as a function of t for $k_{21} = 3.8 \times 10^3$ sec^{-1}, and $k_{10} = 3.0 \times 10^3$, 4.0×10^3, and 1.0×10^4 sec^{-1}, and plotted on semi-logarithmic paper. Rate constants were derived using only one and a half decades of the curve. The derived rate constants are listed in Table II. For k_{21} and k_{10} close, the error in rise and decay rates can be 50%.

If one of the decay constants is known, the other can be derived from measuring the time at which the signal is maximized. This is given by

Table IV-I. Ratio of k_{app}/k_o for Various Amplifier Cut-off Frequencies ($k_o = 1 \times 10^3$ sec^{-1})

ω_o (sec^{-1})	k_{app}/k_o	
	Method 1	Method 2
500	2.05	2.05
100	1.18	1.07
10	1.01	1.005
1	1.002	.997

Table IV-II. Analysis of v=1 Signal with Nearly Equal Rise and Decay Rates

True Value			Observed Value		
k_{21} (10^3 sec^{-1})	k_{10} (10^3 sec^{-1})	t_{max} (μs)	k_{21} (10^3 sec^{-1})	k_{10} (10^3 sec^{-1})	t_{max} (μs)
3.8×10^3	3.0×10^3	295	5.3×10^3	2.7×10^3	295
3.8×10^3	4.0×10^3	256	3.1×10^3	5.9×10^3	256
3.8×10^3	1.0×10^4	156	3.7×10^3	1.1×10^4	156

$$t_{max} = \frac{1}{k_{21}-k_{10}} \ln\left(\frac{k_{21}}{k_{10}}\right). \qquad (31)$$

As can be seen in Table II, observed t_{max} and theoretical values are in good agreement.

The practical outcome of all this is as follows: For HCl and DCl, k_{21} can be measured as a single exponential upon excitation of v=2. For those traces in which k_{10} seems close to k_{21}, k_{10} is derived from the known value of k_{21} and the observed maximum value of the v=1 fluorescence signal.

CHAPTER IV

REFERENCES

1. Th. Förster, Ann. Physik, 2, 55 (1948).

2. D. L. Dexter, J. Chem. Phys., 21, 836 (1953).

3. F. Legay, Chemical and Biological Applications of Lasers, Vol. II, C. B. Moore, ed., Academic Press, New York (1977), Chapter 2.

4. Note that Eqs. (11), (12), and (14) of Ref. 3 should be corrected so that they contain a factor of n^4 when radiative lifetimes have their gas phase values.

5. M. J. Weber, Phys. Rev., B4, 2932 (1971).

6. K. B. Eisenthal and S. Siegel, J. Chem. Phys., 41, 652 (1964).

7. P. G. DeGennes, J. Phys. Chem. Solids, 7, 345 (1958).

8. U. Gösele, M. Hauser, U. K. A. Klein, and R. Frey, Chem. Phys. Lett., 34, 519 (1975).

9. U. K. A. Klein, R. Frey, M. Hauser, and U. Gösele, Chem. Phys. Lett., 41, 139 (1976).

10. M. von Smoluchowski, Z. Physik. Chem., 92, 192 (1917).

CHAPTER V

VIBRATIONAL RELAXATION STUDIES

The interaction between guest internal vibrational motion and the lattice has been studied by a laser-induced, time-resolved fluorescence technique. The magnitude of the observed relaxation rates, and their dependence on experimentally variable parameters such as temperature and concentration, are indicative of the major relaxation channels. Vibrational relaxation rates for HCl and DCl in several different matrices are presented in this Chapter. Most experiments were performed exciting a vibration-rotation transition of the first overtone band, and rates of $v=2 \rightarrow 1$ and $v=1 \rightarrow 0$ decay were deduced. Vibrational energy ultimately is dissipated into lattice phonons, but for HCl and DCl in Ar, relaxation proceeds by way of a highly rotationally excited guest. The initial V→R step is rate-limiting. In molecular matrices, HCl V→R,P relaxation is obscured by rapid V→V transfer to the host. In HCl/Ar, resonant V→V transfer leads to energy diffusion. Dimeric species present in concentrated samples act as energy traps.

Part A reports the experimental results of fluorescence decay experiments for HCl in Ar, N_2, and O_2 matrices, and DCl in Ar. The results are discussed in Part B. The importance of a V→R step in the relaxation mechanism is concluded. Temperature effects indicate the contributions of excited phonon and rotational states to relaxation. V→V transfer phenomena and the null results of fluorescence experiments for the HCl dimer in Ar and HCl in N_2 and O_2 are interpreted.

A. Results

1. HCl/Ar

Typical data and analyses for temporally resolved emission following direct excitation of HCl (v=2) in dilute samples are shown in Figs. 1 and 2. Figure 1 shows broadband emission; it is analyzed as a doubly decaying exponential to give k_{21} and k_{10} rates. Figure 2 distinguishes between v=2 → 1 and v=1 → 0 emission; that the rise of the v=1 → 0 fluorescence matches the decay of v=2 → 1 fluorescence is clear in both the signal and analysis. The fluorescence from v=2 decays as a single exponential over at least one and a half decades. Reciprocal lifetimes, k_{21} and k_{10}, obtained by fitting the data to Eqs. (IV-1) and (IV-2) are presented in Tables I-III. Table I contains relaxation data for isolated molecules. Tables II and III contain all v=1 → 0 relaxation data. Decay times for given experimental conditions were measured from spectrally resolved fluorescence and from the total fluorescence as in Figs. 1 and 2, so each decay rate is measured at least twice. The values listed are either the average of many measurements for equivalent conditions (the error indicated is the standard deviation of the set of measurements) or only one or two measurements (no error indicated). In the latter case an uncertainty of 15% is reasonable. In some experiments v=1 was excited directly. Values for k_{10} obtained in these experiments were consistent with k_{10} values deduced from the v=2 excitation experiments, and are included in Tables I-III. The observed decay rates are much faster than the radiative decay rates of 120 and 63 sec^{-1} calculated in Chapter III for HCl v=2 and v=1 in solid Ar. Hence, the radiative decay channel is not a major relaxation route and is neglected.

Figure V-1a. Broadband fluorescence decay signal from HCl/Ar, M/A = 10,000 ± 1000, 9 K. Excitation is at 5656 cm^{-1}, $R(0)^{35}$ v=0 → 2 transition, with 7 μJ/pulse energy. The trace is the averaged result of 6125 shots.

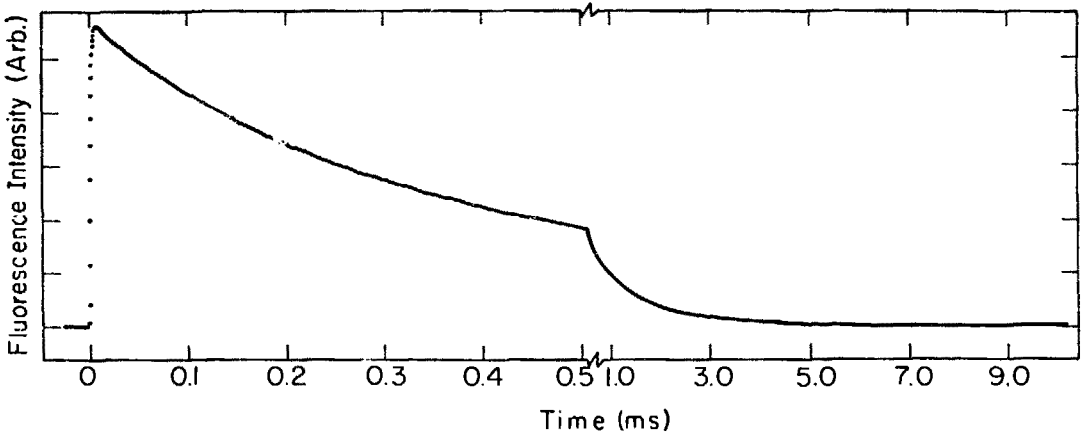

XBL 7710-10001

Figure V-1b. Analysis of broadband decay trace of Figure V-1a.

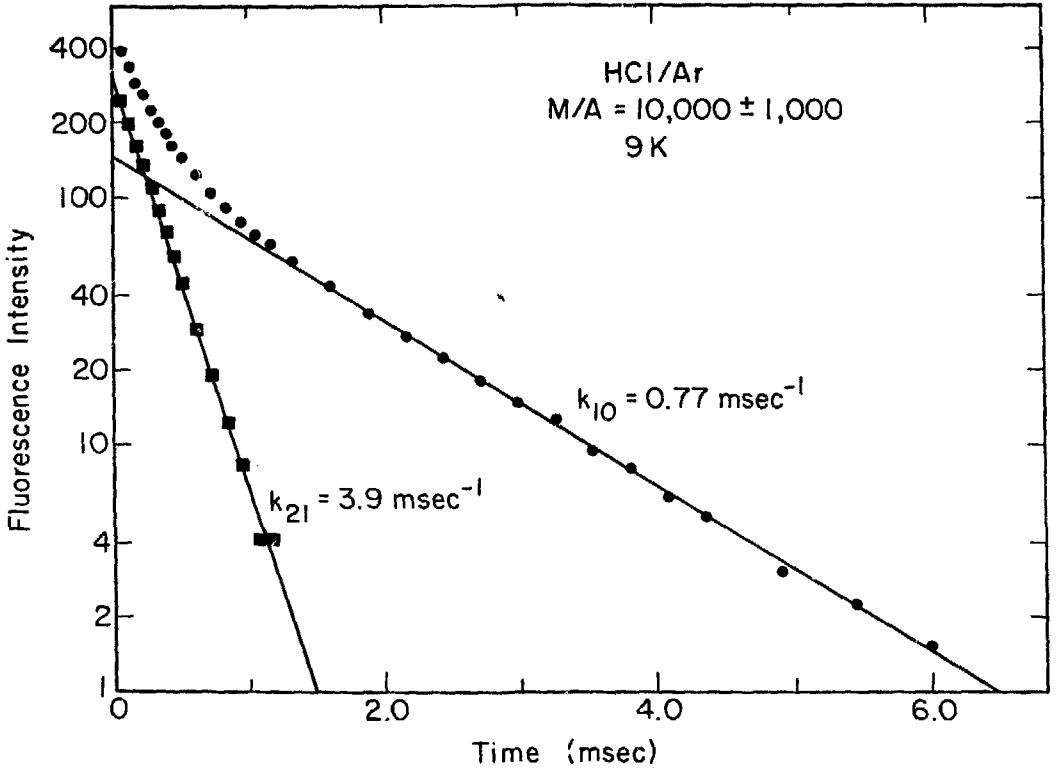

XBL 7710-6899

Figure V-2a. Spectrally resolved decay traces from HCl/Ar, M/A = 5100 ± 100, 18.2 ± 0.2 K. Excitation is at 5656 cm^{-1}, $v=0 \rightarrow 2$ $R(0)^{35}$ transition, with 8 μJ/pulse energy. Curve a is $v=2 \rightarrow 1$ fluorescence and is the averaged signal of 2048 shots. Curve b is the $v=0 \rightarrow 1$ fluorescence and is the averaged result of 4096 shots. The reduced S/N of curve b as compared to curve a is due to poor overlap of the spectrally resolving interference filter and the $v=1 \rightarrow 0$ emission band. The baseline undershoot of curve b is the result of pickup, rather than amplifier distortions.

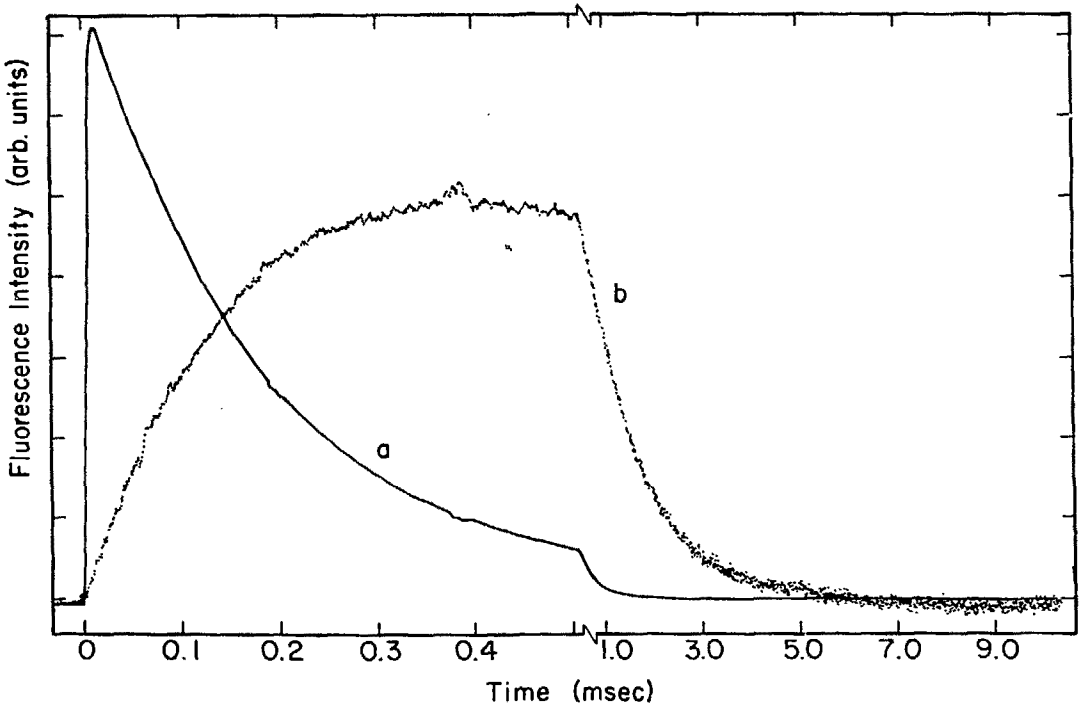

XBL 7710-10007

Figure V-2b. Analysis of spectrally resolved decay traces of Figure V-2a. Curve a (dark dots) is a single exponential. Curve b (open dots and squares) is the sum of a rising and falling exponential. k_{21} is deduced in each trace; the difference of 5% is smaller than typical for such analyses due to the good S/N of the traces, and reflects the difficulty of analyzing double exponentials. The vertical scale is logarithmic and spans two and a half decades.

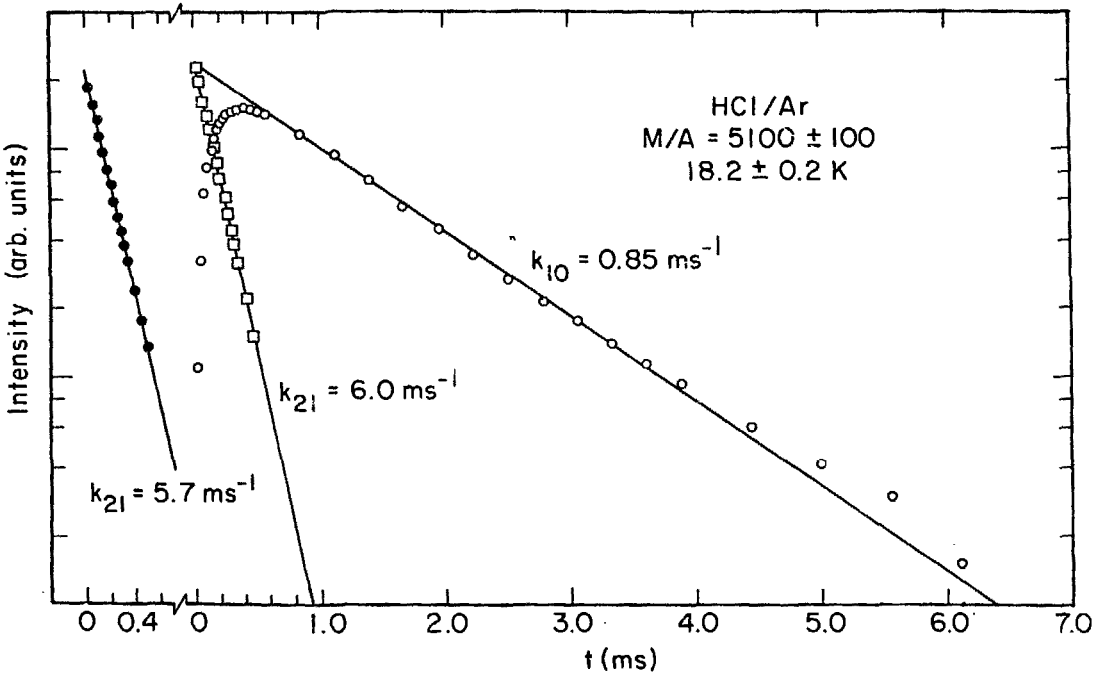

XBL 7711- 10362

Table V-I. Relaxation Rates for Isolated HCl/Ar (10^3 sec^{-1})

M/A	T(K ± 0.4)										
	9.1	12	13	14	15	16	17	18	19	20	21
v=2 → 1											
527±5	3.59±.07										5.6
670±20	3.7±.3									5.5±.2	
930±30[a]	3.6±.5					4.2				4.9	
960±20	4.2±.6						5.7±.7			6.3±.2	
980±30	3.8±.6	4.7			4.6			4.9		5.8	
990±20	4.9±.8[c]		5.9±.6			5.9±1.6				6.5±.3	
1000±20	4.7±.5[c]			5.1				6.6		6.6±1.5[c,d]	
2900±30	4.7±1.2[c]			4.7±1.0		5.6			5.1±.5		6.2±1.6
4000-5000[b]	5.3±.7[c]			5.1	4.9		5.5			5.5	5.6±.9
5100±100	3.7±.2	4.5±.6			5.3±.8			5.6±.5			6.0
10,000±1000	3.7±.2	4.5±.2		4.6±.2			4.9±.3			5.4±.8	
Average	3.8±.4									5.7±.6	
v=1 → 0											
2380±60	.88±.09	.82			.96		1.0[f]				1.2
2900±30	.84±.09			.89		1.0			1.1±.1		1.1±.1
5100±100	.76±.09	.85±.10			.82±.05			.89			.93
10,000±1000	.75±.02	.77		.98						1.0	
Average	.81±.07	.81±.04									1.1±.1

[a] Air-doped sample: HCl/Air/Ar = 1/0.2/930.

[b] HCl is present as an impurity in DCl/Ar, M/A = 1000 sample.

[c] Value discarded in computing averages. See text.

[d] 20.5 K

[e] Direct v=1 excitation.

[f] 17.5 K.

Table V-II. HCl v=1→0 Relaxation Data and Monomer-Dimer Coupling Coefficients

M/A	Mole fractions (10^{-3}) $x_{monomer}$	x_{dimer}	k_{10} ($10^3 sec^{-1}$) 9 K	20 K[c]	$\frac{k(20)}{k(9)}$	R_o[a] (Å)	C_{DA} ($10^{-37} cm^6/sec$)[b] 9 K	20 K
123±2	6.6±.1	.68±.01	>500	>500		5.0		
527±5	1.78±.02	.049±.005	8.5±2.5	27±7	3.1±1.7[g]	5.1	1.8	6.1
600±30[d]	1.58±.08	.028±.002	5.5±.3			4.6	1.9	
670±20	1.46±.06	.030±.005	6.5±1.8	11±3	1.7±0.9	5.0	2.2	3.8
920±30[d]	1.00±.03	.033±.003	.95±.11	1.1	1.2	6.6		
920±30[e]	.50±.02	.14±.02	1.9			16	.091[j]	
930±30[f]	1.00±.03	.026±.003	1.6±.2	2.0	1.3	6.1	.35	.44
960±20	1.03±.03	.017±.005	1.2±.2	1.5	1.3	5.2	.27	.34
980±30	1.00±.03	.020±.003	1.2±.1			5.6	.23	
990±20	.91±.03	.016±.002	1.6±.3	2.1+.3	1.3±.4	5.5	.58	.79
1000±20	.89±.02	.038±.004	2.0±.2	2.2±.6	1.1±.4	7.4	.36	.36
2380±60[d]	.38±.01	.004±.001	.88±.09	1.2	1.4	6.3		
2900±30	.345±.003	<.004	.84±.09	1.1	1.3	<6.7		
5100±100	.196±.004	<.004	.76±.09	.93	1.2	<9.7		
5100±100[e]	.118±.006	.026±.002	.88±.06			24		
10,000±1000	.10±.01	<.004	.76±.02	1.0	1.3	<15		
Average[h]					1.3±.2	5.7±.8[i]	$10^{-37.2±.4}$	$10^{-37.0±.5}$

Footnotes for Table V-II

[a] Calculated from Eq. (7).

[b] Calculated from Eq. (10).

[c] T = 20 ± 1 K.

[d] Direct excitation of v=1.

[e] Sample prepared by annealing sample listed directly above it in the table.

[f] Air-doped sample: HCl/Air/Ar = 1/0.2/930.

[g] This value discarded in averaging k(20)/k(9).

[h] Error is one standard deviation of the data set.

[i] Annealed samples are not included in the average.

[j] This value discarded in averaging C_{DA}.

Table V-III. HCl/Ar v=1 → 0 Relaxation Data-Relaxation Rates for Ensembles of Non-Isolated Molecules, Intermediate Temperature Range (10^3 sec^{-1})

	T (K ± 0.4)							
M/A	11	12	13	14	15	16	17	18
123 ± 2			>500				>500	
600 ± 30[a]		6.2			7.4			7.6
920 ± 30[a]	1.2			1.3			1.2	
930 ± 30[b]						1.8 ± .1		
960 ± 20							1.6 ± .1	
980 ± 30		1.4 ± .2			1.3			1.6
990 ± 20			2.2 ± .1			2.3 ± .2		2.7 ± .2[c]
1000 ± 20				1.6				2.7

[a] Direct v=1 excitation.

[b] Air-doped sample: HCl/Air/Ar = 1/0.2/930.

[c] 18.5 K.

Lifetimes for isolated HCl are insensitive to excitation pulse intensity and frequency. Relaxation data for two samples as a function of excitation intensity are presented in Table IV. Typical samples are calculated to be 2-5% absorbing on the strongest accessible overtone absorption line: $R(0)^{35}$ at 9 K. The excitation pulse was varied in energy by use of neutral density filters. Energy density was varied by sometimes using a 4 cm focal length lens to focus excitation into the sample and by varying the degree of focusing by lens placement. While overall S/N was affected by these maneuvers, the temporal behavior of the system was unaffected to within the experimental uncertainty of 10-15%. The spectral width of the OPO (0.2 cm^{-1}) is less than the width of the HCl absorption line (1-2 cm^{-1}) so it was possible to excite various portions of the line profile--decay times were insensitive to this. Furthermore, excitation on vibration-rotation transitions of the isolated monomer--P(1), R(0), R(1), and $Q_R(00)$--results in the same decay kinetics. Relaxation data as a function of frequency are presented in Table V. Data for other samples as a function of frequency sometimes show more scatter than that in Table V. Since, in cases such as those presented, the data is very consistent, the scatter in other cases is taken to be indicative of random errors in analysis procedure. Excitation on different spots in the matrix gives the same lifetimes. k_{10} increases when the matrix is deposited under conditions which enhance dimer formation; the increase can be correlated to the dimer concentration, as will be discussed below. The decay rate of v=2 is unaffected by deposition conditions.

Decay rates increase slightly with temperature in the range 9-21 K, as is evident in Tables I-III. From the data of Table I, k_{21} increases

Table V-IV. Effect of Excitation Density on Relaxation Rates of HCl/Ar. Excitation on Line Center, $R(0)^{35}$, v=0 → 2 Absorption.

M/A	$(1-\frac{I}{I0})$[a]	Pulse energy (μJ)	Beam[b] waist (μ)	Optical Attenuation[c] (O.D. units)	Energy density (mJ/cm^2)	k_{21} (10^3 sec^{-1})	k_{10} (10^3 sec^{-1})	S/N
4000-5000[d]	.05	5	60	0	44	4.96	1.11	84
			60	0.3	22	4.80	1.19	80
			60	0.5	14	4.82	1.19	40
			60	1.0	4.4	5.07	1.35	16
			60	1.0	4.4	4.38	1.20	19
			260	0	2.4	4.81	1.22	45
980 ± 30	.03	12	60	0	110	4.1 ± .9	1.2 ± .2	50-120
			60	0 5	34	3.82	1.19	65
			60	1.0	11	3.47	1.14	72
			60	1.5	3.4	3.64	1.22	21

[a] Percent absorption. Calculated from measured absorption of R(0) fundamental, using ratio of overtone to fundamental absorption of 1/36.3, from Appendix C.

[b] 4 cm focal length lens in position produces a 60μ spot at 1.78μ (calculated). Collimated beam waist is 260μ in the matrix (calculated).

[c] Beam is attenuated with calibrated neutral density filters.

[d] HCl present is an impurity in a sample DCl/Ar, M/A = 1000. Exact HCl concentration unknown.

Table V-V. Effect of Excitation Frequency on Relaxation Rates of HCl/Ar (v=0 → 2 excitation, 9 K)

M/A	Line	$\bar{\nu}^a$ (cm^{-1})	k_{21} (10^3 sec^{-1})	k_{10} (10^3 sec^{-1})	S/N
1000 ± 20	R(1)	5665.3	5.17	1.72	13
	$R(0)^{35}$	5656.0	4.34	1.93	>100
	$R(0)^{37}$	5651.1	4.44	1.68	30
	$P(1)^{35}$	5622.1	4.39	1.86	21
	$P(1)^{37}$	5617.7	4.97	1.51	7
670 ± 30[b]	$Q_R(00)$	5711.7	4.95		11
	$R(0)^{35}$	5654.5	5.24		80
	$R(0)^{35}$	5656.0	5.26		180
	$R(0)^{35}$	5657.5	5.26		75

[a] $R(0)^{35}$ line center is assigned as 5656 cm^{-1}. Frequency measurements relative to this are accurate to ±0.2 cm^{-1}.

[b] Measurements taken after a slight annealing. Hence k_{21} is faster than isolated molecule rate (3.8×10^3 sec^{-1}).

by a factor of 1.5 ± 0.2, and k_{10} increases by a factor of 1.3 ± 0.2 for this temperature range.

The decay rate of v=1 at 9 K is strongly concentration dependent, as seen in Fig. 3. The data points presented in Fig. 3 are obtained only from samples deposited at 9 K. Data obtained from samples deposited at higher temperatures produces vertical scatter in a plot like Fig. 3, since more dimer is produced in the sample. The v=1 decay rate reaches its concentration independent limit at about M/A = 2000, and only those values corresponding to isolated HCl are included in Table I. The decay rate of v=2 is concentration independent over the entire range M/A = 500-10,000, and v=2 decay rates for all matrices within that range correspond to isolated HCl v=2. Four marked samples in Table I are not included in average values for k_{21} rates. These samples were the earliest experimental work and the high k_{21} values are due to analysis procedure and a less than optimal choice of filters for resolving v=2 → 1 fluorescence. They are included in Table I for completeness, but are likely too high. Since the lowest values for relaxation rates are generally best due to impurity effects, these values are discarded. For M/A < 700, the v=1 decay rate is actually faster than the v=2 decay rate. Equation (IV-2) is still valid in such circumstances, but the rise of v=1 fluorescence corresponds to the v=1 decay rate, and the peak intensity of the v=1 signal is reduced by the ratio of rate constants in Eq. (IV-2). The rapid decay of v=1 in concentrated samples is verified by direct measurement of the v=1 decay rate following v=1 excitation: in a sample of M/A = 600, k_{10} = 5.5 x 10^3 sec^{-1} at 9 K.

Figure V-3. Concentration dependence of relaxation rates. Samples shown were deposited under similar conditions: 9 K and 20-30 m-mole/hour. Data is taken from Tables V-1 and V-2.

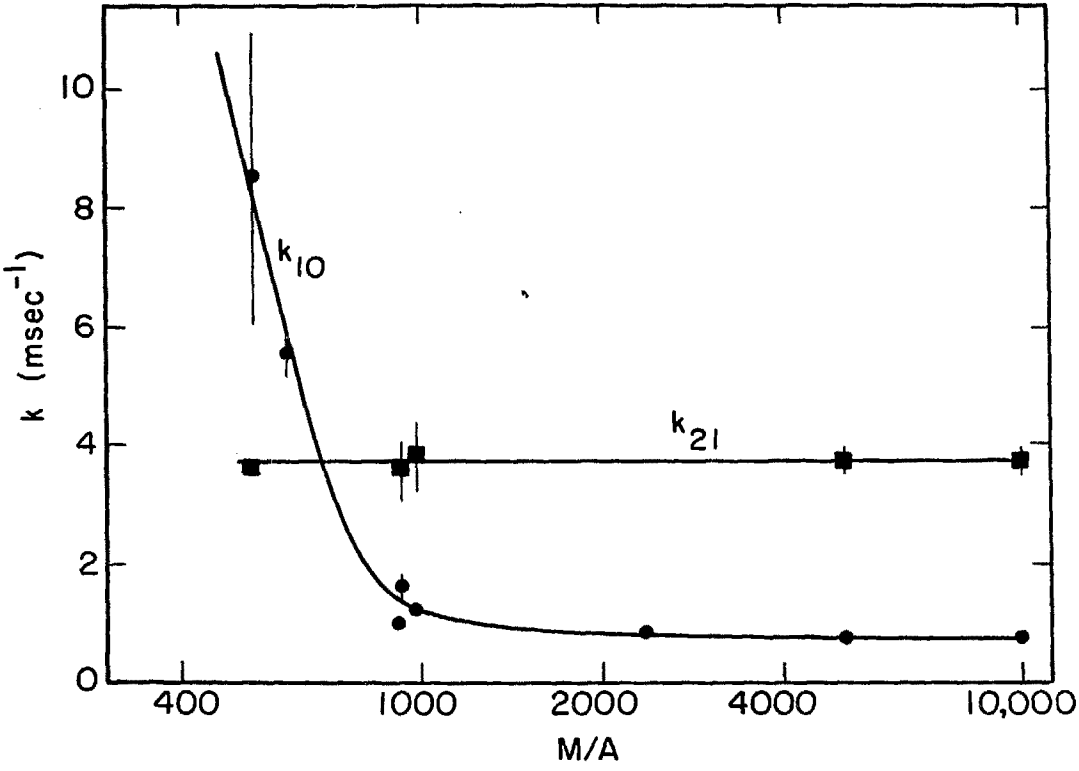

XBL 7710-10004

In a very concentrated sample, M/A = 123, the decay of v=2 fluorescence becomes more rapid and non-exponential. Data for v=2 emission analyzed as a doubly decaying exponential is given in Table VI. The temperature dependence of the decay is much greater for this sample than for the isolated molecule relaxation cases of Table I; rates increase 3.5 and 7 times for k_2 and k_1 between 9 and 21 K. No v=1 emission is observed in this sample, since, presumably, its deactivation is rapid (>2 μs).

At temperatures higher than 9 K the v=1 decay rate increases with concentration analogously to the 9 K behavior; the isolated molecule case always corresponds to M/A greater than 2000. Decay rates of v=1 at 9 K, 20 K, and the ratio of decay rates at the two temperatures is given as a function of monomer and dimer concentrations in Table II. Decay rates at intermediate temperatures are given in Table III. The concentrations are measured from the integrated intensities of the appropriate lines in the IR absorption spectra, and the indicated errors reflect the signal-to-noise ratio of the measured peak in the recorded spectrum. The dimer concentrations were calculated assuming that the square of the transition moment per HCl molecule in the dimer is 2.4 times that of the monomer, and is thus subject to an additional systematic error. The temperature effect is weak and similar for all samples.

Both v=2 and v=1 decay rates increase subsequent to annealing. For dilute samples, k_{21} increases by 20-30% (M/A = 1000, 5000). The increase in k_{10} is often a factor of two or more. In concentrated samples, decays sometimes become non-exponential after annealing. Some values of k_{10} subsequent to annealing are included in Table II--the decay of v=1 is exponential for these samples.

Table V-VI. Relaxation of HCl/Ar M/A = 123 ± 2, v=2 → 1 decay

T =	9.1 K	17 K	21 K
$k_1(10^3\ s^{-1})$	16 ± 2	100	110 ± 20
$k_2(10^3\ s^{-1})$	5.77 ± .15	19	21.4 ± .6
A_1/A_2[a]	.89 ± .11	1.3	1.4 ± .2

[a] Ratio of amplitudes: fast decay/slow decay.

Fluorescence spectra using the CVF as the dispersing element are shown in Fig. 4 for excitation of an HCl/Ar sample of M/A = 1000 to v=2 at 9 and 20 K for R(0) or P(1) excitation. The spectrum is insensitive to excitation line or temperature. The 33 cm^{-1} resolution of the CVF (FWHM) was insufficient to resolve different rotational lines of the same vibrational transition. The ordinate in this figure is obtained by integrating the fluorescence decay curve and correcting for radiative lifetime, measured decay time, and optical thickness effects, as described in Section II.D.9. The result of this correction gives the relative number of vibrational quanta passing through a vibrational level during the relaxation process. That the peak heights for v=2 → 1 and v=1 → 0 transitions are nearly equal, to within experimental error, indicates that v=2 decays by loss of a vibrational quantum to become v=1. If v=2 decayed by a V→V process in which two molecules in v=1 were produced, the v=1 → 0 peak would be twice as large as the v=2 → 1 peak. Also shown in Fig. 4 is a fluorescence spectrum uncorrected for optical density effects.

No emission from any vibrational levels with v>2 is observed. The low frequency tail in the 9 K emission spectrum in Fig. 4 is due to the poor resolution of the CVF rather than to v=3 emission, since this emission does not peak near 2646 cm^{-1}, which is the calculated frequency for the P(1) line of the v=3 → 2 transition. Emission from v=3 is less than 1% of that from v=2 under focused or unfocused excitation.

No fluorescence was observed upon direct excitation of the overtone of the dimer at 5484 cm^{-1} at 9 or 20 K. In particular, for a sample of M/A = 670, no fluorescence was observed from the dimer at 9 K after averaging for 1000 shots. Upon excitation of P(1) at 9 K under otherwise

Figure V-4. Fluorescence spectra of HCl/Ar, M/A = 1000 ± 20. The histograms are arbitrarily normalized line emission spectra calculated for a Boltzmann distribution of rotational levels of the emitting vibrational level; P and R lines are indicated for v=3 → 2, v=2 → 1, and v=1 → 0 bands. No v=3 → 2 emission is observed since the low frequency tails in the spectra do not peak near the calculated emission. Lowest trace is data uncorrected for optical density of v=1 → 0 transitions.

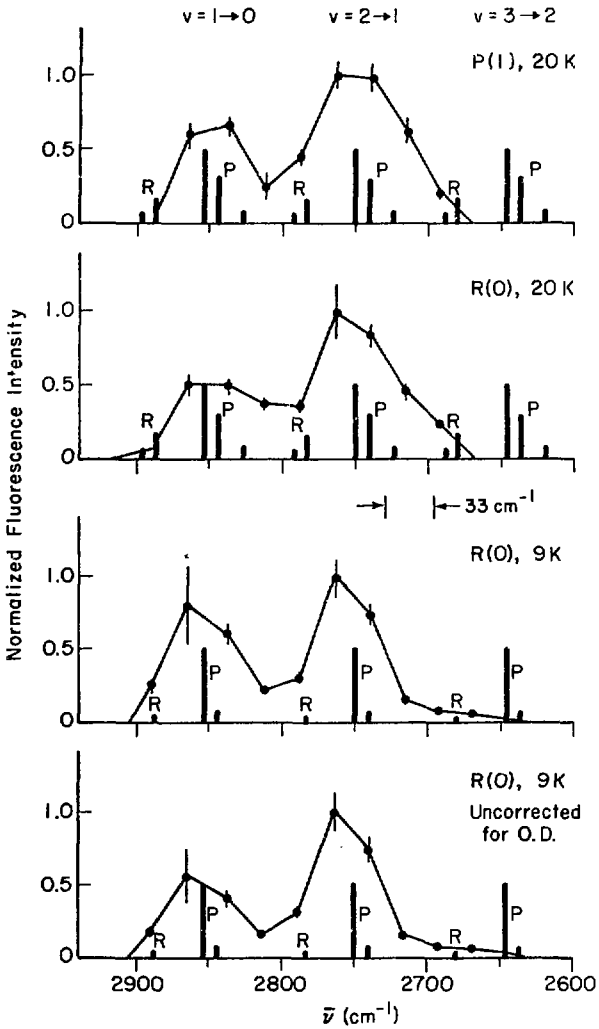

XBL 7711-10361

identical conditions, fluorescence averaged for 4000 shots produced a 240 μs decay (v=2 → 1) with S/N = 80. In this sample the fundamental dimer and P(1) absorption intensities were equal at 9 K. In a search for dimer fluorescence, the OPO was moved in 0.7 cm^{-1} increments for 15 cm^{-1} in both directions from 5484 cm^{-1}, and after signal averaging at each setting no fluorescence was observed. In these experiments, the amplifier high frequency cutoff was 3 MHz. If the ratio of overtone to fundamental absorption is the same for dimer as for monomer, equal absorption intensities of dimer and P(1) means that the number of molecules excited by the laser pulse is the same for both excitation frequencies. Since the dimer absorption coefficient per molecule is greater than that of the monomer, the Einstein A coefficient for the dimer should be greater than that of the monomer. We can conservatively estimate, however, that in the above experiment, P_o as defined by Eq. (II-14) is equal for dimer and P(1) excitation. Then, using Fig. II-5, a dimer decay constant of 6 x 10^7 sec^{-1} should have produced a signal with S/N=1 after averaging 1000 shots. A decay constant of 3 x 10^6 sec^{-1} should have had S/N of 16 after 1000 shots, and would have been plainly visible. That the ratio of overtone to fundamental absorption for the dimer equals that of the monomer is unknown. However, it seems likely that a dimer decay constant of <3 x 10^6 sec^{-1} should have been easily observed.

Presuming that the dimer overtone absorption frequency was misassigned, and looking for emission from overtone excitation of other molecular complexes, such as HCl-N_2 or HCl-H_2O, fluorescence excitation spectra of various samples were scanned from 5720 to 5350 cm^{-1}, at both 9 and 20 K. As discussed in Chapter III, signals are observed only for

isolated monomeric HCl. Even in a sample with M/A = 120, in which about 10% of the HCl existed in dimeric form, no dimer emission was observed. Equation (II-31) may be used to estimate a limit on the dimer relaxation time implied by the lack of a dimer signal. For the sample of M/A = 670 discussed above, the S/N for the P(1) peak was 35, and τ was 240 μs; thus $\tau < 7$ μs for dimer relaxation. The value of 7 μs is consistent with the results of excitation spectra for other samples and is a conservative upper limit for the dimer relaxation time.

In order to see the influence of impurities on the decay rate of isolated HCl, a sample doped with air was prepared (HCl/air/Ar = 1/0.2/930). Excitation of only R(0) and P(1) lines produced observable fluorescence. The excitation spectrum of this sample is identical to those of HCl/Ar shown in Chapter III. In particular, no peak corresponding to the HCl-N_2 complex was observed. The presence of massive impurities does not affect the v=2 decay rate at all (see Table I) and the shortening of the v=1 decay rate may be understood in terms of energy transfer to dimer (see Table II). The amount of air present in this particular sample is equivalent to the leak rate of the apparatus integrated for 2 x 10^6 hours.

2. DCl/Ar

The DCl/Ar system has been studied in much less detail than the HCl/Ar system. Some experiments have been performed exciting DCl to v=2 on several vibration-rotation transitions and monitoring the temporally and spectrally resolved emission. The DCl experiments are more difficult than the HCl experiments because both the absorption cross section and the emission intensity are smaller in DCl than in HCl,

and the fluorescence signal is proportional to the product of the two. Studies of dilute DCl/Ar samples necessitated rather thick samples, and the fluorescence from v=1 was weakened severely by the optical density of v=1. Time resolved fluorescence from v=2 and v=1 subsequent to excitation of v=2 at 9 K are shown in Fig. 5. The decay curve for v=1 → 0 emission is the result of averaging 10,000 shots and shows a S/N of perhaps twelve.

The fluorescence from v=2 is a single exponential over at least one and a half decades. Values for k_{21} are presented in Table VII. In principle, the behavior of v=1 should be describable by Eq. (IV-2). In practice, analysis of fluorescence traces from v=1, such as that shown in Fig. 5, fit the form of Eq. (IV-2), but neither the apparent rise nor the apparent decay rate match the decay rate of v=2, which is at first thought disturbing. The situation for the v=1 → 0 decay is actually that described by problem (B) of Section IV.C.2, however. The true v=1 decay rate is very close to the v=2 decay rate and since the data has only one useable decade due to S/N, the fast rate will be overestimated and the slow rate will be underestimated. In particular, the relaxation time for v=2 in Fig. 5 is 9.1 ± 0.2 ms; the rise and decay times for v=1 emission when analyzed according to Eq. (IV-2) are 3.5 and 17.5 (±0.5) ms. The k_{10} values in Table VII are evaluated using measured k_{21} and Eq. (IV-34), which requires measurement of t_{max}. This method produces a fairly large uncertainty. In the limit that $k_{10} = k_{21}$, Eq. (IV-34) predicts that v=1 fluorescence will peak at a time equal to $1/k_{21}$. From Fig. 5 the peak v=1 → 0 emission is indeed near 9 ms. Broadband decay traces are dominated by the v=2 → 1 signal, since the 1→0 fluorescence is optically attenuated. The broadband decays

Figure V-5. Spectrally resolved fluorescence from DCl/Ar, M/A = 4800 ± 100, 9 K. Excitation is at 4117 cm^{-1}, $R(0)^{35}$ v=0 → 2 transition, with 16 μJ/pulse energy. The v=2 → 1 decay trace is the average of 2048 shots; that of v=1 → 0 is the average of 10,200 shots. The CVF was the spectrally dispersing element for both traces.

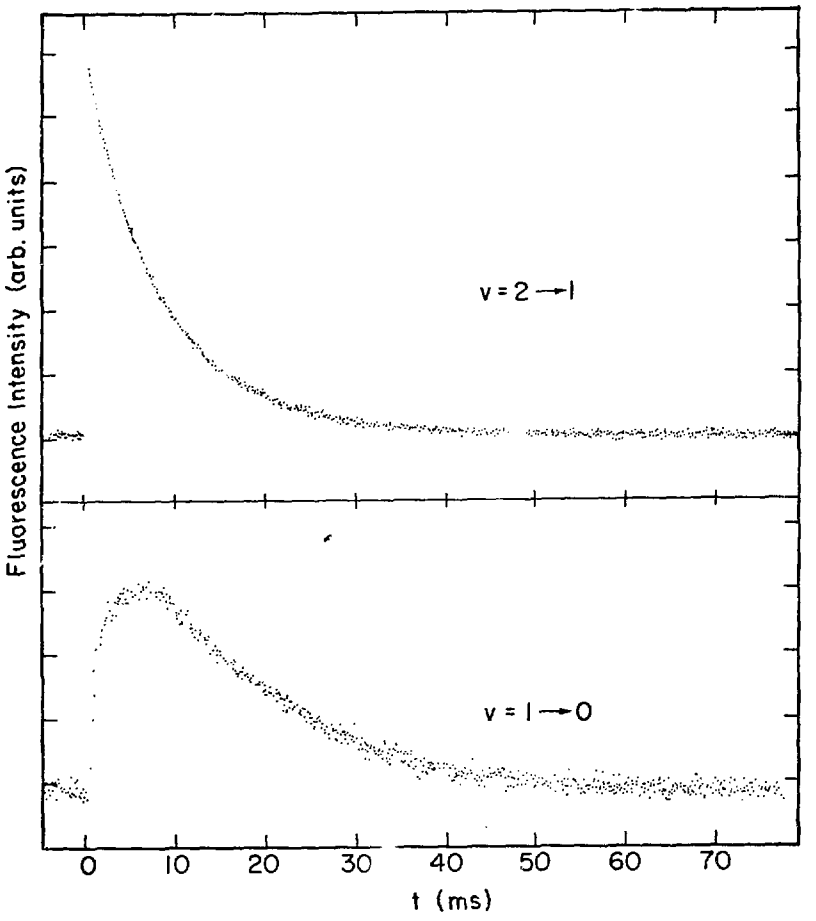

XBL 7710-10356

Table V-VII. DCl Relaxation Rates (sec^{-1})[a]

	M/A	T (K ± 0.4) 9.1	12	15	18	20
v=2 → 1						
	3270 ± 60	110 ± 10	130	170		
	4800 ± 100	120 ± 10	150	180	190	200 ± 10
	Avg	120 ± 15	140 ± 15	180 ± 10		
v=1 → 0						
	3270 ± 60	110 ± 30	140 ± 40	190 ± 80		
	4800 ± 100	110 ± 40	190 ± 100	200 ± 100	185	200 ± 70

[a] Uncertainty is 15% for values with no quoted uncertainty.

appear as single exponentials with decay times longer than $1/k_{21}$ due to the presence of some v=1 → 0 fluorescence; broadband fluorescence decays in 12-13 ms at 9 K. A better way to measure k_{10} would be to excite DCl to v=1 directly with a frequency doubled CO_2 laser.

The DCl relaxation rates are insensitive to which vibration-rotation transition is excited (P(1), R(0), R(1)--both crystal field transitions), to exact position on the line profile excited, and to degree of focusing the excitation. As with HCl/Ar, relaxation rates increase with temperature. The relaxation rate of v=2 increases by a factor of 1.7 between 9 and 20 K. A crude scan of emission frequency was made using the CVF--all fluorescence was in the range between 1965 and 2100 cm^{-1}. In particular, emission from v=3 at 1965 cm^{-1} was not observed after averaging 1000 shots.

An early experiment was performed for a sample of DCl/Ar, M/A = 1000. Fluorescence from v=2 decayed as a double exponential. The fast decay rate was dependent on the spectrally dispersing filter used and varied from (2.8-3.8) x 10^3 sec^{-1} at 9 K to (2.7-4.0) x 10^3 sec^{-1} at 19 K. The slow decay rate was independent of filter and varied from 400 ± 30 to 640 ± 90 sec^{-1} at 9 to 19 K, respectively. The relative amplitude of fast decay to slow decay was 0.5-0.8, depending upon filter. Fluorescence from v=1 was weak (S/N < 10 after 8000 shots), rising in less than 100 μs and decaying with approximately the same rate as v=2 → 1 emission. In this sample, the DCl was only about 75-80% isotopically pure, so HCl was present at M/A of 4000-5000. Upon excitation of DCl, no HCl emission was observed. Some experiments were performed exciting HCl (see Table I)--no DCl emission was observed.

There are several problems with this sample. Appropriate filters for resolving DCl v=2 → 1 and v=1 → 0 emission were unavailable when the experiment was performed; the filters used were only partly resolving and analysis was complicated by this. Also, the DCl used was Merck, Sharpe, and Dohme of Canada, Ltd, of unknown vintage; the gas was distilled before use, but unknown contaminants could have survived the distillation. The kinetic results presented in Table VII should be considered more valid than those for M/A = 1000 until additional experiments for DCl/Ar at M/A = 1000 can be performed.

Fluorescence excitation spectra of DCl/Ar, as with HCl/Ar, reproduce only monomeric absorption features, as discussed in detail in Chapter III. In particular, no dimer emission was observed even when excitation spectra were scanned to 3970 cm^{-1}. Considerations such as those presented for HCl/Ar dimer yield an upper limit for DCl dimer relaxation of 160 μs. Studies of excitation spectra upon annealing were performed for a sample of M/A = 4800 ± 100. Upon annealing, the $R(0)^{35}$ and $R(0)^{37}$ peaks narrowed and resolved into reproducible doublets.

The k_{21} rate for DCl is about 35 times slower than the k_{21} rate for HCl. From Section III.E.1 the radiative decay rate for DCl (v=2) in Ar is calculated to be 36 sec^{-1}, so as much as 30% of the decay of v=2 may be radiative. The radiative decay rate of v=1 of DCl/Ar was calculated as 20 sec^{-1}, so a smaller fraction of the v=1 decay appears to be radiative.

The determination of k_{21} for DCl/Ar is straightforward, since spectrally resolved decays yield single exponentials, and hence the k_{21} values are considered accurate for V→R, P decay. The importance of the DCl result is the enormous decrease in decay rate relative to HCl. It

is unlikely that the v=1 decay rate is as rapid as that of v=2, and it is possible that it is affected by V→V transfer to some impurity present in the sample, as will be discussed in Section B. The k_{10} results are presented in Table VII for completeness. They represent upper limits for the true v=1 decay rate.

3. HCl/N_2 and HCl/O_2

No fluorescence was observed when HCl was suspended in N_2 or O_2 at M/A = 1000. Direct signal averaging experiments were performed at the calculated v=0 → v=2 absorption frequencies of 5604 and 5621 cm^{-1}, respectively, as well as within a frequency range of 10 cm^{-1} to both sides of these frequencies in 0.7 cm^{-1} increments. Assuming the overtone absorption coefficient of these samples is the same as that for HCl/Ar, $\hat{P}_o$ of Eq. (II-14) should be the same as that for HCl/Ar for equal OPO pulse energies. In the signal averaging experiments, 1000 shots of 10 μJ/pulse energy were averaged--such conditions for HCl/Ar produced traces with S/N > 30. From Fig. II-5, no observable signal means that $(V_S/V_N)/X_o < 1/30$, or that $k/\omega_H > 20$. Thus, a lower estimate for decay rates of HCl in N_2 and O_2 is, by this method, 6×10^7 sec^{-1}.

Fluorescence excitation spectra scanned over the ranges 5645-5511 cm^{-1} in N_2 and 5666-5543 cm^{-1} in O_2 yielded no observable peaks. Quantitative data for excitation spectra of different samples can be transferred using Eq. (II-31). For eight excitation spectra for samples of HCl/Ar with M/A = 123 to M/A = 5100, χ has a value of 1.8 ± 0.3 (one standard deviation of the set of values) when S/N is measured for the $R(0)^{35}$ peak, laser power is in μJ/pulse, integrated absorbance of the fundamental is used, and τ is measured from decay experiments. For the

conditions of the excitation spectra of HCl/Ar (20 pulses/sec, 10 μJ/pulse), with measured absorptions for the fundamental region, limits for relaxation times of HCl/N_2 and HCl/O_2 at 9 K may be estimated. For HCl/N_2, $\tau < 8$ μs; for HCl/O_2, $\tau < 17$ μs.

B. Discussion

The important features of the vibrational relaxation of matrix-isolated HCl and DCl are as follows: In Ar, relaxation is non-radiative (aided slightly by radiation for DCl). For HCl/Ar k_{21} is independent of concentration and k_{10} is independent of concentration for M/A > 2000. These correspond to isolated molecule V → R,P rates. The relaxation of HCl v=2 is 35 times faster than that of DCl v=2, and relaxation rates increase slightly (less than a factor of 2) over the temperature range 9-20 K. HCl/Ar v=1 relaxation increases as M/A decreases, and at M/A = 123 is too fast to be observable. Molecular complexes, such as dimer, relax very rapidly as does HCl trapped in molecular solids.

The mechanism for relaxation of isolated HCl and DCl in Ar will be discussed in Section 1; that HCl relaxes more rapidly than DCl is indicative of rotation as the primary energy accepting mode. The temperature effects of isolated molecule relaxation are considered in Section 2. The increase of v=1 relaxation as M/A decreases is considered in terms of diffusion-aided V→V transfer to the dimer in Section 3. In Section 4, the rapid dimer relaxation is considered and in Section 5 the rapid relaxation of HCl in N_2 and O_2 matrices is discussed.

1. Mechanism of Isolated Molecule Relaxation

The vibrational energy of the guest molecule is ultimately dissipated into the degree of freedom which has the lowest energy and the highest density of states--the lattice phonons. Several theoretical treatments of relaxation due to direct coupling between molecular vibration and lattice phonons have been presented.[1-8] Relaxation of a molecular vibration directly into acoustic phonons requires excitation of 30-40 phonons. The prediction of these multiphonon theories is that relaxation rates should show a large temperature effect, due to the many phonons created, and an energy gap law--molecules with a high vibrational frequency relax slower than molecules with a low frequency. The theories cannot simultaneously explain the small experimentally observed temperature effects and the apparent violation of the energy gap law for hydride-deuteride systems, and so fail. The multiphonon V→P theories will be discussed more fully in Chapter VI.

The notion of an energy gap law arises from an attempt to correlate the main relaxation channel with the number of quanta produced in the energy accepting mode (the order of the process). Everything else being approximately equal, the lower the order of a process, the faster it ought to be. Small molecules, especially hydrides, have small moments of inertia and large B constants, and can accommodate large energies in relatively low J states. In particular, if relaxation were totally a V→R process, the rotational state produced would be $J_f = (\nu/hcB)^{\frac{1}{2}}$, where ν and B are the vibrational frequency and rotational constant of the guest. J_f is the order of the V→R relaxation process and is smaller for hydrides than for deuterides. Hence, hydrides should relax more

rapidly than deuterides. The importance of rotation as an accepting mode was originally noted by Brus and Bondybey[9,10] with an argument similar to the preceding one. Legay[11] has successfully correlated the existing experimental results for non-radiative relaxation of small molecules in matrices to an exponentially decreasing dependence of rate on J_f:

$$k \sim \exp(-\alpha J_f). \qquad (1)$$

For V→R relaxation in Ar of HCl v=2 → 1, v=1 → 0, and DCl v=2 → 1, J_f = 15, 16, and 19 where gas phase B values[12] of 10.5 and 5.45 cm^{-1} for HCl and DCl and matrix vibrational frequencies have been used. The V→R process is of much lower order than the V→P process. Furthermore, the increase in order for the three processes above parallels the decrease in relaxation rate for these processes. The vibrational frequency of CO in an Ar matrix, 2138 cm^{-1},[13] is comparable to that of DCl, but for CO, B = 1.9 cm^{-1},[14] and J_f = 34. Hence, V→R relaxation should be much slower for CO than for HCl or DCl. In fact V→R relaxation of CO/Ar is so slow that it relaxes radiatively with a 14 ms decay time.[15]

The physical picture for vibrational relaxation of small guest molecules in solids involves a rate limiting V→R step, in which a high rotational level of the guest is populated, followed by more rapid loss of excess rotational quanta into the phonon modes of the lattice. The entire relaxation process subsequent to excitation of v=2 of HCl/Ar is shown schematically in Figure 6. High rotational levels are shown as free rotor levels shifted by -8 cm^{-1} due to RTC.[16] The separation between J=16 and J=15 for HCl is about 340 cm^{-1}. Since it is unlikely that there will be an exact resonance between initial and final

Figure V-6. Overall schematic of relaxation of HCl(v=2)/Ar. The rate limiting steps are V→R processes, k_{21} and k_{10}. The V→R step produces a highly excited rotational level which can rapidly relax by energy transfer to phonons, n. The phonons shown are 73 cm^{-1} energy, corresponding to HCl/Ar local mode.

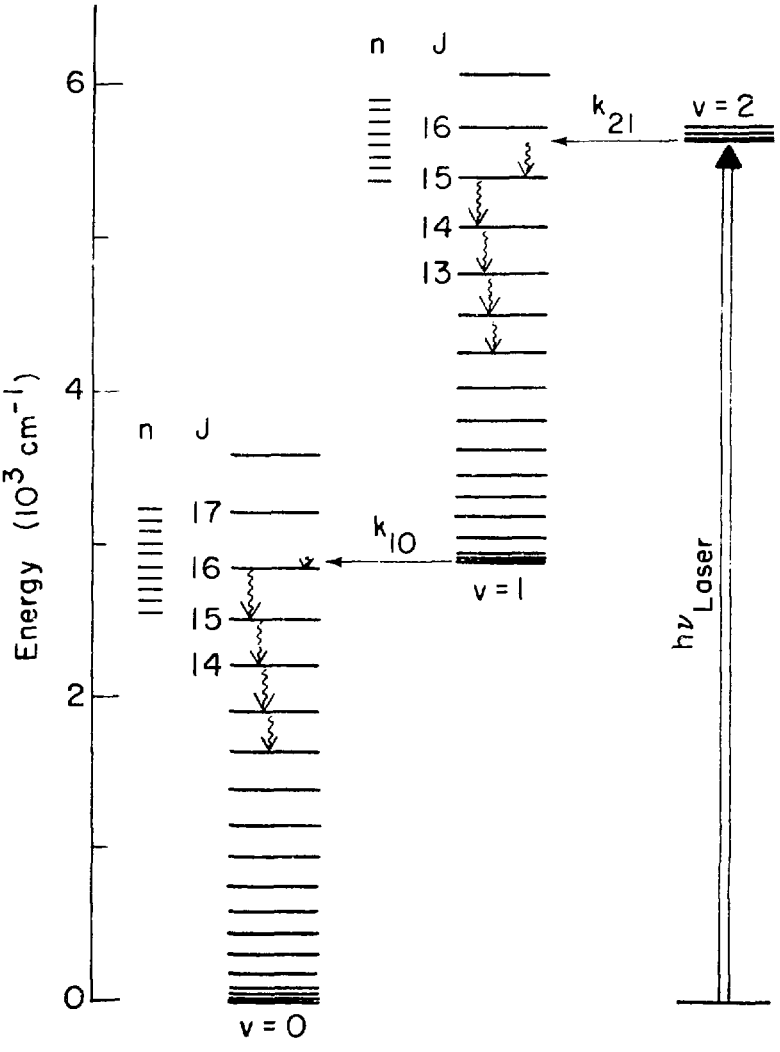

XBL 7710-10002

vibration-rotation levels in the relaxing molecule, some participation by lattice phonons (especially local mode phonons) in the V→R step is necessary to conserve energy. Subsequent rotational relaxation in the high J levels will be a multiphonon process, requiring at least five phonons of the Ar lattice in the case of HCl relaxation from J=15 to J=14.

Rotational relaxation is likely to be very rapid. Mannheim and Friedmann[17] have calculated the widths of J=1 and J=2 of HCl in an Ar lattice at 0 K due to one phonon energy transfer between molecular rotation and lattice vibration, obtaining values of 0.4 and 10 cm^{-1}. These imply relaxation times of J=1 and J=2 of 10 and 0.5 psec. Relaxation from rotational levels requiring more than one phonon (J>3 in an Ar lattice) requires a higher order perturbation theory than in Mannheim and Friedmann's work, but the very fast rates for the first order processes suggest that the higher order processes will also be rapid compared to observed vibrational relaxation.

That the R→P step is not rate limiting follows from the data. The energy spacing between $J_f = (\nu/cB)^{\frac{1}{2}}$ and $J_f - 1$ is the energy that must be disspiated to phonons, and is proportional to $(\nu B)^{\frac{1}{2}}$. The order of the R→P process is proportional to the energy to be dissipated since phonon energies are independent of the guest (almost). Hence, a rate limiting R→P step requires that deuterides relax more rapidly than hydrides since both ν and B are smaller for the deuteride. This conclusion is contrary to experimental observation.

Since R→P is rapid for thermally accessible rotational levels, rotation will thermalize rapidly compared to vibrational relaxation, and vibrational relaxation will be independent of rotational state

prepared in the laser excitation step, as experimentally observed. That excitation on all positions of the line profile produces no observable difference in vibrational relaxation is also rationalized by the R→P process, which homogeneously broadens the absorption line.

The postulate of rotation as the accepting mode successfully explains the observation that HCl relaxes more rapidly than DCl, but there is no direct evidence that high rotational levels are in fact populated subsequent to vibrational relaxation. This situation is analogous to gas phase vibrational relaxation in which V→R models are successful in correlating a great deal of experimental data, but direct evidence of population of a high rotational level is elusive.[18]

It is interesting to note that the ratio of k_{21}/k_{10} for HCl/Ar is approximately five. First order perturbation theories which treat the vibrational degree of freedom as a harmonic oscillator predict that this ratio should be two ($k_{v,v-1} = vk_{10}$). The inverse exponential dependence of k on J_f would serve to increase k_{21} relative to k_{10}, since J_f is smaller for v=2 → 1 than for v=1 → 0 relaxation, due to the vibrational anharmonicity. Accounting for this with a value of $\alpha = 1.2$, which fits the ratio of HCl/DCl rates,[19] the ratio of v=2 → 1 to v=1 → 0 relaxation is still 3.3. The enhancement of k_{21} relative to k_{10} may be due to the fact that the V→R process is more resonant for 2→1 than for 1→0 relaxation. However, the data for relaxation of other rotating diatomics in rare gas solids gives ratios for k_{21}/k_{10} of 4 and 3.5 for OH and OD ($A^2\Sigma^+$) in Ne[9] and 5 for NH ($A^3\pi$) in Ar.[10] Furthermore, gas phase vibrational relaxation studies of HCl indicate that k_{21}/k_{10} has a value of 4 or 5.[20] Apparently V→R processes do not obey a harmonic oscillator scaling law.

The k_{10} rates reported for DCl in Table VII have large uncertainties, but the extremes of k_{10} are within 50% of the k_{21} rate. Other observed k_{10} rates are less than half the k_{21} rates. It is possible that the k_{10} rate is in part due to diffusion aided V→V transfer to some impurity present in sub-spectroscopic concentration. V→V transfer to minute traces of impurities can affect observed relaxation times when the intrinsic relaxation time is very long.[21,22] Further studies of the DCl system are necessary to produce more confidence in the measured k_{10} rates.

2. Temperature Effects

The relaxation rates of HCl/Ar v=2 → 1 and v=1 → 0 increase by factors of 1.5 ± 0.2 and 1.3 ± 0.2 between 9 and 21 K. This temperature effect is quite small, but it is real and it is the largest reported temperature effect for V → R,P relaxation of a matrix-isolated species. Vibrational relaxation rates of NH and ND ($A^3\pi$) are independent of temperature to within 10% for T < 25 K in Ar and T < 37 K in Kr,[10] as are those of NH and ND ($X^3\Sigma$) in Ar for T < 30 K.[23] It has recently been observed[24] that the decay time of isolated CH_3F in Kr increases by a factor of about 1.2 between 10 and 60 K. Two possible causes of a temperature dependence which will be discussed are host effects due to phonon participation and guest effects due to J level dependent relaxation rates.

It is likely that the rate-determining V→R step will involve some phonon participation to conserve energy, as shown in Fig. 6, and stimulated phonon processes will produce a temperature dependence to the rate. For exothermic one phonon processes, the relaxation rate will be

proportional to $1 + \bar{n}$, where $\bar{n} = [\exp(h\omega/kT) - 1]^{-1}$ is the thermal occupation number of a phonon mode of frequency ω. Endothermic processes which require phonon absorption are proportional to $\bar{n}$. Temperature dependences predicted by endothermic processes are too great to fit the experimental observations. The temperature dependence for vibrational relaxation of HCl/Ar is fit by exothermic processes in Fig. 7. The temperature dependence of k_{21} and k_{10} can be fit by phonons of 12 ± 5 and 20 ± 10 cm^{-1}, respectively. More than one phonon may conceivably be involved in the exothermic process. For any higher energy phonons involved (up to 64 cm^{-1} for Ar and 73 cm^{-1} for the HCl/Ar localized mode) the temperature dependence will be negligible in the range 10-20 K (7-14 cm^{-1} thermal energy), so the temperature dependence would be determined by the lowest frequency phonon created during relaxation.

It is likely that detailed relaxation rates increase as the initial rotational level of the guest increases. The intuition behind this statement comes from studies of relaxation in the gas phase. Relaxation rates in the gas phase increase as the velocity of the collision partners increase, and rotational motion effectively adds its tangential velocity to the velocity of the collision pair.[25] The linear translational motion in the solid may be considered to arise from the guest oscillation in its localized mode. Since the ensemble relaxes from a thermal distribution of rotational states, at higher temperatures observed relaxation rates should be faster than at lower temperatures, since contributions from excited rotational levels become more heavily weighted. The temperature dependent relaxation rate will be given by

$$k(T) = \frac{1}{Q(T)} \sum_J g_J \, e^{-E(J)/kT} \, k^J \qquad (2)$$

Figure V-7. Phonon participation in HCl/Ar V→R processes. Data is for temperature dependent isolated molecule V→R rates from Table V-1. Solid curves are normalized to 9 K relaxation rate and are calculated for exothermic phonon processes, which are proportional to $1 + \bar{n}$. Phonon energies: v=2 → 1; a = 7 cm^{-1}, b = 12 cm^{-1}, c = 17 cm^{-1}; v=1 → 0, d = 10 cm^{-1}, e = 20 cm^{-1}, f = 30 cm^{-1}.

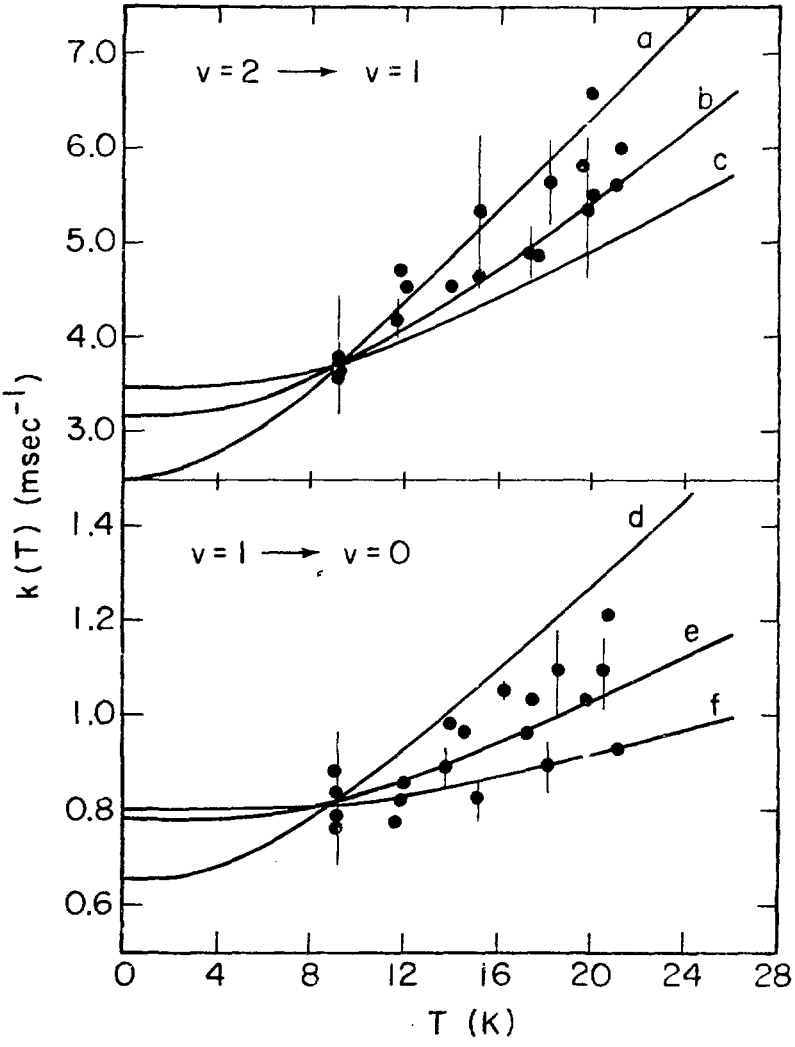

XBL 7710-6896

where Q(T) is the guest partition function (including rotation and the local phonon modes) and g_J, E(J), and k^J are the degeneracy, energy, and relaxation rate of the rotation-translation level J.[26] For HCl/Ar, the partition function can be calculated from the energy level diagram of Fig. III-11:

$$Q(T) = 1 + 3e^{-17/kT} + 5e^{-43/kT} + 3e^{-73/kT} + \ldots \quad (3)$$

with energies expressed in cm^{-1}. Equation (2) can be simplified to a two parameter form if only J=0 and J=1 are considered for HCl/Ar:

$$k(T) = k^1 + n_0(T)[k^0 - k^1] \quad (4)$$

where $n_0(T) = 1/Q(T)$ is the Boltzmann factor for J=0. Equation (4) should not be too unreasonable since from Eq. (3) 89% of the guest HCl is in J=0 or J=1 at 21 K, and an even higher percentage is in J=0 and J=1 at lower temperatures. The data for HCl/Ar is fit to Eq. (4) in Fig. 8. The fit of the data is acceptable, but is not compelling evidence for the validity of Eq. (4). The values for k^0 and k^1 are reasonable for both v=2 → 1 and v=1 → 0 relaxation. For v=2 → 1: $k^0 = (2.9 \pm 0.8) \times 10^3$ and $k^1 = (7.7 \pm 0.3) \times 10^3$ sec^{-1}; for v=1 → 0: $k^0 = (6.6 \pm 2.3) \times 10^2$ and $k^1 = (1.4 \pm 0.1) \times 10^3$ sec^{-1}. The influence of higher J levels can be estimated if a form for k^J is adopted. Assuming that k^J increases linearly with J, so that $k^J = k^0(1+aJ)$, the data for HCl/Ar gives: v=2 → 1: $k^0 = 3.0 \times 10^3$, $k^1 = 6.0 \times 10^3$ sec^{-1}, and $a = 0.99$; v=1 → 0: $k^0 = 6.7 \times 10^2$, $k^1 = 1.1 \times 10^3$ sec^{-1}, and $a = 0.66$. The values of k^0 for the second model are in excellent agreement with those obtained from Eq. (4), and the agreement with k^1 is good. Due to the low population of J ≥ 2 for T<21 K, values for k^0 and k^1 are insensitive to the choice of model.

Figure V-8. J-level dependent relaxation of HCl/Ar. Data of Table V-1 is fit to Eq. (V-4). $n_0(T)$ is the Boltzmann factor for J=0. Results of fit: $v=2 \rightarrow 1$, $k^0 = (2.9 \pm 0.8) \times 10^3$, $k^1 = (7.7 \pm 0.3) \times 10^3$ sec^{-1}; $v=1 \rightarrow 0$, $k^0 = (6.6 \pm 2.3) \times 10^2$, $k^1 = (1.4 \pm 0.1) \times 10^3$ sec^{-1}.

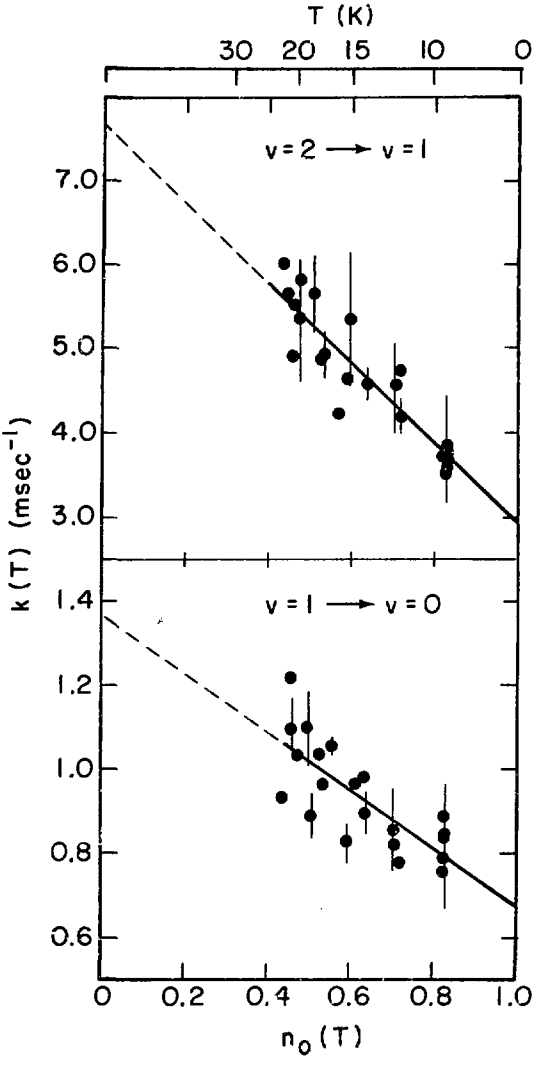

XBL 7710-10003

It is certainly reasonable that the relaxation rate of HCl in its first excited translational state, n=1, will be faster than in n=0. In the temperature range 9-20 K, however, the thermal population of n=1 will be small (from Eq. (3) it will be 0.7% at 20 K), so temperature effects due to the excited translational state will be unobservable if $k^{n=1}/k^{n=0} < 20$.

The temperature dependence for HCl/Ar is probably due to a combination of phonon and rotational effects; it is not possible to experimentally distinguish between the two. That other systems studied exhibit smaller temperature effects must mean that for these systems the rate-determining step involves only high frequency phonons or no phonons at all, and that the detailed rate constants do not vary much from ground to excited rotational state. The explanation for the smaller (null?) temperature dependence of NH and ND relaxation rates relative to HCl is found in the significantly lighter mass of NH and ND, which should make the local mode frequency of NH and ND higher than that of HCl.[27] If phonons created in the relaxation process are predominantly in the local mode, they will not produce an observable temperature dependence. Since the local mode frequency of NH is higher than that of HCl its "velocity" during a collision will be higher than that of HCl, and hence the additional velocity due to rotation will be proportionally smaller and less influential than for HCl. Furthermore, for NH^{10} (but not ND) the first excited rotational level lies higher in energy than J=1 of HCl, and so at any temperature NH will have a smaller population in J=1 than will HCl. All of these reasons would make the temperature dependence of NH smaller than that of HCl, as is observed. The comparison illustrates the importance of the

local mode in determining the temperature dependence of vibrational relaxation rates.

3. Energy Diffusion Related Processes

The increase of k_{10} for HCl/Ar for M/A < 2000 indicates the appearance of a new deactivation channel. Two effects of concentrated samples may contribute to the new relaxation channel: 1) decreased HCl-HCl distances can allow v=1 excitation to more readily diffuse about the sample, as discussed in Chapter IV, thereby increasing the range of V→V transfer to some energy accepting species present in the sample at low concentration. 2) New species which may be energy acceptors, such as the HCl dimer, exist in increasing quantities in concentrated samples. No evidence for non-exponential decay of HCl v=1 is observed, so energy diffusion within the HCl system averages the environments of different HCl molecules and the kinetics of the V→V transfer from v=1 can be described by a rate expression given by Eqs. (IV-16) or (IV-17). The population of v=1 behaves according to Eq. (IV-27) with b=0.

The calculations for the diffusion constant, Eq. (IV-13), and the number of hops, Eq. (IV-14) involves sums over all lattice sites starting with the nearest neighbors. If an HCl molecule had another HCl as its nearest neighbor, it would be part of a dimer and could not participate in diffusion of monomer vibrational energy. In fact, HCl molecules in close sites could exert strong forces on each other, and what is observed as isolated molecules may be separated by a minimum number of lattice shells, or, a minimum distance, R_o. Thus, the sum from which Eq. (IV-13) is derived,[11] and the sum in Eq. (IV-14) should

be started at a lattice shell for sites separated by at least R_o. The sum may be replaced by an integral with only a small error which diminishes rapidly as R_o increases. Following Legay,[11] the diffusion coefficient is, for dipole-dipole coupling:

$$D = \frac{C_{DD}x_D}{6} \sum_i \frac{1}{L_i^4}$$

where L_i is the distance from site 0 to the i^{th} lattice site. Replacing the sum by an integral

$$D = \frac{\rho C_{DD}x_D}{6} \int_{R_o}^{\infty} \frac{4\pi R^2 dR}{R^4} = \frac{2\pi\rho C_{DD}x_D}{3R_o} \tag{5}$$

where ρ is the number density of lattice sites (number/cm^3). The number of hops of the excitation in time t, N, is given by

$$N = x_D C_{DD} t \sum_i \frac{1}{L_i^6} \rightarrow \rho x_D C_{DD} t \int_{R_o}^{\infty} \frac{4\pi R^2 dR}{R^6}$$

$$N = \frac{4}{3}\pi\rho \frac{x_D C_{DD} t}{R_o^3} \tag{6}$$

Requiring R_o to be greater than the nearest neighbor distance implies a non-statistical distribution of HCl monomers. The following model is reasonable. All HCl molecules in the matrix closer to another HCl than R_o are able to aggregate (most likely to dimers), perhaps during deposition, and hence are removed from the monomer system. Monomers more distant than R_o are sufficiently translationally restrained during deposition (or annealing) so that they do not aggregate. Thus, for mutual separations greater than R_o the monomer distribution

is random. Given an HCl molecule at the origin, the random probability of another being within R_o of the first is $\frac{4}{3}\pi R_o^3 \rho x_{HCl}$, where x_{HCl} is the HCl mole fraction. This expression is valid when the probability is much less than one; a more general expression for pair probabilities is given by Allamandola, et al.[22] Molecules closer than R_o become dimers, so the probability of two molecules being within a distance R_o is equal to the relative concentrations of HCl molecules in dimer to HCl monomers; hence

$$\frac{x_{dimer}}{x_{monomer}} = \frac{4}{3}\pi R_o^3 \rho x_{HCl} \qquad (7)$$

where x_{HCl} is the mole fraction for HCl of all forms--it is the reciprocal M/A value. From the measured monomer and dimer concentrations of Table II, values of R_o are calculated. R_o is in the range of 5-7 Å, for the unannealed samples, which corresponds to a distance of about two nearest neighbor separations. Physically, this seems very reasonable: HCl molecules deposited within a lattice spacing aggregate, those further away are translationally restrained from aggregating. Upon annealing, R_o increases--the two values shown in Table II are 16 and 24 Å. This is also physically reasonable, since limited translation occurs during annealing. It is likely that the range of R_o values subsequent to annealing will be large, since the degree of aggregation depends greatly on the conditions of the diffusion process which vary somewhat from sample to sample; only two annealed samples are listed in Table II, however.

Calculation of the diffusion constant or number of hops requires calculation of the dipole-dipole coupling constant, Eq. (IV-10), for HCl

monomer as both donor and acceptor. Energy diffusion is a resonant process, and can occur on all transitions between thermally occupied levels. The overlap integral in Eq. (IV-10) should therefore be a sum of overlap integrals for each coupled transition, weighted by the Boltzmann factors for the initial level of both donor and acceptor molecules. Assuming that the lineshapes are Lorentzian the overlap integral for each transition is given by Eq. (IV-12), and the overall overlap integral of Eq. (IV-10) may be written as:

$$\int \frac{f_D(\nu) f_A(\nu)}{\nu^6} d\nu = \sum_t \frac{1}{\nu_{a,b}^6} \frac{1}{\pi \Delta\nu_{a,b}} p(J_a') \; p(J_b'') \qquad (8)$$

where $\nu_{a,b}$ and $\Delta\nu_{a,b}$ are the frequency, (cm^{-1}) and linewidth (FWHM) of the transition t connecting the rotational level J_a' of v=1 with J_b'' of v=0. $p(J_a')$ and $p(J_b'')$ are Boltzmann factors for the rotational levels. The relevant transitions for HCl/Ar are R(0), P(1), R(1), and P(2). Diffusion constants for HCl (v=1) and (v=2) at 9 and 20 K are calculated from Eqs. (IV-10), (5) and (8), using Boltzmann factors from Eq. (3) and an average R_o value of 6 Å, and are given in Table VIII for several different M/A ratios. The number of hops made during the V→R lifetime of the excitation, N, calculated by Eq. (6) with R_o = 6 Å, and t equal to 1.3 and 1.0 ms for v=1 and 0.28 and 0.18 ms for v=2 at 9 and 20 K, is included in Table VIII.

Most of the resonant transfer occurs via P(1) and R(0) transitions, since the broadening of the level J=2 and its small thermal population make the terms in Eq. (8) corresponding to R(1) and P(2) very small: at 9 K less than 0.1% and at 20 K less than 6% of the resonant energy transfer involves J=2. For transfer on the R(0) and P(1) transitions,

Table V-VIII. Diffusion Constant and Hops for v=1 and v=2 of HCl/Ar[a]

M/A	v=0 ↔ v=1				v=0 ↔ v=2			
	D(9K) (cm^2/sec)	N(9K)[b]	D(20K) (cm^2/sec)	N(20K)[c]	D(9K) (cm^2/sec)	N(9K)[d]	D(20K) (cm^2/sec)	N(20K)[e]
100	1.2(-7)	8.6(4)	8.1(-8)	4.5(4)	1.4(-11)	2.2	9.7(-12)	1.0
500	2.4(-8)	1.7(4)	1.6(-8)	9.0(3)	2.9(-12)	.44	1.9(-12)	.20
1000	1.2(-8)	8.6(3)	8.1(-9)	4.5(3)	1.4(-12)	.22	9.7(-13)	.10
2500	4.7(-9)	3.4(3)	3.2(-9)	1.8(3)	5.7(-13)	8.9(-2)	3.9(-13)	4.0(-2)
5000	2.4(-9)	1.7(3)	1.6(-9)	9.0(2)	2.9(-13)	4.4(-2)	1.9(-13)	2.0(-2)
10,000	1.2(-9)	8.6(2)	8.1(-10)	4.5(2)	1.4(-13)	2.2(-2)	9.7(-14)	1.0(-2)

[a] Powers of ten given in parenthesis: $2.4(-8) = 2.4 \times 10^{-8}$.

[b] t = 1.3 ms.

[c] t = 1.0 ms.

[d] t = 0.28 ms.

[e] t = 0.18 ms.

the overlap is reduced by broadening of the transition as temperature increases. This is offset by an increase in the product of Boltzmann factors, the net result being a slight decrease in D and N as temperature increases. N is also shortened since the V→R time which limits the number of hops decreases as the temperature increases.

That relaxation of v=2 should be concentration independent is immediately obvious upon examination of Table VIII, since for M/A > 500, v=2 excitation on the average makes less than one hop during its V→R lifetime. The immobility of v=2 excitation is due to the fact that the overtone transition moment is quite small and hence C_{DD} is small (see Eq. (IV-10)). Because v=2 excitation is essentially confined to the molecule initially excited by the laser pulse, only acceptor species present in massive concentrations or with enormous C_{DA} values could compete with V→R relaxation; no such acceptors are present. At M/A = 100 the average HCl-HCl distance has shortened enough to enable some movement of v=2 excitation; this motion of v=2 along with the presence of large amounts of polymeric species in a concentrated sample may rationalize the observation that decay of v=2 is not a simple exponential at M/A = 123. It is unlikely that the decay of v=2 at M/A = 123 is due to V→V transfer to HCl v=0, establishing equilibrium between v=2 and v=1. If equilibrium were established, it would, due to anharmonicity of the vibration, be weighted toward v=2. In this case, the amplitude for the initial fast decay would be small. If, neglecting the previous conclusion, the initial fast decay of the v=2 fluorescence were due to establishment of equilibrium between v=2 and v=1, fluorescence from v=1 should have been of comparable intensity to that of v=2 (neglecting small optical density effects) since the

amplitudes of fast and slow decay of v=2 are nearly equal. Thus, non-resonant V→V transfer within the HCl monomer system is not reasonable in this sample. That the v=2 decay is independent of concentration for M/A > 500 argues against any such V→V processes in more dilute samples.

It is apparent from Table VIII that v=1 excitation moves substantially during its lifetime; even in the most dilute sample of M/A = 10,000 v=1 excitation makes several hundred hops. At M/A = 1000 v=1 excitation makes 9000 hops. How much motion of the v=1 excitation is enough to be considered fast diffusion? As a result of making N hops, the excitation samples the environment around N sites. If the local environment of at least one of these sites has an acceptor species nearby, the excitation is able to sample the strongest donor-acceptor interaction at least once during its V→R lifetime; this should correspond to the case of fast diffusion since the strongest and weaker donor-acceptor interactions are experienced by the same quantum. How close to the monomer upon which the excitation resides corresponds to "nearby?" If the acceptor were in the nearest neighbor shell, the HCl molecule would not be isolated and hence would not be a member of the set of isolated molecules through which the excitation diffuses; indeed, it may act as an energy sink. We may take the sphere of neighbors beyond the first nearest neighbors as "nearby." For fcc lattices, there are 42 sites between one and two nearest neighbor distances.[28] The number of nearby sites experienced by a v=1 quantum during its V→R lifetime is $42N$, so the condition for fast diffusion is

$$42Nx_A \gtrsim 1. \qquad (9)$$

Equation (9) may be overly stringent, since nearby could mean the range extending to one shell beyond the R_o calculated in Table II. If Eq. (9) is satisfied, however, almost certainly the fast diffusion limit is applicable. For M/A = 1000 at 9 K, the data of Table VIII suggests that for $x_A > 3 \times 10^{-6}$ V→V transfer is in the fast diffusion regime.

Various candidates which can accept HCl (v=1) excitation are shown in Fig. 9. It has been observed that non-resonant V→V transfer probabilities decrease as the energy gap between donor and acceptor increases.[29] The infrared active vibrational level of the HCl dimer, 2818 cm^{-1}, is more nearly resonant with HCl v=1 than is any other HCl polymer species or impurity likely to be found in Ar or HCl gas, or matrix, with the exception of the HCl-N_2 complex. However, the HCl-N_2 complex could be reduced to subspectroscopic concentration and was for most samples. The dimer is always present in concentrated samples, however, and in samples with dimer but no visible HCl-N_2 absorption, the k_{10} rate is faster than the isolated molecule value of $8. \times 10^2$ sec^{-1}. It is possible that HCl-N_2 also acts as an energy acceptor, however, and its uncontrolled and often unknown (subspectroscopic) concentration could be responsible for some scatter in the V→V data. The most likely and prominent acceptor for v=1 excitation is the HCl dimer. Indeed, transfer of excitation by a coupled P(1) transition of the monomer with a Δv=1 transition of the dimer is exothermic by 36 cm^{-1}, which corresponds to a peak in the phonon spectrum of Ar,[30] resulting in a large density of final states for this process. Diffusion aided V→V transfer to the dimer is shown schematically in Fig. 10.

From Table II, at M/A ~ 1000, $x_{dimer} \geq 1 \times 10^{-5}$. The condition of Eq. (9) is satisfied by a factor of five. This is in the direction of

Figure V-9. Possible energy acceptors for HCl/Ar. No rotational structure of the monomer transitions are shown. HCl-N_2 and HCl dimer are the species resonant with HCl v=1 within the range of lattice phonons. The HCl trimer is lower in energy than the P(1) transition of HCl v=1 (2854 cm^{-1}) by 67 cm^{-1}, which lies between the Debye frequency for Ar, 64 cm^{-1}, and the local mode frequency, 73 cm^{-1}.

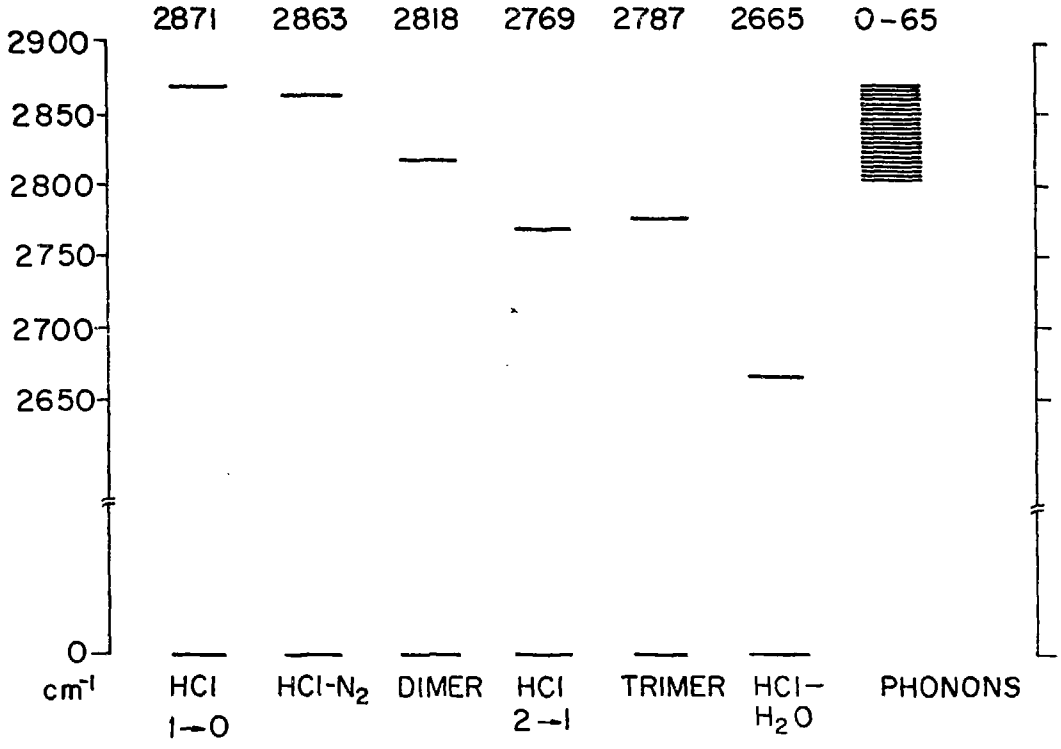

XBL7612-10765

Figure V-10. Schematic of diffusion-aided V→V transfer from HCl v=1 to dimer. Diffusion within the HCl system is shown to occur on coupled R(0) or P(1) transitions. Transfer to dimer coupled with a P(1) monomer transition is exothermic by 36 cm^{-1}, as illustrated.

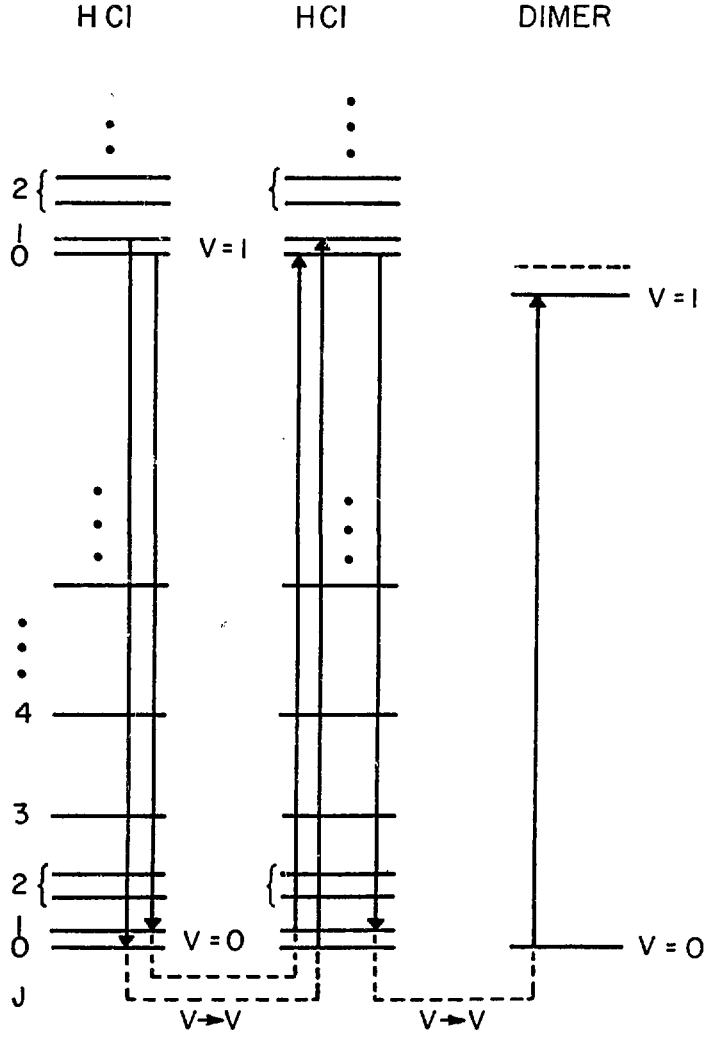

XBL 7710-10005

fast diffusion, but not overwhelmingly so. For M/A = 500, $x_{dimer} \sim 5 \times 10^{-5}$, and using Table VIII, each quantum of v=1 should experience 36 close dimers--this should certainly be the fast diffusion regime.

The relative distribution of monomers and dimers is unknown. We have argued only that they cannot be first nearest neighbors. Equation (IV-16) is applicable in the fast diffusion limit if the contribution from nearest neighbors, which is a factor of $12.00/d_o^{6}$ [28] is removed from the sum. Hence

$$k-k_0^D = \frac{2.45 x_A C_{DA}}{d_o^6} \qquad (10)$$

where $d_o = 3.76$ Å in Ar. Values for C_{DA} for monomer-dimer coupling are calculated from Eq. (10) and presented for 9 and 20 K data in Table II. Values are calculated only for those samples for which the uncertainty in $(k-k_0^D)$ is less than 100%.

The values of C_{DA} in Table II vary by factors of 20. This reflects, partly, the combination of uncertainties in measuring monomer and dimer concentrations, and the ract that the uncertainty in k is made more prominent when k_0^D is subtracted from it. The very low value of C_{DA} for the annealed sample of M/A = 920 may reflect the fact that the monomer concentration has declined after annealing to the point where diffusion may no longer be rapid and that dimers have become separated from monomers by a longer distance after diffusion. For this sample, however, $42Nx_{dimer} \sim 25$. The average for C_{DA} is performed on logarithms of C_{DA}, and the error is one standard deviation of the fit. The average value for C_{DA} from HCl monomer to dimer, 6×10^{-38} cm^6/sec^{-1} (range is 1.6×10^{-37} to 2.5×10^{-38}), should be compared to the HCl monomer C_{DD} value, for R(0) or P(1) transitions, which is 4.6×10^{-35} cm^6/sec at 9 K,

calculated from the data in Appendix C. Coupling to dimer is 10^{-2} - 10^{-3} times weaker than monomer-monomer coupling. Since V→V transfer to dimer occurs with creation of a phonon, the V→V process of Eq. (IV-10) could be viewed as overlap of the HCl monomer transition with a phonon sideband of the dimer transition. No phonon sideband to the dimer transition is spectroscopically observed, and this is entirely consistent with the C_{DA} value which indicates that such a sideband would be at least 300 times less intense than the dimer zero phonon line, since the dimer integrated absorption coefficient is larger than that of the monomer.

The values of C_{DA} at 20 K are a bit higher than those at 9 K, although the error limits of the 9 and 20 K values overlap. Four factors could cause a temperature dependence to the monomer-dimer V→V rate: a) the diffusion constant decreases with temperature, b) stimulated phonon processes increase with temperature increasing the rate, c) linewidths of transitions participating in the non-resonant V→V step increase with temperature increasing effective spectral overlap of donor and acceptor, and d) the Boltzmann distribution of participating levels changes with temperature. In the temperature range between 9 and 20 K none of these factors could be expected to change the V→V rate very much.

It is conceivable that diffusion aids V→V transfer to an unidentified trace contaminant in the system. For fast diffusion the relaxation rate has a concentration dependent part that varies with x_A and for intermediate diffusion it varies as $x_{HCl}^{3/4} x_A$, since $D \propto x_{HCl}$. If an impurity is systematically present at small concentration in the Ar used in these experiments, it will be present at fixed mole fraction, x_i, in

all samples. For fast energy diffusion, the v=1 decay rate will be independent of concentration, since $x_A = x_i$ is constant for all samples; experiment negates this possibility. For intermediate diffusion, the v=1 decay rate will be proportional to $(x_{HCl\ monomer})^{3/4}$, since resonant energy transfer occurs only within the HCl monomer system. Comparison of the samples of M/A = 527 and M/A = 2380 in Table II suggests that this could not explain reality, since the ratio of diffusion constants for these samples is 3.2, and this is the maximum value for the ratio of relaxation rates, while the experimental ratio of relaxation rates is 10±3. A second possibility is that a systematic impurity is introduced with the HCl, in which case the impurity concentration, x_i, is proportional to x_{HCl}. Again comparing the samples of M/A = 527 and M/A = 2380, the fast diffusion predicts a maximum ratio of rates of (2380/527) = 4.5, which is too small to explain the data. For the intermediate diffusion case, the predicted relaxation rate is proportional to $(x_{HCl\ monomer})^{3/4}(x_{HCl})$ and yields a numerical value of 14 for the maximum value of the ratio of rates for the M/A = 527 and M/A = 2380 samples, within experimental uncertainty of the measured result. However, intermediate diffusion to an impurity introduced with the HCl could not explain the results of the two annealed samples (M/A = 920 and M/A = 5100) listed in Table II, since in these cases the HCl monomer concentration decreases relative to the unannealed sample, and presumably x_i would be unaffected by annealing, yet the relaxation rate increases. Thus, analysis of the concentration dependent data of Table II on the assumption that an impurity in fixed relative proportion to either the HCl or the Ar is responsible for the increase of k_{10} with concentration fails. Furthermore, it is difficult to conjecture a

contaminant of HCl or Ar that would match the vibrational energy of HCl as well as the species of Fig. 9, so on energy gap considerations the concentration dependence of k_{10} should not be due to a reagent contaminant.

The results of this section depend a great deal on the models chosen to represent the HCl monomer distribution and the monomer-dimer distribution. The particular values for C_{DA} depend on the decision that only first nearest neighbor positions cannot be occupied by dimer. If, in fact, the minimum monomer-dimer separation is taken to be equal to the R_o values of Table II, the 9 K average value of C_{DA} becomes $10^{-37\pm0.4}$. The range of C_{DA} values, however, is unchanged. C_{DA} is only a factor of two different from the value in Table II. In view of the range of individual values of C_{DA}, the difference is negligible. If the fast diffusion limit is valid, it is likely that the distribution of dimers would not be so non-random that the true C_{DA} value is different from $10^{-37\pm1}$ cm^6/sec.

The selection of the fast diffusion limit depends on the value of R_o, since this affects N. As R_o increases, the number of hops decreases. The calculation of R_o from dimer/monomer ratios seems reasonable and the resulting R_o values seem physically reasonable. Nevertheless, the condition of Eq. (9) is fulfilled by a small margin, and a larger R_o might argue against a fast diffusion situation for the present samples. The criterion imposed for Eq. (9) may be too stringent, however, so even with a larger R_o, the fast diffusion regime could be appropriate.

A problem concerning the distribution of HCl monomers arose in connection with the resonant dipole-dipole rotational energy transfer mechanism for line broadening in Chapter III. The model presented was

over-simplified, but suggested that for HCl/Ar, M/A = 123, the minimum separation between isolated monomers consistent with observed linewidths was R_o = 37 Å. The very large value for R_o may in part be an artifact of the over-simplified model. Since the linewidth depends on R_o^{-3}, however, it is hard to see how a proper averaging procedure, as discussed in Section III.D.3, could alter R_o by a factor of 7. The value of R_o for line broadening ought to be consistent with R_o values determined from dimer/monomer concentration ratios and V→V transfer considerations, since all refer to the same sample. Proper treatment of the rotational line-broadening mechanism, hopefully, will resolve the problem. For a value of R_o = 37 Å, Eq. (6) predicts that, for M/A = 123, v=1 excitation makes only 300 hops.

It is worthwhile to comment on the DCl v=1 → 0 relaxation again. The large value of k_{10} relative to k_{21} makes it unlikely that k_{10} is due totally to V → R,P relaxation, so that a non-resonant V→V process to some acceptor must be occurring. That k_{10} is of the same order of magnitude as k_{21} indicates a weak V→V coupling to the acceptor, however, due to either a small C_{DA} or low acceptor concentration. The identity of the acceptor is unknown. For the dilute samples listed in Table VII, no dimer is observed. The measured value of k_{21} should certainly be free of V→V effects, since DCl v=2, like HCl v=2, is not mobile in dilute samples.

In summary, it seems probable that the concentration dependence of the HCl/Ar v=1 relaxation rate is due to non-resonant V→V transfer to the HCl dimer. Quantitative analysis of this process depends upon the microscopic distribution of HCl monomers and dimers in the matrix, which must be at least partially non-random. The most reasonable choices concerning

the microscopic monomer and dimer distributions lead to the result that monomer-dimer coupling is about 10^{-2}-10^{-3} times weaker than monomer-monomer coupling.

4. Dimer Relaxation

No fluorescence is observed upon excitation of the HCl dimer, implying that the relaxation of the IR active dimer vibration is faster than 0.3 μs. Two explanations are possible. First, the 2818 cm^{-1} vibration of the dimer may decay into the 232 cm^{-1} bending mode of the dimer.[31] This process is lower order than the V→R relaxation of the isolated monomer, and would be expected to be more rapid.

The second explanation involves the symmetric vibration of the dimer. Rapid equilibration between asymmetric and symmetric vibrations of the dimer would favor excitation in the symmetric mode if the symmetric mode is lower in energy. Then, even if excitation persisted for long times, it might not be detectable since the IR fluorescing mode has only a small population. Simple calculations based on a cyclic geometry[32] or a head to tail geometry[33] for the dimer both predict a symmetric mode at 2795 cm^{-1}, 23 cm^{-1} below the IR active asymmetric mode. In these calculations the intermolecular force constant coupling the two adjacent HCl molecules into a dimer is taken equal to the intermolecular force constant of solid HCl.[34] Equilibrium between two modes separated by 23 cm^{-1} requires 3% and 19% population in the higher mode at 9 and 20 K. If fluorescence was not detectable at 9 K due to small population in the IR active mode, it would have been visible at 20 K unless deactivation is rapid or the modes were separated by more than 60 cm^{-1}. The latter figure comes from analysis of the sample of M/A =

670, discussed in Section A. A splitting of 60 cm^{-1} is too large to be consistent with the HCl-HCl intermolecular force constant derived from spectra of pure solid HCl.[34]

5. Relaxation in N_2 and O_2 Matrices

Spectroscopic observations indicate that at thermal energies below 20 K HCl does not undergo rotation in the molecular matrices N_2 and O_2. It is unlikely that the barrier to rotation is as large as 2800 cm^{-1}, however, so at energies corresponding to that of a vibrational quantum, rotational motion should be less restricted. V→R relaxation into rotational motion should occur on a time scale similar to that for HCl/Ar. V→V transfer from HCl to the vibron band of the host lattice is a possibility in N_2 and O_2 host lattices that is not present in an Ar lattice, and it is possible that the lack of observable fluorescence from HCl in the molecular lattices is due to such rapid V→V transfer. Transfer from HCl to the vibron band of α-N_2 at 2327 cm^{-1} [35] is exothermic by about 500 cm^{-1} and would be a low order process if excess energy is absorbed by local modes or lattice phonons. Hence, phonon (local mode) assisted V→V transfer should be rapid. Once the excitation has entered the host vibron band it cannot be observed in fluorescence, although it may persist for times as long as one second.[36] It is somewhat surprising that V→V transfer to the α-O_2 vibron mode at 1552 cm^{-1} [37] is so fast that no HCl fluorescence is observed, since 1200 cm^{-1} must be disspiated into phonons or local modes. However, α-O_2 has an acoustic phonon mode of 79 cm^{-1} [37] so the order of the V→V process with respect to phonon or local mode participation is less than 15.

The suggestion that the rapid relaxation in N_2 and O_2 is due to rapid V→V transfer from HCl to the host vibron band cannot be tested for pure N_2 and O_2 lattices. To confirm the suggestion, however, a study of HCl in a CO lattice would be useful. The crystal structure of CO is nearly identical to that of N_2 (see Table II-1) so that the behavior of HCl in CO should be similar to that in N_2. (Guest-host interactions will be dipole-dipole instead of dipole-quadrupole, however.) V→V transfer to the host would be visible as CO fluorescence. Also, a N_2 matrix doped with CO as well as HCl could indicate that V→V processes are responsible for HCl deactivation, since CO should trap the vibrational energy and subsequently fluoresce. CO fluorescence would be unaffected by self-trapping.

CHAPTER V

REFERENCES

1. A. Nitzan and J. Jortner, Mol. Phys., 25, 713 (1973).

2. A. Nitzan, S. Mukamel, and J. Jortner, J. Chem. Phys., 60, 3929 (1974).

3. A. Nitzan, S. Mukamel, and J. Jortner, J. Chem. Phys., 63, 200 (1975).

4. J. Jortner, Mol. Phys., 32, 379 (1976).

5. D. J. Diestler, J. Chem. Phys., 60, 2692 (1974).

6. S. H. Lin, J. Chem. Phys., 61, 3810 (1974).

7. S. H. Lin, K. P. Lin, and D. Knittel, J. Chem. Phys., 64, 441 (1976).

8. S. H. Lin, J. Chem. Phys., 65, 1053 (1976).

9. L. E. Brus and V. E. Bondybey, J. Chem. Phys., 63, 786 (1975).

10. V. E. Bondybey and L. E. Brus, J. Chem. Phys., 63, 794 (1975).

11. F. Legay in Chemical and Biological Applications of Lasers, Vol. II, C. B. Moore, ed., Academic Press, New York (1977), Chapter 2.

12. D. H. Rank, D. P. Eastman, B. S. Rao, and T. A. Wiggins, J. Opt. Soc. Am., 52, 1 (1962).

13. H. Dubost, Chem. Phys., 12, 139 (1976).

14. G. Herzberg, Spectra of Diatomic Molecules, Van Nostrand, Princeton (1950).

15. H. Dubost and R. Charneau, Chem. Phys. 12, 407 (1976).

16. H. Friedmann and S. Kimel, J. Chem. Phys., 43, 3925 (1965); calculated for the limit of large J from Eq. (49) of this paper.

17. P. D. Mannheim and H. Friedmann, Phys. Stat. Sol., 39, 409 (1970); see also Chapter III.

18. See however, C. D. Downey, D. W. Robinson, and J. H. Smith, J. Chem. Phys., 66, 1685 (1977).

19. See Chapter VI.

20. R. G. Macdonald and C. B. Moore, to be published.

21. S. R. J. Brueck and R. M. Osgood, Chem. Phys. Lett., 39, 568 (1976).

22. L. J. Allamandola, H. M. Rojhantalab, J. W. Nibler, and T. Chappell, J. Chem. Phys., 67, 99 (1977).

23. V. E. Bondybey, J. Chem. Phys., 65, 5138 (1976).

24. L. Abouaf-Marguin, B. Gauthier-Roy, and F. Legay, Chem. Phys., 23, 443 (1977).

25. C. B. Moore, J. Chem. Phys., 43, 2979 (1965).

26. The rotational level structure is taken to include the first excited level of the local mode vibration of the guest molecule, (three-fold degenerate).

27. A. S. Barker and A. J. Sievers, Rev. Mod. Phys., 47, Suppl. 2 (1975).

28. J. O. Hirschfelder, C. F. Curtiss, and R. B. Bird, Molecular Theory of Gases and Liquids, Wiley, New York (1954), p. 1037.

29. J. Goodman and L. E. Brus, J. Chem. Phys., 65, 1156 (1976).

30. D. N. Batchelder, M. F. Collins, B. C. G. Haywood, and G. R. Sidey, J. Phys. C, Sol. State Phys., 3, 249 (1970).

31. B. Katz, A. Ron, and O. Schnepp, J. Chem. Phys., 47, 5303 (1967).

32. A. J. Barnes, H. E. Hallam, and G. F. Scrimshaw, Trans. Faraday Soc., 65, 3150 (1969).

33. L. F. Keyser and G. W. Robinson, J. Chem. Phys., 45, 1694 (1966).

34. R. Savoie and A. Anderson, J. Chem. Phys., 44, 548 (1966).

35. A. Anderson, T. S. Sun, and M. C. A. Donkersloot, Can. J. Phys., 48, 2265 (1970).

36. K. Dressler, O. Oehler, and D. A. Smith, Phys. Rev. Lett., 34, 1364 (1975).

37. J. E. Cahill and G. E. Leroi, J. Chem. Phys., 51, 97 (1969).

CHAPTER VI

THEORETICAL ASPECTS OF RELAXATION OF AN ISOLATED GUEST

The energy initially put into a matrix isolated molecule in the form of localized vibrational excitation will ultimately be randomized into the lowest energy, highest density, thermally accessible modes--the delocalized lattice phonons. For HCl in Ar, one quantum of molecular vibration of 2871 cm^{-1} (v=1) must produce at least 45 delocalized phonons (ω_D = 64 cm^{-1} for solid Ar). In this Chapter, we consider the theoretical aspects of the vibrational relaxation of an isolated guest molecule in a host lattice, using HCl/Ar as the most frequent example. The first theoretical treatments considered the direct coupling between lattice phonons and the molecular vibrations. These multiphonon theories predicted large temperature effects on relaxation and the existence of an energy gap law: molecules with the highest frequencies relax most slowly. Experiment has shown that relaxation rates are nearly independent of temperature and that the energy gap law is often violated (by hydride-deuteride pairs, in particular). As discussed in Chapter V, these experimental observations imply that guest rotation is the primary accepting mode in vibrational relaxation in solids. Theories of V→R relaxation in solids are just beginning to appear.

In spite of the lack of success of the multiphonon theories, they will be dealt with in Section A, since they are interesting in their own right. The quantitative results of HCl and DCl relaxation will be compared to the predictions of the theories, and the conclusion that multiphonon theories cannot explain vibrational relaxation in solids will be verified.

A new theory for V→R relaxation will be proposed in Section B. In this binary collision model, relaxation will be viewed in a conceptually similar manner to relaxation in the gas phase; relaxation will result from a collisional event of low probability. The model verifies the role of rotation as the energy accepting mode, and fits the HCl/Ar and DCl/Ar data very well. The theory is not intended to be overly quantitative. Its goal is to point out the major effects, provide a physical picture for relaxation, and correlate sets of existing data.

In Section C, two recent theories of V→R relaxation in solids will be reviewed. Finally, in Section D, the various theories will be compared.

A. Multiphonon Theories

In the multiphonon theories molecular vibration is coupled directly into lattice phonons, resulting in a high order process. The order is $N = \omega/\omega_p$, where ω is the molecular vibrational frequency and ω_p is the frequency of the phonon mode into which the molecular vibration relaxes, assuming an Einstein model for the crystal. The theories will be applied, here, to relaxation of HCl and DCl in Ar. The experimental details and results for these systems have been presented in Chapter V, and will be used as needed.

Multiphonon theories are of two types. In the first type, the molecule-medium interaction is taken to be linear in the coordinate of the molecular vibration.[1-6] The temperature dependence is due to the creation of N bosons (the phonons) for which stimulated processes are possible. The physical basis of the energy gap law is that lower order processes are more probable than higher order processes, and hence, for a particular phonon frequency, ω_p, rates decrease as ω increases.

Jortner and co-workers[3,4] and Lin and co-workers[5,6] have described the vibration-phonon interaction in terms of an exponential interaction between guest molecule and host atoms. The form of the energy gap law and temperature effect are given in Eqs. (1)[4] and (2),[6] respectively.

$$k(0) = D \exp(S)\, S^N/N! \qquad (1)$$

$$\frac{k(T)}{k(0)} = 1 + e^{-h\omega_p/kT}\left(N + 2S + \frac{S^2}{N+1}\right) \qquad (2)$$

k(0) is the decay rate at T=0 K; D is a factor relating to the magnitude of the interaction between the guest molecule and the host lattice with all molecules at their equilibrium positions, $N = (\omega/\omega_p)$ is the order of the process, and S is a phonon coupling strength related to the range parameter of the exponential interaction and to the normal mode coordinates of the lattice. S is estimated to be in the range 1-10.[3] In deriving these equations, the lattice is approximated as an Einstein crystal in that it is assumed that only one phonon mode of frequency ω_p is involved in the relaxation process. The value of S should be independent of isotopic composition of the guest molecule. The value of D is proportional to $(\mu\omega)^{-1}$ where μ and ω are the reduced mass and frequency of the molecular vibrator.

Assuming that for the accepting phonon mode of Ar $\omega_p = 60\ cm^{-1}$, the v=2 → 1 relaxations of HCl (2767 cm^{-1}) and DCl (2029 cm^{-1}) are processes of order N = 46.1 and 33.8, respectively. The presence of N! in the denominator of Eq. (1) causes relaxation rates to fall off rapidly with increasing order of the relaxation process. Large values of S due to very strong coupling of phonons with the molecular vibration can overcome this effect, however, and in fact, for S=44 Eq. (1) can yield

agreement with the observed ratio of 35 for the HCl to DCl rates at 9 K. A value of S=44 is considered unreasonably large.[3] Moreover, use of a value of S=44 in Eq. (10) to predict a temperature effect produces values of 1.0, 3.4, and 4.8 for the relaxation rates at 9, 20, and 24 K relative to the relaxation rate at 0 K. The 20 and 24 K results are much too large relative to the 9 K value to agree with experiment. The V→P process with an exponential repulsive interaction cannot simultaneously fit the isotope effect and temperature dependence of the HCl/Ar results.

A second V→P model invokes a Born-Oppenheimer type approximation to separate molecular vibration (vibron) motion from lattice vibrational motion.[7,8] Relaxation is due to non-adiabatic coupling of vibron and phonon motion by the anharmonic terms of the lattice-molecule potential function. Lin's formulation[7] predicts an energy gap law and temperature dependence given by Eqs. (3) and (4).

$$k(0) \sim \frac{B_\alpha}{\omega^3} \frac{e^{-\tilde{S}} \tilde{S}^N}{N!} \left(\frac{N}{\tilde{S}} + \frac{\tilde{S}}{N} \right) \tag{3}$$

$$\frac{k(T)}{k(0)} = 1 + e^{-h\omega_p/kT} \left(N - 2\tilde{S} + \frac{\tilde{S}^2}{N} + \frac{\tilde{S}^2}{N(N+1)} \right) \tag{4}$$

All symbols have been previously defined except $\tilde{S}$, which is a T=0 K phonon mode density weighted sum of the q^2Q anharmonic coupling, and B_α is the qQ coupling term in the potential energy expression. q and Q are the vibron and phonon geometric normal mode coordinates, and Eqs. (3) and (4) have been written for the Einstein crystal approximation. $\tilde{S}$ is the vibron equivalent of the Huang-Rhys factor[9] for optical excitation of impurities in crystals, and has spectroscopic implications. In the case of weak coupling to the lattice, $\tilde{S}$ is small and the absorption spectrum of the guest consists of a strong zero phonon line (ZPL) and a

weak phonon wing; the reverse is implied in the case of strong coupling, $\tilde{S}$ large.[9] The relative weight of the ZPL to the total integrated absorption is $\exp(-\tilde{S})$.[9]

The temperature effects for HCl/Ar can be fit with two ranges of $\tilde{S}$ values, due to the negative term in Eq. (4). Values of $\tilde{S}$ of 0-10 or 80-90 and 5-30 or 70-90 will fit the v=2 → 1 and v=1 → 0 results, respectively. B_α and $\tilde{S}$ should not depend much on isotopic composition[8] since the potential energy of the guest-host lattice system is due primarily to electronic interactions, which are independent of isotopes. For the case of HCl vs DCl, the normal mode structure of the lattice should be essentially identical, so the expansion coefficients in the potential energy expression should be not too different. Assuming this is the case, Eq. (3) was used to fit the ratio of the HCl/Ar to DCl/Ar v=2 → 1 rates at 9 K, with a resulting value for $\tilde{S}$ of 54-60. This value predicts a very small temperature effect between 9 and 20 K, less than 1.1 for HCl/Ar v=2 → 1. However, $\tilde{S}$ = 54 corresponds to the case of strong coupling, and requires a strong phonon wing in the IR absorption spectrum of HCl/Ar. The ZPL should account for a fraction of only 3×10^{-24} of the absorption; there should be no ZPL. In reality (Chapter III) no phonon wing is observed. Thus, the vibron-phonon model has difficulty explaining the results of the HCl/Ar system.

The multiphonon theories may be useful in explaining relaxation of low frequency molecular vibrations, or in accounting for the creation of a few phonons in a predominantly V→R step. They do not, however, explain the major features of relaxation of a high frequency guest vibration.

B. V→R Binary Collision Model

1. Introduction

In a low density gas, vibrational relaxation is a collisional event. Typically, relaxation is an improbable occurrence and many (>1000) collisions are required. In condensed phases, the concept of a collision is not well defined. Nevertheless, the isolated binary collision (IBC) model[10] asserts that, even in condensed phases, relaxation is given by

$$k = \Gamma P \tag{5}$$

where k is the relaxation rate, Γ is a collision frequency, and P is a relaxation probability per collision. In an early theory of vibrational relaxation in doped solids, Sun and Rice[11] utilized the IBC viewpoint. The collision frequency was due to motion of the guest and its nearest neighbor in the lattice normal modes, and the relaxation probability was the corresponding gas phase V→T probability. Sun and Rice predicted slow relaxation rates, but their model also predicted a large temperature effect and an energy gap law, both of which are consequences of multiphonon relaxation processes. The temperature effect arises from the collision frequency, and results from treating the lattice normal modes classically. The energy gap law is a result of the assumed V→T channel. (Note the correspondence between V→T and V→P processes, which is very clear from the results of Sun and Rice.) The original intent of Sun and Rice was to indicate that relaxation in solids might be slow, however, and was not to formulate a quantitative theory.

In this section the relaxation in doped solids is treated according to a binary collision viewpoint. The collision frequency is due to guest-neighbor motion in lattice normal modes. However, these phonon modes are now treated as quantum harmonic oscillators, and at the low temperatures appropriate to matrices, their motion is dominated by zero point effects. Hence, collision frequency becomes a very weak function of temperature.

Rotation has been identified as the primary accepting mode. Legay[12] has correlated experimental data to the expression:

$$k \propto e^{-\alpha J_f} \tag{6}$$

where $J_f = (\nu/cB)^{\frac{1}{2}}$ is the rotational level populated by V→R relaxation. In the present model, rotation is introduced into the probability expression using an effective reduced mass in the standard V→T formula. The effective reduced mass is dominated by the rotational reduced mass for molecules with light atoms, and the velocity after relaxation is carried away by the rotational motion of the light atom of the rotor. The importance of V→R and the violation of the energy gap law upon H to D substitution are consequences of this.

In the binary collision viewpoint, relaxation results from close encounters between guest and neighbors. The important part of the potential responsible for relaxation is the short range repulsive part--at short ranges this should be independent of the presence of other atoms in the solid and can be well approximated from gas phase potential data. The potential acting near the guest equilibrium site, which is responsible for the spectral perturbations of the guest, is ineffective in inducing relaxation.

A collision frequency is formulated in terms of quantized phonon modes in Section 2. The collision frequency is dominated by the guest local mode, when a local mode is present, and otherwise is weighted toward the higher frequencies of the lattice. The collision frequency can vary somewhat in numerical value, depending upon choice of parameters, but the conclusion that it is not strongly temperature dependent is independent of detailed model.

The relaxation probability in terms of V→R,T processes is formulated in Section 3. Various fits to data are attempted in Section 4. Legay's correlation, Eq. (6), is derived from a simple approximation to a more detailed expression. The available experimental data is fit by empirically determining the parameters for the model. The parameters so determined assume reasonable values. The model fits the experimental results for the HCl/Ar and DCl/Ar systems better than for other systems. In this case, potential parameters from HCl V→R,T relaxation by gaseous Ar do very well. Implications of the theory concerning different host media are then presented. Finally, comparisons of this model with an IBC model in liquids is made.

2. Collision Frequency

In this section the frequency of collisions between two neighboring molecules in a crystal lattice will be calculated. The concept of a collision is perhaps a bit ambiguous for a solid, in which neighboring atoms or molecules are always close and are continually under the influence of intermolecular forces. We shall, however, adopt the point of view of Sun and Rice[11] and define a collision to occur when the separation between two neighbors is reduced from the equilibrium value

by a distance q_o. The motion of atoms and molecules of the lattice will be described in terms of normal modes of the lattice, each mode considered as a quantum harmonic oscillator. The collision frequency will depend, in the low temperature regime appropriate to the present model, primarily on the zero point motion of the normal modes, and will be a very weak function of temperature for temperatures below half the Debye temperature of the crystal.

The position of the atom at lattice site ℓ may be described in terms of the lattice normal modes (i.e., phonons), labeled by f, as

$$q_\ell(t) = \sum_f b_{\ell f} \sqrt{E_f} \cos(\omega_f t + \psi_f) \tag{7}$$

where q is the geometrical displacement of the atom from its equilibrium position, E_f, ω_f, and ψ_f, are the energy, angular frequency, and initial phase of normal mode f, and $b_{\ell f}$ is an element of the transformation matrix between atom displacements and normal coordinates. We have neglected polarization of both atom displacement and normal modes. Polarization can be included within the ℓ subscript of q and b, so that for N unit cells, ℓ can have 3N values. Assume that a guest molecule occupies the site ℓ=0. The separation between the guest and its neighboring atom at site ℓ=1 is

$$\begin{aligned} d_o - \delta(t) &= d_o + q_1(t) - q_0(t) \\ &= \sum_f (b_{1f} - b_{0f}) \sqrt{E_f} \cos(\omega_f t + \psi_f) \end{aligned} \tag{8}$$

where d_o is the lattice spacing between adjacent sites.

A collision is defined as an event in which the separation between neighbors is reduced to $d_o - q_o$ (or when $\delta(t) - q_o = 0$) and the separation is decreasing. (This is referred to as an "upward zero" of $\delta(t) - q_o$.)

Slater[13,14] has calculated the frequency of upward zeros for $\delta(t) - q_o$ for an assembly of quantized, energy weighted normal modes (as in Eq. (7)), Γ, with the result

$$\Gamma = \nu \exp(-\frac{1}{2} q_o^2 \sigma^{-2}) \tag{9}$$

where

$$\nu = \tau/2\pi\sigma \tag{10}$$

$$\sigma^2 = \frac{1}{2} kT \sum_f b_f^2 \phi(\omega_f^2) \tag{11}$$

$$\tau^2 = \frac{1}{2} kT \sum_f b_f^2 \omega_f^2 \phi(\omega_f^2) \tag{12}$$

$$b_f = b_{1f} - b_{0f} \tag{13}$$

$$\phi(\omega_f^2) = \frac{\hbar\omega_f}{2kT} \coth(\frac{\hbar\omega_f}{2kT}) \tag{14}$$

σ^2 and τ^2 are the widths of gaussian distributions of expectation values of coordinate and velocity of $\delta(t)$. A key feature in Slater's derivation is the well-known result that the velocity and coordinate distributions for a harmonic oscillator in a stationary state behave classically[15] and are gaussian in form. The distribution of any function of velocity and coordinates of the quantum harmonic oscillator is also gaussian,[15] and in particular so are the sums of Eqs. (11) and (12) which are sums over harmonic oscillators. $\phi(\omega_f^2)$, as defined in Eq. (14), is the average energy in mode f divided by kT. As T becomes large,

$\coth(\hbar\omega_f/2kT)$ becomes $\exp(-\hbar\omega_f/kT)$ and the result of Slater's classical theory[14] is obtained. When $T\to 0$, $\coth(\hbar\omega_f/2kT)$ becomes 1, and $\phi(\omega_f^2)$ is the ratio of zero point energy to kT. The mean velocity of motion in the coordinate $\delta(t)$ is $\sqrt{\frac{2}{\pi}}\,\tau$. ν is a mean frequency which lies between the highest and lowest frequencies of the lattice; it is weakly temperature dependent.

In quantum-mechanical lattice-dynamical calculations, it is more conventional to use mass weighted normal coordinates, instead of Slater's energy weighted coordinates. Following the conventions of Dawber and Elliott[16]

$$q_\ell = \sum_f \chi(\ell,f)\, d(f) \tag{15}$$

$$d(f) = \sqrt{M}\, Q_f \tag{16}$$

M is the mass of an atom of the lattice, d(f) is the mass weighted normal mode, Q_f is a geometrical normal mode, and $\chi(\ell,f)$ is an element of the transformation matrix from mass-weighted normal coordinates to lattice site displacements. The expectation value of Q_f behaves classically[15] and

$$\langle Q_f \rangle = Q_f(0)\, \cos(\omega_f t+\psi_f)$$

$$E_f = \frac{1}{2} M\omega_f^2 [Q_f(0)]^2$$

where $Q_f(0)$ is the maximum amplitude for Q_f. In terms of energy

$$d(f) = \sqrt{\frac{2E_f}{\omega_f^2}}\, \cos(\omega_f t+\psi_f) \tag{17}$$

The connection between Slater's energy-weighted normal coordinates and the mass-weighted normal coordinates is made by comparing Eqs. (15) and (17) with Eq. (7), with the result:

$$b_{\ell f} = \sqrt{2}\,\frac{\chi(\ell,f)}{\omega_f} \tag{18}$$

The expression for σ^2 and τ^2 can now be related to mass-weighted coordinates and can be made more compact:

$$\sigma^2 = \frac{\hbar}{2}\sum_f \frac{|\chi(f)|^2}{\omega_f}\coth\left(\frac{\hbar\omega_f}{2kT}\right) \tag{19}$$

$$\tau^2 = \frac{\hbar}{2}\sum_f |\chi(f)|^2\,\omega_f\coth\left(\frac{\hbar\omega_f}{2kT}\right) \tag{20}$$

$$\chi(f) = \chi(1,f) - \chi(0,f) \tag{21}$$

Values of $\chi(\ell,f)$ are available in many situations. For a pure lattice (no guest molecules)[16]

$$\chi(\ell,f) = (NM)^{-\frac{1}{2}}\, e^{-i\underset{\sim}{k}_f\cdot\underset{\sim}{R}_\ell}\,\sigma_f^*(\underset{\sim}{k}_f) \tag{22}$$

where $\underset{\sim}{k}_f$ is the wave vector for normal mode f, $\underset{\sim}{R}_\ell$ is the position vector of the ℓ^{th} lattice site, M is the mass of the atom comprising the lattice, and N is the number of atoms in the macroscopic crystal. $\underset{\sim}{\sigma}(\underset{\sim}{k}_f)$ is a dimensionless, unit eigenvector of the dynamical matrix of the crystal[17]--it depends on mode and polarization. For a simple cubic lattice with central forces only, the average value for $|\sigma_f(\underset{\sim}{k}_f)|^2$ is one-third.[16]

In the limit that a guest atom at ℓ=0 is moving totally in a localized mode,[18]

$$\chi(0,L) = 1/\sqrt{M} \tag{23}$$

where L labels the local mode and M' is the mass of the guest molecule. Formulae for $\chi(0,f)$ can be calculated for intermediate situations in which the local mode extends beyond site $\ell=0$ and some motion of the guest at $\ell=0$ is due to participation in bulk lattice modes.[18,19] $\chi(\ell,f)$ for $\ell\neq 0$ has not been explicitly calculated for such cases.

For matrix isolated molecules, the guest molecule is (for Ar, Kr, and Xe lattices) often lighter than the host atom, and the guest-host van der Waals interaction is often stronger than the host-host interaction (except for Xe matrices). Such conditions generally result in the formation of a localized mode at the site of the guest.[18] In certain fortuitous cases, such as HCl and HBr in Ar, Kr, and Xe lattices, the ratio of mass and force constant changes upon substitution of the guest for a host atom is such as to produce nearly complete localization.[20] The basic physical situation of interest here is then one in which the major part of the motion of the guest can be considered to be due to the local mode, and the motion of the guest's nearest neighbors is primarily in bulk phonon modes.

Four tractable models which explore various extremes of the physically relevant situation described above are discussed: (1) Guest motion is totally due to a localized mode, the remainder of the crystal is rigidly frozen; (2) Guest motion is totally due to a localized mode and the remainder of the crystal is described by a single highly degenerate phonon frequency; (3) Guest motion is totally due to a localized mode and the remainder of the cystal is described by a Debye model; and (4) The guest behaves as if it had the same mass and force constant as a host atom--no localized mode is present and the crystal is described by a Debye model. The χ's used in these models are given in Table I.

Table VI-I. Lattice Dynamical Models[a]

Model	Guest motion	Host motion	$\chi(0,f)$	$\chi(0,L)$	$\chi(1,f)$	$\chi(1,L)$	$g(\omega)$[b]
1	Local mode	Frozen	0	$(M')^{-\frac{1}{2}}$	0	0	$\delta(\omega-\omega_L)$
2	Local mode	Einstein mode	0	$(M')^{-\frac{1}{2}}$	$\frac{e^{-ik_E d}}{\sqrt{3}}(NM)^{-\frac{1}{2}}$	0	$\delta(\omega-\omega_L) + 3N\delta(\omega-\omega_E)$
3	Local mode	Debye spectrum	0	$(M')^{-\frac{1}{2}}$	$\frac{e^{-ik_f d}}{\sqrt{3}}(NM)^{-\frac{1}{2}}$	0	$\delta(\omega-\omega_L) + 3N\omega^2/\omega_D^3$
4	Debye spectrum	Debye spectrum	$\frac{(NM)^{-\frac{1}{2}}}{\sqrt{3}}$	0	$\frac{e^{-ik_f d}}{\sqrt{3}}(NM)^{-\frac{1}{2}}$	0	$3N\omega^2/\omega_D^3$

[a] L designates local mode; f designates delocalized modes; E designates Einstein frequency.

[b] Density of states in (number/$\sec^{-1}$).

The models are discussed below. The local mode angular frequency will be labeled ω_L. This mode is three-fold degenerate. However, only one mode will correspond to motion between the guest and a particular neighbor, so the appropriate weighting factor for local modes in Eqs. (19) and (20) is one.

Model 1:

This is a harmonic oscillator cell model. From Eqs. (19) - (21):

$$\sigma_1^2 = \frac{\hbar}{2M'\omega_L} \coth\left(\frac{\hbar\omega_L}{2kT}\right)$$

$$\tau_1^2 = \frac{\hbar\omega_L}{2M'} \coth\left(\frac{\hbar\omega_L}{2kT}\right)$$

$$\nu_1 = \omega_L$$

Model 2:

In this model, the bulk lattice vibrations are treated in an Einstein model, with a 3N-fold degenerate mode of frequency ω_E. From Eqs. (19) - (21):

$$\sigma_2^2 = \frac{\hbar}{2M\omega_E} \coth\left(\frac{\hbar\omega_E}{2kT}\right) + \frac{\hbar}{2M'\omega_L} \coth\left(\frac{\hbar\omega_L}{2kT}\right)$$

$$\tau_2^2 = \frac{\hbar\omega_E}{2M} \coth\left(\frac{\hbar\omega_E}{2kT}\right) + \frac{\hbar\omega_L}{2M'} \coth\left(\frac{\hbar\omega_L}{2kT}\right)$$

Model 3:

This is perhaps the most realistic of the four models. The sums in Eqs. (19) and (20) are, for the lattice modes, replaced by an integral weighted by the Debye density of states, $g(\omega)$, given by

$$g(\omega) = \begin{cases} 3N\omega^2/\omega_D^2 & 0 < \omega < \omega_D \\ 0 & \omega_D < \omega \end{cases} \tag{24}$$

where ω_D is the Debye frequency of the lattice. The results are:

$$\sigma_3^2 = \frac{\hbar}{2M'\omega_L}\coth\left(\frac{\hbar\omega_L}{2kT}\right) + \frac{\hbar}{2M\omega_D}\int_0^{x_D} \frac{x\coth\left(\frac{x}{2}\right)dx}{x_D^2} \tag{25}$$

$$\tau_3^2 = \frac{\hbar\omega_L}{2M'}\coth\left(\frac{\hbar\omega_L}{2kT}\right) + \frac{\hbar\omega_D}{2M}\int_0^{x_D} \frac{x^3\coth\left(\frac{x}{2}\right)dx}{x_D^4} \tag{26}$$

where $x = \hbar\omega/kT$ and $x_D = \hbar\omega_D/kT$. The integrals in Eqs. (25) and (26) can be evaluated numerically. Values for these integrals are tabulated in Table II.

Model 4:

This is the only model in which the guest and its nearest neighbor both have non-zero amplitudes in the same mode(s). From Table I and Eq. (21):

$$\chi(f) = \frac{2i\sin(k_f d/2)e^{-ik_f d/2}}{\sqrt{3}(NM)^{\frac{1}{2}}}$$

where d is the nearest neighbor distance. In a Debye model the phonon velocity is assumed constant. The dispersion relation is

$$k = v_D/\omega$$

$$v_D = \omega_D/(6\pi^2\rho)^{1/3}$$

where v_D is the Debye velocity of sound and ρ is the density of lattice sites per cm^3. In terms of x,

Table VI-II. Integrals for Model 3

x_D	I_σ [a]	Err-σ [b]	I_τ [c]	Err-τ [d]
.5	4.0277E+00	-3.8365E-13	1.3500E+00	-2.7711E-13
1.0	2.0550E+00	-1.8474E-12	6.4561E-01	-1.0303E-12
1.5	1.4145E+00	1.4579E-13	4.9316E-01	-5.4759E-12
2.0	1.1065E+00	-3.8664E-12	3.9764E-01	3.4467E-11
2.5	9.3103E-01	-7.7157E-11	3.4444E-01	4.8495E-10
3.0	8.2029E-01	-5.4203E-10	3.1302E-01	2.3737E-09
3.5	7.4607E-01	-2.2652E-09	2.9322E-01	7.2972E-09
4.0	6.9407E-01	-6.0345E-09	2.8029E-01	1.6381E-08
4.5	6.5640E-01	-1.4623E-08	2.7122E-01	2.8569E-08
5.0	6.2835E-01	-2.4734E-08	2.6568E-01	3.9250E-08
5.5	6.0700E-01	-3.6476E-08	2.6154E-01	4.8235E-08
6.0	5.9042E-01	-1.8824E-08	2.5862E-01	2.1382E-08
6.5	5.7733E-01	3.0486E-08	2.5652E-01	-2.8717E-08
7.0	5.6664E-01	1.4021E-07	2.5500E-01	-1.0998E-07
7.5	5.5832E-01	3.3276E-07	2.5388E-01	-2.2850E-07
8.0	5.5131E-01	6.2383E-07	2.5305E-01	-3.7800E-07
8.5	5.4548E-01	1.0132E-06	2.5242E-01	-5.4647E-07
9.0	5.4059E-01	1.5018E-06	2.5194E-01	-7.1982E-07
9.5	5.3644E-01	2.0503E-06	2.5157E-01	-8.8151E-07
10.0	5.3289E-01	2.6301E-06	2.5129E-01	-1.0170E-06
10.5	5.2983E-01	3.1566E-06	2.5106E-01	-1.1113E-06
11.0	5.2715E-01	3.5958E-06	2.5088E-01	-1.1544E-06
11.5	5.2487E-01	3.8785E-06	2.5074E-01	-1.1356E-06
12.0	5.2285E-01	3.9356E-06	2.5063E-01	-1.0641E-06
12.5	5.2105E-01	-2.2756E-11	2.5053E-01	5.6434E-12
13.0	5.1947E-01	4.2259E-11	2.5045E-01	-5.9853E-12
13.5	5.1805E-01	1.6049E-10	2.5039E-01	-3.5002E-11
14.0	5.1678E-01	3.4622E-10	2.5034E-01	-6.9887E-11
14.5	5.1565E-01	6.0548E-10	2.5029E-01	-1.1385E-10
15.0	5.1462E-01	9.3738E-10	2.5026E-01	-1.6446E-10
15.5	5.1369E-01	1.3291E-09	2.5022E-01	-2.1859E-10
16.0	5.1285E-01	1.7543E-09	2.5020E-01	-2.7069E-10
16.5	5.1208E-01	2.1715E-09	2.5018E-01	-3.1505E-10
17.0	5.1138E-01	2.5267E-09	2.5016E-01	-3.4516E-10
17.5	5.1074E-01	2.7510E-09	2.5014E-01	-3.5445E-10
18.0	5.1015E-01	2.7672E-09	2.5012E-01	-3.3684E-10
18.5	5.0961E-01	2.4937E-09	2.5011E-01	-2.8663E-10
19.0	5.0911E-01	1.8457E-09	2.5010E-01	-2.0068E-10
19.5	5.0865E-01	7.4422E-10	2.5009E-01	-7.5562E-11
20.0	5.0822E-01	-8.8015E-10	2.5008E-01	8.9212E-11
20.5	5.0783E-01	-3.0823E-09	2.5007E-01	2.9261E-10
21.0	5.0746E-01	-5.8575E-09	2.5007E-01	5.3180E-10
21.5	5.0712E-01	-8.3347E-09	2.5006E-01	8.0220E-10
22.0	5.0681E-01	-9.0983E-09	2.5006E-01	9.6621E-06
22.5	5.0650E-01	-8.3776E-09	2.5005E-01	2.6836E-06
23.0	5.0622E-01	-6.6262E-09	2.5005E-01	3.6797E-06
23.5	5.0596E-01	-5.8415E-09	2.5004E-01	3.6529E-06
24.0	5.0571E-01	-6.0226E-09	2.5004E-01	3.6052E-06
24.5	5.0548E-01	-6.1670E-09	2.5004E-01	3.5350E-06
25.0	5.0526E-01	-6.2741E-09	2.5003E-01	3.4565E-06

[a] $$I_\sigma = \frac{1}{x_D^2}\int_0^{x_D} x\coth(x/2)\,dx$$

[b] Error associated with numerical integration of I_σ.

[c] $$I_\tau = \frac{1}{x_D^4}\int_0^{x_D} x^3\coth(x/2)\,dx.$$

[d] Error associated with numerical integration of I_τ.

$$\frac{k_f d}{2} = \frac{(6\pi^2\rho)^{1/3}}{2}\,\frac{x}{x_D}$$

For Ar, d = 3.8 Å and $\rho = 2.6 \times 10^{22}$ cm^{-3}, so $k_f d/2 = 2.32\, x/x_D$. Finally,

$$\sigma_4^2 = \frac{2\hbar}{M\omega_D}\int_0^{x_D} \frac{x \coth(\frac{x}{2})\sin^2(2.32x/x_D)dx}{x_D^2} \tag{27}$$

$$\tau_4^2 = \frac{2\hbar\omega_D}{M}\int_0^{x_D} \frac{x^3\coth(\frac{x}{2})\sin^2(2.32x/x_D)dx}{x_D^4} \tag{28}$$

The integrals of Eqs. (27) and (28) correspond to the special case of an Ar lattice. They are evaluated numerically, and the results are given in Table III.

The expression for Γ, Eq. (9), gives the frequency of collision between the guest and one of its nearest neighbors. For a simple cubic lattice, the total collision frequency will be 6Γ, since there are six nearest neighbors located along three orthogonal axes. For fcc and hcp lattices, there are 12 nearest neighbors. However, $|\sigma_f(\underset{\sim}{k})|^2$, discussed after Eq. (22), will not necessarily have an average value of one-third in these lattices, so multiplying Γ by 12 for these lattices may not be correct. We will take the three dimensional collision frequency to be 6Γ.

From the values of σ^2 and τ^2 calculated for each model, the collision frequency Γ is calculated from Eqs. (9) and (10), once a choice has been made for q_o. The choice of q_o ought to be related to the guest molecule-host atom intermolecular potential, and this will be discussed in Section 4b. In general, q_o will be in the range of 0.1-0.5 Å. It is worthwhile at this point to illustrate the behavior of Γ by specific choices of q_o and defer discussion of choosing q_o. The value of Γ will

Table VI-III. Integrals for Model 4

x_D	I_σ [a]	Err-σ [b]	I_τ [c]	Err-τ [d]
.5	2.4522E+00	-9.4655E-07	1.0835E+00	5.4651E-06
1.0	1.2593E+00	-3.6636E-07	5.6107E-01	3.6272E-06
1.5	8.7542E-01	1.0752E-07	3.9521E-01	1.9565E-06
2.0	6.9235E-01	5.8715E-07	3.1763E-01	4.7005E-07
2.5	5.9122E-01	1.0741E-06	2.7561E-01	-5.5178E-07
3.0	5.2F29E-01	1.5EEDE-06	2.5033F-01	-1.2592E-06
3.5	4.8742E-01	2.0E66E-06	2.3441E-01	-1.7588E-06
4.0	4.5586E-01	2.4418E-06	2.2402E-01	-1.6165E-06
4.5	4.4027E-01	2.6241E-06	2.1746E-01	-1.7E25E-06
5.0	4.2643E-01	2.5557E-06	2.1235E-01	-1.2E14E-06
5.5	4.1635E-01	2.2499E-06	2.0907E-01	-7.7062E-07
6.0	4.0EE11E-01	1.5476E-06	2.0678E-01	-2.7572E-08
6.5	4.0333E-01	5.0653E-07	2.0516E-01	7.6416E-07
7.0	3.9E1CE-01	-6.2CEEE-07	2.0359E-01	1.5257E-06
7.5	3.9585E-01	-2.3425E-06	2.0315E-01	2.1922E-06
8.0	3.9333E-01	-3.5422E-06	2.0254E-01	2.7175E-06
8.5	3.9132E-01	-5.4927E-06	2.0220E-01	3.0777E-06
9.0	3.85FCE-01	-6.6725E-06	2.0175E-01	3.2E54E-06
9.5	3.8855E-01	-7.5254E-06	2.0150E-01	3.2502F-06
10.0	3.8756E-01	-F.7155E-06	2.0138E-01	3.1723E-06
10.5	3.8C75E-01	-9.0511E-06	2.0116F-01	2.9301E-06
11.0	3.8EC9E-01	-6.5453E-06	2.0105E-01	2.617EE-06
11.5	3.8555E-01	-8.4235E-06	2.0094E-01	2.2402E-06
12.0	3.851CE-01	-7.4513E-06	2.0084F-01	1.8321E-06
12.5	3.8472E-01	4.7164E-11	2.0075E-01	-1.1636E-11
13.0	3.8441E-01	-8.0337E-11	2.0066F-01	1.5158E-11
13.5	3.8415E-01	-2.7410E-10	2.0059E-01	5.9583E-11
14.0	3.8392E-01	-5.2566E-10	2.0051E-01	1.0E27E-10
14.5	3.8374E-01	-8.4566E-10	2.0046E-01	1.6E45E-10
15.0	3.8356E-01	-1.2024F-09	2.0041E-01	2.1210E-10
15.5	3.8344E-01	-1.5E75E-09	2.0036E-01	2.5E47E-10
16.0	3.8332E-01	-1.9C16E-09	2.0032E-01	2.9486E-10
16.5	3.8322E-01	-2.1E13F-09	2.0029E-01	3.1705E-10
17.0	3.8313E-01	-2.3E62E-09	2.0026E-01	3.2175E-10
17.5	3.8305E-01	-2.3500E-09	2.0024E-01	3.0644E-10
18.0	3.8296E-01	-2.2419E-09	2.0022E-01	2.7C45E-10
18.5	3.8292E-01	-1.8855E-09	2.0020E-01	2.1226E-10
19.0	3.8287E-01	-1.3014E-09	2.0019E-01	1.3643E-10
19.5	3.8282E-01	-4.7764E-10	2.0018E-01	4.1E62E-11
20.0	3.8278E-01	5.8443E-10	2.0017E-01	-6.7870E-11
20.5	3.8275E-01	1.6746E-09	2.0016E-01	-1.4767E-10
21.0	3.8271E-01	2.3710E-09	2.0016F-01	-2.1503E-10
21.5	3.F26EE-01	2.0415E-09	2.0015E-01	-4.4526E-10
22.0	3.8266E-01	2.2033E-09	2.0015E-01	-4.6552E-07
22.5	3.8264E-01	2.2026E-09	2.0015E-01	-5.5202E-07
23.0	3.8261E-01	2.1891E-09	2.0013E-01	-3.3155E-07
23.5	3.8260E-01	2.1661E-09	2.0013E-01	-2.4147E-07
24.0	3.8259E-01	2.1322E-09	2.0013E-01	-1.7C76E-07
24.5	3.8256E-01	2.0769E-09	2.0012E-01	-1.0397E-07
25.0	3.8255E-01	2.0169E-09	2.0013E-01	-4.1531E-08

[a] $$I_\sigma = \frac{1}{x_D^2}\int_0^{x_D} x\coth(x/2)\,\sin^2(2.32x/x_D)\,dx.$$

[b] Error associated with numerical integration of I_σ.

[c] $$I_\tau = \frac{1}{x_D^4}\int_0^{x_D} x^3\coth(x/2)\,\sin^2(2.32x/x_D)\,dx.$$

[d] Error associated with numerical integration of I_τ.

be very sensitive to the choice of q_o. However, the qualitative behavior of Γ will not. The main temperature dependence of Γ comes from the factor σ^2 in the exponent; ν is only slightly temperature dependent. As q_o decreases, the effect of a changing σ^2 is diminished, and the temperature dependence of Γ diminishes. Also, for small values of q_o, Γ is always close to ν and the absolute magnitude of Γ increases as q_o decreases. ν is a weighted average of the phonon frequencies available to the lattice. For the models studied, ν decreases by up to 15% between 0 K and the lattice Debye temperature, becoming temperature independent above the Debye temperature.

Results for the four models, specified to parameters relevant to HCl/Ar, are presented in Fig. 1. Values used are ω_L = 73 cm^{-1}, ω_D = 64 cm^{-1}, ω_E = 30 cm^{-1}, and q_o = 0.16 Å. The value chosen for ω_E corresponds to a mode near the first peak in the density of phonon states for an Ar lattice. The values plotted correspond to the collision frequency of HCl with one of its nearest neighbors. The total collision rate is six times that shown in Fig. 1, as discussed previously. The general qualitative behavior of Γ is independent of model. The temperature dependence is weak, since σ^2 and τ^2 are dominated by the zero point motion of the higher energy phonons available to the system. The temperatures for which Γ doubles are 69.5, 92.5, and 69 K for Models 1, 3, 4 with q_o = 0.16 Å. The infinite temperature limit for Model 2 has $\Gamma(\infty) = 1.4\ \Gamma(0)$. For q_o = 0.25 Å the temperature dependence is higher; doubling temperatures for Models 1-4 are 41, 53, 43, and 37 K. For all models, however, Γ is not overly temperature sensitive in the range 0-30 K. The temperature dependence is greatest for models with the lowest range of phonons, since the temperature onset of stimulated

Figure VI-1. Collision frequency as a function of temperature. Frequency is that of collision between a guest HCl molecule and one nearest neighbor Ar atom. Curve a = Model 2; curve b = Model 3; curve c = Model 4; curve d = Model 1. q_o = 0.16 Å.

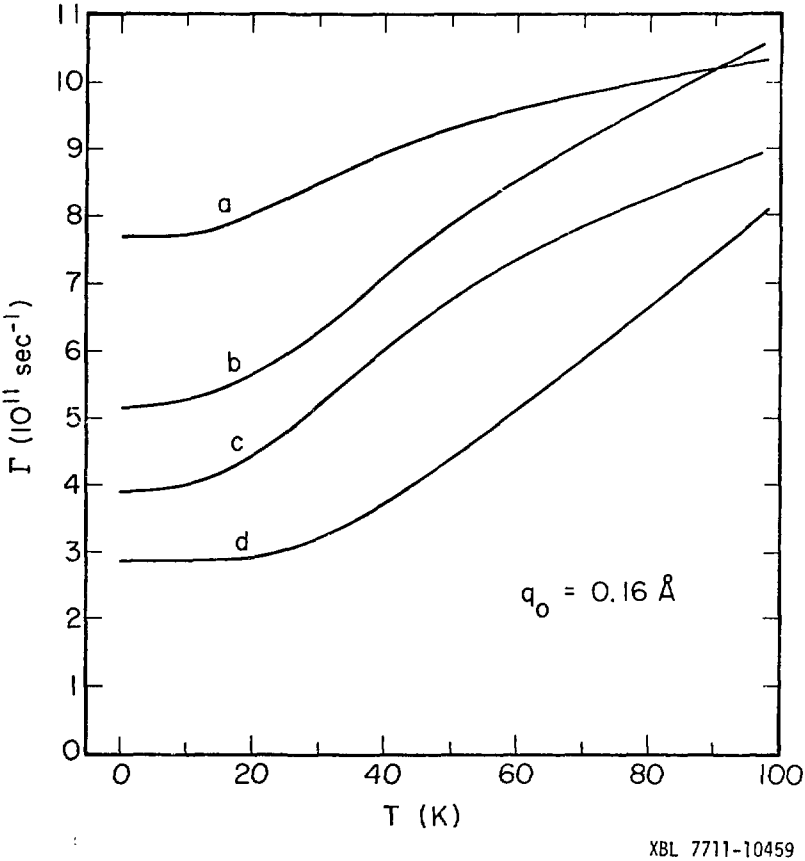

XBL 7711-10459

phonon processes decreases as phonon frequency decreases. Thus, model 4, which has the lowest range of phonons, has the strongest temperature effect.

It is worthwhile examining Model 3 in a bit more detail to elucidate the contributions to Γ. Table IV presents values for σ and τ for Model 3 as a function of temperature. Contributions due to local and bulk phonon modes, representing the first term and the integral in Eqs. (25) and (26), respectively, are distinguished. Both σ^2 and τ^2 are dominated by the local mode contribution, which, since it has a high frequency (73 cm^{-1}), shows little temperature effect below 30 K. The contributions to σ^2 and τ^2 from bulk phonons are much more temperature dependent. The temperature dependence of σ^2 results from the bulk phonon contributions, which varies from 30 to 50% as T varies between 0 and 92 K. This in turn is responsible for the temperature effect of Γ. Note that τ^2 is largely dominated by the nearly temperature independent local mode contribution; this is due to the factor of ω in the numerator in Eq. (20). While this does not affect Γ much, it has important physical implications. Since $\sqrt{\frac{2}{\pi}}\,\tau$ is the mean relative velocity between the guest and its nearest neighbor, it is seen that when a local mode exists, the relative velocity can be expressed in terms of the local mode only, to a very good approximation.

As mentioned previously, the magnitude of Γ depends on the value for q_o. The variation of Γ with q_o is illustrated in Table V for Model 3 for HCl/Ar. The collision frequency decreases by 3 orders of magnitude as q_o increases from 0.16 to 0.42 Å. Furthermore, the temperature dependence of Γ is greatest for the largest q_o. $\Gamma(31)/\Gamma(0)$ is 6.2 when q_o = 0.42 Å, and only 1.2 when q_o = 0.16 Å. In matching experimental data, a value of q_o consistent with small temperature effects ($\Gamma(20)/\Gamma(0)$ <2) must be chosen.

Table VI-IV. Details of Model 3 for HCl/Ar:
$\omega_L = 73\ cm^{-1}$, $\omega_D = 64\ cm^{-1}$, $a_o = 0.25\ Å$[a]

T (K)	σ_L^2	σ_P^2	σ^2	τ_L^2	τ_P^2	τ^2	Γ[b]	$\Gamma/\Gamma(0)$
	(10^{-18} cm^2)			(10^8 cm^2/sec^2)			(10^{10} sec^{-1})	
0	.640	.327	.967	1.20	.238	1.44	7.66	1.00
4.97	.640	.333	.973	1.20	.238	1.44	7.81	1.02
10.2	.640	.353	.993	1.20	.240	1.44	8.20	1.07
15.3	.641	.387	1.03	1.20	.247	1.45	9.12	1.19
20.4	.648	.430	1.08	1.21	.251	1.46	10.3	1.34
26.3	.664	.487	1.15	1.25	.280	1.53	12.2	1.59
30.7	.684	.537	1.22	1.28	.298	1.58	13.9	1.82
36.8	.719	.607	1.32	1.35	.328	1.68	16.9	2.20
46.0	.787	.723	1.51	1.48	.380	1.86	22.4	2.92
61.3	.924	.923	1.85	1.73	.472	2.20	32.1	4.19
92.0	1.24	1.34	2.58	2.33	.573	2.90	50.3	6.57

[a] Local mode contributions are subscripted by L; bulk phonon contributions are subscripted by P.

[b] Collision frequency between HCl and one nearest neighbor, Eq. (9).

Table VI-V. Variation of $\Gamma(T)$, $[10^{11}\ sec^{-1}]$, with q_o, Model 3[a]

	q_o(Å)			
T (K)	.16	.25	.31	.42
0	5.16	.766	.135	2.12×10^{-3}
5.0	5.21	.781	.139	2.25×10^{-3}
10.2	5.26	.820	.153	2.67×10^{-3}
15.3	5.47	.912	.178	3.60×10^{-3}
20.4	5.68	1.03	.216	5.26×10^{-3}
30.7	6.35	1.39	.352	1.31×10^{-2}
46.0	7.59	2.24	.736	5.13×10^{-2}
92.0	10.3	5.03	2.63	.553

[a] Parameters chosen for HCl/Ar: $\hbar\omega_D = 64\ cm^{-1}$; $\hbar\omega_L = 73\ cm^{-1}$; M = 40 amu; M' = 36 amu. Γ is collision frequency between HCl and one nearest neighbor Ar atom.

The major qualitative results of the calculation can be summarized: a) the collision frequency is something less than the highest phonon frequency of the crystal, b) for cryogenic temperatures, P is dominated by zero point motion effects, and is not a strong function of temperature, and c) when a local mode is present, it dominates the factors determining the collision frequency.

3. Relaxation Probability

The relaxation probability from vibrational state k to k-1 of a diatomic molecule, BC, upon collision with an atom, A, is given by the Jackson-Mott distorted wave calculation as[21,22]

$$P_k^{k-1}(v_i) = \frac{32\pi^4}{h}\frac{m^2\gamma^2}{\mu_{BC}}\frac{\nu k}{a^2}\frac{\sinh(\pi z)\sinh(\pi z^*)}{[\cosh(\pi z)-\cosh(\pi z^*)]^2} \tag{29}$$

$$z = \frac{4\pi m}{ah} v_i$$

$$z^* = \frac{4\pi m}{ah} v_f$$

$$\gamma = \frac{m_C}{m_B+m_C}$$

where m is the translational reduced mass of A and BC; v_i and v_f are the initial and final relative velocities of A and BC; μ_{BC} is the reduced mass of BC; m_B and m_C are the masses of atoms B and C (atom C is the heavy atom of the diatomic); ν is the vibrational frequency of BC (sec^{-1}); and a is the range parameter of the exponential repulsive interaction between A and BC. Knowledge of the initial translational velocity allows calculation of the final velocity, since the final kinetic energy must exceed the initial kinetic energy by $h\nu$. Thus, the probability is a function of the initial relative velocity. In the present application,

Eq. (29) will be modified, following a proposal of Nikitin,[23,24] to include rotational motion of BC. Equation (29) will be rearranged in a manner appropriate to the physical condition present in a low temperature solid that the initial kinetic energy of the colliding pair is much smaller than hν.

Nikitin[23,24] has introduced rotation into the one-dimensional model of Eq. (29) by using an effective reduced mass, μ^+, in place of m in Eq. (29):

$$(\mu^+)^{-1} = m^{-1} + A\mu_R^{-1} \tag{30}$$

where μ_R is a rotational reduced mass ($\mu_R = I/d^2$, I is the moment of inertia of BC and d is the distance from the center of mass to the light atom of BC) and A is a factor related to the asymmetry of BC and the most effective geometry for collisions to induce relaxation. The origin of Eq. (30) and the physical model which produces it are discussed below.

Nikitin assumes that the relative translation and rotation of A and BC can be described by classical dynamics on the electronic potential hypersurface of the A-B-C triatomic system. The classical turning point, R, of a trajectory between A and BC will be a function of the relative translational energy of A and BC as well as the angle θ between the line of centers of A and BC and the BC internuclear axis. At the classical turning point, only the component of velocity normal to the equipotential lines on the A-B-C hypersurface will be effective in producing relaxation, since in this direction the potential is changing most rapidly. A local cartesian coordinate system can be constructed at the classical turning point, and the velocity of collision in the

plane tangent to the equipotential surface is averaged. The resulting expression for a vibrational transition is analogous to Eq. (29) except that the reduced mass is now that due to motion along the gradient of the potential surface, and is given by Eq. (30), where A is a function of θ and R. The position (R_{min}, θ_{min}) on the A-B-C hypersurface for which μ^+ is a minimum will have the greatest probability for vibrational relaxation. Hence, in an average over all trajectories those that have a turning point near (R_{min}, θ_{min}) will dominate relaxation. Instead of averaging over all possible collision geometries, the relaxation probability is equal to the maximum probability when μ^+ is minimized times a steric factor which is the fraction of collisions occurring in geometries near (R_{min}, θ_{min}). μ^+ is taken as the value at (R_{min}, θ_{min}). At this position, $A = (R_{min}/d)^2 \sin^2\delta$ where δ is the angle between the line connecting the center of mass of BC with R_{min} and the normal to the equipotential surface.[52] A is calculated from the equipotential surfaces of the diatomic molecule, and is almost a molecular constant for BC--it should depend only weakly on the identity of A. For the hydrogen-halide molecules, Nikitin calculates a value of A = 0.22.[25]

For transitions in which rotational quantum numbers must change, it is necessary to have torques, or, equivalently, a region of low symmetry in which the potential contains non-spherical components. The appropriate position is the classical turning point (R_{min}, θ_{min}) which, for real molecules, contains Legendre polynomial components of high order in the potential, thus allowing large changes of rotational quantum number.

Physically, A is due to deviation of the A-B-C potential surface from spherical symmetry, and μ^+ combines the effect of translational and

rotational velocity in climbing a potential wall. For highly asymmetric rotators, rotational motion of the diatomic about its center of mass can produce effective translational velocities as high as $\dot{\theta}d$, where d is the distance from the center of mass to the light atom of BC and $\dot{\theta}$ is the rotational velocity of BC. This velocity has been used in an early formulation of V→R relaxation.[26] For spherical diatomics, the line of centers between A and BC will always be normal to the equipotential surfaces, so A=0, and the effective reduced mass will equal the translational reduced mass. In this situation, there are no torques so there are no changes in rotational quantum number. Although Nikitin calculates a value of 0.22 for HCl, A is best treated as an empirical parameter. Steele and Moore[27] have found values of A from 0.6 to 1.0 are appropriate for explaining vibrational relaxation of HCl by rare gas atoms, and suggest the best value of a = 0.7.

The effects of rotation are introduced into the one-dimensional model of Eq. (29) by replacing m with $\mu^{\dagger}$. The effective reduced mass apportions kinetic energy between translational and rotational motion. The initial relative velocity of A and BC is due to rotational and translational motion due to the local mode. As discussed previously, when the local mode is present, it dominates τ(Table IV), and the contributions of bulk phonons to the relative velocity of A and BC can be neglected. Thus, the initial and final velocities can be calculated from

$$\frac{1}{2}\mu^{\dagger}v_i^2 = (n + \frac{1}{2})\,h\nu_L + hcBJ(J+1) \qquad (31)$$

$$\frac{1}{2}\mu^{\dagger}v_f^2 = \frac{1}{2}\mu^{\dagger}v_i^2 + h\nu \qquad (32)$$

where n and J are the quantum numbers for local mode oscillation and rotation, respectively, of the initial state of BC. For the ground state of BC, $(1/2)\mu^{\dagger}v_i^2 = (1/2)h\nu_L$, the zero point energy of the local mode. It is clear that the final velocity is much greater than the initial velocity; hence, $z^* >> z$. The final factor in Eq. (29) can be written as:

$$\frac{\sinh(\pi z^*)\sinh(\pi z)}{[\cosh(\pi z)-\cosh(\pi z^*)]^2} = e^{-\pi(z^*-z)}\,[1-e^{-2\pi z}] \tag{33}$$

where a term $\exp[\pi(z-z^*)]$ has been neglected. For $z>0.7$ the term in brackets may also be neglected. For most combinations of physical parameters $z>0.7$ holds, and the term in brackets is dropped. From Eqs. (31) and (32), noting that $(1/2)\mu^{\dagger}v_i^2 << h\nu$,

$$\pi(z^*-z) = \frac{4\pi^2}{a}\left(\frac{2\mu^{\dagger}\nu}{h}\right)^{\frac{1}{2}}\,[1-G(n,J)+2G(n,J)^2] \tag{34}$$

$$G(n,J) = \left[\left(n+\frac{1}{2}\right)\frac{\nu_L}{\nu} + \frac{cBJ(J+1)}{\nu}\right]^{\frac{1}{2}} \tag{35}$$

G^2 is much smaller than G and is henceforth neglected. Equations (34) and (33) are substituted into (29) to give

$$P_{k,n,J}^{k-1} = \frac{32\pi^4}{\mu_{BC}}\,\frac{(\mu^{\dagger})^2\gamma^2}{a^2}\,\nu k\,\exp\left[-\frac{4\pi^2}{a}\sqrt{\frac{2\mu^{\dagger}\nu}{h}}\,[1-G(n,J)]\right] \tag{36}$$

In Eq. (36) the probability expression takes detailed account of the initial state of BC. The final level is not strictly accounted for. $P_{k,n,J}^{k-1}$ is the probability for relaxation from initial state (k,n,J) to all states with vibrational quantum number k-1. In future usage, P_k^{k-1} will be a thermally averaged probability over all initial rotation-translation states. Similarly, $k_{k,n,J}^{k-1}$ will be the rate constant for

relaxation of initial state (k,n,J) and k_k^{k-1} will be the thermally averaged rate constant for vibrational relaxation of level k. The ratio of rotational to translational energy in the final state should be approximately $[(m-\mu^\dagger)/\mu^\dagger]$.

The overall relaxation rate is the sum of Boltzmann-weighted probabilities times a collision frequency, which is taken to be independent of initial state:

$$k_k^{k-1}(T) = s\Gamma \sum_{n,J} \frac{g_{J,n} e^{-E(J,n)/kT}}{Q(T)} P_{k,n,J}^{k-1} \qquad (37)$$

where $g_{J,n}$ and E(J,n) are the degeneracy and energy of the rotation-translation level (J,n), Q(T) is the rotation-translation partition function, and s is a steric factor. The steric factor arises from the physical notion that $\mu^\dagger$ is minimized for a narrow range of R and θ, and only the fraction of collisions with a turning point near (R_{min}, θ_{min}) are effective in inducing relaxation.

4. Results and Discussion

The model developed here assumes that relaxation can be viewed in terms of uncorrelated collisions in the solid, and that these collisional events can be described in terms of velocities due to guest rotation and translational motion in the phonon modes of the solid. Rotation is treated in a quasi-one dimensional manner by the concept of effective reduced mass. The model produces a rough correlation between available experimental results to the V→R mechanism. The validity of the assumptions and the physical picture of relaxation that emerges are discussed below. The value of the present theory lies more in correlating data than in ab initio predictions of relaxation rates. Effects of temperature

and host matrix are considered. Finally, the picture of relaxation in the solid is connected to relaxation in the liquid and gaseous phases.

a) Correlations

For molecules with small moments of inertia, $\mu^\dagger$ is dominated by μ_R and can be written

$$\mu^\dagger = \frac{\mu_R}{A}\left(1-\frac{\mu_R}{Am}\right)$$

$$\mu_R = \frac{I}{d^2} = \frac{h}{8\pi^2 cBd^2}$$

Substitution of these results into Eq. (36) gives

$$P_{k,n,J}^{k-1} \propto \exp\left[-\frac{2\pi}{ad\sqrt{A}}\sqrt{\frac{\nu}{cB}}\left(1-\frac{\mu_R}{2Am}\right)[1-G(n,J)]\right] \qquad (38)$$

This is Legay's correlation, Eq. (6), since $J_f = (\nu/cB)^{\frac{1}{2}}$. Moreover, the slope of Legay's correlation, α, is given by $2\pi/ad\sqrt{A}$. For reasonable molecular parameters, A=1, a=5 Å^{-1}, and d=1 Å, α=1.3. A plot of available experimental relaxation data[28] for matrix isolated molecules in the form of Eq. (38) is shown in Fig. 2. The slopes of curves a and b are 0.97 and 0.75, respectively, close to the value estimated above. Figure 2 ignores the variation of relaxation rate due to the pre-exponential factors in Eq. (36) and to the collision frequency and Boltzmann sum of Eq. (37). This may be responsible for some of the large scatter.

Equation (38) is approximate and the small correction factors $(1-\mu_R/2Am)$ and $1-G(n,J)$ have been neglected in Fig. 2. A more accurate way to correlate relaxation data might be to assume collision frequencies, Γ, are the same for different guest molecules, and reduce Eq. (36) to the form

Figure VI-2. Correlation of non-radiative relaxation rates in matrices to Eq. (38). ● = Ar matrix, ■ = Ne matrix, ▲ = Kr matrix, □ = N_2 matrix, ○ = data point corresponding to radiative-decay limited relaxation. Arrows indicate that the data point is a limit. Data is from Reference 12, Table 3, except: DCl/Ar--Chapter V; NH, ND/Ar--Reference 36, and C_2^---L. J. Allamandola, et al., J. Chem. Phys., 67, 99 (1977). Curve a is the best fit line for all non-radiative decay rates; curve b is the best fit excluding the NH* and ND* data. The slopes of curves a and b correspond to α (Eq. (6)) of 0.97 and 0.75.

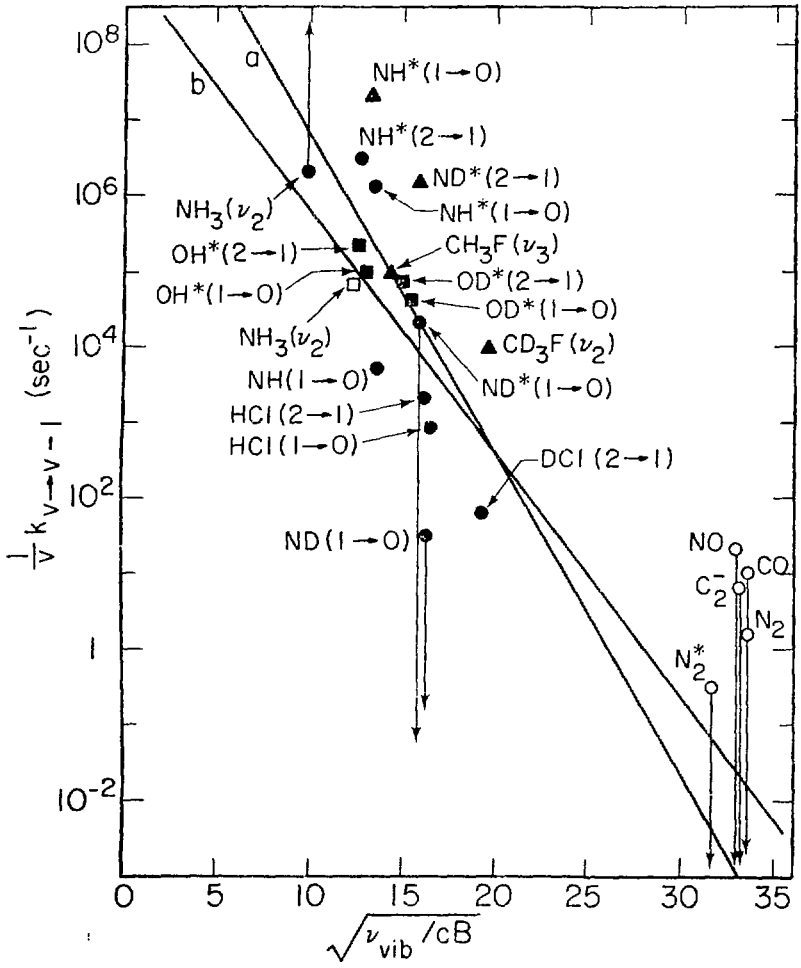

XBL 7711-10458

$$P^* = \frac{\mu_{BC}}{(\mu^\dagger)^2 \nu k} P \propto \exp\left[-\frac{4\pi^2}{a}\sqrt{\frac{2\mu^\dagger \nu}{h}}\,(1-G(n,J))\right]$$

A plot of $\ln P^*$ vs $\sqrt{\mu^\dagger \nu}$ can be made if a value is selected for A, so that $\mu^\dagger$ can be calculated from μ_R and m. For a common value of A, such plots produce a much poorer correlation than the plot of Fig. 2. Molecules for which ν/cB is relatively large, such as DCl, have large bond lengths, d, and those with small ν/cB, such as OH, have smaller bond lengths. In the plot of $\ln P^*$ vs $\sqrt{\nu\mu^\dagger}$, all data points are shifted toward nearly equal values of $\sqrt{\nu\mu^\dagger}$, while $\ln P^*$ shows the same range as that of Fig. 2. In other words, the correlation to the more "exact" equation (36), is not as good as that of the approximate equation (38). It is possible to avoid this dilemma if A in fact varies substantially from molecule to molecule, and is correlated with d and a in such a way as to make Eq. (38) more valid than Eq. (36) with a common value of A.

The collision frequency, Γ, should not be overly dependent on isotopic substitution or on vibrational state of the guest, since the phonon spectrum of the solid (including local mode) is not very sensitive to such changes in guest properties. The validity of the present model can be tested by comparison of hydride and sister deuteride relaxation rates, since not only should Γ be the same for both, but A should be the same as well. Using Eq. (36) and the approximations leading to Eq. (38), produces, for the lowest temperatures (n = J = 0):

$$\frac{k(H)}{k(D)} = \frac{P_k^{k-1}(H)}{P_k^{k-1}(D)} = \left(\frac{\mu_R^H}{\mu_R^D}\right)\left(\frac{\nu}{\nu_D}\right)\exp\left\{-\frac{2\pi}{ad\sqrt{A}}\,[1-G(0,0)]\right.$$

$$\left.\times\left[\sqrt{\frac{\nu_H}{cB_H}} - \sqrt{\frac{\nu_D}{cB_D}}\right]\right\} \qquad (39)$$

To arrive at this expression, it is assumed that $\mu_R = \mu_{BC}$, and that $G(0,0) << 1$ for both the hydride and deuteride. Also, $(1-\mu_R/Am)$ has been set equal to unity. From measured rates, a value for the product $(a\sqrt{A})$ can be determined.

Comparison of rates of relaxation from v=2 to relaxation from v=1 is another means of determining $(a\sqrt{A})$ from experimental data. Using the same assumptions as above gives

$$\frac{k_{21}}{k_{10}} = \frac{2\nu_{2\to1}}{\nu_{1\to0}} \exp\left\{-\frac{2\pi}{ad\sqrt{A}}\left[1-G(0,0)\right]\left[\sqrt{\frac{\nu_{2\to1}}{cB}} - \sqrt{\frac{\nu_{1\to0}}{cB}}\right]\right\} \qquad (40)$$

Correlations of relevant experimental data by Eqs. (39) and (40) are presented in Table VI. The following points can be noted: Correlations of k_{21} relative to k_{10} always lead to larger values of $(a\sqrt{A})^{-1}$ than hydride-deuteride correlations for the same molecule. This may indicate that the oscillator matrix element for the intra-molecular vibration increases faster than harmonic ($k_{v\to v-1} > vk_{1\to0}$). This point has been noted in Chapter V. Considering only the hydride-deuteride results, and taking A=1 gives potential range parameters, a, of 4-10 $\mathring{A}^{-1}$. This is the appropriate order of magnitude, but generally range parameters are less than 6 $\mathring{A}^{-1}$.[29] We will now consider the individual cases in more detail.

The data for HCl/Ar is well fit by this model. Steele and Moore,[27] from a study of relaxation of HCl and DCl by rare gas atoms in the gas phase, find a value of A = 0.6-1.0 and a = 2.9-4.0 $\mathring{A}^{-1}$. From the matrix results, a value of A = 1.0 implies a = 4.0 $\mathring{A}^{-1}$, at the edge of the range of the gas phase results.

The ratios of OH*/OD* relaxation in Ne can be analyzed for v-2 → 1

Table VI-VI. Correlations of V→R Rates

A: Hydride-Deuteride Correlations, Eq. (39)

System	k_H	k_D	μ_R^H	μ_R^D	ν_H	ν_D	B_H	B_D	d_H	d_D	$a\sqrt{A}$
	(sec^{-1})		(amu)		(cm^{-1})		(cm^{-1})		(Å)		($Å^{-1}$)
HCl/Ar 2→1 (9K)	3.8×10^3	110	1.03	2.11	2767	2029	10.5	5.54	1.23	1.20	4.0
OH*/Ne 2→1 (4K)	4.0×10^5	1.4×10^5	1.06	2.25	2784	2099	17.4	9.19	0.91	0.86	13
OH*/Ne 1→0 (4K)	9.0×10^4	3.9×10^4	1.06	2.25	2970	2200	17.4	9.19	0.91	0.86	16
NH*/Kr 1→0 (4K)	1.8×10^7	1.4×10^6	1.07	2.29	2953	2214	16.7	8.84	0.97	0.91	6.6
CH_3F/Kr ν_3 1→0(8K)	9.1×10^4	9.1×10^3	2.98	6.07	1036	987	5.10	2.55	1.05	1.04	9.6

B: k_{21}/k_{10} Correlation, Eq. (40)

System	k_{21}	k_{10}	$\nu_{2\to1}$	$\nu_{1\to0}$	B	d	$a\sqrt{A}$
	(sec^{-1})		(cm^{-1})		(cm^{-1})	(Å)	($Å^{-1}$)
HCl/Ar (9K)	3.8×10^3	810	2767	2871	10.5	1.23	1.5
OH*/Ne (4K)	4.0×10^5	9.0×10^4	2784	2970	17.4	0.91	2.9
OD*/Ne (4K)	1.4×10^5	3.9×10^4	2099	2200	9.19	0.86	3.6
NH*/Ar (4K)	6.2×10^6	1.2×10^6	2718	2977	16.7	0.97	3.3

and v=1 → 0 rates. The two results are very consistent, indicating, perhaps, that whatever is responsible for the enhancement of k_{21} relative to k_{10} is not dependent upon isotope. To fit these results with the present model requires either a large value of A or a. For A=1, the value of the range parameter is 10 $\mathring{A}^{-1}$. Ne should certainly appear more repulsive than Ar, but a factor of 2 in a is unlikely.

The NH*/ND* data for Kr can be fit with reasonable values of a and A. The actual rates for these systems are quite high, however, and since the relaxation of NH^* in Kr is so much faster than in Ar, it may be that the present model is not really applicable to NH*. This will be discussed in more detail later.

Comparison of CH_3F and CD_3F relaxation in Kr suggests either a large value for a or A. Since the vibrational mode of CD_3F studied is not its lowest energy mode, it is possible that the reported relaxation rate is due partially to an intra-molecular V→V process, and that the true V→R,P rate is somewhat smaller than reported. If this were so, the present model would fit the data with smaller a or A values.

In summary, the binary collision model almost fits experimental data with reasonable potential parameters a and A. Only for HCl are these parameters available from gas phase studies--the fit of matrix data with gas phase parameters is satisfactory in this case.

b) Potential Parameters

For an ab initio estimate of the relaxation rate, Eq. (37), it is necessary to calculate Γ which requires specification of q_o. Furthermore, it is necessary to specify the range parameter, a. The choice of q_o is fairly arbitrary since the definition of a collision is somewhat

arbitrary. It is clear, however, from Table V, that q_o must be small enough so that the temperature dependence of Γ does not exceed the experimentally measured temperature dependence of the relaxation rate. For HCl/Ar, q_o should be less than 0.3 Å. The probability expression is strongly dependent on the choice of a.

The intermolecular potential between HCl and Ar has been determined from molecular beam elastic scattering studies[30] and from analysis of spectra of the gas phase Ar-HCl van der Waals molecule.[31] The isotropic short range part of the potential is described by a Morse potential:

$$V(x) = D_e\left[e^{-2\beta(x-1)} - 2e^{-\beta(x-1)}\right]$$

$$x = r/r_e \tag{41}$$

where r_e is the position of the potential minimum and D_e is the well-depth of the potential. The parameters r_e, D_e, and β for the potential of Farrar and Lee[30] and the two potentials of Holmgren, Waldman, and Klemperer[31] are given in Table VII. Also given in Table VII is a potential for Ar-Ar.[32] The Morse potential can be matched to an exponential potential of the form

$$V = V_o\, e^{-ar} - E_o \tag{42}$$

by requiring continuity of the potential and its first two derivatives at the matching point, r_m. The value of a so obtained is dependent upon the matching point.

The point at which potentials are matched, r_m, can be identified with a classical turning point on the potential energy surface. However, since initial and final kinetic energies differ by the energy of the vibrational quantum, the classical turning point for the entrance and

Table VI-VII. Fit of Morse Potential to Exponential Potential for HCl/Ar and Ar/Ar

	Potential			
	FL[a]	HWK-I[b]	HWK-II[b]	Ar-Ar[c]
r_e (Å)	4.00	3.80	3.88	3.76
D_e (cm^{-1})	133	131	132	97.8
β	7.00	7.3	6.6	6.28
Match for (J,n) = (0,0): E = 37 cm^{-1}				
r_m (Å)	3.76	3.57	3.63	3.46
V_o ($10^{12} cm^{-1}$)	8.36	14.1	1.29	.0436
E_o (cm^{-1})	151	150	150	116
a ($Å^{-1}$)	6.85	7.34	6.58	5.90
q_o (Å)[d]	0	0.19	0.13	0.30
Match for (J,n) = (0,1): E = 110 cm^{-1}				
r_m (Å)	3.64	3.46	3.49	3.33
V_o ($10^{10} cm^{-1}$)	6.76	11.5	1.29	.185
E_o (cm^{-1})	170	171	172	133
a ($Å^{-1}$)	5.50	5.91	5.23	4.92
q_o (Å)[d]	0.12	0.30	0.27	0.43
Match for average turning point: E = 1400 cm^{-1}				
r_m (Å)	3.16	3.04	3.03	2.82
V_o ($10^8 cm^{-1}$)	5.59	11.2	2.29	.672
E_o (cm^{-1})	327	319	319	262
a ($Å^{-1}$)	4.03	4.42	3.92	3.78
q_o (Å)[d]	0.60	0.72	0.73	0.84
Match for exit channel: E = 2900 cm^{-1}				
r_m (Å)	3.00	2.89	2.83	2.63
V_o ($10^8 cm^{-1}$)	3.61	6.88	1.43	.477
E_o (cm^{-1})	419	414	428	348
a ($Å^{-1}$)	3.87	4.25	3.75	3.64
q_o (Å)[d]	0.76	0.87	0.93	1.13

[a] Ref. 30. [b] Ref. 31. [c] Ref. 32. [d] $q_o \equiv 3.76$ Å $- r_m$.

exit channels is quite different. The collision distance, q_o, can be taken equal to $d_o - r_m$, (d_o is the nearest neighbor separation in the lattice) once r_m has been chosen. The minimum of the HCl-Ar gas phase potentials occur at larger distances than d_o = 3.76 Å for an Ar lattice. Nevertheless, the steep rise of the potential should not be too different in the solid from its behavior in the gas phase, so $d_o - r_m$ should be a reasonable choice for q_o. The systematic error in this procedure is to underestimate q_o.

Potential parameters for matching the HCl/Ar Morse potentials (and Ar/Ar) to Eq. (42) at various turning points are compiled in Table VII. The matching points considered are the turning point of the incoming channel for (J,n) = (0,0) and (J,n) = (0,1), the turning point of the exit channel, E = hν = 2900 cm^{-1}, and at an average energy of the two turning points: 1400 cm^{-1}. Values for q_o and a are dependent upon both the matching point and the potential used. The van der Waals potentials, HWK I and II[31] are perhaps more suitable in the low energy region of the well, while the potential determined from molecular beam scattering is more appropriate for the higher energy matching points: 1400 and 2900 cm^{-1}. No particular choice for q_o and a is compelling. For reasons previously mentioned, a small value for q_o is desirable. Matching potentials at the turning point of (J,n) = (0,0), and averaging q_o obtained from the van der Waals potentials gives q_o = 0.16 Å--this value has been used for numerical evaluation of Γ in much of this Chapter. It is an illustrative value but not required by experimental evidence. In this region, the repulsive parameter a is quite large, and some of the high values of a implied by the correlations of Table VI may be partly rationalized as sampling of the potential in this region. In the higher energy regions, a decreases to more usual values of 3-5 $Å^{-1}$, and

q_o increases to 0.6-0.9 Å. This large a value of q_o will produce a value of Γ which shows a substantial temperature effect (>2 for HCl/Ar between 9 and 20 K). Perhaps a reasonable value for q_o is the average of the turning points for entrance and exit channels. Using HWK I and II for the entrance channel and FL at 2900 cm^{-1} for the exit channel gives q_o = 0.45 Å.

The ambiguity discussed here argues that q_o and a should be empirically adjusted, and the fit values can then be compared to values obtained from other sources.

c) Numerical Results

From the potential parameters discussed above, it is possible to calculate Γ and P_k^{k-1}, and by fitting the result to experimentally measured relaxation rates, a value for the steric factor, s, will be determined. From Model 3 with q_o = 0.16 Å, the collision frequency for HCl/Ar is (Fig. 1)

$$\Gamma = 6(5.15 \times 10^{11}) = 3.1 \times 10^{12} \text{ sec}^{-1}$$

Numerical results for HCl/Ar and DCl/Ar are presented in Table VIII, using Γ as above and calculating the relaxation probability from Eq. (36). The values marked in Table VIII correspond to choices of $a\sqrt{A}$ consistent with the correlations of Table VI. The values for the steric factor with this choice are in the range of 10^{-5} - 10^{-6}. This is quite small by gas phase standards, but might reflect the highly particular nature of effective collisions in the solid and the fact that collision energies in the solid are so small that the range of geometries sampled during a collision is limited. The small values of s may also reflect

Table VI-VIIIA. Numerical Estimation of the Steric Factor, s.[a]

System	k(sec^{-1})	a($Å^{-1}$)	A	$\mu^{\dagger}$(amu)	P[b]	S
HCl/Ar	3.8×10^{3}	6.7	0.36[c]	2.48	8.2×10^{-5}	1.5×10^{-5}
v=2→1		2.9	0.7	1.37	3.6×10^{-10}	3.4
		3.2	0.7	1.37	5.6×10^{-7}	2.2×10^{-3}
		4.8	0.7[c]	1.37	2.5×10^{-5}	4.9×10^{-5}
		4.0	1.0[c]	0.98	1.4×10^{-5}	8.6×10^{-5}
DCl/Ar	110	6.7	0.36[c]	4.49	5.5×10^{-6}	6.5×10^{-6}
v=2→1		2.9	0.7	2.61	2.2×10^{-13}	160
		3.2	0.7	2.61	2.1×10^{-10}	0.17
		4.8	0.7[c]	2.61	2.1×10^{-6}	1.7×10^{-5}
		4.0	1.0[c]	1.90	1.0×10^{-6}	3.5×10^{-5}
OH*/Ne	9.0×10^{4}	4.0	1.0	0.95	4.9×10^{-6}	6.0×10^{-3}
v=1→0		6.0	1.0	0.95	9.2×10^{-4}	3.2×10^{-5}
		16.0	1.0[c]	0.95	0.25	1.2×10^{-7}
		8.0	2.0	0.50	3.6×10^{-2}	8.1×10^{-7}
NH($X^{3}\Sigma$)/Ar	5.3×10^{3}	4.0	1.0	0.97	4.1×10^{-5}	4.2×10^{-5}
v=1→0		6.6	1.0	0.97	2.1×10^{-3}	8.0×10^{-7}

[a] For all systems, Γ is taken equal to 3.1×10^{12} sec^{-1}.

[b] Collisional relaxation probability - Eq. (36).

[c] $a\sqrt{A}$ taken from Table VI.

Table VI-VIIIB. Input Parameters for Calculations of Table VIIIA

System	m(amu)	μ_R(amu)	μ_{BC}(amu)	(1-G)	$\bar{\nu}(cm^{-1})$
HCl/Ar	18.9	1.03	0.97	0.89	2767
DCl/Ar	19.2	2.11	1.89	0.87	2029
OH*/Ne	9.2	1.06	0.94	0.89[a]	2970
NH/Ar	10.9	1.07	0.93	0.87	3131

[a] The local mode frequency for OH/Ne is unknown. The factor (1-G) is set equal to that of HCl/Ar.

an overestimate for Γ, due to a value of q_o that is too small. Choosing a larger value of q_o will reduce Γ (see Table V) and allow a larger value of s. However, as q_o decreases the temperature variation of Γ increases to, perhaps, too large an extent. The choice of a = 2.9 Å^{-1} and A = 0.7 corresponds to the best values derivable from gas phase studies of HCl/Ar V → R,T relaxation.[27] This leads to steric factors in excess of unity. However, for a slight increase of a to 3.2 Å^{-1}, well within the range of fit to the gas phase results, the value of s decreases to 2.2 x 10^{-3}. The gas phase steric factor is estimated to be 0.025, and the gas phase data, as with the matrix data, can be fit with a fair range of potential parameters. It is encouraging, however, that the range of parameters that fit the gas phase V → R,T data overlaps the range that fits the matrix V → R,P data.

Also presented in Table VIII are fits to the V → R,P data for OH*/Ne[43] and NH($X^3\Sigma$)/Ar.[36] The collision frequencies Γ, are taken equal to that for HCl/Ar. For OH* the local mode frequency is unknown, so (1-G) is taken equal to 0.89, which is the value for HCl/Ar. For OH*/Ne values of $a\sqrt{A}$ consistent with Table VI lead to steric factors that are 10^{-6} - 10^{-7}. This is due to the large relaxation probability caused by a very short-ranged potential with a 8 Å^{-1}. For more normal choices of a, 4-6 Å^{-1}, the steric factor is in a range consistent with those of HCl and DCl. For NH/Ar, a local mode of frequency 110 cm^{-1} is assumed since the local mode frequency has not been measured. The value of 110 cm^{-1} is obtained from the 73 cm^{-1} local mode frequency of HCl/Ar, assuming the NH-Ar and HCl-Ar interactions are equal so that the ratio of NH/Ar to HCl/Ar local mode frequencies is $(M_{HCl}/M_{NH})^{\frac{1}{2}}$, where M is the molecular mass. Hence, (1-G) = 0.87. No correlation is available from

Table VI. A choice of $a = 4\ \text{Å}^{-1}$, A=1 leads to a steric factor consistent with the HCl/Ar results.

A term $[1-e^{-2\pi z}]$ was dropped after Eq. (33). For the data of Table VIII, the set of values with the smallest value of z is OH*/Ne with $a = 16\ \text{Å}^{-1}$. Assuming a value of 70 cm^{-1} for the local mode frequency leads to a value of $[1-e^{-2\pi z}] = 0.67$--a 30% error in the calculated steric factor. In view of the range of possible fits, this factor is unimportant. For HCl/Ar, the value of the dropped factor is greater than 0.99.

It is amusing to calculate the V → R,P rate predicted by the binary collision model for CO/Ar. As a guess, $a = 4.0\ \text{Å}^{-1}$, and A = 0.7, so $\mu_{BC} = 6.86$, $\mu_R = 21.0$, $\mu^{\dagger} = 10.6$ amu. The spectroscopic parameters are[44] $\nu = 2138\ cm^{-1}$, $B = 1.93\ cm^{-1}$, $\nu_L = 80\ cm^{-1}$, so G(0,0) = 0.14. Then, $P^0_{1,0,0} = 1.3 \times 10^{-18}$, and for a collision frequency of $3.1 \times 10^{12}\ sec^{-1}$ and a steric factor of one, the calculated V→R rate is $4.1 \times 10^{-6}\ sec^{-1}$. This is much slower than the radiative decay rate of CO/Ar, 70 sec^{-1},[45] and is unobservable.

d) Physical Notions

According to the present model, relaxation is due to sampling of the guest-host potential far from the guest equilibrium position. The forces responsible for spectral perturbations on the guest (see Chapter III) act near the equilibrium position of the guest and are not responsible for relaxation. Vibrational relaxation is a dramatic event: large amounts of energy must be transferred from intramolecular vibration into degrees of freedom with much smaller characteristic energies. This requires a force which has Fourier components at the guest vibrational

frequency--such a force must vary rapidly. The exponential repulsion experienced upon close guest-host encounter is such a force. During such an encounter, the potential experienced by the guest is totally dominated by the particular host atom with which it collides. The presence of the other atoms in the crystal becomes a small perturbation to the guest-host interaction during close encounter and the collision can be described in terms of a binary encounter; that is, with a gas phase potential. This is the physical explanation justifying the use of the binary collision model for relaxation in the solid.

The validity of IBC theory in liquids has been a matter of some debate.[33] Zwanzig[10] has shown that for vibrational relaxation in liquids, the effect of interference between collisions scales as Γ/ν. For the present systems, $\Gamma \sim 3 \times 10^{12}$ sec^{-1} and $\nu \gtrsim 3 \times 10^{13}$ sec^{-1}, so collision events should essentially be isolated and binary. Davis and Oppenheim[33] have argued that for vibrational relaxation in liquids, collisions most effective in inducing vibrational relaxation involve large velocities, and since velocity equilibration may take a few collisions, effective collisions will occur in groups of two or three. The situation where velocity is due to harmonic motion within lattice phonon modes, however, is somewhat different than in liquids, since velocity will change on the time scale of oscillation of the normal modes which is actually a shorter time than the mean time between collisions; hence, Zwanzig's analysis should be correct for solids. In any event, Davis and Oppenheim suggest that even in liquids, interference effects between collisions should be negligible for vibrational energies exceeding 700 cm^{-1}.

For a V→R transition with a change in rotational quantum number ΔJ, the potential causing the transition must have a term in its series expansion corresponding to a ΔJ^{th} order Legendre polynomial. At a lattice site of high symmetry, terms corresponding to high order Legendre polynomials have very small amplitudes or are obtained only by high order perturbation theory. When the guest is displaced by an amount q_o from its lattice site, however, it is in a position (R_{min}, θ_{min}) of lowered symmetry where expansion of the potential may have larger amplitudes for terms of high order Legendre polynomials--hence V→R processes are favored away from the equilibrium site.

From Fig. 2 it is apparent that relaxation of NH* and ND* in Ar and Kr are the fastest points, and that relaxation of NH* in Kr is an order of magnitude faster than relaxation in Ar. As will be discussed below, an increased relaxation rate in Kr is not predicted by the binary collision model. Goodman and Brus[34] have suggested that relaxation of NH* and ND* in Ar and Kr proceeds via chemically interacting ArNH* and KrNH* species and that relaxation is more rapid in Kr because the larger polarizability of Kr compared to Ar produces a stronger attractive interaction. More recently, Goodman and Brus[35] have studied OH* in Ar, Kr, and Xe matrices and find that relaxation is too fast to be measured ($>10^7$ sec^{-1}). They interpret their results in terms of a chemically interacting species in these matrices. The attractive interaction between OH* and Ne is weak, however, and OH*/Ne behaves like a freely rotating system instead of a van der Waals molecule.[35] The more rapid interaction in Kr and Xe matrices than in Ar is indicative of an attractive interaction which is not described by the present binary collision model, which requires a repulsive interaction. Strictly speaking, then,

relaxation of NH* may be outside the domain of the present model. Curve b of Fig. 2 is the correlation of data points neglecting the NH* points. The relaxation of $NH(X^3\Sigma)$[36] is much slower than that of $NH(A^3\Pi)$, however, and as can be seen in Fig. 2, is close to the HCl results. For $NH(X^3\Sigma)$ the repulsive forces may dominate relaxation.

e) Temperature Effects

The temperature dependence of the relaxation rate arises from Γ and from the thermal average of P, Eqs. (9) and (37). These are equivalent to the stimulated phonon effects and the J-level dependent effects discussed in Chapter V.

The temperature dependence of Γ is weak, as has been discussed in Section B.2, above. Its correspondence to stimulated phonon processes is now discussed. For an exothermic phonon assisted process, the rate is described by $R = R_o(1+\bar{n})$, where $\bar{n} = [e^{\hbar\omega/kT} - 1]^{-1}$ is the phonon thermal occupation number. For small T,

$$R = R_o(1+e^{-\hbar\omega/kT}) \tag{43}$$

For the collision model, assume only one phonon mode is important. Then, the temperature dependence is due to σ^2 where, at low temperature

$$\sigma^2 = \frac{\hbar}{2M\omega}\coth(\frac{\hbar\omega}{2kT}) = \frac{\hbar}{2M\omega}(1+2e^{-\hbar\omega/kT}+\ldots).$$

The collision frequency becomes (note that ν is independent of T when only one phonon mode contributes to Γ):

$$\Gamma = \nu e^{-q_o^2/2\sigma^2}$$

$$= \nu e^{-M\omega q_o^2/\hbar}\left(1 + \frac{2q_o^2 M\omega}{\hbar} e^{-\hbar\omega/kT}+\ldots\right) \tag{44}$$

The forms of Eqs. (43) and (44) are similar. If $2q_o^2$ is the maximum amplitude of the phonon mode of frequency ω, then $2q_o^2 M/\hbar = 1$ and Eqs. (43) and (44) become identical. In reality, Γ is due to a sum over many phonon modes--its temperature dependence is due to the sum of phonon temperature effects for many modes.

The temperature dependence of $P_{k,n,J}^{k-1}$ is due to the G(n,J) term. Physically, this is due to the fact that increasing rotational and translational excitation of the guest increases the initial collision velocity. The dependence of $P_{1,n,J}^0$ on (n,J) for HCl and $NH(X^3\Sigma)$ in Ar is illustrated in Table IX. The rotational spacing of $NH(X^3\Sigma)$ in Ar is taken from Bondybey and Brus.[37] The value of $a\sqrt{A}$ has been taken from Table VI for HCl/Ar. For NH/Ar, the value used is also 4.0 Å^{-1}. The temperature dependence decreases as $a\sqrt{A}$ increases. For HCl/Ar, the predicted temperature increase is a factor of 1.6 between 10 and 20 K, in reasonable agreement with the observed ratios of 1.5 and 1.3 for $v=2 \rightarrow 1$ and $v=1 \rightarrow 0$ relaxation. For NH/Ar the temperature dependence is a factor of 1.8 between 10 and 30 K. Bondybey,[36] however, experimentally observes that the relaxation rate increases by less than a factor of 1.1 between 4 and 30 K, so the temperature dependence is overestimated.

The calculated ratio of vibrational relaxation from J=1 to that from J=0 is in accord with the experimental observations for HCl/Ar, presented in Chapter V. The ratio of $k^{J=1}/k^{J=0}$ was, from the data presented in Chapter V, with each k^J assumed temperature independent, 2.7-2.0 for k_{21} and 2.1-1.7 for k_{10}. From Table IX, the predicted ratio is 1.8.

Table VI-IX. Level Dependent V→R Relaxation Probabilities and Temperature Effects

	HCl(v=2→1)/Ar[a]		NH($X^3\Sigma$), (v=1→0)/Ar[a]	
(n,J)	G(n,J)	$\frac{P(n,J)}{P(0,0)}$[b]	G(n,J)	$\frac{P(n,J)}{P(0,0)}$[b]
0,0	0.11	1.00	0.13	1.00
0,1	0.14	1.80	0.17	2.23
0,2	0.19	4.80	0.22	6.05
0,3	0.24	12.8	0.29	24.5
1,0	0.20	5.84	0.23	7.39

Boltzmann Averaged Probabilities: $P(T)/P(0)$[c]

	10K	20K	30K
HCl/Ar	1.20	1.85	2.67
NH/Ar	1.11	1.45	1.98

[a] Parameters used: a = 4.0 Å^{-1}, A = 1.0 for both systems. HCl/Ar: ω_L = 73 cm^{-1}, B = 10.5 cm^{-1}, ν = 2767 cm^{-1}, d = 1.23 Å, μ_R = 1.03 amu, m = 18.9 amu; NH/Ar: ω_L = 110 cm^{-1}(estimate), B = 16.7 cm^{-1}, ν = 3131 cm^{-1}, d = 0.97 Å, μ_R = 1.07, m = 10.9 amu.

[b] From Eq. (38).

[c] From Eq. (37). For HCl/Ar, Q(T) is given by Eq. (V-3). For NH($X^3\Sigma$), Q(T) is calculated from energy levels of Ref. 37: $Q(T) = 1 + 3e^{-24/kT} + 2e^{-83/kT} + 3e^{-104/kT} + \ldots$

A large local mode frequency, ν_L, leads to a small temperature dependence, since σ^2 is dominated by contributions from ν_L, and the onset of stimulated phonon processes in the local mode occurs at relatively high temperature. For large ν_L, G(n,J) is dominated by the contributions from the zero point motion of the local mode, and effects of excited J states will be small compared to the local mode zero point motion.

The main conclusions of this section are qualitative. Quantum effects such as zero point motion and Boltzmann distributions heavily weighted toward the ground rotational-translational state prevent V → R,T rates from being strongly temperature dependent.

f) Effects of Host Lattice

The present model predicts some effects as the host lattice is changed. In matrices, the vibrational frequency changes very slowly from host to host so the overall order and $\sqrt{\nu/cR}$ factor that dominates the probability factor will not change much. Furthermore, rotational spacing should not change enough to influence the Boltzmann factors and G(n,J) factors of Eq. (37). The host matrix will influence Γ by way of σ^2 and q_o. In going from Ar to Kr, the delocalized lattice frequencies decrease, since $h\omega_D$ = 64 cm^{-1} for Ar and 50 cm^{-1} for Kr; thus σ^2 will decrease slightly. The Kr lattice parameter is larger than that of Ar, and hence q_o should be larger for Kr than for Ar. Both of these effects reduce the magnitude and increase the temperature dependence of Γ. The probability expression will be affected by a decrease in the repulsive parameter, a, from Ar to Kr. This will reduce the value of the collisional relaxation probability.

All of these effects are small, and relaxation behavior in Kr should be very similar to that in Ar. All effects which do vary between Ar and Kr do so in a way that decreases the relaxation rate and increases its temperature dependence. In particular, the vibrational relaxation of HCl in a Kr matrix should be slower than in Ar, and should exhibit an increase in relaxation of more than a factor of 1.7 between 9 and 20 K. Unfortunately, values for the HCl-Kr repulsive parameter in the gas phase are not available, so a more detailed prediction cannot be made. The large increase in relaxation rate of NH* in Kr compared to Ar is in discord with the conclusions of the present model. As mentioned previously, this suggests that NH* vibrational relaxation is due to attractive forces.[34]

g) Extension to Other Media

It is interesting to speculate and compare the present model with models of vibrational relaxation in gas and liquid phases. Relaxation is usually considered a collisional phenomenon in the fluid phases[29] and the Mott-Jackson probability expression used in the present model is the basis of relaxation theories in other phases (for example, SSH theory[38] in the gas phase). In low pressure gases, collisions are binary and are described by standard gas kinetic theory. The status of binary collision theory in dense gases and liquids is still a subject of debate.[33] In liquids, however, a cell model for collision frequencies is often successful.[39]

Recently, Delande and Gale[40] have measured vibrational relaxation rates in low temperature solid, liquid, and gaseous H_2. The results are successfully interpreted in a binary collision model, with the density

dependence predicted by the cell model collision frequency expression. Brueck et al.[41] have measured relaxation of CH_3F (ν_3) in liquid Ar and O_2. If their results are interpreted in a binary collision model, their collisional relaxation probability is within an order of magnitude of measured room temperature gas phase relaxation probabilities.[41] Neither of these studies speculate on the physically determining features of the relaxation probability. It is possible that rotation is important, and that this could account for the observation of only one order of magnitude variation in relaxation probability of CH_3F between 300 and 77 K.

It would be very satisfying if binary collision formulae could be smoothly extrapolated from one phase to another. In a binary collision model, the probability expression should be independent of phase. The collision frequency should, however, vary from phase to phase. In the liquid phase, the cell model collision frequency is[42]

$$\Gamma_{cell} = \frac{(8kT/\pi M)^{\frac{1}{2}}}{[\rho^{-1/3} - \sigma]} \tag{45}$$

where M is the molecular mass, ρ is the number density of the host medium, and σ is a hard sphere collision diameter. When $\rho^{-1/3} >> \sigma$, Eq. (45) reduces to the standard gas phase collision frequency. Equation (45) predicts a collision frequency which varies as $T^{\frac{1}{2}}$. The high temperature limit of the solid phase collision frequency, Eq. (9), is independent of temperature. In no regime can the temperature dependence of Γ be made to be $T^{\frac{1}{2}}$. Thus, solid phase collision frequencies do not extrapolate to the liquid phase. This may reflect a fundamental difference between solids and liquids; solids have long-range order which produces well-defined phonon modes, liquids have only short-range order.

5. Summary and Conclusions

Vibrational relaxation in solids has been treated from a binary collision viewpoint. The collision frequency is determined by the motion of a guest and its nearest neighbor due to lattice phonons. The phonons dominant in determining the collision frequency are the high frequency phonons--especially a localized mode when it is present. Due to the low temperatures in matrices, the higher energy phonon modes are dominated by zero point motion and the collision frequency varies very slowly with temperature. The collision frequency is close to the local mode frequency.

The relaxation probability is determined adequately by gas phase repulsive interaction parameters. The probability depends slightly on initial quantum state of the relaxing guest. The temperature dependence of relaxation is small since at low temperatures only the ground quantum state is strongly populated. Inclusion of an effective reduced mass, $\mu^{\dagger}$, introduces rotation as an energy acceptor mode, and the correlation of Legay[12] suggesting the dominance of rotation as an accepting mode is confirmed.

The theory works well for HCl and DCl in solid Ar. Gas phase repulsive potential parameters describing V-R,T relaxation[27] approximate the values implied by the matrix results. It is necessary to postulate a steric factor, and the magnitude of this, 10^{-2} - 10^{-6}, reflects the precision of the geometry necessary for collisions effective in vibrational relaxation. The value of the steric factor is a bit low and is affected by the choice of q_o. As q_o increases, Γ decreases, and s increases, becoming more conventional in magnitude: 0.1-0.01. As q_o increases, however, the temperature dependence of Γ increases and the T

dependence predicted by the model increases. Hence, in choosing parameters to match experimental results, q_o should be taken large to produce reasonable values of s, but not so large as to predict a large temperature dependence for Γ, and hence for the vibrational relaxation rate.

The fit for other molecules is less successful. In particular, the enhancement of the NH* relaxation rate in Kr is not predicted--it is likely that relaxation of NH* is dominated by attractive interactions,[34] and so is outside the realm of the present model. The OH*/Ne and CH_3F/Kr data can be fit to the present model, but require repulsive parameters, a (or anisotropy factors, A) larger than usual for gas phase interactions. This may be due to the inapplicability of the present model to OH* (attractive interactions?) and CD_3F (intra-molecular V→V processes?), however. It would be desirable to have more data for closed shell diatomic systems, such as HCl and DCl in Kr and Xe, and HBr in the rare gas matrices, to more critically evaluate the success of the present model.

The model has some shortcomings. The concept of a collision is somewhat arbitrary. In particular, the choice of q_o is arbitrary. The actual calculated values can vary over several orders of magnitude. Small changes of a or A, which appear in an exponent, necessitate large changes in the steric factor, s. The conceptual framework of the binary collision model is quite appealing, however.

C. Golden Rule Formulation of V→R Rates

Two theoretical treatments of V→R relaxation in solids using the golden rule formalism of time-dependent perturbation theory have appeared

recently. In both treatments, the guest occupies a lattice site and the force responsible for transitions is the sum of forces over many neighbors. For the large changes of rotational quantum number which occur in V→R relaxation, a large anisotropy in the inter-molecular potential is necessary.

1. Theory of Freed and Metiu

Freed and Metiu[46] have constructed their model to rationalize Legay's correlation, Eq. (6), and to agree with experimental observations of very slight temperature dependences for relaxation rates. The role of phonons, localized and bulk, is explicitly neglected except that phonons provide a density of final states for the relaxation process. The interaction force is taken to be linear in the intramolecular vibrational coordinate, and to have an angular dependence given by:

$$F(\phi) = \sum_k F_k \cos(nk\phi) \tag{46}$$

where ϕ is the rotational coordinate of the guest (diatomic) species, n is a symmetry number for the lattice (4 for a planar cubic lattice, 6 for a planar hexagonal lattice, etc.), and F_k is an expansion coefficient that presumably decreases rapidly with increasing k. The force of Eq. (46) is also fit to a two parameter form:[46]

$$F(\phi) \approx V_o \exp(\alpha \cos n\phi) \tag{47}$$

In this expression, V_o and α (not to be confused with the α of Eq. (6)) are adjustable parameters. A general expression for relaxation is obtained from the golden rule taking matrix elements of free plane rotor states of the force of Eqs. (46) or (47).[47] A change in rotational

quantum number is caused by a high order term in Eq. (46) such that $\Delta J = nk$. In the limit that $T \to 0$ and $\Delta J/n = k \gg 1$, the relaxation rate is

$$k(0) \quad \frac{V_o^2}{2\mu\hbar\omega^2} \exp[-\gamma\sqrt{k}] \tag{48}$$

$$\gamma = \frac{2}{n}\left[\ln\left(\frac{2\sqrt{\omega/B}}{n\alpha}\right) - 1\right] \tag{49}$$

where μ, ω, and B are the guest reduced mass, angular vibrational frequency, and vibrational constant. Equation (48) is analogous to Legay's correlation, Eq.(6). The value of γ, however, depends substantially on (ω/B), and hence on the identity of the guest molecule.

Freed, et al.[48] have evaluated the force of Eq. (46) as a sum of Morse potential interactions between each atom of the diatomic guest and every atom of the lattice--such sums needed more than 250,000 terms for convergence to 1% precision. In this sum, contributions of order k arise from the k^{th} and more distant shells of neighbors. For HCl/Ar, then, with $\Delta J = 16$, and a cubic lattice with n=4, relaxation is due to forces from the fourth nearest shell of neighbors--atoms closer than this are not arranged with enough asymmetry to cause relaxation with large ΔJ. The decrease of F_k with k is a consequence of the distance of the k^{th} shell of neighbors.

The calculation of the interaction force[48] verified that Eq. (47) is a good approximation to Eq. (46). Using a pseudo-$(Ar)_2$ guest in a cubic Ar lattice (n=4), values of $\alpha = 0.9$ and $V_o = 1.33 \times 10^{-3}$ erg/cm best matched Eq. (47) to Eq. (46).[48]

With these values, we may substitute parameters for HCl/Ar into Eqs. (48) and (49). The predicted 0 K relaxation rate is 1.1×10^{10}

sec^{-1}, six and a half orders of magnitude faster than the experimental result. The ratio of HCl to DCl relaxation is, however, calculated to be 45--in very good agreement with the experimentally observed ratio of 35. Freed et al.[48] comment that since $(Ar)_n$ is rather bulky, V_o is probably much larger than for real guest molecules, and this may partly explain the calculated rate for HCl/Ar.

Equation (48) is similar to Legay's correlation, but the value of γ changes so that a plot of ln(k) vs $(\omega/B)^{\frac{1}{2}}$ is not linear (see Fig. 2 of Ref. 46). The temperature dependence of the model of Freed and Metiu is difficult to describe--for (ω/B) in the range below 300, extrapolation of trends from Fig. 1 of Ref. 46 suggests that there may be a small but noticeable temperature effect. The absolute rate calculated for HCl/Ar by Eqs. (48) and (49) is too high, but V_o could be severely overestimated. For realistic systems of perturbed rotors and distorted lattice sites, values of k less than $\Delta J/n$ may be effective for relaxation, however, and then the F_k's for smaller k would contribute, increasing the relaxation rate relative to that of a free rotor.

This model produces something akin to Legay's correlation. It may greatly over-simplify phonon and symmetry effects, and that may be responsible for the problems with the theory when it is subjected to close scrutiny.

2. Theory of Gerber and Berkowitz

Gerber and Berkowitz have also treated relaxation by a golden rule formalism, and they take explicit account of the role of phonons. In their first paper[49] it is shown that local phonon modes are more important as energy acceptors than delocalized modes. In a subsequent

paper,[50] relaxation rates are calculated for NH and ND in Ar. In the calculation, only nearest neighbor forces are considered and an exponential repulsive interaction is assumed; the molecular eigenstates are considered as free rotor states. The calculations show that the dominant relaxation channel produces as large a ΔJ as possible consistent with an exothermic process, and the residual energy is emitted as localized phonons and up to one bulk phonon. The details of the calculation are referenced to a future paper;[50] in particular, the origin of the large anisotropy necessary to produce a large ΔJ is not discussed in detail; it is partially due to the anisotropy of a heteronuclear diatomic guest. The calculated non-radiative lifetime for NH/Ar is within a factor of 2.2 of the measured value--excellent agreement.

The temperature dependence in this model is due to stimulated phonon processes and J-level dependent relaxation rates. Since only a few phonons are produced, stimulated phonon processes do not produce observable temperature effects over the range 0-30 K. The relaxation rate of NH, J=1 is calculated to be 28 times faster than relaxation of J=0. From the measured energy of J=1 of NH/Ar, 24 cm^{-1},[37] the relative populations of J=1 and J=0 at 30 K are 0.49 and 0.51 (neglecting J=2). The contribution of J=1 to the relaxation rate cannot be neglected at 30 K, and the rate predicted at 30 K is 14 times that at 0 K, in which all population resides in J=0. Thus, in spite of the claim to the contrary,[50] this model yields a substantial temperature effect for NH/Ar, in disagreement with experiment.[36]

No general correlation equivalent to Eq. (6) arises in this model, and the bulky relaxation expression shown[50] does not appear amenable to simple evaluation for a variety of systems. Much of the computational

detail has not yet been presented, however. In any event, the calculated 0 K relaxation rate of NH/Ar is in excellent accord with experiment.

D. Comparison of Theories

The salient physical features of observed non-radiative decay rates in solids are: 1) For hydride/deuteride systems, an energy gap law is violated since the hydrides relax more rapidly than deuterides; and 2) Measured rates show a very weak temperature dependence, increasing by less than a factor of two between 9 and 20 K, if they show any temperature dependence at all. The multiphonon theories cannot explain both observations simultaneously, as was illustrated for the case of HCl/Ar in Section A. By postulating rotation as the accepting mode, the observations are qualitatively explained.[12,37,43] The theories presented in Sections B and C differ in their physical viewpoint, and are compared below.

In the binary collision model, the potential responsible for relaxation is the short-ranged repulsive interaction between the guest and a host atom dominant upon close encounter, by analogy to the gas phase. In the solid, the potential around the guest equilibrium position is quite flat and hence would not contain Fourier components large enough to cause vibrational relaxation in an impulsive process. In the golden rule formulation, the potential responsible for relaxation is that acting at the equilibrium position of the guest. The force acts continuously, instead of occasionally as in the binary collision model.

Both types of model require large anisotropies to induce large changes of ΔJ necessary in relaxation. In the binary collision model, the anisotropy is due to the displacement, q_o to a position at which the site symmetry is destroyed and to the non-spericity of the guest molecule,

which is introduced by means of the effective reduced mass μ', which combines translational and rotational reduced masses. In the golden rule formulations the anisotropy arises from the lattice as well. In the theory of Freed and Metiu[46] the anisotropy is due to the regular arrangement of distant shells of lattice sites--hence relaxation is caused by forces exerted by distant neighbors. The anisotropy in the model of Gerber and Berkowitz[50] is partly due to the anisotropy of a heteronuclear guest molecule, since the different atoms of the guest sample different ranges of interactions with the nearest neighbors of the lattice. This picture is in accord with that producing the effective reduced mass. Detailed discussion of the full nature of the anisotropy in this model has not yet been presented.

The binary collision model and Freed and Metiu's model[46] strive for simple forms which illustrate Legay's correlation, and in appropriate situations the correlation can be derived in these theories. Freed and Metiu's version of the correlation, Eqs. (48) and (49) exhibits a more complicated dependence of k on J_f than Eq. (6), however. The theory of Gerber and Berkowitz[50] requires a fair amount of computational effort and a general correlation such as Eq. (6) has not yet emerged.

The binary collision model is intended to give a rough estimate of relaxation rates and to correlate data for similar types of systems. For HCl/Ar, use of parameters that describe gas phase V-R,T relaxation works well for the solid. There are unknown factors, such as the steric factor and q_o, which allow substantial manipulation of the calculation to fit experimental results. Freed and Metiu's theory has the same goal of providing rough estimates and correlations. It seems rather unreasonable, however, that the forces inducing relaxation arise from the

fourth neighbor shell. Even so, the rate calculated from their model seems high. Perhaps the neglect of more local anisotropies in the nearest neighbor shell or in the guest itself is a serious omission. The model of Gerber and Berkowitz is quite detailed, and if accurate potential data is available, it may do very well in calculating relaxation rates. Based on what has been published,[49,50] it appears that each evaluation of a rate for a new system is a complex calculation, however. Hence, it is difficult to apply their model. It is perhaps too early to comment on their model in great detail.

One of the appealing features of the binary collision model is that it can be extrapolated from the solid phase to liquids and gases. It shows that the physical notions dominating the relaxation process are independent of phase and are primarily due to close bimolecular forces. The physical picture of relaxation of the binary collision model is quite different from that of the golden rule theories. A unification of the two viewpoints would be satisfying. Mukamel[51] has observed that the collision frequency, Γ, of the binary collision model has a similarity in form to phonon coupling parameters that arise in the multiphonon theories,[1-8] and that this may be the link between the binary collision model and a golden rule formulation. It will be interesting to see how the theory of V→R relaxation in solids develops.

CHAPTER VI

REFERENCES

1. A. Nitzan and J. Jortner, Mol. Phys., 25, 713 (1973).
2. A. Nitzan, S. Mukamel, and J. Jortner, J. Chem. Phys., 60, 3929 (1974).
3. A. Nitzan, S. Mukamel, and J. Jortner, J. Chem. Phys., 63, 200 (1975).
4. J. Jortner, Mol. Phys., 32, 379 (1976).
5. S. H. Lin, J. Chem. Phys., 61, 3810 (1974).
6. S. H. Lin, H. P. Lin, and B. Knittel, J. Chem. Phys., 64, 441 (1976).
7. S. H. Lin, J. Chem. Phys., 65, 1053 (1976).
8. D. J. Diestler, J. Chem. Phys., 60, 2692 (1974).
9. M. H. L. Pryce in Phonons, R. W. H. Stevenson, ed., Oliver and Boyd, Edinburgh (1966).
10. R. W. Zwanzig, J. Chem. Phys., 34, 1931 (1961).
11. H.-Y. Sun and S. A. Rice, J. Chem. Phys., 42, 3826 (1965).
12. F. Legay, Chemical and Biological Applications of Lasers, Vol. II, C. B. Moore, ed., Academic Press, New York (1977).
13. N. B. Slater, Proc. Roy. Soc. Edinburgh A, 64, 161 (1955).
14. N. B. Slater, Theory of Unimolecular Reactions, Cornell, Ithaca, New York (1959).
15. A. Messiah, Quantum Mechanics, Wiley, New York (1958), Chapter XII.
16. P. G. Dawber and R. J. Elliott, Proc. Roy. Soc. (London), A273, 222 (1963).
17. M. Born and K. Huang, Dynamical Theory of Crystal Lattices, Oxford University Press, Oxford (1954).
18. P. D. Mannheim, Phys. Rev., B5, 745 (1972).
19. P. D. Mannheim and S. S. Cohen, Phys. Rev., B4, 3748 (1971).
20. P. D. Mannheim, J. Chem. Phys., 56, 1006 (1972).

21. J. M. Jackson and N. F. Mott, Proc. Roy. Soc. (London), A137, 703 (1932).

22. M. S. Child, Molecular Collision Theory, Academic Press, London (1974), Section 7.2.

23. E. E. Nikitin, Teor. Eksp. Khim., 3, 185 (1967).

24. E. E. Nikitin, Theory of Elementary Atomic and Molecular Processes in Gases, Clarendon Press, Oxford (1974).

25. G. A. Kapralova, E. E. Nikitin, and A. M. Chaikin, Chem. Phys. Lett., 2, 581 (1968).

26. C. B. Moore, J. Chem. Phys., 43, 2979 (1965).

27. R. V. Steele and C. B. Moore, J. Chem. Phys., 60, 2794 (1974).

28. The data is taken from Table 3 of Reference 12.

29. K. F. Herzfeld and T. A. Litovitz, Absorption and Dispersion of Ultrasonic Waves, Academic Press, New York (1959).

30. J. M. Farrar and Y. T. Lee, Chem. Phys. Lett., 26, 428 (1974).

31. S. L. Holmgren, M. Waldman, and W. Klemperer, J. Chem. Phys., to be published.

32. J. M. Parson, P. E. Siska, and Y. T. Lee, J. Chem. Phys., 56, 1511 (1972).

33. P. K. Davis and I. Oppenheim, J. Chem. Phys., 57, 505 (1972).

34. J. Goodman and L. E. Brus, J. Chem. Phys., 65, 3146 (1976).

35. J. Goodman and L. E. Brus, J. Chem. Phys., submitted.

36. V. E. Bondybey, J. Chem. Phys., 65, 5138 (1976).

37. V. E. Bondybey and L. E. Brus, J. Chem. Phys., 63, 794 (1975).

38. R. N. Schwartz, Z. I. Slawsky, and K. F. Herzfeld, J. Chem. Phys., 22, 767 (1954).

39. W. M. Madigosky and T. A. Litovitz, J. Chem. Phys., 34, 489 (1961).

40. C. Delande and G. M. Gale, Chem. Phys. Lett., 50, 339 (1977).

41. S. R. J. Brueck, T. F. Deutsch, and R. M. Osgood, Chem. Phys. Lett., 51, 339 (1977).

42. P. K. Davis, J. Chem. Phys., 57, 517 (1972).

43. L. E. Brus and V. E. Bondybey, J. Chem. Phys., 63, 786 (1975).

44. H. Dubost, Chem. Phys., 12, 139 (1976).

45. H. Dubost and R. Charneau, Chem. Phys., 12, 407 (1976).

46. K. F. Freed and H. Metiu, Chem. Phys. Lett., 43, 363 (1977).

47. Equations (2) and (4) of Reference 46 contain algebraic errors in the factors before the summation.

48. K. F. Freed, D. L. Yeager, and H. Metiu, Chem. Phys. Lett., 49, 19 (1977).

49. M. Berkowitz and R. B. Gerber, Chem. Phys. Lett., 49, 260 (1977).

50. R. B. Gerber and M. Berkowitz, Phys. Rev. Lett., 39, 1000 (1977).

51. S. Mukamel, private communication (1977).

52. P. F. Zittel and C. B. Moore, J. Chem. Phys., 58, 2004 (1973).

APPENDIX A

RELATIONS AMONG EINSTEIN COEFFICIENTS, TRANSITION MOMENTS, ETC., IN GASES AND DIELECTRIC MEDIA

The Einstein A coefficient can be written in a Fermi golden rule type expression

$$A = \frac{2\pi}{\hbar} |\langle \underset{\sim}{\mu} \cdot \underset{\sim}{E} \rangle|^2 \rho(\varepsilon)$$

$$= \frac{2\pi}{3\hbar} |\mu|^2 |E|^2 \rho(\varepsilon) \qquad (1)$$

where μ is the molecular dipole transition moment, $\underset{\sim}{E}$ is the electric field due to zero point fluctuations of the vacuum responsible for spontaneous emission, and $\rho(\varepsilon)$ is the number of photon states at energy $\varepsilon = h\nu$ for a transition of frequency ν. When the molecule is placed in a dielectric medium of refractive index $n = \sqrt{\epsilon}$, where ϵ is the dispersionless dielectric constant, $|\mu|^2$, $|E|^2$, $\rho(\varepsilon)$ and the transition frequency ν may change. In particular, $\rho(\varepsilon)$ is proportional to the volume of momentum space occupied by photon states of energy $h\nu$:[1] this is proportional to $p^3 = (h\nu n/c)^3$. The ratio of $|E|^2$ in the dielectric to the gas is

$$\left|\frac{E_{eff}}{E_g}\right|^2 = \left|\frac{E_{eff}}{E_s}\right|^2 \left|\frac{E_s}{E_g}\right|^2$$

where E_{eff} is the effective field acting at the site of the molecule and E_s is the bulk electric field in the dielectric. The field E_{eff} is calculated by forming a spherical cavity at the site of the molecule and calculating the field at the center of this cavity due to polarization of the remainder of the dielectric[2], and is

$$E_{eff}^2 = \left(\frac{n^2+2}{3}\right)^2 E_s^2.$$

The ratio of fields in the dielectric to vacuum is $|E_s/E_g| = 1/n$. Finally, allowing μ and ν to be dependent on environment, all the factors relevant to Eq. (1) can be collected, and the ratio of A in the dielectric(s) to the gas is

$$\frac{A_s}{A_g} = n\left(\frac{n^2+2}{3}\right)^2 \left|\frac{\mu_s}{\mu_g}\right|^2 \left(\frac{\nu_s}{\nu_g}\right)^3 \tag{2}$$

The ratio of A and B coefficients in a dielectric is[3]

$$A = \frac{8\pi h\nu^3 n^3}{c^3} B$$

so

$$\frac{B_s}{B_g} = \frac{1}{n^2}\left(\frac{n^2+2}{3}\right)^2 \left|\frac{\mu_s}{\mu_g}\right|^2 \tag{3}$$

Strickler and Berg[3] give the expression for the integrated molar extinction coefficient $\varepsilon(\nu)$ in a dielectric as

$$B = \frac{2303c}{hnN} \int \frac{\varepsilon(\nu)d\nu}{\nu}$$

where N is Avogadro's number. Converting to absorbance, $\alpha(\nu) = 2303\,\varepsilon(\nu)/N$, where concentration is now measured in number/cm^3, and assuming a narrow absorption line so that $\Delta\nu \ll \nu$, gives the expression for the integrated absorbance, in units of cm/molecule:

$$A = \int \alpha(\nu)d\nu = \frac{hn\nu}{c} B \tag{4}$$

The ratio of integrated absorbances in solid and gas is given by Eqs. (3) and (4):

$$\frac{A_s}{A_g} = \frac{1}{n}\left(\frac{n^2+2}{3}\right)^2 \frac{\nu_s}{\nu_g}\left|\frac{\mu_s}{\mu_g}\right|^2. \tag{5}$$

This reduces to the result of Polo and Wilson[4] when $\nu_s = \nu_g$ and $\mu_s = \mu_g$.

For completeness, the relation between A and $\mathring{A}$ in a dielectric is

$$A = \frac{8\pi\nu^2 n^2}{c^2}\mathring{A} \tag{6}$$

All of the above treatment neglects any effects due to polarization of the dielectric by the guest molecule. Fulton[5] has formulated the problem to include such effects. The difference between his more exact treatment and the present results should be small.[6] The present results are accurate for a reasonable estimation of the changes in radiative lifetime and absorption coefficient when a molecule is taken from gas phase to a solid.

APPENDIX A

REFERENCES

1. M. Lax, J. Chem. Phys., 20, 1752 (1952).

2. P. Debye, Polar Molecules, Dover, New York (1958).

3. S. J. Strickler and R. A. Berg, J. Chem. Phys., 37, 814 (1962).

4. S. R. Polo and M. K. Wilson, J. Chem. Phys., 23, 2376 (1955).

5. R. L. Fulton, J. Chem. Phys., 61, 4141 (1974).

6. Equations (2) and (5) above result from Fulton's Eqs. (72) and (45) when his parameter $\xi = 0$. From Fig. (1) of Ref. 5, $\xi < 0.1$ for systems with $\epsilon < 5$. Reference 5 does not allow for variations in ν and μ.

APPENDIX B

DIPOLE-DIPOLE ENERGY TRANSFER: CONVOLUTION FROM DONOR TO ACCEPTOR POPULATION

This is a mathematical appendix in which Eqs. (IV-24) and (IV-27) are derived. The rate equations, Eqs. (IV-22), (IV-23) and (IV-26) are valid when acceptors are concentrated enough or relax rapidly enough so that acceptors always appear unexcited to donors.

Equation (IV-24):

We start with Eqs. (IV-22) and (IV-23). Let

$$n_A(t) = \eta(t)\, e^{-k_o^A t} \tag{1}$$

Equation (IV-23) becomes

$$e^{-k_o^A t}\frac{d\eta}{dt} = k_{ET}(t)\, n_D(t)$$

$$= (a+bt^{-1/2})\, n_D(t) \tag{2}$$

This can be rearranged in integral form

$$\eta(t) = \int_o^t (a+b\xi^{-1/2})\, n_D(\xi)\, e^{k_o^A \xi}\, d\xi \tag{3}$$

The behavior of $n_D(t)$ is given by Eq. (IV-21). Equation (3) becomes

$$\eta(t) = n_D(0) \int_o^t (a+b\xi^{-1/2})\, \exp[(k_o^A - k_o^D - a)\xi - 2b\xi^{1/2}]\, d\xi$$

Let

$$p^2 = k_o^D + a - k_o^A$$

$$y = p\sqrt{\xi} + b/p$$

Then, after straightforward manipulation

$$n(t) = \frac{2n_D(0)}{p} e^{-(b/p)^2} \left\{ \frac{a}{p} \int_{b/p}^{p\sqrt{t}+b/p} ye^{-y^2}\, dy + \left(b - \frac{ab}{p^2}\right) \int_{b/p}^{p\sqrt{t}+b/p} e^{-y^2}\, dy \right\} \tag{4}$$

The integrals in Eq. (4) are

$$\int_{\alpha}^{\beta} ye^{-y^2}\, dy = \frac{1}{2}(e^{-\alpha^2} - e^{-\beta^2}) \tag{5}$$

$$\int_{\alpha}^{\beta} e^{-y^2}\, dy = \frac{1}{2}\sqrt{\pi}[\mathrm{erf}(\beta) - \mathrm{erf}(\alpha)] \tag{6}$$

where erf is the error function.[1] Performing the integrations in Eq. (4) and recalling Eq. (1) leads to the final result, Eq. (IV-24).

A special case of Eq. (IV-24), the limit of no diffusion (case A, page 211), has been derived by Birks.[2]

Equation (IV-27):

Let

$$n_1(t) = n(t)\, e^{-k_{21}t} \tag{7}$$

Then, Eq. (IV-26) becomes

$$\frac{dn}{dt} = k_{21}N_o + (k_{21} - k_{10} - a - bt^{-1/2})\, n \tag{8}$$

where $n_2(t) = N_o e^{-k_{21}t}$ has been used. Equation (8) is solved by reduction to quadrature.[3]

$$\eta(t) = \eta(0)\, e^{-c(t)} + k_{21} N_o e^{-c(t)} \int_o^t \exp[c(\xi)]\, d\xi \qquad (9)$$

$$c(t) = \int_o^t (a + b\zeta^{-\frac{1}{2}} + k_{10} - k_{21})\, d\zeta$$

$$= 2bt^{\frac{1}{2}} - qt \qquad (10)$$

where $q = k_{21} - k_{10} - a$.

The integral of Eq. (9) is evaluated with the substitution

$$w = \sqrt{q\xi} - b/\sqrt{q}$$

to give

$$\int_o^t \exp[c(\xi)]\, d\xi = e^{-b^2/q}\left[\frac{2}{q}\int_{-b/\sqrt{q}}^{\sqrt{qt}+b/\sqrt{q}} we^{-w^2}\, dw + \frac{2b}{q^{3/2}}\int_{b/\sqrt{q}}^{\sqrt{qt}\pm b\sqrt{q}} e^{-w^2}\, dw\right] \qquad (11)$$

The integrals in Eq. (11) are given by Eqs. (5) and (6). Combining Eqs. (9) - (11) and recalling Eq. (7) gives the final result, Eq. (IV-27).

APPENDIX B

REFERENCES

1. M. Abramowitz and I. A. Stegun, eds., Handbook of Mathematical Functions, Dover, New York (1965), Chapter 7.

2. J. B. Birks, J. Phys. B., At. Mol. Phys., 1, 946 (1968).

3. E. R. Benton in Handbook of Applied Mathematics, C. E. Pearson, ed., Van Nostrand Reinhold, New York (1974), Chapter 6.

Appendix C. Properties of Some Guest Molecules

	$H^{35}Cl$	$D^{35}Cl$	$^{12}C^{16}O$	Ref.
Gas Phase:				
ω_e (cm^{-1})	2991.0	2145.2	2169.8	1,2
$\omega_e x_e$ (cm^{-1})	52.85	27.18	13.29	1,2
B (cm^{-1})	10.59	5.49	1.923	1,2
Dipole moment (D)	1.11	1.10	0.13	3
Lennard-Jones parameters: ϵ/k (K)	360	(360)	100	4
σ (Å)	3.3	(3.3)	3.8	4
$S_{0\to1}$ (10^{-18} cm/molecule)[a]	5.52	2.7	10.6	5,6,7
$S_{0\to2}$ (10^{-18} cm/molecule)[a]	.152	.043	.084	5,6,7
$A_{1\to0}$ (sec^{-1})[b]	33.9	10.5	30.3	8,9,10
$A_{2\to0}$ (sec^{-1})[b]	2.82	.646	1.0[c]	8,9,7
$A_{2\to1}$ (sec^{-1})[b]	63.7	19.1		8,9
Ar Matrix:				
ω_e (cm^{-1})	2974	2133	2165.1[d]	11,12
$\omega_e x_e$ (cm^{-1})	52	27	13.29	11,12
Local mode (cm^{-1})	73	72	80	13,14
a_{RTC} (Å)	.093	.059		15
Linewidths (cm^{-1}), 9K				
R(0), P(1)	1.1	1.1	0.47[e]	11,14
R(1)	10	1.5[f]		16,11
Linewidths (cm^{-1}) 20 K				
R(0), P(1)	2.4	2.7	5.[e]	11,17
R(1)	10	2.9[f]		16,11
Boltzmann factors				
9 K J=0	.831	.598		11
J=1	.165	.363		11
J=2[g]	4.3×10^{-3}	.0281 9.89×10^{-3}		11
20 K J=0	.467	.305		11
J=1	.412	.443		11
J=2[g]	.106	.139 .0694		11

Appendix C Footnotes

[a] Absorption band intensity.

[b] Einstein A coefficient.

[c] Calculated from corresponding absorption coefficient.

[d] Dubost and Charneau, Ref. 12, use a matrix vibrational shift and the gas phase ω_e. This is equivalent to, and is presented as, a matrix dependent ω_e.

[e] Linewidth for non-rotating CO monomer.

[f] Linewidth for $T_{1u} \rightarrow T_{2g}$ transition. The width for $T_{1u} \rightarrow E_g$ may be about 3 cm^{-1}, but S/N is low.

[g] For DCl, J=2 is split into T_{2g} and E_g. Upper level given is T_{2g}, lower level is E_g.

APPENDIX C

REFERENCES

1. D. H. Rank, D. P. Eastman, B. S. Rao, and T. A. Wiggins, J. Opt. Soc. Am., 52, 1 (1962).

2. D. H. Rank, A. G. St. Pierre, and T. A. Wiggins, J. Mol. Spect., 18, 418 (1965).

3. A. L. McClellan, Tables of Experimental Dipole Moments, Vol. I, Freeman, San Francisco (1963); Vol. II, Rahara, El Cerrito (1973).

4. J. O. Hirschfeld, C. F. Curtiss, and R. B. Bird, Molecular Theory of Gases and Liquids, Wiley, New York (1954).

5. R. A. Toth, R. H. Hunt, and E. K. Plyler, J. Mol. Spect., 35, 110 (1970).

6. W. S. Benedict, R. Herman, G. E. Moore, and S. Silverman, J. Chem. Phys., 26, 1671 (1957).

7. R. A. Toth, R. H. Hunt, and E. K. Plyler, J. Mol. Spect., 32, 85 (1969).

8. J. K. Cashion and J. C. Polanyi, Proc. Royal Soc. (London), A258, 529 (1960).

9. F. G. Smith, J. Quant. Spect. Radiative Trans., 13, 717 (1973).

10. R. C. Millikan, J. Chem. Phys., 38, 2855 (1963).

11. J. M. Wiesenfeld, Thesis, University of California, Berkeley, 1978.

12. H. Dubost and R. Charneau, Chem. Phys., 12, 407 (1976).

13. H. E. Hallam, Vibrational Spectroscopy of Trapped Species, Wiley, New York (1973), Chapter 3.

14. H. Dubost, Chem. Phys., 12, 139 (1976).

15. H. Friedmann and S. Kimel, J. Chem. Phys., 47, 3589 (1967).

16. P. D. Mannheim and H. Friedmann, Phys. Stat. Sol., 39, 409 (1970).

17. J. M. Wiesenfeld, unpublished results.